CONTINUOUS-WAVE, SINGLY-RESONANT OPTICAL PARAMETRIC OSCILLATORS PUMPED INTERNAL TO Nd:YVO_4 LASERS

David James Mark Stothard

A Thesis Submitted for the Degree of PhD
at the
University of St Andrews

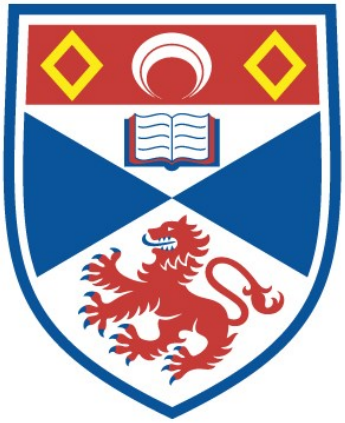

2002

Continuous-wave, singly-resonant optical parametric oscillators pumped internal to Nd:YVO_4 lasers

David J. M. Stothard, MPhys (Hons)

A thesis submitted to the University of St Andrews
in application for the degree of Doctor of Philosophy

30th September, 2001

Declarations

I, David James Mark Stothard, hereby certify that this thesis, which is approximately 46,500 words in length, has been written by me, that it is a record of the work carried out by me and that it has not been submitted in any previous application for a higher degree.

David J. M. Stothard September 30th, 2001

I was admitted as a research student in October 1997 and as a candidate for the degree of Doctor of Philosophy in 1998; the study for which this is a record was carried out in the University of St. Andrews between 1997 and 2000.

David J. M. Stothard September 30th, 2001

We hereby certify that the candidate has fulfilled the conditions of the Resolutions and Regulations appropriate for the degree of Doctor of Philosophy in the University of St. Andrews and that the candidate is qualified to submit this thesis in the application for that degree.

Malcolm H. Dunn September 30th, 2001

Majid Ebrahimzadeh September 30th, 2001

Copyright Declaration

In submitting this thesis to the University of St. Andrews I understand that I am giving permission for it to be made available for use in accordance with regulations of the University Library for the time being in force, subject to any copyright vested in the work not being affected thereby. I also understand that the title and abstract will be published, and that a copy of the work may be made and supplied to any *bona fide* library or research worker.

David J. M. Stothard September 30th, 2001

Abstract

The advent of new quasi phase matched materials and high spectral / spatial quality pump sources has led to a renaissance in the development of continuous-wave optical parametric oscillators for the coherent generation of broadly tunable light in the mid infrared spectral region. This thesis describes a novel technique which overcomes the threshold constraints of the singly resonant oscillator (SRO) and stability constraints of the doubly resonant oscillator (DRO) traditionally associated with these devices by placing a singly resonant optical parametric oscillator in the high circulating field found within the cavity of a laser: the *intracavity optical parametric oscillator*.

An SRO based upon the nonlinear material periodically poled $LiNbO_3$ (PPLN) operating internal to an all solid state, 1W diode pumped Nd:YVO_4 mini-laser is demonstrated and characterised. This system exhibits SRO threshold at only 330mW of external diode pump power, and produced a total of 70mW of extractable idler at 1W diode pump power. Through multi-parameter tuning of the poled nonlinear material we demonstrate broad tuning of the non-resonant idler through the spectrally important range 3.1 – 4μm. Novel cavity design desensitises the system to the effects of thermal lensing in the nonlinear medium, resulting in stable spatial and mean power outputs. The short term pump field stability is characterised by intensity modulation brought about by the onset of relaxation oscillations; a consequence of placing the SRO within the cavity of the pump laser.

A comparative study of SRO's based upon PPLN and the new material periodically poled $RbTiOAsO_4$ (PPRTA) pumped internal to a high power fibre coupled diode pumped Nd:YVO_4 laser cavity is undertaken and presented. We see that although the nonlinearity and interaction length of the PPRTA is smaller than that of PPLN, the system based upon PPRTA outperforms or is at least comparable with that based upon PPLN in every respect with the exception of idler tuning range. We attribute this to the reduced sensitivity of this material to the effect of thermal lensing. Up to 440mW of extracted idler was produced by each system. The reduction of interferometric feedback of the pump field by the signal cavity mirror was found to eliminate the onset of relaxation oscillations in the case of PPRTA but not PPLN, due to thermal air currents dominating the triggering process in

this system. Recently published Sellmeier equations and temperature derivatives for PPRTA are compared with the experimentally observed temperature tuning behaviour.

The inclusion of an optical parametric oscillator within the cavity of the pump laser impacts significantly upon the transient dynamics of the pump laser in which it resides. We show experimental evidence of this effect and outline a strategy to minimise the effects of relaxation oscillations in the context of a simple numerical model which shall be derived.

Possible future avenues of research are discussed in the context of the results and conclusions obtained over the course of this research program.

Acknowledgements

As I sit here thinking of what to write in this section of my thesis, I find myself smiling as I cast my mind back to the people that I have had the very good fortune to work, argue and otherwise interact with during my time here in St. Andrews. First and foremost, I want to extend my sincere gratitude towards my two supervisors, Dr. Majid Ebrahimzadeh and Professor Malcolm H. Dunn. Apart from being a source of constant encouragement, support and good ideas throughout this research program, they have both given me a great deal of autonomy in which I could explore other areas of interest, most notably electronics and instrumentation, and always turned a blind eye as long as I was doing *something* constructive. I am teeming with gratitude towards them.

As soon as I joined the CW-OPO group here at St. Andrews, I was made to feel that both my presence was welcome and my opinion valued. My fellow group members have since offered me unfailing support and advice. I thank Graham for always managing to point me in the right direction (a quick suggestion from him would often lead weeks of fruitful research), to Ian for answering all my stupid questions (and for forgiving me for losing all those bits of equipment) and lastly to Tom, whose enthusiasm and down-to-earth attitude towards the subject as been inspirational, and whose quality of friendship has been unfailing.

In the last couple of years, the group swelled as new research students arrived. I thank Costas for making me smile every time he walked into the room, Alison for her assistance during certain aspects of my research, and Michael who has provided me with endless amusement by finding mistakes in Ian's thesis. Pierre and Philip joined us all too briefly from overseas to lend a helping hand which they did with amazing determination: their contribution and warm friendship was felt long after their departure.

There have been other people in the department who have also helped make my time here so memorable. I thank Graham, David, James, Gavin, Anna, Duncan, Donald, Steve, the technical staff (and in particular George who, no matter how much he insulted me or the quality of my work, always managed to be witty, amusing and even *charming*), the electronics technicians and, of course, the secretarial staff. I must say a special thanks to

Cameron for the both the wealth of equipment which he always seemed to have at his fingertips (which he never seemed to mind lending me), and for all the useful chats we have had. Half an hour talking through and experimental problem with him would often put an end to weeks of frustration in the laboratory. The man is a living legend.

Of course, not all of my time was spent in the laboratory – I *did* have the occasional weekend off! I must thank all of my fellow residents that made Fife Park the social epicenter it was, and all the other people that have offered me friendship and support during and before my time here: Stewart, Ben, Bruno, Angela, Sam, Fiona, Jorge, Dan, Richard, Mary, Rachel, Helen, Justin, Nathan, Julia and Dr. Tilley.

A special thanks is reserved for Kurt, a Romanian gentleman who has the heart of a poet, the charm of an intellectual and the manner of a primate: a lovelier fellow you will never meet, and someone I am proud to have as my friend.

Over the last year, my life here in St. Andrews has been transformed by the woman I love: Kate. I thank her for opening my eyes to the pleasures of a simple (!) meal, the enjoyment to be had from a glass of fine wine, the hidden fascinations of how chimpanzees see the world (or not, as apparently the case may be), for pushing me to think further and, more than anything else, for allowing me to know the happiness that comes from being with somebody I care about so much. She is a wonderful person in every respect.

Lastly, I must thank my family: my mother, father and brother. The love, support and encouragement they have always shown me has been the greatest asset I have ever had, and I think the largest single factor behind any success I have achieved. From the moment they allowed me to have my own shed, my curiosity about the way things worked was nurtured by them in a way no teacher or lecturer ever could. Even when my exploits would lead to circuit breakers tripping, smoke emerging from my bedroom and junk piled high throughout the house, they tried not to spoil my fun *too* much (although having said that, even though my mother would never admit to it, I know that she is secretly relieved that never again will she have to endure the reception on her television being disrupted by some 'experiment' I might conduct). They are three very special people to whom I dedicate this thesis.

Table of contents

1. Introduction

2. Theoretical Background

3. *Diode pumped solid-state lasers*

4. *Continuous-wave operation of a 1W diode pumped Nd:YVO_4 – PPLN ICSRO*

5. *High power operation of a Nd:YVO_4 ICSRO based upon PPLN and PPRTA*

6. *A numerical analysis of relaxation oscillations*

7. *Conclusions*

Appendix A

Appendix B

1: Introduction

1.1 Introduction

Since their inception in the early 1960's, progress in the application of lasers has been closely linked to both their temporal and spectral qualities. Continuous wave (cw) lasers in particular offer an excellent narrow line width source for high-resolution spectroscopic techniques. Whilst there are many established tunable laser systems operating in the visible and near IR region of the spectrum, such as dye, Titanium sapphire, excimer, semiconductor and transition metal solid-state gain based lasers, the mid- to far-infrared (2~5μm) region is very poorly served, even though there is an ever-increasing demand for tunable sources in this region as more spectroscopic applications are devised, such as trace gas detection and meteorological sensing. Although in recent years semiconductor devices such as lead salt and quantum well laser diodes have, to some extent, addressed this gap in the wavelength coverage of laser systems, these devices typically have a very low power output in the μW range, are not broadly tunable and can be difficult to implement.

Although lasing species may be developed in the future to cover this optical band, alternative mechanisms for producing tunable light in the mid infra-red are available and this thesis shall investigate one of these, the *intracavity optical parametric oscillator* operated internal to diode-pumped solid state Nd:YVO_4 lasers.

1.2 Basic principles of Optical Parametric Oscillators

The optical parametric oscillator is a frequency converter. It is a device in which a coherent stream of pump photons, propagating in a nonlinear material, is converted into two photons of lower energy (i.e. longer wavelength), termed the signal and idler, such that the sum of the frequencies (or energies) of these two waves is equal to that of the pump photon, such that

$$\nu_p = \nu_s + \nu_i \tag{1.1}$$

By convention, the higher energy (i.e. shorter wavelength) photon is signified as the signal (figure 1.1). These two generated waves retain the coherent and spectral properties of the laser pump source. The resulting signal/idler pair is determined by the momentum conservation relation that maintains the relative phase between the pump, signal and idler waves. The momentum conservation relation, or more commonly the *phase-matching* condition, requires that the sum of the wave vectors of the generated photons equals that of the pump photon. As many signal/idler pair combinations can satify the momentum conservation relation, the optical parametric generation is very broadly tunable over the transparency range of the nonlinear medium. The parametric gain derived from the nonlinear process is very low. By placing the nonlinear crystal in a cavity which exhibits feedback at the signal, idler or both fields, an *optical parametric oscillator* is formed (figure 1.1). Now the optical parametric process occurs in the presence of at least one resonant field, significantly reducing device threshold.

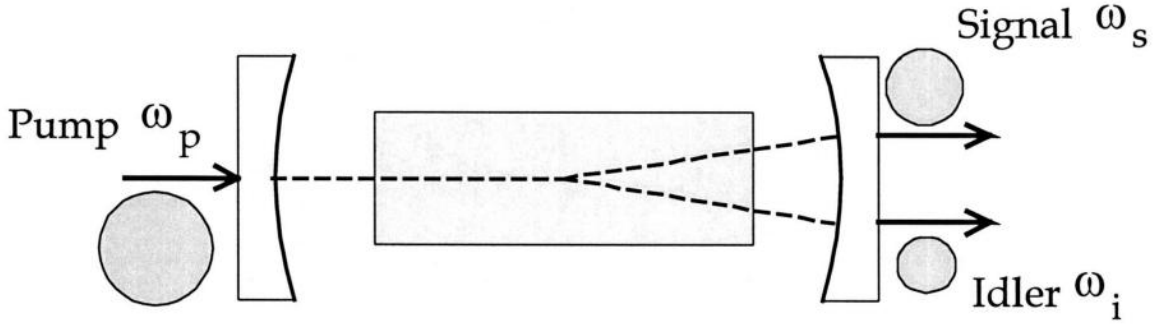

Figure 1.1: *Schematic of OPO, The high energy pump photon is split into lower energy signal and idler photons.*

Many of the major advances in optical parametric oscillator research have been closely linked with new cavity geometries, which are generally developed to reduce device threshold or enhance the tuning characteristics of the device. For instance, in the *pump-enhanced* scheme, the mirrors forming the cavity about the nonlinear crystal exhibit feedback at either the signal or idler fields and the pump field. Active cavity length control keeps the cavity on resonance with the (single frequency) pump field, enabling the optical parametric process to occur as a product of two circulating fields, reducing OPO threshold to easily obtainable power levels. Particular examples of different cavity geometries are described later in this introductory chapter. This thesis will deal with a recently developed scheme which places the OPO *inside* the cavity of the pump laser

where the circulating field is extremely high. OPO threshold therefore occurs at extremely low external pump powers. The *intracavity optical parametric oscillator* (ICOPO), therefore, offers output powers in the 10's mW to >1W level in the mid-infrared band of the spectrum at very modest pump powers compared to other pumping geometries.

The other principle factor which has led to significant advances in this field has been developments in the nonlinear crystals which are at the heart of these devices. Early examples of OPO's were based upon birefringently phase matched crystals which are characterised by relatively low nonlinear gain, and the tuning mechanisms associated with them had significant problems in terms of the operation of the device. Recently, a new method phase matching, *quasi-phase matching* (QPM) has been developed which obviated all of these problems whilst exhibiting extremely large nonlinear gain. This thesis will concentrate on the application of these QPM periodically-poled materials in the context of the intracavity approach.

The development of all solid-state lasers has opened up many new and exciting field applications for laser systems which were previously restricted to the research laboratory. A major component in the advance of these devices has been the appearance of high power, long lifetime laser diodes which form the optical pump source for these systems. One of the principle objectives of the research described in this thesis was to unite these recent advances in diode pumped solid state laser technology with the low threshold, broad tunability exhibited by ICOPO's to produce a laser system which, as well as being interesting from a scientific point of view, would point to a strategy for the development of a practical source of mid-infrared light for use in field applications.

1.3 Diode pumped solid-state lasers

Over the last decade or so, diode-pumped solid-state lasers (DPSSL's) have revolutionised laser devices in terms of efficiency, simplicity and reliability. By matching the spectral output of a diode-laser to that of an absorption band in the laser gain media, coupling efficiency between the pump source and gain media is improved over that of gas filled arc lamps by many orders of magnitude. This, coupled with the very high electrical-to-optical efficiency and brightness of laser diodes has led to extremely compact high

power systems which out perform their flash lamp pumped counterparts in every category, except perhaps where very high output power are required. A detailed discussion of the many fine attributed exhibited by DPSSL's is present later in this thesis.

1.4 New opportunities for nonlinear materials

The traditional method of obtaining phase matching is through the use of birefringence of the nonlinear crystal [1]. Such phase matching schemes are one of two types: in type I phase matching, the two longer wavelengths in a three wave interaction have the ordinary polarisation whilst the shortest wavelength is polarised in the extraordinary axis. With type II phase matching, one of the two longer wavelengths have the same polarisation as the shorter wavelength field (Figure 1.2). For example, in the case of second harmonic generation (SHG) or a degenerate OPO in $LiNbO_3$, which is a type I phase matched interaction, phase matching requires that both wavelengths experience the same refractive index within the nonlinear material. Figure 1.3 shows that in this crystal there are two solutions for phase matching along the crystal axis at 25°C. Such solutions have no wave-vector miss-match (Δk=0) and satisfy the energy conservation condition for SHG that the shorter wavelength is half the value of the longer wavelength. Unfortunately, the solutions are of little practical use since they do not match the wavelengths of any common laser lines.

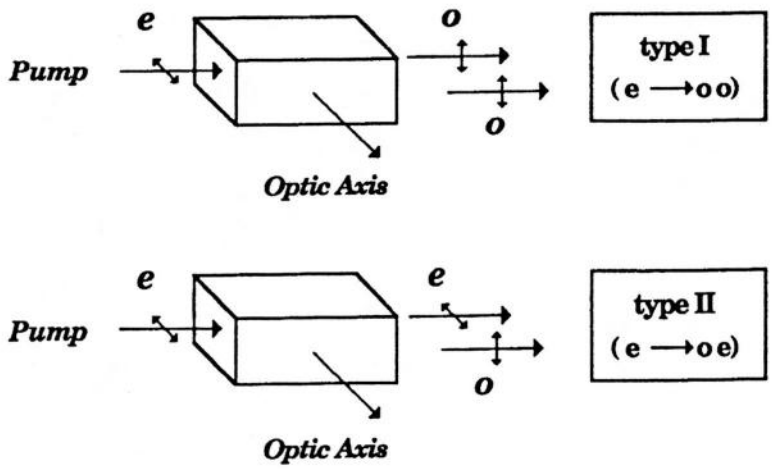

Figure 1.2: *Birefringent phase matching schemes.*

Fortunately, some degree of tunability in the phase matching condition can be obtained by adjusting the angle of the crystal relative to the propagation direction. Light polarised in the plane containing the optic axis and the propagation vector experiences a refractive index that varies between the refractive index of the ordinary and extraordinary axis, n_o and n_e respectively [1]. At 25°C, a phase matching solution can be found for the 1.064μm pumped degenerate OPO at $\theta = 45°$. However, no such solution is possible for the important interaction of 532nm SHG, demonstrating the difficulty in uniting a given nonlinear process, nonlinear crystal and pump laser wavelength.

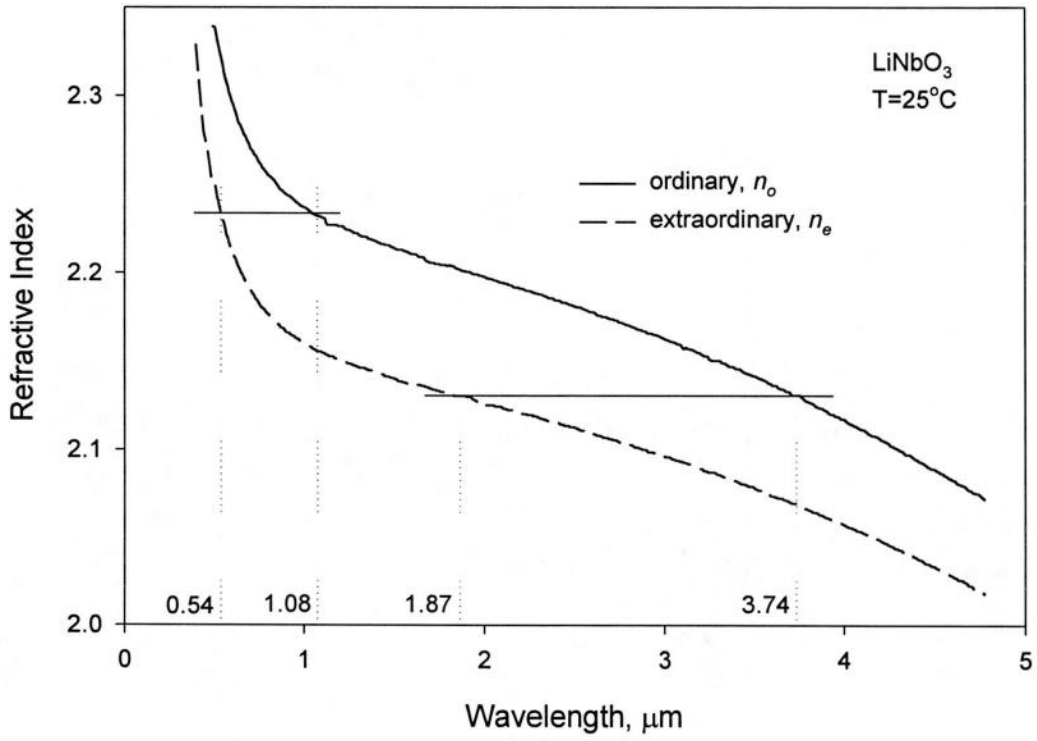

Figure 1.3: *Type I birefringent phase matching solutions for SHG (or degenerate OPO) in $LiNb0_3$ at 25 °C. The horizontal lines indicate the interactions which simultaneously satisfy phase matching ($n_{2\omega}=n_{\omega}$) and energy conservation ($\lambda_{2\omega}=\lambda_{\omega}/2$). Solutions are obtained for SHG of 0.54μm from 1.08μm and 1.87μm from 3.74μm [2]*

Although angle tuning of the phase matched condition helps offer more phase matching possibilities, it is at the cost of introducing walk-off of the Poynting vector for the extraordinary wave which propagates at an angle to the optic axis in the anisotropic crystal. Walk-off reduces the spatial overlap between the interacting waves, which limits useful crystal length and the ability to focus tightly, thus reducing efficiency. Another manifestation of propagation at non-normal incidence is that the acceptance angle is

limited since Δk is linear with angle, a condition referred to as critical phase matching. For these reasons, propagation at normal incidence is preferred, in which case there is no first-order dependence of Δk with angle (non-critical phase matching) and there is no walk-off.

Non-critical phase matched solutions can be found by employing the temperature dependence of the refractive indices and this allows tunability in the phase matching conditions without the drawbacks of angle tuning. In $LiNbO_3$, the rate of change of the index with temperature is much greater for the extraordinary index than for the ordinary index, and therefore the birefringence of the crystal is a function of crystal temperature [3, 4]. At normal incidence, a phase matching solution for the 1.064μm pumped degenerate OPO can be found at 525°C and SHG can be phase matched at –20°C. Unfortunately, these are not convenient temperatures for practical devices. Some relief can be found by altering the composition of the nonlinear crystal to facilitate phase matching conditions to occur at mode convenient temperatures, but the development process for new materials is slow and expensive and so alternative phase matching techniques are valuable.

Periodically poled Materials

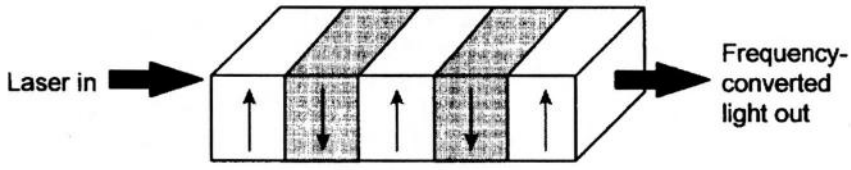

Figure 1.4: *Periodically poled material. The sign of the nonlinear coefficient is 'flipped' every period to correct for phase mismatch [2]*

Quasi phase matching (QPM) is an alternative approach to conventional birefringent phase matching that does not require finding a coincidence of material properties to obtain the phase matched condition $\Delta k=0$. Instead the oscillatory solution $\Delta k\neq 0$, where power flows between up- and down-conversion as the relative phases of the interacting fields changes, but whenever the relative phase mismatch of the interacting waves slips by π (i.e. after one coherence length), the mismatch is reset to zero so that the overall process proceeds with power flowing in the desired direction. Quasi phase matching can

be implemented by building into the crystal a nonlinear coefficient with a grating pattern of period $2l_c$, where l_c is the coherence length within the medium (figure 1.4) [2].

Quasi-phase matching was first proposed over thirty years ago by Armstrong [5]. In this challenging paper he discusses the possibility of manufacturing a nonlinear medium comprising several thin crystal layers, each with a thickness equal to the coherence length l_c, but with the sign of the nonlinear coefficient inverted in alternative layers to reset the phase as described above. Although this scheme was never demonstrated due to the practical difficulties in producing such a wafer stack, periodically poling has come to prominence due to a combination of crystal growth, lithographic and high voltage techniques. The grating period required for a given nonlinear process is first applied to the surface of the bulk material in the form of a metal electrode mask. A high voltage pulse is then applied to the mask in order to invert the nonlinear coefficient. A particularly successful example of a nonlinear crystal produced in this way is periodically-poled $LiNbO_3$ (PPLN) which is available with multiple gratings in a single chip, in long interaction lengths, has a very large nonlinearity and a high dispersion of refractive index with temperature. Devices based upon this material typically exhibit low threshold, due to the high nonlinearity and long interaction length, and broad tunability as a consequence of the multiple/fanned gratings and large refractive index dependence upon temperature.

QPM has several important advantages over conventional birefringent phase matching schemes. QPM allows an arbitrary selection of operating temperature and angle, so that non-critical phase matching at convenient temperature is possible at any wavelength throughout the transparency of the material. The interaction can also be tailored to take advantage of the highest component of the nonlinear susceptibility tensor of the material. In many cases this means that all of the interacting fields have the same polarisation which makes birefringent phase matching impossible. The use of QPM therefore extends the utility of existing materials, and enables the use of materials that exhibit no birefringence or are even optically isotropic. A more complete description and theoretical basis of QPM appears in the following chapter.

1.5 OPO cavity geometries

Once the phase matching scheme has been decided upon, a suitable cavity geometry for the cw OPO must be refined. The strength of the interaction depends on the intensities of the three waves. It is generally a weak process, and efficient conversion requires that at least one of the generated fields be resonated through the nonlinear medium. The properties of the resonant cavity at the three interacting wavelengths determine the power and stability properties of the cw OPO. Cavity configurations broadly fall into four categories, outlined in figure 1.5. Each design is characterised by its threshold and stability qualities.

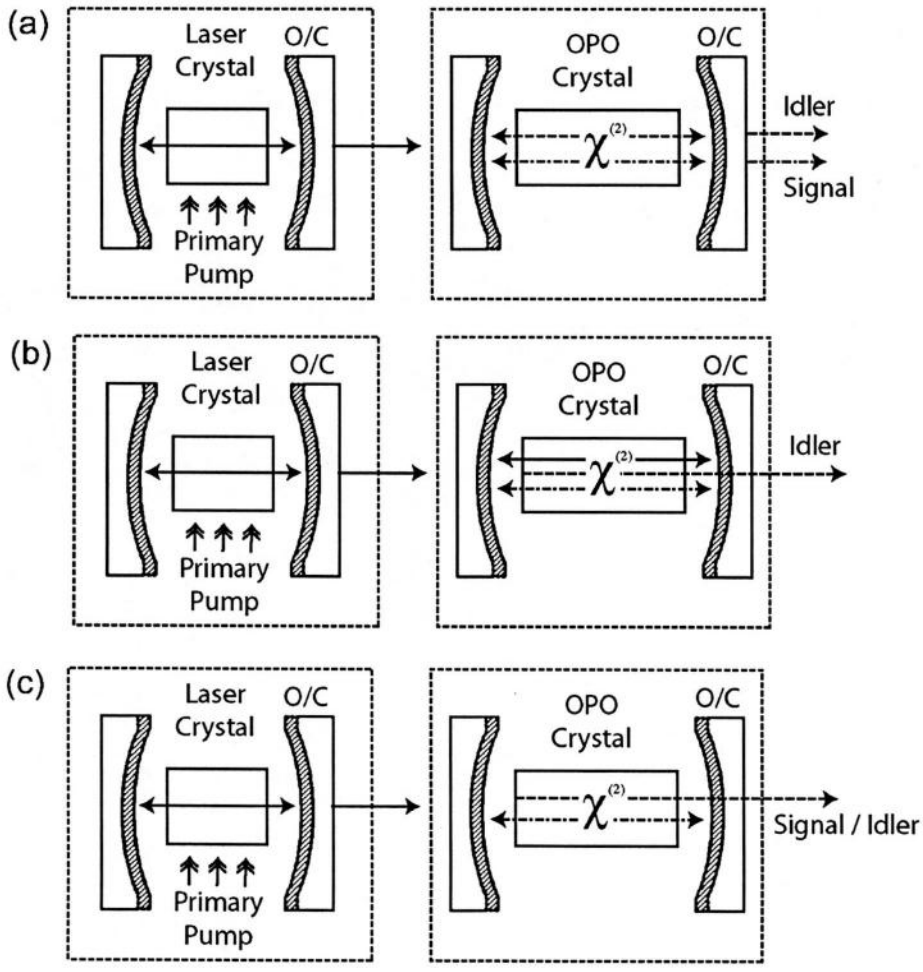

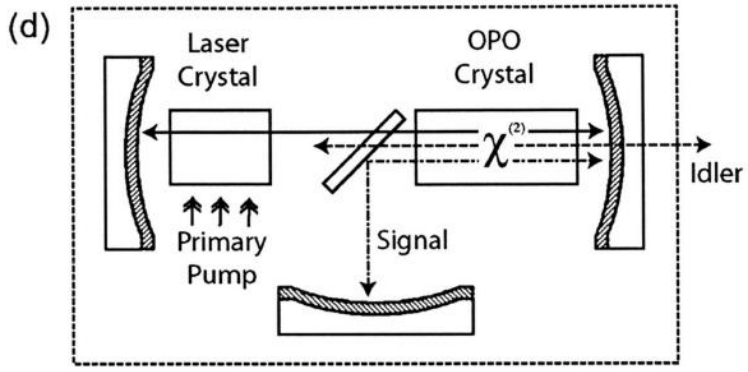

Figure 1.5: *CW OPO cavity configurations. (a) doubly resonant, (b) pump enhanced singly resonant, (c) externally pumped singly resonant and (d) intracavity singly resonant OPO [6].*

The most practically robust and simple OPO configuration is that of the externally pumped singly resonant OPO (SRO) [7] shown in figure 1.5 (c). In this system, one of the down converted waves is resonated within the cavity whilst the other exits after a single pass. Frequency perturbations in the pump field are taken up in the non-resonant field, obviating the need to keep the cavity actively locked. Unfortunately these devices exhibit operational thresholds that are typically in the multi-watt region, even with state of the art poled nonlinear materials. Significant reduction in thresholds (reduced to typically 10's of milliwatts) are observed by resonating more than one field within the cavity, figures 1.5 (a) and (b). In the doubly resonant (DRO) configuration (figure 1.5 (a)), both the signal and idler fields are resonant within the OPO cavity. This scheme was the basis of the very first experimental demonstration of a CW OPO [8], pumped by a frequency doubled Nd:YAG laser. The performance of this device was so poor in terms of spectral and amplitude stability that DRO research was effectively abandoned until the development of frequency stable pump sources in the early 1970's [9]. The observed instabilities observed in this paper are a consequence of the prohibitive cavity resonance requirements of the DRO. In order to keep both the signal and idler waves on resonance, the cavity length of the OPO must be stabilized to within ~1nm [10, 11], adding significant complexity to the mechanical design of the OPO and mandating the use of accurate servo-control of the cavity length. Servo control is complicated by the fact that such systems produce a discontinuous error signal, that is, when the DRO is off resonance there is no signal for the servo-loop to lock to. This very high requirement for cavity stability, coupled with difficulty in tuning the DRO smoothly whilst keeping both the signal and idler on resonance has hampered the development of these devices into practical sources for spectroscopic applications, although recent developments in pump sources and cavity

refinements [12-15] have brought about the modest realisation of the potential of the DRO, particularly to the field of high resolution spectroscopy [16].

Whilst still requiring active cavity length control, the pump-enhanced SRO (PE-SRO) (figure 1.5(b)) has emerged as a practical source for tunable, narrow linewidth coherent radiation. In the pump-enhanced scheme, the OPO cavity is held on the resonance with the single frequency pump source and either the signal or idler passively resonates whilst the other exits the cavity after one pass. Operation is easier to achieve than in the case of the DRO as cavity stability requirements are much relaxed, typically 10's of nm, and the pump beam always provides an error signal even in the absence of down-conversion. The first operational device which employed this cavity geometry was demonstrated by Robertson et. al. [17] in 1994. Several examples of stable, smoothly tunable PE-SRO's have since been demonstrated [18-21].

It is clear that to obtain a practical field device that exhibits robust temporal and amplitude performance, the prohibitive stability requirements of the double resonance constraint must be removed without the concomitant increase in threshold. Such a device must possess the passive stability of the SRO whilst having external pump thresholds comparable to that of the PE-SRO and DRO cavity configurations. Such favorable characteristics are exhibited by the OPO cavity configuration shown in figure 1.5 (d). In this scheme, the SRO is placed inside the cavity of a high finesse laser to take advantage of the very high circulating fields present and thereby overcome the high SRO threshold. Active cavity stability schemes are no longer required: perturbations of the pump and SRO cavity length are taken up in the frequency space of the pump, signal and idler fields. As no external cavity is being held on resonance with the pump field, the pump laser need not exhibit single longitudinal mode operation as multi-mode operation is transferred into the non-resonant OPO output. In this, the intracavity OPO, both the pump and resonated signal or idler wave share a common arm of the laser cavity and one mirror coated to be highly reflecting at their two wavelengths. A dichroic beamsplitter is placed in the cavity to differentiate between the pump and resonated OPO field. This beam splitter is antireflection coated (and therefore transparent) to the pump whilst being highly reflective at the resonated OPO wavelength. A third mirror completes the SRO cavity.

Early pioneering work was accomplished on the ICSRO by Colville et. al. [22]. In this system, an OPO based upon the birefringently phase matched crystal KTA was pumped internal to a Titanium sapphire (Ti:S) laser. This laser was itself pumped by an argon ion laser capable of delivering up to 15W. The Ti:S laser served as an excellent test bed for the development of the ICSRO as such a system is very tolerant to the inclusion of intracavity elements and the associated loss they cause. The broad tunability of the Ti:S laser is also of great benefit. This facilitates a simple mechanism for tuning the signal and idler when a birefringent crystal is employed. The system exhibited excellent down conversion efficiency (that is, the total down-converted power approached the optimum output coupled power available from the Ti:S laser), but the overall wall plug efficiency of the system was extremely poor due to the low efficiency (typically 0.1%) of the argon ion pump laser. Utilising more efficient pump sources, such as laser diodes, address this efficiency problem. By employing a diode pump source matched to the absorption band of Nd laser gain crystals, external pump powers required to reach OPO threshold are typically in the 100mW region [23], comparable with that of pump enhanced systems. High gain Nd doped crystals pumped by solid state laser diodes are particularly suitable for implementation in compact intracavity OPO's and this technique will be a common theme running throughout this thesis.

For a comprehensive review of CW-OPO's, see [24]

1.6 Thesis overview

In this thesis, the design, realisation and demonstration of three ICSRO's shall be described, all pumped internal to solid-state Nd:YVO_4 laser cavities. Chapter four describes a miniature low pump power, low threshold ICSRO [23] utilizing a 50mm long PPLN crystal and pumped by a single stripe, 1W diode laser. We shall see the attraction of the intracavity technique in that SRO threshold was attained with only 330mW of diode pump power in this compact, novel design. The temperature tuning capability of the periodically-poled nonlinear material employed in this system meant that the lack of tuning capability of the Nd pump laser did not limit the spectral coverage of the idler output; over 900nm of tuning was observed in the non-resonant idler.

Power scaling of this device is described, which led to the design of a high power fiber-coupled laser diode pumped Nd system. Two SRO's [25] were developed using this laser as a test bed; one based upon a 25mm long piece of PPLN, the other utilising the new nonlinear material PPRTA crystal, 20mm in length. The results of these two systems are described and contrasted.

In the following chapter, chapter 2, a theoretical basis for the work described in this thesis is laid down. In it we will briefly discuss the origins of nonlinear optics, the nature of second order nonlinear susceptibility and see how it is responsible for the nonlinear frequency mixing processes crucial for the operation of both OPOs and many other nonlinear optical devices. We then go on to consider the optical parametric process and phase matching acceptance parameters. Quasi phase matched materials are central to the operation of all of the devices demonstrated over the course of this research, and so the various parameters of this technique are then discussed in detail. The chapter closes with an analysis of the power and threshold characteristics of ICSROs.

Chapter three presents an introduction to and discussion of the many meritorious attributes of diode pumped solid-state lasers. The historical development and state of the art technology of the diode laser pump source is first considered, as developments in diode pumped laser technology are generally linked to technological improvements in the laser diodes upon which they depend. Although using laser diodes to pump solid-state laser gain media is relatively straightforward, some operational considerations are necessary and these are then discussed with the practical application of laser diodes in mind. The discussion is then expanded to include the pumping of solid-state laser gain media by diode lasers in terms of spectral matching, pumping geometries and thermal loading effects in the laser crystal. The chapter concludes by focusing upon the many favourable characteristics of Nd:YVO_4, the laser gain medium used throughout the course of this research.

The inclusion of the SRO within the cavity of a laser has a significant impact upon the transient dynamics of such a system, the consequences of which are revealed in the experimental chapters. In chapter six we will model the dynamics of the ICSRO laser system and try to formulate an experimental strategy to minimise the deleterious effects that the ICSRO has upon the parent laser transient behaviour.

The observations and results obtained over the course of this research programme and described in this thesis are then summarised in the final chapter, with suggestions of possible further avenues of research in which to realise some of the potential held by these unique devices.

References:

1 F. Zernicke and J. E. Midwinter, *Applied Nonlinear Optics*. (Wiley, New York, 1973).

2 L. E. Myers, *Periodically poled materials for nonlinear optics*. in *Advances in lasers and applications,* D. M. Finlayson, B. D. Sinclair, Eds. (Scottish Universities Summer School in Physics, Edinburgh, 1998).

3 D. H. Jundt, G. A. Magel, M. M. Fejer and R. L. Byer, "Periodically Poled $LiNbO_3$ for High-Efficiency 2^{nd}-Harmonic Generation," *Applied Physics Letters* **59**, 2657-2659 (1991).

4 G. J. Edwards and M. Lawrence, "A temperature-dependent dispersion equation for congruently grown lithium niobate," *Optical and Quantum Electronics* **16**, 373 (1983).

5 J. A. Armstrong, N. Bloembergen, J. Ducuing and P. S. Pershan, "Interactions between Light Waves in a Nonlinear Dielectric," *Physical Review* **127**, 1918 (1962).

6 T. J. Edwards, *Continuous-wave, singly-resonant optical parametric oscillation internal to the Ti: sapphire laser*, thesis, St. Andrews University (2000).

7 W. R. Bosenberg, A. Drobshoff, J. I. Alexander, L. E. Myers and R. L. Byer, "93% pump depletion, 3.5-W continuous-wave, singly resonant optical parametric oscillator," *Optics Letters* **21**, 1336 (1996).

8 R. G. Smith, J. E. Geusic, H. J. Levinstein, J. J. Rubin, S. Singh and V. Uitert, "Continuous optical parametric oscillation in $Ba_2NaNb_5O_{15}$," *Applied Physics Letters* **12**, 308-310 (1968).

9 F. G. Colville, *An analysis of the performance characteristics of continuous-wave optical parametric oscillators*, PhD thesis, University of St Andrews (1994). (Includes a comprehensive review of cw OPO's up to 1994).

10 R. C. Eckardt, C. D. Nabors, W. J. Kozlovsky and R. L. Byer, "Optical Parametric Oscillator Frequency Tuning and Control," *Journal of the Optical Society of America B-Optical Physics* **8**, 647-667 (1991).

11 A. J. Henderson, M. J. Padgett, F. G. Colville, J. Zhang and M. H. Dunn, "Doubly-resonant optical parametric oscillators: Tuning behaviour and stability requirements," *Optics Communications* **119**, 256 (1995).

12 R. Al-Tahtamouni, K. Bencheikh, R. Storz, K. Schneider, M. Lang, J. Mlynek and S. Schiller, "Long-term stable operation and absolute frequency stabilization of a doubly resonant parametric oscillator," *Applied Physics B - Lasers and Optics* **66**, 733-739 (1998).

13 A. J. Henderson, P. M. Roper, L. A. Borschowa and R. D. Mead, "Stable, continuously tunable operation of a diode-pumped doubly resonant optical parametric oscillator," *Optics Letters* **25**, 1264-1266 (2000).

14 M. Bode, P. K. Lam, I. Freitag, A. Tunnermann, H. A. Bachor and H. Welling, "Continuously-tunable doubly resonant optical parametric oscillator," *Optics Communications* **148**, 117-121 (1998).

15 T. Ikegami, S. Slyusarev, S. I. Ohshima and E. Sakuma, "Long term operation of a CW doubly resonant optical parametric oscillator," *Japanese Journal of Applied Physics Part 1-Regular Papers Short Notes & Review Papers* **35**, 2690-2691 (1996).

16 G. M. Gibson, M. H. Dunn and M. J. Padgett, "Application of a continuously tunable, cw optical parametric oscillator for high-resolution spectroscopy," *Optics Letters* **23**, 40 (1998).

17 G. Robertson, M. J. Padgett and M. H. Dunn, "Continuous-Wave Singly Resonant Pump-Enhanced Type-II $LiNbO_3$ Optical Parametric Oscillator," *Optics Letters* **19**, 1735-1737 (1994).

18 M. Scheidt, B. Beier, K. J. Boller and R. Wallenstein, "Frequency-stable operation of a diode-pumped continuous-wave RbTiOAsO4 optical parametric oscillator," *Optics Letters* **22**, 1287-1289 (1997).

19 M. E. Klein, D. H. Lee, J.-P. Meyn, B. Beier, K.-J. Boller and R. Wallenstein, "Diode-pumped continuous-wave widely tunable optical parametric oscillator based on periodically poled lithium tantalate," *Optics Letters* **23**, 831 (1998).

20 D. Chen, D. Hinkley, J. Pyo, J. Swenson and R. Fields, "Single-frequency low-threshold continuous-wave 3-μm periodically poled lithium niobate optical parametric oscillator," *Journal of the Optical Society of America B-Optical Physics* **15**, 1693 (1998).

21 G. A. Turnbull, D. McGloin, I. D. Lindsay, M. Ebrahimzadeh and M. H. Dunn, "Extended mode-hop-free tuning by use of a dual-cavity, pump-enhanced optical parametric oscillator," *Optics Letters* **25**, 341-343 (2000).

22 F. G. Colville, M. H. Dunn and M. Ebrahimzadeh, "Continuous-wave, singly resonant, intracavity parametric oscillator," *Optics Letters* **22**, 75 (1997).

23 D. J. M. Stothard, M. Ebrahimzadeh and M. H. Dunn, "Low pump threshold, continuous-wave, singly resonant, optical parametric oscillator," *Optics Letters* **23**, 1895 (1998).

24 I. D. Lindsay, *High spatial and spectral quality diode-laser-based pump sources for solid-state lasers and optical parametric oscillators*, PhD thesis, St. Andrews university (1999).

25 D. J. M. Stothard, P.-Y. Fortin, M. Ebrahimzadeh and M. H. Dunn, CLEO (The Optical society of America, Baltimore, USA, (2001),

2: Theoretical Background

2.1 Introduction

In this chapter we shall discuss the theoretical basis for the operation of ICSRO's, and second order nonlinear optics is general. We will begin by briefly reviewing the origins of nonlinear optics and the frequency mixing process that result from the $\chi_S^{(2)}$ interaction. The discussion will then focus upon optical parametric generation, phase matching and, in particular, quasi phase matching and its associated requirements in terms of acceptance bandwidths and material tolerances. We will conclude by considering the threshold and power characteristics of intracavity SRO's.

2.2 The origins of nonlinear optics

When an electric field is applied to a dielectric material, the material becomes polarised. The resulting polarisation depends upon the strength of the applied electric field and the dielectric susceptibility of the medium. In most cases, particularly before the availability of the laser, the applied electric field is much less than the inter-atomic field and the resultant polarisation, P, is linear and can be expressed as

$$P = \chi_s \varepsilon_0 E \tag{2.1}$$

where ε_0 is the permittivity of free space and χ_S is the linear (or first order) dielectric susceptibility.

With the intense fields obtained with focussed laser beams, the electric field in the medium is comparable to the inter-atomic field, and the polarisation reaction of the medium is no longer linear. We must expand the expression (2.1) to include higher order terms:

$$P = \varepsilon_0 \cdot \left(\chi_s^{(1)} E + \chi_s^{(2)} E^2 + \chi_s^{(3)} E^3 + ... \right) \tag{2.2}$$

where $\chi_S^{(1)}$, $\chi_S^{(2)}$ and $\chi_S^{(3)}$ are the first, second and third order susceptibilities respectively. It is these higher order susceptibilities that are responsible for nonlinear optical effects. The second order susceptibility, $\chi_S^{(2)}$, is responsible for nonlinear interactions such as second harmonic generation (SHG), the linear electro-optic effect and most importantly in the context of this thesis, sum- and difference-frequency mixing. There are many other interesting optical phenomina that arise due to the third order susceptibility, $\chi_S^{(3)}$, such as the Kerr effect [1], two-photon absorption [2] and Raman & Brillouin scattering [3-5]. In this chapter we will limit ourselves to a discussion of the nonlinear process coupled through the $\chi_S^{(2)}$ nonlinear susceptibility, as it is this interaction that is the basis upon which the OPO is founded.

2.3 Frequency mixing through the $\chi_s^{(2)}$ susceptibility.

We shall consider the second order term of (2.2), i.e.

$$P^{(2)} = \varepsilon_0 \chi_s^{(2)} E^2 \tag{2.3}$$

Consider a superposition of two optical fields at different frequencies, ω_1 and ω_2, propagating in the z direction through a nonlinear material. The resultant field is

$$E = \left[E_1 \cos(k_1 z - \omega_1 t) + E_2 \cos(k_2 z - \omega_2 t)\right] \tag{2.4}$$

where k_1, ω_1 and k_2, ω_2 are the wave-vectors and angular frequencies of E_1 and E_2 respectively. Substitution of (2.4) into (2.3) yields

$$\begin{aligned} \mathrm{P} = \tfrac{1}{2}\varepsilon_0 \chi^{(2)} [\mathrm{E}_1^2(\cos(2k_1 z - 2\omega_1 t)) + \mathrm{E}_2^2(\cos(2k_2 z - 2\omega_2 t)) \\ +2\mathrm{E}_1\mathrm{E}_2(\cos\{(k_1 + k_2)z - (\omega_1 + \omega_2)t\}) \\ +2\mathrm{E}_1\mathrm{E}_2(\cos\{(k_1 - k_2)z - (\omega_1 - \omega_2)t\}) \\ +\mathrm{E}_1^2 + \mathrm{E}_2^2] \end{aligned} \tag{2.5}$$

This expression contains all of the terms relating to the fundamental processes of the $\chi_S^{(2)}$ coupled interactions. Examination of these terms shows that the second order nonlinear polarisation simultaneously gives rise to frequency components at twice the frequency of

the interacting fields (SHG), the difference frequency (DFG) and the sum-frequency (SFG). The two remaining frequency-independent terms in (2.5) describe optical dc rectification across the dielectric medium. The frequency dependent components of (2.5) that fall within the transparency range of the medium represent the fundamental processes of $\chi_S^{(2)}$ nonlinear optics. It is the preferential selection of one of these processes, at the expense of the others, that is one of the primary design criteria of any efficient nonlinear optical device. This process, known as *phase matching*, will be discussed later in this chapter.

2.4 Optical Parametric Generation

The optical parametric down conversion process involves an input pump wave propagating within a nonlinear optical medium with frequency ν_p being converted into two output waves, termed the signal and idler, at frequencies ν_s and ν_i respectively. This process takes place such that energy is conserved, i.e

$$\nu_p = \nu_s + \nu_i \tag{2.6}$$

This process is related to the DFG process described above in that we can regard the (strong) pump wave as interacting with the (weak) signal wave to generate the idler wave through the DFG process, namely $\nu_i = \nu_p - \nu_s$, and then the generated idler wave interacting with the pump wave through the DFG process, to generate more signal wave, namely $\nu_s = \nu_p - \nu_i$, a net effect under appropriate conditions being the amplification of the signal wave. The nonlinear medium, when immersed in the pump wave, hence acts as an amplifier for the signal wave. By incorporating such a medium within a suitable cavity, an oscillator generating both signal and idler waves results.

The parametric down conversion process can also be described as a high energy pump photon being split into two lower energy photons. For a given pump frequency, there is a continuous choice of signal and idler pairs which will satisfy the energy conservation condition. However, the specific pair of frequencies which will be down converted are

determined by the momentum conservation, or phase matching condition, which is described by the wave-vector mismatch Δk. Efficient parametric down conversion requires that

$$\Delta k = k_p - k_s - k_i = \frac{2\pi}{c} \cdot (n_p \nu_p - n_s \nu_s - n_i \nu_i) = 0 \tag{2.7}$$

where n_p, n_s and n_i are the refractive index of the pump, signal and idler frequencies within the nonlinear optical material, and k_p, k_s and k_i are the corresponding wave-vector magnitudes. For perfect phase matching, the relative phase between each wave is maintained throughout the nonlinear medium.

All anisotropic materials exhibit birefringence, that is, a refractive index dependence upon the polarisation state of the light and direction of propagation. The most common method of satisfying the phase matching condition is to make use of this birefringence to compensate for material dispersion. Within the transparency range of an optical material, dispersion leads to an increase of refractive index as the frequency is increased. This causes the relative phase of the pump, signal and idler fields to change with propagation and thus sets the limit on the length of crystal that can be used. The phase matched condition becomes more difficult to maintain as the crystal becomes longer. The effect of phase mismatch on the efficiency of the nonlinear process is given by

$$efficiency \ \alpha \ l^2 \cdot \mathrm{sinc}^2\left(\frac{\Delta k l}{2}\right) \tag{2.8}$$

The sinc^2 nature of efficiency as a function of Δk is shown in figure 2.1. Useful parametric gain exists for $|\Delta k| \leq \frac{\pi}{l}$, where l is the length of the nonlinear material [6].

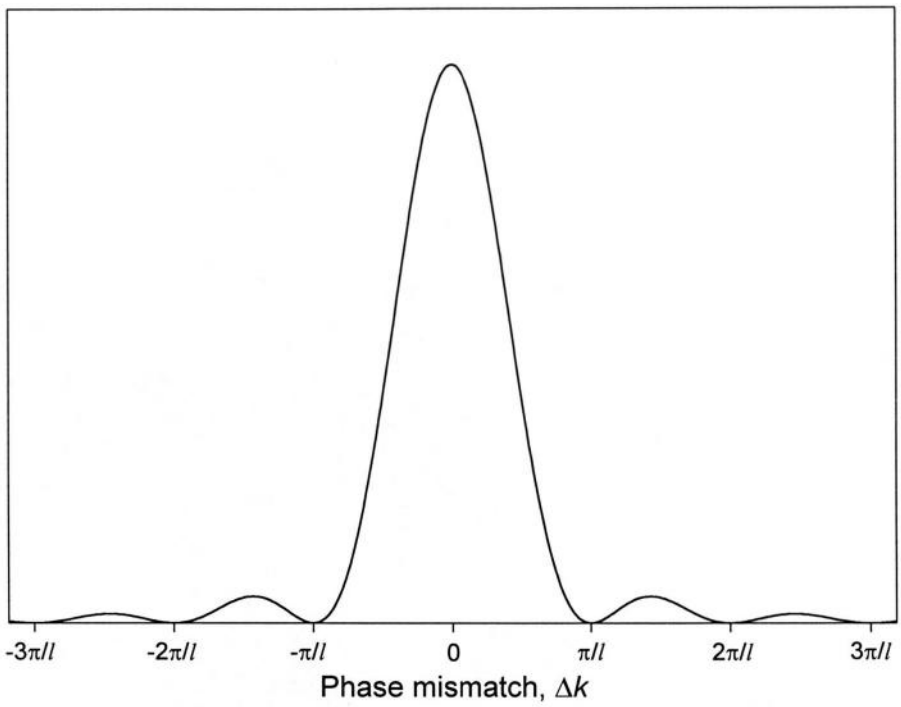

Figure 2.1: *The efficiency of the parametric down-conversion process for a given phase mismatch, Δk, follows a sinc^2 relationship.*

In a birefringently phase matched material, the phase matched condition is often controlled by altering the orientation or temperature of the nonlinear crystal. As all of the systems described in this thesis employ quasi-phase matched materials (outlined in the following section of this chapter), these mechanisms will not be discussed here. For a full description phase matched tuning mechanisms in birefringent nonlinear crystals, see [7].

2.5 Quasi phase matching

An alternative technique to birefringent phase matching of different waves propagating in a nonlinear crystal is the recently developed and novel concept quasi phase matching (QPM), where the relative phase mismatch between the interacting fields are corrected at regular intervals using a structural periodicity built into the nonlinear medium [8-10] (figure 2.2).

Due to normal dispersion within the material, the pump, signal and idler waves propagate at different phase velocities. It is crucial that the correct phase relationship is maintained

between the three interacting waves if power is to flow in the desired direction, i.e. from pump to signal and idler. The continuously changing phase relationship between non phase matched pump, signal and idler therefore leads to an oscillation in the direction of power flow as indicated in trace a in figure 2.3. The distance over which the relative phase of the waves changes by π is called the *coherence length*, l_C, and is typically a few micrometers in length.

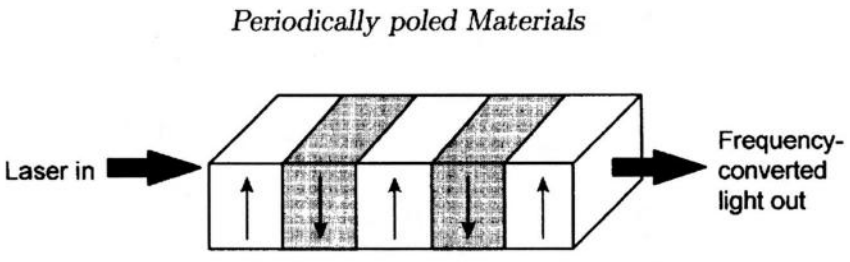

Figure 2.2: *Periodically poled material. The sign of the nonlinear coefficient is 'flipped' every period to correct for phase mismatch [11].*

Continuous growth of the signal and idler fields requires the repeated inversion of the relative phase between the waves after an odd number of coherence lengths. This can be achieved by modulating the sign of the nonlinear coefficient that maintains the proper phase-relationship for the growth of the generated waves. The highest conversion efficiency occurs when the sign of the nonlinear coefficient is reversed every coherence length, referred to as *first order* QPM.

QPM materials have several advantages over birefringently phase matched crystals. They can be (and generally are) designed such that one is able to take advantage of the highest d coefficient (subject to a $2/\pi$ scaling factor due to slight phase mismatch in each domain) of the nonlinear material, whereas operation is restricted to the d coefficient which happens to coincide with the phase matched angle with a birefringently phase matched crystal (d here corresponds to nonlinear susceptibility). The phase matched scheme is a flexible engineered variable and is not dictated by the dispersion properties of the crystal. This allows interactions of a material which fall outside the capability of birefringently phase matched schemes to be investigated.

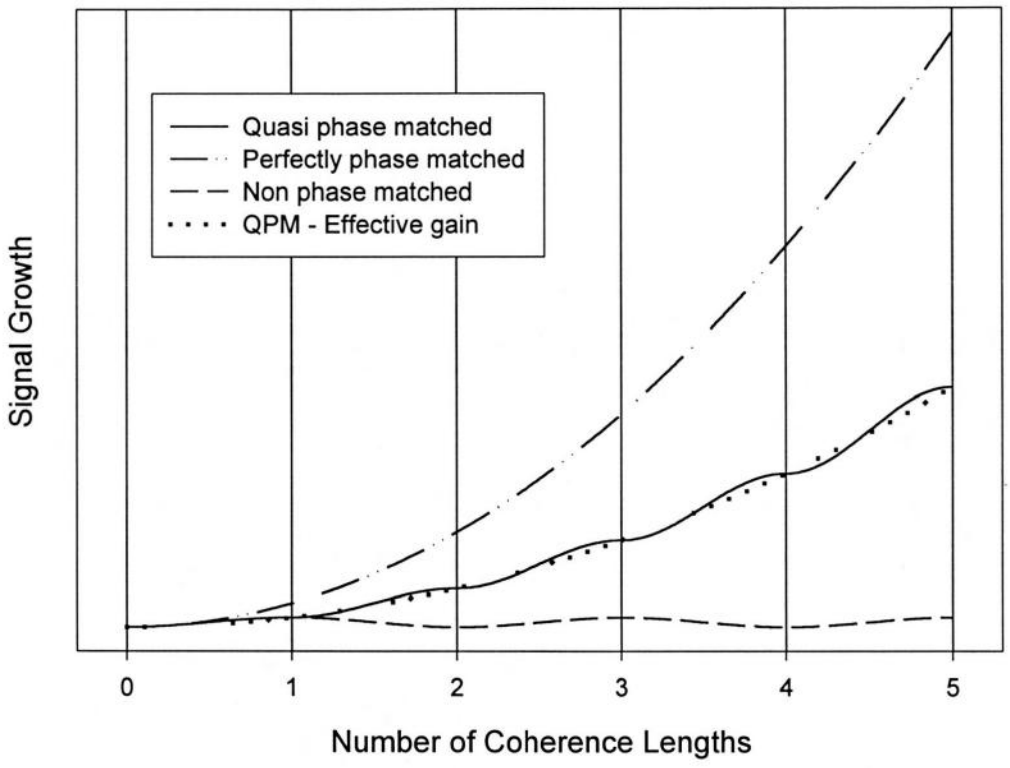

Figure 2.3: *The effect of quasi phase matching on conversion efficiency. Here, the sign of the nonlinear coefficient is reversed every coherence length (indicated by the vertical lines) – first order QPM.*

The interacting waves are, in general, polarised along a principal optical axis of the crystal and so walk-off is no longer a prohibitive factor in the implementation of a particular phase matched interaction. This allows for longer crystals and tight focussing inside the crystal. The common polarisation of the interacting waves facilitates temperature tuning schemes that are inaccessible to birefringently phase matched materials: although the birefringence of a material (i.e. the difference between n_o and n_e) may change little with temperature, the individual indices may show considerable dispersion with temperature.

The theory of QPM is discussed in detail by Fejer [10] and Myers [11], and is summarised below.

For QPM, the effective nonlinear coefficient is given by

$$d_Q = d_{eff} \cdot G_m \tag{2.9}$$

where d_{eff} is the same as that for single domain bulk material and G_m is the Fourier coefficient for the periodic modulation, given by

$$G_m = \frac{2}{m\pi} \cdot \sin(m\pi D) \tag{2.10}$$

Here, $D=l_d/\Lambda$ is the duty cycle where l_d is the length of the reversed domain and Λ is the domain period. The optimum value of the duty cycle depends on the QPM order m (D_{opt}=50% for m=1). The effective nonlinear coefficient for QPM is largest for a first order process with a 50% duty cycle. In this case the nonlinear coefficient is given by

$$d_Q = \frac{2}{\pi} \cdot d_{eff} \tag{2.11}$$

The wave-vector mismatch is now given by

$$\Delta k_Q = k_p - k_s - k_p - k_m \tag{2.12}$$

where k_m is the m^{th} order grating wave vector, which is given by

$$k_m = \frac{2\pi m}{\Lambda} \tag{2.13}$$

Therefore, perfect first order phase matching is achieved when

$$\Delta k_Q = k_p - k_s - k_i - \frac{2\pi}{\Lambda} = 0 \tag{2.14}$$

For ideal periodic structures, QPM can only be achieved for m^{th} orders where m is an odd number [10].

QPM is commonly implemented in ferroelectric crystals by a periodic reversal of the spontaneous polarisation P_S. Changing the sign of P_S, corresponding to changing the sign of the nonlinear coefficient, is achieved by momentarily applying an electric field using lithographically defined electrodes [12, 13]. Such crystals are said to be *periodically poled* with a domain (grating) period Λ.

QPM allows longer crystals to be used than with traditional birefringently phase matched (BPM) techniques, and has the added advantage that interacting waves can be chosen to access the largest nonlinear coefficient (i.e. d_{33} in $LiNbO_3$, $KTiOPO_4$ and $RbTiOAsO_4$). With an appropriate choice of grating period, essentially any wavelength combination within the transparency range of the nonlinear material can be phase matched in a non-critical geometry. QPM allows phase matching to occur at arbitrary temperatures with no walk-off and extends the frequency utility of existing materials. To date, the most readily available and well characterised QPM material is periodically poled lithium niobate (PPLN), although there is much interest in the development of alternative crystals such as PPKTP and PPRTA which have many significant advantages over PPLN, such as increased resistance to thermal lensing and photo-refractive damage, and a lower coercive field required to flip the domains in the manufacturing process, leading to the availability of larger apertured crystals.

2.5.1 QPM Acceptance parameters

One of the consequences of need to phase match a nonlinear interaction in order to provide efficient conversion from one frequency to another is that the phase matching condition will itself determine the frequency and bandwidth over which the interacting fields will actively participate. As stated above, constructive interaction exists when the interacting fields are phase matched, that is, that the modulus of the phase mismatch between the interacting fields is no more that π/l [6]. Thus, for a particular phase matching scheme, we can formulate expressions acceptance parameters for the temperature, angle and frequency for a specified nonlinear process. The problem of acceptance parameters in nonlinear optical processes has been investigated by Barnes and Corcoran [14] and the following overview follows their analysis.

We shall initially consider a birefringently phase matched interaction and then go on to modify these expressions to accommodate QPM case. Consider a collinear birefringently phase matched interaction evaluated around the perfectly phase matched condition. The function of Δk may be expanded as a Taylor series about the point Δk_0:

$$\Delta k = \Delta k_0 + \left.\frac{\partial \Delta k}{\partial \lambda_i}\right|_{\lambda_{i-pm}} \delta\lambda_i + \frac{1}{2}\left.\frac{\partial^2 \Delta k}{\partial \lambda_i^{\,2}}\right|_{\lambda_{i-pm}} \delta\lambda_i^{\,2} + \ldots\ldots \tag{2.15}$$

where, for the case of perfect phase matching, Δk_0=0 and $\lambda_{i\text{-}pm}$ is the value of λ_i at which Δk=Δk_0. Taking the definition of acceptance bandwidth $\Delta k \leq |\pi / \lambda|$ and setting Δk to 0 for a bandwidth around the phase matched condition, we have

$$\left.\frac{\partial \Delta k}{\partial \lambda_i}\right|_{\lambda_{i-pm}} \delta\lambda_i + \frac{1}{2}\left.\frac{\partial^2 \Delta k}{\partial \lambda_i^{\,2}}\right|_{\lambda_{i-pm}} \delta\lambda_i^{\,2} + \ldots\ldots = \pm\frac{\pi}{L} \tag{2.16}$$

The full expression for the phase mismatch Δk in terms of the interacting wavelengths is

$$\Delta k = 2\pi \cdot \left[\frac{n_p(\lambda_p)}{\lambda_p} - \frac{n_s(\lambda_s)}{\lambda_s} - \frac{n_i(\lambda_i)}{\lambda_i}\right] \tag{2.17}$$

where the subscripts p, s and i refer to the pump, signal and idler fields respectively. The functional dependence of the indices of refraction of these waves has been indicated, as it is the derivative of these indices that will determine the resultant bandwidth. Recalling the energy conservation relation

$$\frac{1}{\lambda_p} = \frac{1}{\lambda_s} + \frac{1}{\lambda_i} \tag{2.18}$$

and noting that the full bandwidth, from (2.17), is given by

$$\Delta\lambda_i = 2\delta\lambda_i \tag{2.19}$$

the first derivative with respect to the pump wavelength will be

$$\frac{\partial \Delta k}{\partial \lambda_p} = 2\pi \cdot \left[\left. \frac{\partial n_p(\lambda_p)}{\partial \lambda_p} \right|_{\lambda_p} \frac{1}{\lambda_p} - \frac{n_p(\lambda_p)}{{\lambda_p}^2} - \left. \frac{\partial n_s(\lambda_s)}{\partial \lambda_s} \right|_{\lambda_s} \frac{\lambda_s}{{\lambda_p}^2} + \frac{n_s(\lambda_s)}{{\lambda_p}^2} \right] \tag{2.20}$$

with the first derivative of (2.15) dominating the acceptance bandwidth in the overwhelming number of cases. Equation (2.20) can be used to express the wavelength acceptance bandwidth using (2.16) and (2.19) resulting in the following expression

$$\Delta\lambda_p = \frac{1}{L} \cdot \left[\left. \frac{\partial n_p(\lambda_p)}{\partial \lambda_p} \right|_{\lambda_p} \frac{1}{\lambda_p} - \frac{n_p(\lambda_p)}{{\lambda_p}^2} - \left. \frac{\partial n_s(\lambda_s)}{\partial \lambda_s} \right|_{\lambda_s} \frac{\lambda_s}{{\lambda_p}^2} + \frac{n_s(\lambda_s)}{{\lambda_p}^2} \right]^{-1} \tag{2.21}$$

Let us take, for example, the pump acceptance bandwidth of the nonlinear crystal $LiNbO_3$, a nonlinear crystal used extensively in the period of this research (albeit in the QPM regime). The Sellmeier equations governing the refractive indices of $LiNbO_3$ are given by [15, 34] and are as follows

$$n_x(\lambda) = \sqrt{4.9048 + \frac{0.117680}{\lambda^2 - 0.047500} - 0.027169 \cdot \lambda^2} \tag{2.22a}$$

$$n_y(\lambda) = \sqrt{4.5820 + \frac{0.099169}{\lambda^2 - 0.044432} - 0.021950 \cdot \lambda^2} \tag{2.22b}$$

$$n_z(\lambda) = \sqrt{4.4988 + \frac{0.099545}{\lambda^2 - 0.044537} - 0.022320 \cdot \lambda^2} \tag{2.22c}$$

where λ is in μm. To calculate the appropriate wavelength parameters at Δk=0 we may solve equation (2.17) for pump, signal and idler polarisations along the *y*, *y* and *z* axis respectively (for collinear pumping along the *x* axis) by using (2.18) and the Sellmeier equations (2.22b&c) (setting Δk=0 and λ_p=1.064μm). The phase matched signal and idler

wavelengths calculated by this method are 1.500μm and 3.661μm respectively. Substitution of the pump and calculated signal wavelengths into (2.21) for a crystal interaction length of 25mm gives a pump acceptance bandwidth of $\Delta\lambda_p$=5.54nm. This is the maximum bandwidth of an input pump beam that will contribute constructively to the nonlinear process in the phase mismatch range $\Delta k \leq |\pi / \lambda|$. As the Nd:$YVO_4$ laser gain media used throughout the term of this work has a $1/e^2$ gain bandwidth of only 1.1nm, all of the pump field would contribute constructively to down conversion in this example. Clearly, further narrowing of the pump bandwidth will have a positive impact upon efficiency as the wavelength extremes of the phase mismatch range provide a less efficient contribution to down conversion than the central wavelengths for which $\Delta k \approx 0$. Similar acceptance parameters may be calculated for the temperature acceptance bandwidth of a process. The appropriate expression is given by

$$\Delta T = \frac{1}{L}\left[\frac{1}{\lambda_p}\frac{\partial n_p}{\partial T}\bigg|_T - \frac{1}{\lambda_s}\frac{\partial n_s}{\partial T}\bigg|_T - \frac{1}{\lambda_i}\frac{\partial n_i}{\partial T}\bigg|_T\right]^{-1} \tag{2.23}$$

Temperature derivatives have been measured for many nonlinear materials and are comprehensively documented by Dmitriev [15]. Angular acceptance bandwidths may also be calculated in the same manner [14].

We have already stated that the QPM process provides additional flexibility to the phase matching process by adding a further user-engineered parameter to the phase mismatch expression as follows

$$\Delta k_m = k_p - k_s - k_i - \frac{2m\pi}{\Lambda} \tag{2.24}$$

where Λ is the grating period of the nonlinear material. Clearly, as the grating period Λ is independent of wavelength, any derivative with this parameter with respect to wavelength will vanish and the expression for the pump acceptance bandwidth will be identical to that for the BPM case

$$\Delta\lambda_p = \frac{1}{L}\cdot\left[\left.\frac{\partial n_p(\lambda_p)}{\partial\lambda_p}\right|_{\lambda_p}\frac{1}{\lambda_p} - \frac{n_p(\lambda_p)}{\lambda_p^{\,2}} - \left.\frac{\partial n_s(\lambda_s)}{\partial\lambda_s}\right|_{\lambda_s}\frac{\lambda_s}{\lambda_p^{\,2}} + \frac{n_s(\lambda_s)}{\lambda_p^{\,2}}\right]^{-1} \tag{2.25}$$

There is one important difference between the evaluation of this expression when considering the BPM and the QPM case. In almost every circumstance, the two interacting fields will be polarised along only one crystal axis for the QPM case and so the values of $n_P(\lambda)$ and $n_S(\lambda)$ in equation (2.25) need only be derived from one Sellmeier equation (for PPLN and PPRTA, this is $n_Z(\lambda)$). Thus, from (2.22c) and (2.25) the QPM acceptance bandwidth for a 25mm long PPLN crystal has a value of 1.3nm compared to 1.7nm for a similar crystal which was phase matched birefringently. As before, it is possible to derive expressions for the temperature and angular acceptance bandwidth of QPM materials. In the case of temperature acceptance bandwidth, the grating period may well be a function of temperature as the material thermally expands. An additional term must therefore be added to (2.23) to give

$$\Delta T = \frac{1}{L}\left[\left.\frac{1}{\lambda_p}\frac{\partial n_p}{\partial T}\right|_T - \left.\frac{1}{\lambda_s}\frac{\partial n_s}{\partial T}\right|_T - \left.\frac{1}{\lambda_i}\frac{\partial n_i}{\partial T}\right|_T - m\frac{\partial}{\partial T}\left(\frac{1}{\Lambda}\right)\right]^{-1} \tag{2.26}$$

where the term

$$\frac{\partial}{\partial T}\left(\frac{1}{\Lambda}\right) \tag{2.27}$$

must be calculated from a knowledge of the thermal expansion coefficient of the material concerned. The angular acceptance bandwidth of a QPM material is obtained from an analysis that is significantly more involved than that for the BPM case [10]. In addition to the refractive index dependence upon crystal angle, the angular shift of apparent grating period must be taken into account. For most cases, the high effective nonlinearity of QPM materials mean that in practice, tight focussing conditions are rarely employed and the interaction propagation constants k_j may be assumed to lie along a common direction.

2.5.2 QPM tolerances

In periodically poled structures, efficiency is reduced for departures from the ideal grating structure. The effects of period and duty cycle errors on the conversion efficiency have been investigated in [10] and [11]. The point where the power conversion efficiency is halved can be used to calculate the tolerances of these errors.

Constant errors in the domain period, where the periodicity of the domains is otherwise perfect, causes a shift in the phase matching curve from the desired operating point which in turn reduces conversion efficiency. The tolerance of period is [10]

$$\frac{\delta\Lambda}{\Lambda} = \frac{1.77}{Nm'} \tag{2.28}$$

where $\delta\Lambda$ is the period error, m' is the phase matching order, $N=L/ml_c$ is the number of domains in the sample of length L and l_c is the coherence length. For m=1 and N=1000, the tolerance on the grating period is ~0.2%. We can therefore see than very small errors in the domain period lead to large reductions in conversion efficiency.

Random errors in the domain period cause a broadening of the phase matching curve due to a normal distribution of errors with standard deviation σ_l. Fejer gives the tolerance on the mean square error to be

$$\frac{\sigma_l}{l_c} < \frac{0.72}{\sqrt{N}} \tag{2.29}$$

For N=1000, the tolerance for random period errors is ~2%.

Departures from the desired domain duty cycle, usually 50%, reduce the parametric gain but do not affect the phase matched bandwidth. The tolerance on *rms* duty cycle error is

$$\frac{\sigma_l}{l_c} = \frac{\sqrt{2\ln 2}}{\pi} \tag{2.30}$$

The tolerance for the duty cycle is therefore ~38%. Sensitivity to duty cycle errors is therefore very small, with *rms* errors as large as $l_C/3$ resulting in <50% reduction in efficiency.

The FWHM angular acceptance bandwidth for a non-critical QPM interaction is given by [10]

$$\delta v = 2\sqrt{1.772 \cdot \frac{n_2}{n_1} \cdot \frac{l_c}{L} \cdot \cos v} \tag{2.31}$$

where n is the angle of the fundamental wave vector to the z axis. Here the bandwidth depends inversely upon the square root of the device length L and is comparable to that of a non-critical BPM interaction.

In summary, efficient QPM is very sensitive to both constant and random period errors, whilst being much more tolerant to errors in the duty cycle. As the lithographic techniques used in the electric-field poling process in crystals such as PPLN, PPRTA and PPKTP is extremely well defined, errors in periodicity have not been a serious issue in the application of periodically poled nonlinear crystals.

2.6 ICSRO threshold and power analysis

To fully characterise an ICSRO it is useful to derive an understanding of its threshold and power behaviour. This will facilitate the appropriate characteristics of the external pump power required for the SRO to reach threshold and a meaningful measurement of the conversion efficiency to take place.

The earliest treatment of continuous wave OPO power characteristics was accomplished by Oshman and Harris [16] in 1968, where the DRO pumped internal to a laser cavity was

considered. Their analysis identified three distinct regimes of operation. The first of which, the *stable efficient* mode, operated with a fixed-phase relationship between the pump, signal and idler of $\Delta\phi=\pi/2$. In the second regime, deemed the *stable inefficient* mode of operation, a perfect phase relationship between the three fields is lost, i.e. $\Delta\phi\neq\pi/2$, and increasing pump powers begin to drive the phase between the interacting fields rather than their amplitude. In the last regime, which occurs at pump rates ~3 times above OPO threshold, there is no fixed phase relationship between the interacting fields which leads to a breakdown in cw operation. This area of operation was thus termed the *repetitively pulsing* regime. This early treatment, then, pointed to serious problems with power scaling of these devices. The high threshold requirements of the SRO meant that whilst there were several early reports of cw ICDRO's [17-19], experimentalists lacked the laser sources and nonlinear materials with which to construct a cw ICSRO and thus a treatment of this device was not considered until the mid 1980's [20] and then later a study of a pulsed device [21]. These studies have been extended [22] and the pertinent conclusions are included here. For a further discussion and detailed derivation of the expressions used in this analysis, see [23].

2.6.1. Power Analysis

A simplified ICSRO is shown in figure 2.4. The high finesse laser and signal cavities are discriminated by a dichroic beam splitter, antireflection coated at λ_p and highly reflecting at λ_s. The $\chi_s^{(2)}$ nonlinear medium of length l is placed at one end of the laser cavity and its end face coincides with the cavity origin, z=0. The laser gain medium is located in the pump field branch of the cavity and is externally pumped through the end mirror. The idler field is non-resonant and exits the cavity after one pass.

The standing wave cavity shown in figure 2.4 will, in practice, produce a multi longitudinal mode laser field due to the effects of spatial hole burning in the homogeneously broadened laser gain medium. For this analysis, we assume that all of the oscillating modes fall within the pump wavelength acceptance bandwidth of the nonlinear material.

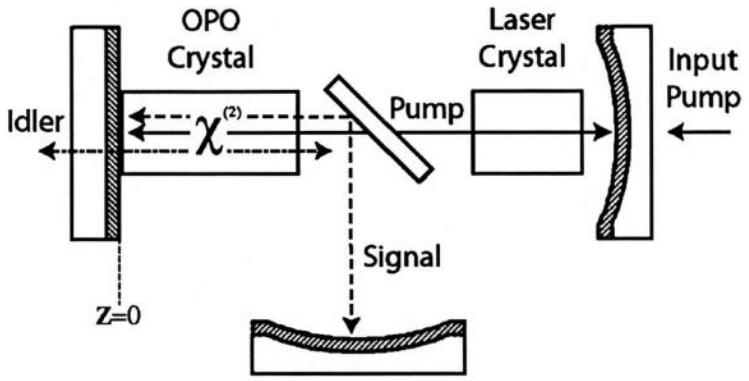

Figure 2.4: *ICSRO cavity geometry schematic [24].*

As there is no energy storage mechanism in the nonlinear material, spatial hole burning effects will not be present and resonant signal is assumed to be oscillating on a single mode. This assumption is in good agreement with experimental observations [25, 26]. Overall cavity lengths are L_p and L_S for the pump and signal cavities, respectively. The gaussian pump and signal fields are defined as [22]

$$E_p(z,r,t) = \sum_j 2E_{pj}(t)\exp\left(-r^2/w_p{}^2\right)\sin\left(k_{pj}z\right)\cos\left(\omega_{pj}t+\phi_{pj}\right) \tag{2.32}$$

$$E_s(z,r,t) = 2E_s(t)\exp\left(-r^2/w_s{}^2\right)\sin\left(k_s z\right)\cos\left(\omega_s t+\phi_s\right) \tag{2.33}$$

where $k_{pj}=n_{pj}\omega_{pj}/c$ and $k_S=n_S\omega_S/c$ with n_p and n_S averaged over the length of the cavity. The laser and signal waist radii are given by w_p and w_S, respectively. The analysis assumes that each of the j longitudinal modes of the laser mixes with the single frequency signal mode to produce j idler longitudinal modes. For the standing wave cavity shown in figure 2.4, the parametric interaction must be investigated for both $\pm z$ directions, hence equations (2.32) and (2.33) may be expressed generally in the form

$$E_p(z,r,t) = \frac{1}{2}\left\{E_p^+(z,r,t) - E_p^-(z,r,t)\right\} + c.c \tag{2.34}$$

$$E_s(z,r,t) = \frac{1}{2}\left\{E_s^+(z,r,t) - E_s^-(z,r,t)\right\} + c.c \tag{2.35}$$

$$E_p^{\pm}(z,r,t) = \sum_j E_{pj}^{\pm}(t)\exp(\pm ik_{pj}z)\exp(-i[\omega_{pj}t + \phi_{pj}^{\pm}])\exp(-r^2/w_p{}^2) \quad (2.36)$$

$$E_s^{\pm}(z,r,t) = E_s(t)\exp(\pm ik_s z)\exp(-i[\omega_s t + \phi_s^{\pm}])\exp(-r^2/w_s{}^2) \quad (2.37)$$

with the travelling-wave field components having $\pm k_{pj,s}z$ being denoted with ±. Equations (2.34) to (2.37) may be substituted into the Maxwell wave equation by inserting appropriate polarisation terms for the parametric process and taking care to preserve the directional interaction notation. The polarisation term of the idler is found to re-radiate idler field components in both directions given by

$$E_i^{\pm}(z,r,t) = \sum_j E_{ij}^{\pm}(t)\exp(\pm ik_{ij}z)\exp(-i[w_{ij}t + \phi_{ij}^{\pm}]) \quad (2.38)$$

The important consequence of the singly resonant condition is that the idler exits from the cavity after only one pass. Thus, for each pass of the nonlinear medium, the initial idler phase is dictated by the dominant resonant pump and signal fields, maintaining a fixed phase relationship given by $\Delta\phi_j=\phi_{pj}-\phi_s-\phi_{ij}=\pi/2$, liberating the parametric interaction from the inefficient, phase driven regimes of the power-scaled ICDRO. This sets no upper ceiling on the power to which the ICSRO can be scaled.

The coupled rate equations of the ICSRO can be derived following the example of [27]. The fields within the optical resonator are commonly described using Lamb's self-consistency equations [28]. These equations describe the longitudinal modes arising from polarisation source terms that re-radiate consistent fields identical to the driving fields. The resonant laser field contains polarisation terms that are dependent upon the laser and nonlinear media, whereas the signal field is self-consistent with the nonlinear polarisation source terms only. Both terms are coupled through the $\chi_s^{(2)}$ nonlinear process which has significant implications for the transient dynamics of the ICSRO [29]. The relevant consistency term for the pump and signal fields, with cavity decay times of τ_p' and τ_s', are given by

$$\frac{\partial E_s(t)}{\partial t} + \frac{E_s(t)}{\tau'_s} = -\frac{\omega_s}{2\varepsilon_0 n_s^2}\mathrm{Im}\left[\mathbf{P}_s^+(t) + \mathbf{P}_s^-(t)\right] \tag{2.39}$$

$$\frac{\partial E_{pj}(t)}{\partial t} + \frac{Epj(t)}{\tau'_p} = -\frac{w_{pj}}{2\varepsilon_0 n_p^2}\mathrm{Im}\left[\mathbf{P}_s^+(t) + \mathbf{P}_s^-(t)\right] - \frac{w_{pj}}{2\varepsilon_0 n_p^2}\mathrm{Im}[\mathbf{P}_{laserj}(t)] \tag{2.40}$$

where the parametric polarisation $\mathbf{P}_{pj}^{\pm}(t)$ and $\mathbf{P}_S^{\pm}(t)$ are related to the nonlinear polarisation terms through volume integrals over the crystal length and radial transverse coordinates to give

$$\mathrm{Im}\left[\mathbf{P}_s^{\pm}(t)\right] = -\frac{2}{1+\omega_s^2/\overline{\omega}_s^2}\frac{\varepsilon_0 l d_{eff}^2}{cn_i}\frac{l}{2L_s}\mathrm{sinc}^2\left(\frac{\Delta kl}{2}\right)E_s(t)\sum_j \omega_{ij}E_{pj}(t)^2 \tag{2.41}$$

$$\mathrm{Im}\left[\mathbf{P}_{pj}^{\pm}(t)\right] = -\frac{2}{1+\omega_p^2/\overline{\omega}_p^2}\frac{\varepsilon_0 l d_{eff}^2}{cn_i}\frac{l}{2L_p}\mathrm{sinc}^2\left(\frac{\Delta kl}{2}\right)E_{pj}(t)\sum_j \omega_{ij}E_s(t)^2 \tag{2.42}$$

where the relative phase difference of the parametrically coupled fields have been set as $\Delta\phi^+=\pi/2$ and $\Delta\phi^-=\pi/2-\Delta kl$, and the waist radius of the nonlinear polarisation $\overline{\omega}_{s,p}$ is given by [30]

$$\frac{1}{\overline{\omega}_{s,p}^2} = \frac{1}{\omega_i^2} + \frac{1}{\omega_{p,s}^2} \tag{2.43}$$

where ω_x with its respective subscript denote the waist sizes in the pump ($x=p$), signal ($x=s$) and idler ($x=i$) fields, respectively. The final substitution to be made is to replace the laser polarisation term $\mathrm{Im}\left[\mathbf{P}_{laserj}^{\pm}(t)\right]$ in equation (2.40) with the expression [23]

$$\frac{G_j E_{pj}}{G_{j-th}\tau'_p} \tag{2.44}$$

to give

$$\tau_p' \frac{\partial E_{pj}}{\partial t} = \left(\frac{G_j}{G_{j-th}} - 1 \right) E_{pj} - \frac{\tau_p' w_p C_{pj}}{\varepsilon_0 n_p^2} \tag{2.45}$$

where G_j is the saturated laser gain of the j^{th} longitudinal mode and $G_{j\text{-}th}$ is the threshold gain required for the oscillation of the j^{th} mode. By introducing the following photon flow expressions for the resonant modes, the analysis of the steady-state power characteristics can be further simplified

$$\gamma_s = n_s c \varepsilon_0 E_s^2 \pi \omega_s^2 / 4\hbar w_s \tag{2.46}$$

$$\gamma_{pj} = n_p c \varepsilon_0 E_{pj}^2 \pi \omega_p^2 / 4\hbar w_{pj} \tag{2.47}$$

The laser photon flow threshold value may be obtained from (2.41) and (2.39) and is given by

$$\left[\sum_j \gamma_{pj} \right]_{th} = \frac{n_p n_s^2 n_i c^2 \varepsilon_0 L_s}{\hbar \omega_p \omega_s \omega_i \tau_s' d_{eff}^2 l^2} \cdot \frac{\pi (w_p^2 + w_s^2)}{2} \cdot \frac{1}{\mathrm{sinc}^2 (\Delta k l / 2)} \tag{2.48}$$

The result is the multi longitudinal mode threshold expression for the ICSRO. Within it the photon flow of each laser mode contributes to the threshold of the OPO. If the laser bandwidth is sufficiently small, all of the j modes produced by the laser will fall within the phase matched bandwidth of the nonlinear process and the multi-mode laser will achieve OPO threshold at the same level as that of a single frequency laser, consistent with the analysis of Harris [31].

The normalised gain, signal power and laser power are given by

$$N_j = G_j / G_{j-th} \tag{2.49}$$

$$P_s = \gamma_s / \left[\sum \gamma_{pj} \right]_{th} \tag{2.50}$$

$$P_{pj} = \gamma_{pj} / \left[\sum \gamma_{pj}\right]_{th} \tag{2.51}$$

which yield appropriate expressions for (2.39) and (2.40) as

$$\tau_s \frac{\partial P_s}{\partial t} = P_s\left(\sum P_{pj} - 1\right) \tag{2.52}$$

$$\tau_p \frac{\partial P_{pj}}{\partial t} = P_{pj}\left(N_j - 1 - FP_s\right) \tag{2.53}$$

where

$$F = \frac{\tau'_p n_s L_s}{\tau'_s n_p L_p} \tag{2.54}$$

is the ratio of the laser and signal cavity finesse and τ_p, τ_s are the pump and signal photon cavity lifetimes. The final expression that completes the set of ICSRO rate equations is the expression which describes the laser saturated gain:

$$\tau_u \frac{\partial N_j}{\partial t} = \sigma_j - N_j\left(1 + xP_{pj} + x\mu \sum_{k \neq j} P_{pk}\right) \tag{2.55}$$

where τ_u is the upper state lifetime of the laser medium, σ_j is a pumping rate term equal to the number of times that the j^{th} mode is pumped above oscillation threshold and x is a saturation parameter given by

$$x = \frac{\left[\sum_j \gamma_{pj}\right]}{\gamma_{sat}} \tag{2.56}$$

with the saturation parameter γ_{sat} representing the laser saturation photon flow. Cross saturation between pairs of modes is represented by the coefficient $\mu<1$, a concept

introduced in the analysis of SHG [32] to account for partial inhomogeneous broadening caused by spatial hole burning.

2.6.2. The ICSRO in the steady state

To solve equations (2.51) to (2.53) in the steady state, the time derivatives are set to zero. For a single frequency pump laser, the general solutions below laser threshold are

$$P_p^0 = 0 \tag{2.57}$$

$$N^0 = \sigma \tag{2.58}$$

$$P_s^0 = 0 \tag{2.59}$$

where we see that increasing pump power simply leads to a linear increase in laser gain. Once the laser is above threshold, but before sufficient power is circulating in the laser cavity to bring about the onset of SRO threshold ($\sigma_{th\text{-}L} \leq \sigma \leq \sigma_{th\text{-}SRO}$),

$$P_p^0 = \frac{\sigma - 1}{x} \tag{2.60}$$

$$N^0 = 1 \tag{2.61}$$

$$P_s^0 = 0 \tag{2.62}$$

Equations (2.60) to (2.62) now describe the operation of a normal single frequency laser with its gain clamped at its value at laser threshold. The laser power is now increasing linearly with the laser pumping rate. The SRO is still below threshold and is merely acting as linear loss inside the cavity of the laser. As the pumping rate is increased still further, sufficient power will exist inside the laser cavity to bring the SRO to threshold ($\sigma_{th\text{-}SRO} \leq \sigma$) and the steady state solutions become

$$P_p^0 = 1 \tag{2.63}$$

$$N^0 = \frac{\sigma}{1+x} \tag{2.64}$$

$$P_s^0 = \frac{(N^0 - 1)}{F} \tag{2.65}$$

Equation (2.63) shows that the laser field photon flow that is now clamped at the value it was at SRO threshold, a concept outlined in 1962 by Siegman [33] as a possible nonlinear optical power limiter. Further increases in the laser pumping rate σ lead to a linear increase in the laser gain which is coupled through the nonlinear process to produce a linear increase in the down converted signal and idler fields. This 'optical zener' effect is shown in figure 2.5 where the photon flow pumping thresholds, $\sigma_{th\text{-}L}$ and $\sigma_{th\text{-}SRO}$, have been replaced with their respective pumping power thresholds, P_{th}^{L} and P_{th}^{SRO}.

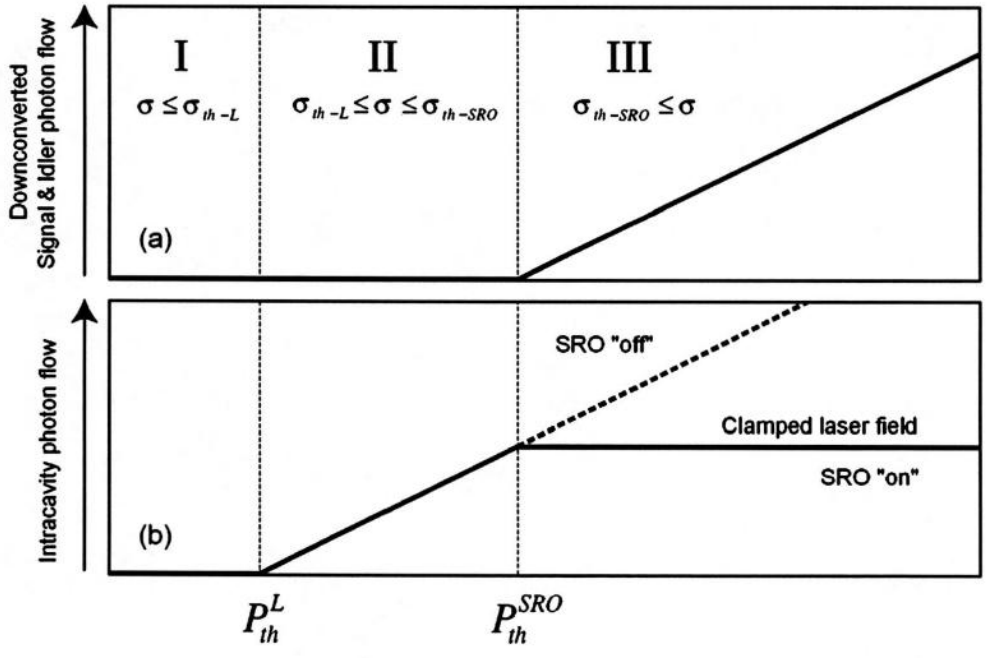

Figure 2.5: *(a) Down converted power characteristics of an ICSRO. The three regions of the figure are described by the three sets of equations (2.57)-(2.59), (2.60)-(2.62) and (2.63)-(2.65). (b) Intracavity laser photon flow in each region of operation. Note clamping in region III.*

The extension of this analysis to involve multi-frequency pumping lasers introduces further terms relating to the cross-saturation coefficient μ in (2.55) and appropriate summations over these modes. The overall nature of the treatment remains identical to the single frequency case when power optimisation and behaviour are considered. One consequence of the multi-mode case is that a small amount of narrowing of the pump laser field is experienced as the longitudinal modes operating at the periphery of the laser gain bandwidth experience sufficient loss through nonlinear output coupling into the down converted field for them to die out once the SRO is above threshold [22].

In chapter six we shall discuss the transient dynamics of the ICSRO with particular emphasis on the impact of using a laser gain media with a relatively long upper state lifetime, as the Nd:YVO_4 crystals used in the experimental work possessed.

2.6.3. ICSRO power optimisation

It can be seen from (2.57) to (2.65), and figure 2.5, that once above threshold the ICSRO acts as a nonlinear output coupler to the parent laser cavity. The concept of optimum output coupling, the value of output coupling for which extracted laser power is maximised, is extended to this nonlinear output coupling mechanism and is discussed in this section.

Examination of (2.50), (2.56) and (2.45) to (2.65) yields

$$\gamma_s = \gamma_{sat} \frac{\alpha_p}{\alpha_s} \left(\sigma - \sigma_{th-SRO}\right) \left(1 - \frac{\sigma_{th-L}}{\sigma_{th-SRO}}\right) \tag{2.66}$$

where the substitution F=α_S / α_P has been made where α_S and α_P are the round trip losses for the signal and pump resonant cavies, respectively. Equating the round trip losses of the pump and signal cavities in the steady state gives an idler output of

$$(\gamma_i)_{out} = \gamma_{sat}\alpha_p(\sigma - \sigma_{th-SRO})\left(1 - \frac{\sigma_{th-L}}{\sigma_{th-SRO}}\right) \tag{2.67}$$

We may express the total down converted power P_{DC} of the laser to signal & idler photon flow in terms of input laser power and thresholds by combining (2.66) and (2.67)

$$P_{DC} = \gamma_{\max}\left(P_{in} - P_{th}^{SRO}\right)\left(1 - \frac{P_{th}^{L}}{P_{th}^{SRO}}\right) \tag{2.68}$$

where P_{in} is the pumping power, P_{th}^{L} is the pump power at laser threshold and P_{th}^{SRO} the pump power at SRO threshold. The term $\gamma_{\max}$ is equal to the output slope efficiency of the laser and accounts for the coupling efficiency between the external pump power and the circulating laser field. The expression of $\gamma_{\max}$ is

$$\gamma_{\max} = \eta_{in}\eta_{abs}\frac{\lambda_{p-in}}{\lambda_p} \tag{2.69}$$

where η_{in} is the optical coupling efficiency of the external pump laser at $\lambda_{p\text{-}in}$ to the laser gain medium, η_{abs} is the amount of this pump power that is usefully absorbed and $\lambda_{p\text{-}in}$ and λ_p are the wavelengths of the external pump laser and pump laser, respectively. Optimisation of (2.68) for a specific external pump power P_{in} is realised through the solution of the equation

$$\frac{\partial P_{DC}}{\partial P_{th}^{SRO}} = 0 \tag{2.70}$$

which gives the SRO threshold condition that satisfies the maximum down converted power obtainable for a specific input power and laser threshold as

$$P_{th}^{SRO} = \sqrt{P_{th}^{L} \cdot P_{in}} \tag{2.71}$$

This expression can be used to derive the maximum obtainable down conversion for a specific laser threshold and input pump power under optimum conditions, which is

$$\left(P_{DC}\right)_{\max} = \gamma_{\max}\left(\sqrt{P_{in}} - \sqrt{P_{th}^{L}}\right)^{2} \tag{2.72}$$

This expression is identical to that which describes the maximum power obtainable from the parent pump laser in the absence of SRO operation, which is

$$\left(P_{out}^{L}\right)_{\max} = \gamma_{\max}\left(\sqrt{P_{in}} - \sqrt{P_{th}^{L}}\right)^{2} \tag{2.73}$$

Therefore, under *optimum* conditions, from (2.68) and (2.73) we have

$$\gamma_{\max}\left(P_{in} - P_{th}^{SRO}\right)\left(1 - \frac{P_{th}^{L}}{P_{th}^{SRO}}\right) = \gamma_{\max}\left(\sqrt{P_{in}} - \sqrt{P_{th}^{L}}\right)^{2} \tag{2.74}$$

and

$$P_{in} = \frac{\left(P_{th}^{SRO}\right)^{2}}{P_{th}^{L}} \tag{2.75}$$

These optimisation conditions are shown in Figure 2.6 where the appropriate functions are plotted as a function of increasing power.

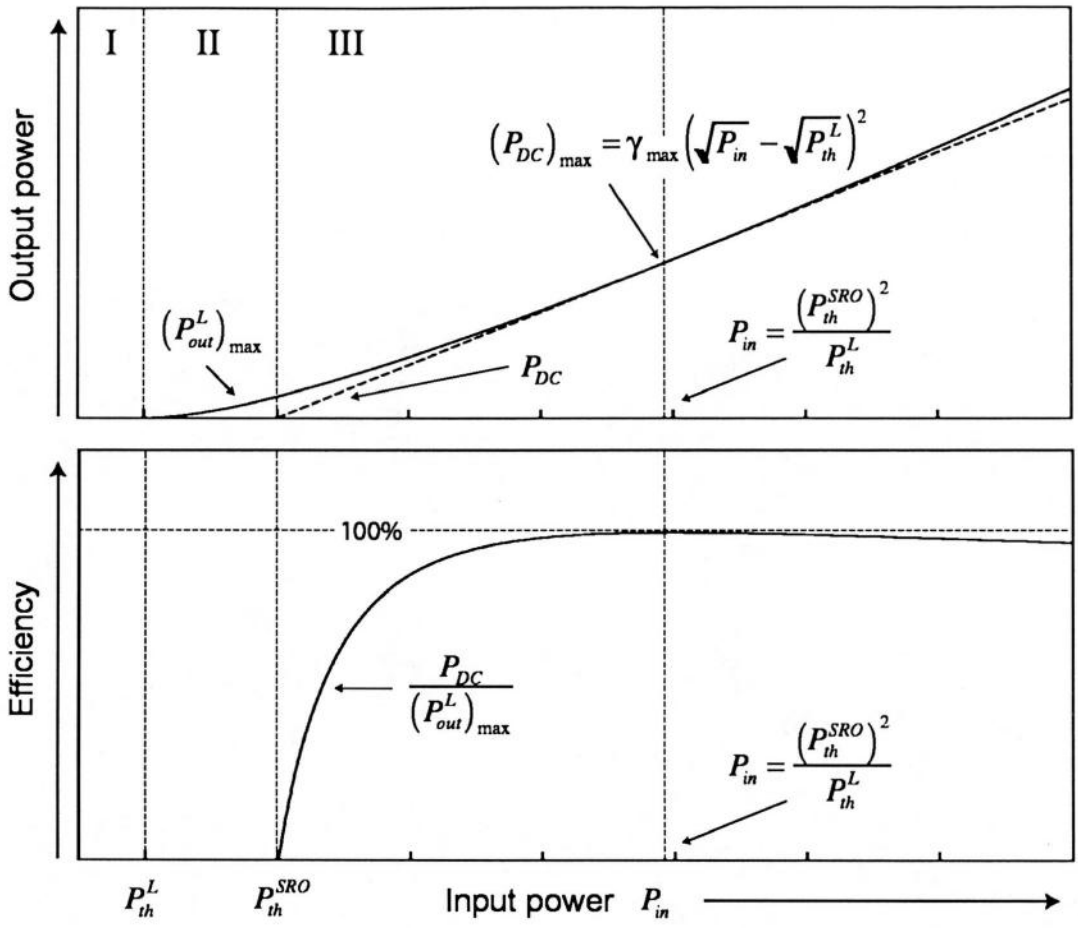

Figure 2.6: *ICSRO down conversion parameters. Region I, II and III correspond to the same regions as that in figure 2.5.*

From this figure, we see that, once above threshold, the SRO rapidly approaches 100% efficiency under the optimum laser and SRO threshold condition (2.75). To maximise output power at the non-resonant idler field and input pump power, therefore, the SRO threshold should be set to satisfy (2.75). Under ideal operating conditions, the pump laser cavity will only output couple power in the form of down converted signal and idler fields and not at the pump wavelength due to the very high finesse of the pump laser cavity.

2.7 Conclusions

In this chapter we introduced and briefly discussed the origins of nonlinear optics and how coupling through the $\chi_S^{(2)}$ nonlinear susceptibility was responsible for the optical frequency mechanisms SHG, SFM and DFG. We then went on to discuss optical

parametric generation and the $sinc^2$ nature of the phase matched bandwidth, the region over which useful parametric gain exists. The concept of quasi phase matching as an extremely flexible tool for the implementation high gain nonlinear devices was then introduced and requirements it places on laser pump sources in terms of acceptance parameters. The bulk tolerances of QPM materials were then discussed and conclusions drawn that although small deviations from the ideal design criterion result in significant reductions in device efficiency, production technologies are such that these do not represent a serious restriction on their deployment in nonlinear devices. Finally, the steady state theory of the ICSRO as derived by Turnbull [23] was outlined and the subsequent optimisation analysis re-expressed in terms of experimentally measured power levels.

References

1 R. W. Minck, R. W. Terhune and C. C. Wang, "Nonlinear Optics," *Applied Optics* **5**, 1595-1612 (1966).

2 W. Kaiser and G. C. B. Garrett, "Two-Photon Excitation in CaF2;Eu2+," *Physical Review Letters* **7**, 229-231 (1961).

3 R. Y. Chiao and B. P. Stoicheff, "Brillouin scattering in liquids excited by a He-Ne laser," *Journal of the Optical Society of America* **54**, 1286-1287 (1964).

4 G. Eckhardt, R. W. Hellwarth, F. J. McClung, S. E. Schwarz, D. Weiner and E. J. Woodbury, "Stimulated Raman scattering from organic liquids," *Physical Review Letters* **9**, 455-457 (1962).

5 Y. R. Shen and N. Bloembergen, "Theory of stimulated Brillouin and Raman scattering," *Physical Review* **137**, A1787-A1805 (1965).

6 A. Yariv and W. H. Louisell, "Theory of the Optical Parametric Oscillator," *IEEE Journal of Quantum Electronics* **QE-2**, 418-424 (1966).

7 I. D. Lindsay, *High spatial and spectral quality diode-laser-based pump sources for solid-state lasers and optical parametric oscillators*, PhD thesis, St. Andrews university (1999).

8 J. A. Armstrong, N. Bloembergen, J. Ducuing and P. S. Pershan, "Interactions between Light Waves in a Nonlinear Dielectric," *Physical Review* **127**, 1918 (1962).

9 P. A. Franken and J. F. Ward, "Optical harmonics and nonlinear phenomena," *Review of Modern Physics* **35**, 23 (1963).

10 M. M. Fejer, G. A. Magel, D. H. Jundt and R. L. Byer, "Quasi-Phase-Matched Second Harmonic Generation: Tuning and Tolerances," *IEEE Journal of Quantum Electronics* **QE-28**, 2631 (1992).

11 L. E. Myers, *Periodically poled materials for nonlinear optics*. in *Advances in lasers and applications,* D. M. Finlayson, B. D. Sinclair, Eds. (Scottish Universities Summer School in Physics, Edinburgh, 1998).

12 M. Yamada, N. Nada, M. Saitoh and K. Watanabe, "First-order quasi-phase matched LiNbO3 waveguide periodically poled by applying an external field for efficient blue second-harmonic generation," *Applied Physics Letters* **62**, 435 (1993).

13 W. K. Burns, W. McElhanon and L. Goldberg, "Second harmonic generation in field poled, quasiphase-matched bulk LiNbO3," *IEEE Photonics Technology Letters* **6**, 252 (1994).

14 N. P. Barnes and V. J. Corcoran, "Parametric generation processes: spectral bandwidth and acceptance angles," *Applied Optics* **15**, 696-699 (1976).

15 V. G. Dmitriev, G. G. Gurzadyan and D. N. Nikogosyan, *Handbook of nonlinear optical crystals*. (2nd ed.) (Springer-Verlag, Berlin, Heidelberg, New York, 1997).

16 M. K. Oshman and S. E. Harris, "Theory of Optical Parametric Oscillation Internal to the Laser Cavity," *IEEE Journal of Quantum Electronics* **QE-4**, 491-502 (1968).

17 R. G. Smith and J. V. Parker, "Experimental observation of and comments on optical parametric oscillation internal to the laser cavity," *Journal of Applied Physics* **41**, 3401 (1970).

18 E. O. Ammann, J. M. Yarborough, M. K. Oshman and P. C. Montgomery, "Efficient internal optical parametric oscillation," *Applied Physics Letters* **16**, 309 (1970).

19 J. Falk, J. M. Yarborough and E. O. Ammann, "Internal optical parametric oscillation," *IEEE Journal of Quantum Electronics* **QE-7**, 359 (1971).

20 Tran-Ba-Chu and M. Broyer, "Intracavity single resonance optical parametric oscillator," *Journal de Physique* **45**, 1599 (1984).

21 T. Debuisschert, J. Raffy, J.-P. Pocholle and M. Papuchon, "Intracavity optical parametric oscillator: study of dynamics in pulsed regime," *Journal of the Optical Society of America B-Optical Physics* **13**, 1569 (1996).

22 G. A. Turnbull, M. H. Dunn and M. Ebrahimzadeh, "Continuous-wave, intracavity optical parametric oscillators: an analysis of power characteristics," *Applied Physics B-Lasers and Optics* **66**, 701 (1998).

23 G. A. Turnbull, *Continuous-wave intracavity optical parametric oscillators*, PhD thesis, St Andrews University (1999).

24 T. J. Edwards, *Continuous-wave, singly-resonant optical parametric oscillation internal to the Ti: sapphire laser*, thesis, St. Andrews University (2000).

25 F. G. Colville, M. H. Dunn and M. Ebrahimzadeh, "Continuous-wave, singly resonant, intracavity parametric oscillator," *Optics Letters* **22**, 75 (1997).

26 T. J. Edwards, G. A. Turnbull, M. H. Dunn, M. Ebrahimzadeh and F. G. Colville, "High-power, continuous-wave, singly resonant, intracavity optical parametric oscillator," *Applied Physics Letters* **72**, 1527-1529 (1998).

27 T. Debuisschert, J. Raffy, J. P. Pocholle and M. Papuchon, "Intracavity optical parametric oscillator: Study of the dynamics in pulsed regime," *Journal of the Optical Society of America B-Optical Physics* **13**, 1569-1587 (1996).

28 W. E. Lamb, Jr., "Theory of an optical maser," *Physical Review* **134**, A1429 (1964).

29 G. A. Turnbull, D. J. M. Stothard, M. Ebrahimzadeh and M. H. Dunn, "Transient Dynamics of CW Intracavity Singly Resonant Optical Parametric Oscillators," *IEEE Journal of Quantum Electronics* **35**, 1666-1672 (1999).

30 G. D. Boyd and A. Ashkin, "Theory of Parametric Oscillator Threshold with Single-Mode Optical Masers and Observation of Amplification in LiNbO3," *Physical Review* **146**, 187-198 (1966).

31 S. E. Harris, "Threshold of multi-mode parametric oscillators," *IEEE Journal of Quantum Electronics* **QE-2**, 701 (1966).

32 T. Baer, "Large amplitude fluctuations due to longitudinal mode-coupling in diode-pumped intracavity doubled Nd:YAG lasers.," *Journal of the Optical Society of America B-Optical Physics* **3**, 1175 (1986).

33 A. E. Siegman, "Nonlinear optical effects: an optical power limiter," *Applied Optics* **1**, 739-744 (1962).

34 D. H. Jundt, "Temperature-dependent Sellmeier equation for the index of refraction n_e in congruent lithium niobate," *Optics Letters* **22**, 1553 (1997).

3: Diode pumped solid-state lasers

3.1. Introduction

Interest in diode pumped solid-state lasers (DPSSL's) has seen an upsurge in the past fifteen years or so, thanks mainly in the development of their laser diode pump sources. In this chapter we shall discuss the development of laser diodes and their use in pumping solid state laser gain media in a historical context, the associated technology of high brightness laser diode fabrication, the implementation and various merits of DPSSL's and concomitant thermal issues.

3.2. Laser diodes

To fully understand and appreciate the history and implementation of DPSSL's, it is first necessary to explore the development of the technology core to their design: the laser diode.

3.2.1. A Brief History

The first mention of the possibility of coherent light generated by stimulated emission from the recombination of electron-hole pairs at a semiconductor p-n junction came from Watanabe and Nishizawa [1] in 1957. Difficulties in the preparation of the semiconductor junction with sufficient quality meant that its first demonstration was not until five years later; a p-n junction of GaAs cooled to 77K with liquid nitrogen [2] (figure 3.1). Due to the poor carrier confinement in such a simple structure, very high current densities approaching $\sim 10^5 Acm^{-2}$ were required to achieve stimulated emission, restricting the operation of these devices to pulsed operation due to thermal constraints.

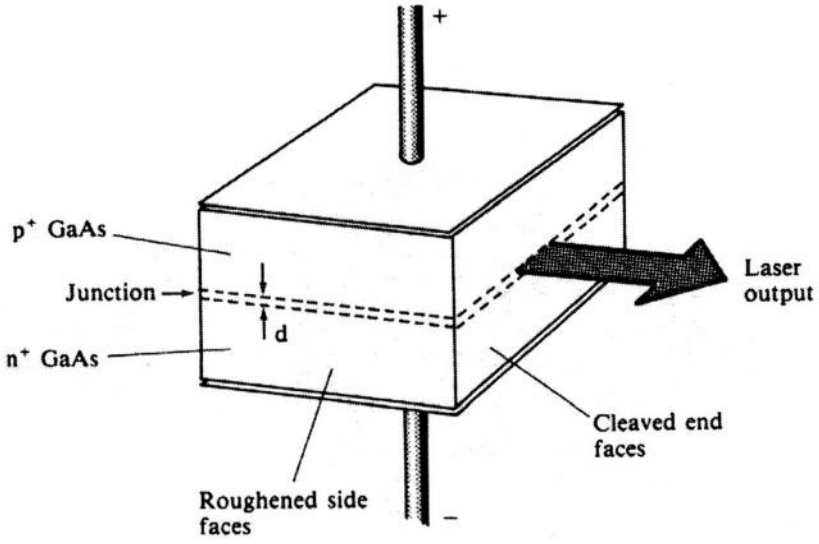

Figure 3.1: *Simple p-n homojunction GaAs laser diode.*

The operation of such homojunction lasers was limited in two respects: Very high operating currents are required in order to achieve stimulated (rather than spontaneous) emission due to the recombination of charge carriers over the entire area of the junction, and diffraction of the generated light from the plane of the junction into the strongly absorbing p- and n- regions surrounding the active region, both of which increase laser threshold to prohibitively high levels. The current densities required to achieve laser operation are such that the device temperature rapidly increases due to ohmic heating, causing catastrophic damage and therefore restricting operation to the pulsed regime [3].

In 1964 Kroemer [4] proposed the idea of a heterojunction structure in the hope of ameliorating the latter of these drawbacks. Again, limitations in the technology and fabrication techniques of the day meant that it was another six years until such a device was demonstrated by Hayashi and Panish in 1970 [5]. Further development of this technique led to the 'double heterostructure' design, formed by a sandwich of the active region of p-GaAs and n-GaAs surrounded by p-AlGaAs and n-AlGaAs layers [6]. Such designs have three main advantages over simple homojunction devices:

- The refractive index of the GaAs is slightly higher than that of the surrounding AlGaAs, thereby forming an optical waveguide and hence improving the confinement of the light produced in the active region.

- The band gap of GaAs (~1.3eV) is significantly smaller than that of AlGaAs (~1.3-2.2eV), confining the injected holes and electrons to the active region. This gives increased carrier density and correspondingly higher gain in the active layer, therefore reducing the current threshold required for lasing action.

- The different band gap energies also reduce absorption of laser light by the surrounding AlGaAs layers thereby improving performance.

These features are illustrated in figure 3.2 below.

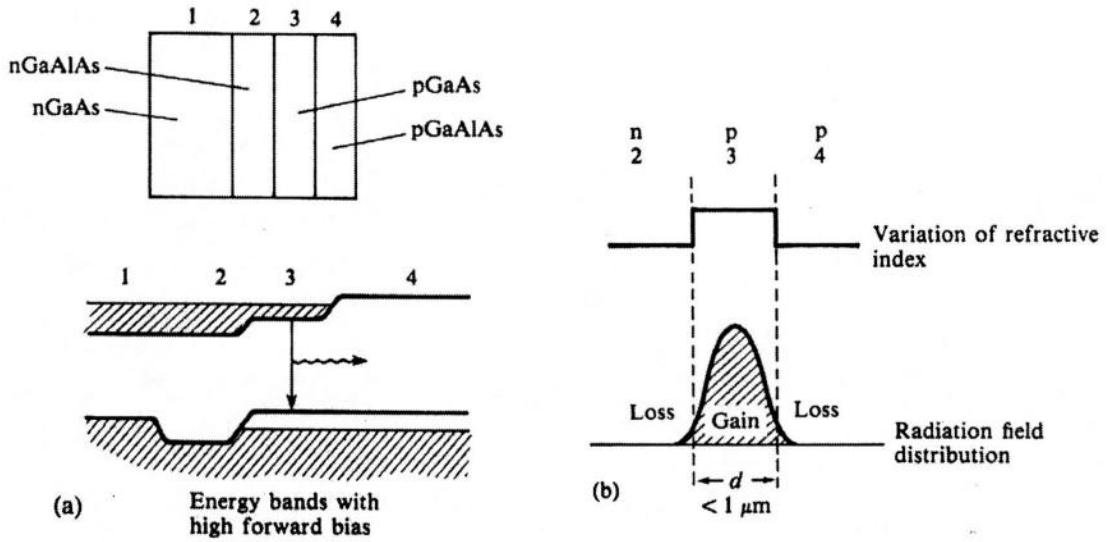

Figure 3.2: *Structure of the double heterostructure laser (a). Also shown (b) is how the structure aids the confinement of both carriers and optical radiation to the active gain region [7].*

A subsequent development of the double heterostructure design that came about in the 1980's was the concept of the quantum well. Such structures addressed the first limitation of homojunction designs where the charge carriers were allowed to re-combine throughout the active region, leading to high current density thresholds. Quantum wells provide a means of charge confinement into two dimensional potential energy wells, leading to very high carrier densities and therefore low current density threshold. There are two main ways in which quantum wells are implemented in modern laser diodes: 'multiple quantum wells' and 'single quantum well, separate confinement' structures.

Multiple quantum wells (MQW) are typically fabricated by growing alternate thin (~5-20nm) layers of GaAs and AlGaAs in the active region to form miniature heterojunctions as shown in figure 3.3. Charge confinement by proton implantation is then introduced to give many separate emitting regions.

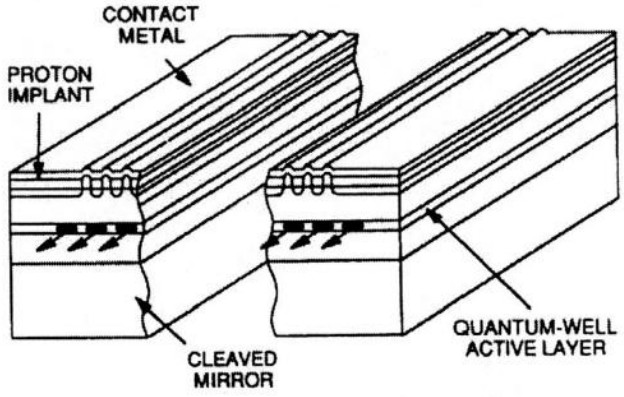

Figure 3.3: *Multiple Quantum Well heterostructure laser[7].*

The alternative approach is to employ a single quantum well, separate confinement heterostructure design (SQW-SCH), as shown in figure 3.4. In this design, charge carriers are confined using proton implantation into the p-GaAs layer. In addition to this, there is a single p-GaAlAs active layer surrounded by layers of a higher refractive index in order to give further optical confinement.

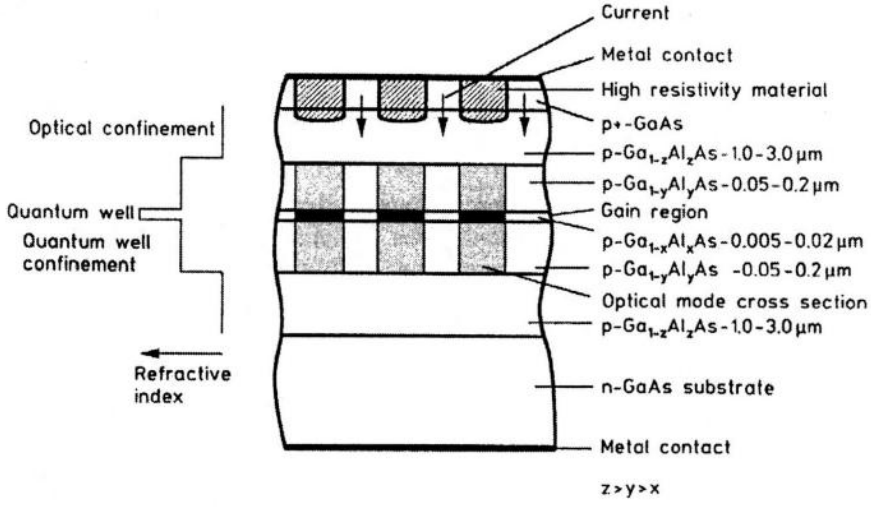

Figure 3.4: *Gain-guided, single quantum well separate confinement heterostructure stripe laser. Note that the thickness of the layers is greatly exaggerated. Optical mode cross section is actually ~5μm wide and ~0.5μm high [7].*

The thin active region incorporating a quantum well active layer structure therefore provides very low thresholds and high electrical to optical efficiency. Such a small emitting surface poses one problem, however, due to the power of the device limited by the peak flux at the output facet. Spreading the beam over an area larger than the gain region increases the extractable power from such devices. The standard procedure is to deposit layers adjacent to the active region, each of which has a slightly lower refractive index lower than that of the active region and thus forming an optical waveguide structure. In the SQW-SCH structure, the overlap between the optical mode and the gain region is only about ~4%, which results in a large effective aperture of the laser on the order of 0.3 to 0.5μm. This substantially reduces the energy density at the output facet and enhances reliability by minimising the risk of catastrophic facet damage. The cavity length of such devices is typically between 250 to 350μm.

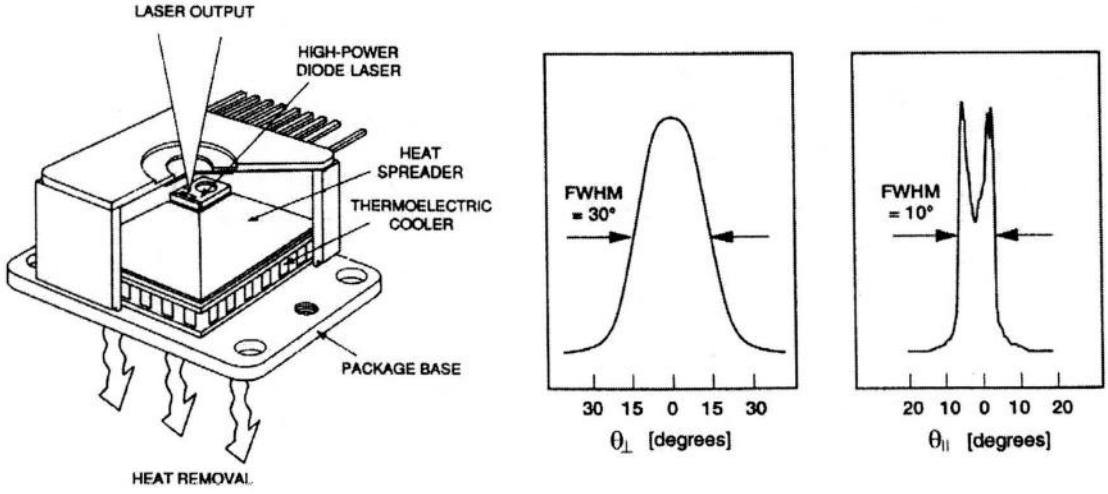

Figure 3.5: *Typical mechanical structure of a modern high power, high brightness laser diode (SDL-2460), and the spatial profile of such a device [8].*

A typical modern array MQW, high brightness AlGaAs laser diode is shown in figure 3.5, along with its spatial profile. The electrical to optical efficiency of such a device is on the order of ~40% with a threshold current density of ~100Acm^{-2} [8]. CW output powers up to ~4W are available from such devices with a multimode output polarised 20:1 in the plane perpendicular to the junction. The emission facet varies from 50-500μm, depending upon the maximum output power of the device. Typical spectral line-widths are of the

order of ~2.5nm, well within the peak absorption band of commonly used Nd^{3+} doped hosts.

The output beam emerging from the facet of the diode is in the form of a light cone which is oval in shape. In the plane perpendicular to the active layer the beam divergence is largest, about 30-40° FWHM, and is determined by diffraction from the multilayer structure. In the plane parallel to the gain region the divergence is smaller, approximately 10°, and depends upon the stripe width, cavity length and various material parameters. The two lobes in the far-field pattern is characteristic of phase coupling between adjacent stripe lasers in cw arrays. In the so-called 'leaky mode' regime, the optical field width is greater than that of the gain region and stripe separation, and so adjacent stripes are phase coupled. The particular gain and mode structure of the lasers cause adjacent stripes to couple 180° out of phase. In consequence, the far-field pattern has two lobes symmetrically positioned about the normal of the facet [9]. Reshaping the highly astigmatic pump beam emitted from a line source such as this into a quasi-circular spot, which is required by the end pumped systems considered in this thesis, is a challenging task.

When higher powers (>4W) are required for scaled pumping techniques, emitters such as those described above are serially repeated on a single substrate to form a monolithic bar structure. Practical processing considerations limit the length of such structures to about 1cm. An example of such a 1cm monolithic stripe emitter is shown in figure 3.6. The device, composed of 20 ten-stripe sub arrays spaced on 500μm centres, produces an output of ~10W in cw operation. The spacing of the emitters, which amounts to a fill factor of approximately 20%, is determined by thermal limitations. Even higher powers are obtained by arranging many such arrays into a two dimensional matrix, giving potential output powers measured in hundreds of watts cw. Two principle drawbacks of employing such integrated diode arrays are the potential for wide line width and the very poor quality of the resulting spatial mode. The first of these problems is somewhat obviated by the fact that modern fabrication techniques allow the individual emitters to be grown with greater repeatability, and the solid-state gain media pumped by such high power arrays have in general a short absorption depth and long interaction length, thereby

ensuring efficient absorption of the pump light even if the pump light wavelength is somewhat off the material peak absorption feature. A very effective way to improve the spatial properties of multi-stripe emitters is to couple their output into a multimode (~500μm diameter) optical fibre. Although this results in fresnel loss at either end of the fibre, and inevitable coupling loss at the diode end, throughput on the order of ~80% can be achieved with the optical loss offset by excellent circularity in the resulting mode. Such a system is employed in a high power Nd:YVO_4 system described in chapter 5 of this thesis. We shall see that coupling the pump light from such a fibre-coupled diode is more straightforward and efficient when compared to single stripe, low power direct diode coupled DPSSL's.

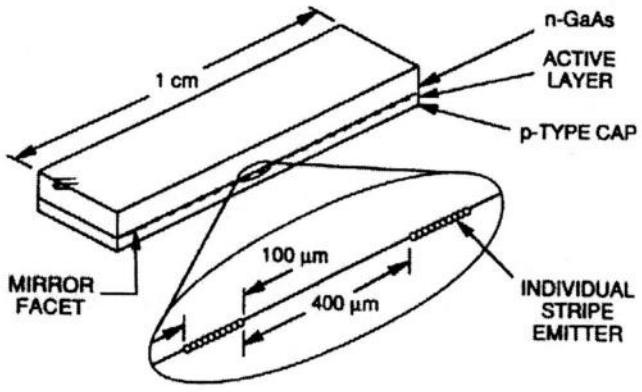

Figure 3.6: *Monolithic 1-cm bar for CW output operation.*

3.2.2. Operational considerations

Before the successful deployment of laser diodes as a pump source for solid-state gain media can take place, several key operational factors have to be considered to exploit such devices to their full potential, in terms of efficiency and operational reliability.

3.2.2.1. Spectral properties

The meritorious pumping efficiency demonstrable by DPSSL's is principally due to the excellent spectral overlap between the emission of the laser diode and the peak absorption line in the laser gain medium. The spectral properties of laser diode arrays which are most critical for the pumping of solid-state lasers are therefore the centre wavelength and the

spectral width of the diode emission. As the semiconductor band gap is a function of temperature, the centre wavelength emitted by laser diodes also varies with the device temperature. This necessitates the use of servo-controlled temperature control loops to maintain the diode wavelength at the peak absorption of the gain medium. In GaAlAs diodes, the central wavelength scans at a rate of approximately 0.3nm/°C, and so the material composition is chosen such that the desired operating wavelength falls at an appropriate junction temperature that is convenient to maintain.

This need to maintain the temperature of the diode over a relatively narrow range mandates the use of a relatively sophisticated cooling system compared to what one might employ in a flash-lamp pumped system, where one is simply concerned with the rapid removal of heat. For lower power diodes (<4W), one usually employs a servo-locked thermo-electric cooler to stabilise the temperature of the laser diode. For higher powered devices, the amount of thermal power in need of removal from the diode/sub-mount assembly is typically equal to the operating power of even large peltier coolers, leading to inefficient and ineffective thermal control. In such cases a liquid coolant, such as water, is pumped through a manifold to remove heat, which then passes through a servo-controlled heat exchanger to pass the unwanted heat into the surrounding environment. Such systems have a relatively slow response time, but are capable of removing hundreds of watts of thermal power - more than adequate for most cases.

Although the bandwidth of individual emitters is very narrow, compositional changes and temperature gradients leads to significant line broadening for high power, multi-stripe arrays. Typical spectral width of a single bar or small stacked array is of the order of ~4-5nm (figure 5.3), with state-of-the-art devices exhibiting ~2.5nm bandwidth. The bandwidth of the Nd:YAG absorption line at 808nm is 2nm for an absorption coefficient larger than $3.8cm^{-1}$. Nd:YLF, with a weaker absorption, has a bandwidth of 2nm for an absorption coefficient of larger than $2cm^{-1}$. In systems with only a short absorption path (i.e. thin gain medium) it is important to have a narrow spectral emission from the diode array in order to efficiently absorb most of the pump radiation. In optically think materials, such as large diode pumped lasers with rod of slab dimensions on the order of 10-15mm, spectral width become less important as all of the pump radiation is eventually

absorbed. Nd:YVO_4, with its much higher absorption coefficient than that of Nd:YAG, relaxes bandwidth constraints even further.

3.2.2.2. Operational Lifetime

Laser diodes suffer from two failure mechanisms: catastrophic failure brought about by a unique event and device degradation which takes place under normal use [10]. Laser diodes, like all semiconductors, are extremely susceptible to electrostatic discharges and voltage transients. Inadequate electrostatic precautionary measures often lead to premature device failure or even immediate destruction of the diode active region. Even when diode lasers have been embedded in their destination application, protection is needed from transients induced into power leads due to nearby discharges, such as the operation of a fluorescent tube. Precautionary measures can be as simple as soldering four rectifying diodes in parallel with the laser; three forward biased and one reverse, as shown in figure 3.7. Such diodes, which cost fractions of a penny, protect the laser by becoming an effective short circuit under transient conditions, thereby allowing the destructive voltage spike a safe path to ground. Under normal operation there is insufficient bias to break the three forward-biased rectifying diodes down into their conducting regime and as such are essentially transparent to the drive electronics except under atypical operating conditions, such as laser diode going open circuit after failure.

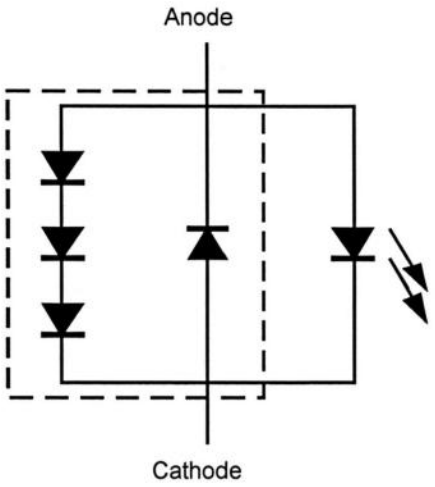

Figure 3.7: *Simple method of protecting a laser diode once embedded. The four rectifying diodes (boxed) protect the laser diode from forward- and reverse- biased transients.*

Careful considerations have to be given to the drive electronics associated with diode laser systems. Due to the very low forward bias resistance of these devices, power sources need to have an extremely low internal resistance for the efficient transfer of power. They need to be operated in a constant current, rather than voltage, mode to prevent excessive current densities occurring in the active region of the laser diode. Such excessive currents lead to catastrophic optical damage of the diode facets and, coupled with insufficient cooling, can lead to the melting or even vaporisation of the wire bonds within the diode structure. Good design features in laser diode drivers include a slow ramp-up of current when the diode is switched on to minimise thermal shock effects in the diode, and a protective relay incorporated to short circuit the laser diode when not in use. Careful and unsparing design lavished on the laser diode drive electronics pays dividends in the long and reliable operational lifetime of these expensive pump sources.

Under proper operating conditions, laser diodes degrade in a fairly predictable manner which manifests itself in a gradual decrease in output power over time. Operational lifetime is inversely related to both the current and temperature at which the diode is utilised. Indeed, diodes can often be run at power levels significantly higher than their rated value without catastrophic destruction taking place but the onset of degradation occuring in much shorter time scales than one might expect [11]. It is not uncommon for a typical 1W laser diode to exhibit an operation lifetime on the order of 10^5 hours, but as a rule of thumb this figure is reduced by a factor of two for every ten degree increase in operational temperature. The effect of over-driving the diodes is even more significant; empirical observation point to the diode lifetime falling off with the square of the number of times above the maximum rated current the device is operated at [12]. The longest lifetime is achieved in high power laser diodes which are operated uninterrupted for long periods of time, thereby reducing the stresses induced into the diode structure by thermal cycling.

Degradation of AlGaAs diodes is usually attributed to oxidisation and migration of aluminium under high power operation. This causes structural defects which spread throughout the laser diode forming light absorbing clusters. Dark lines or spots in the

output beam are a manifestation of such damage. Recently manufacturers have started to offer aluminium free active layer laser diodes [13] in the hope of abating this effect.

3.3. Diode pumped solid-state lasers

Having reviewed the historical development and technological virtues of laser diodes, we can now examine and perhaps more fully appreciate their use and various merits in the excitation of solid-state gain media. Lasers based upon solid-state materials have a distinct advantage over those based on liquids or gasses, since the lasing medium has an inherent robustness and essentially infinite operating lifetime. Solid-state lasers generally allow simpler cavity design and ease of operation. Traditionally, these devices have been pumped with water cooled flash or arc lamps. With an operational lifetime of only two to three thousand hours, the increased complexity that forced water cooling brings and the extremely low efficiency of the flash lamp pump method, many of the merits of solid-state laser media have been difficult to exploit. Progressive interest in the use of diode lasers to excite solid-state media have realised the practical demonstration of many devices which have significant advantages over their broadband lamp pumped counterparts.

3.3.1. Historical overview

Many of the significant breakthroughs in the development of compact, high efficiency diode pumped solid-state lasers came about due to advances in diode lasers as described in the previous section. The development of new solid-state gain materials has taken place in parallel with that of the laser diode pump sources.

The pumping of paramagnetic ion solid-state lasers dates back to the early 1960's, although initial progress was slow due to the poor quality of the pump sources. The first mention of the use of semiconductor emitters to pump a solid-state laser was by Newman [14] who found that the 880nm emission from a bank of GaAs diodes (essentially L.E.D.'s) could excite fluorescence near 1.064μm in a Nd:$CaWO_4$ crystal. He realised that the small size and simple structure of the diodes could make possible the direct coupling

of the pump field into the lasing medium in the absence of any complex coupling optics. Due to the relatively narrow linewidth and small solid angle of the diodes (in comparison to lamp pump sources) he concluded that significant improvements in electrical to optical efficiency could be claimed.

The first diode-laser pumped solid-state laser was demonstrated in 1964 by Keys and Quist [15] shortly after the development of the first GaAs diode lasers. The excited lasing medium was $CaF_2:U^{3+}$ with its principle transition occurring at 2.163μm. A schematic of this device is shown in figure 3.8. The five diode lasers were arranged in a side pumping or transverse geometry, in which the pump radiation is incident on the gain medium in a direction perpendicular to the resonator axis. An additional gold coated integrating chamber was placed around the gain medium to maximise the absorption of the pump radiation.

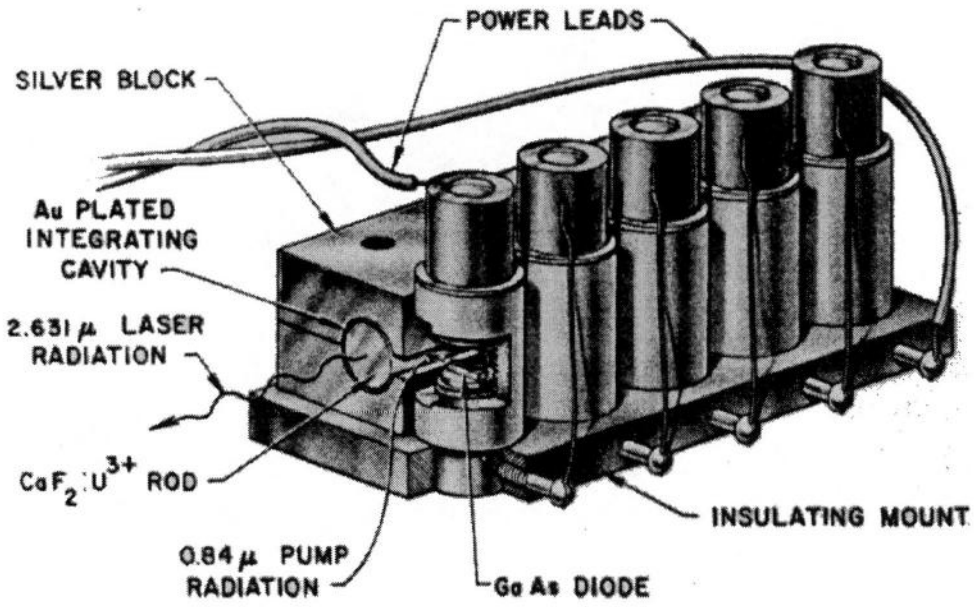

Figure 3.8: *Schematic of the first diode laser pumped solid-state laser based upon U^{3+}:CaF_2, after [15]. The diodes are arraigned for pumping in a transverse geometry.*

The entire assembly was placed in a liquid helium dewar as these early diodes needed to be cooled to obtain operation, and the lower laser level of $CaF_2:U^{3+}$ is only 609cm^{-1} above the ground state. Thus chilling the medium reduced the thermal population of this level and, hence, threshold. They obtained quasi-cw operation of their device with pulse widths

of the order of ~500μs, and pump power thresholds of ~3W. Interestingly, they noted that gain media based upon the Nd^{3+} ion would be ideal candidates for diode pumping.

The Nd^{3+} ion is an excellent dopant for semiconductor-pumped solid-state lasers. It exhibits strong absorption in the emission bands of GaAs, GaAlAs and GaAsP semiconductor lasers. The absorption spectra of two Nd^{3+} doped materials, Nd:YAG and Nd doped phosphate glass are shown about 800nm in figure 3.9. Ions excited into the pump bands relax efficiently to the upper lasing manifold, from where two four level transitions; $^4F_{13/2}$-$^4I_{13/2}$ at 1320nm and $^4F_{3/2}$-$^4I_{11/2}$ at 1064nm, and one three level transition $^4F_{3/2}$-$^4I_{13/2}$ at 946nm. Lasing action is therefore achieved with low operational thresholds.

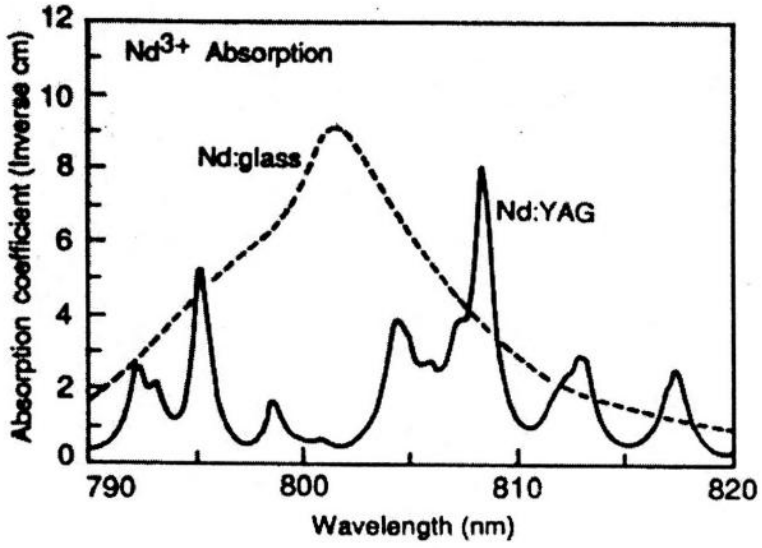

Figure 3.9: *Absorption spectrum in 1.1% doped Nd:YAG and 3% doped glass around 800nm [16].*

By the early 1970's, Nd:YAG had become the Nd^{3+} doped host of choice for lamp pumping due to its superior combination of spectroscopic, thermo-mechanical and growth properties. Yttrium othovanadate (YVO_4) had also shown initial promise as an excellent candidate to host Nd^{3+} [17], but could not be grown in sufficient volume without the inclusion of scattering centres and colour centre defects. The unavailability of high quality crystals of the size required for flash lamp pumping proved to be the major obstacle for further development. It was not until diode laser technology had matured two decades later that the meritorious characteristics of this crystal could be fully exploited.

Ross [18] demonstrated the diode pumped Nd:YAG laser in 1968. Although the YAG rod was operated at room temperature, the diode needed to be chilled to 170K in order to shift its output to the absorption band of Nd:YAG at 867nm. The gain medium was transversely pumped by a single GaAs diode. Ross noted how a combination of diode laser and solid-state gain medium technology led to the demonstration of the best features of both: the extremely high electrical to optical efficiency of the diode laser, coupled with the excellent spatial and frequency properties associated with solid-state gain media and 'conventional' cavity geometries. He also noted that the long upper state life time of Nd:YAG could act as an optical storage mechanism, allowing the collection of radiation from many diode pump sources into the medium and releasing the energy in a high peak power pulse. All of this coupled with the inherent compactness which the two technologies lend themselves to. While diode laser technology has improved substantially since the publication of Ross's paper, these advantages still exist today.

Early work on DPSSL's used transverse pumping geometries (figure 3.10a), which were convenient when poor quality pump light or a number of different sources were being used. The transverse geometry, however, exhibits very poor efficiency because of the poor spatial overlap between the pump volume and lasing mode. Pumping a laser rod from the side can also set up complicated thermal gradients, which have an adverse effect on the quality of the intracavity mode.

The alternative longitudinally, or end, pumped geometry was first demonstrated in 1973 [19, 20] giving much improved efficiency, but with only limited possibilities for power scaling. However, as the brightness of diodes has increased, end pumping has become a more attractive technique because of the good pump/laser mode overlap and ability to favour TEM_{00} operation.

With improvements in diode laser technology in the early 1980's to allow higher powers and longer operational lifetimes, the interest in semiconductor pump sources to pump Nd^{3+} doped crystals increased. These advances allowed previously unusable crystals, such as Nd:YVO_4 to once again become the subject of scrutiny. The high gain achievable in Nd:YVO_4 and the strong absorption of the diode pump radiation require crystals only a

few millimetres in length. With the constraint of large crystal size removed, and improvements in crystal growing technology, material of high optical quality became available.

Advances in diode technology and research into various solid-state gain media have born fruit in the last ten years by the commercialisation of many solid-state diode pumped devices. Indeed, almost all but the highest power 1μm lasers available commercially employ laser diodes as their pump source, due to economic, reliability and efficiency issues.

3.3.2. Realisation of a DPSSL

In this section we shall consider the issues which face the designer of a laser diode pumped solid-state laser system.

3.3.2.1. Coupling schemes

One of the most challenging tasks facing the designer of an efficient DPSSL is the efficient coupling of the pump radiation from the laser diode into the laser gain medium. In contrast to flash lamps, the radiation emitted from laser diodes is highly directional, therefore there are many possible pump geometries available for transferring the pump radiation into the solid-state gain medium. Since the output beams of laser diodes can be shaped and focussed, the principle consideration in the coupling design is to maximise the spatial overlap between the internal resonator laser mode and the pumped volume.

As discussed in the previous section, two principal methods have been adopted in the diode pumping of solid state gain media: side and end pumped configurations (figure 3.10). Analogous to flash lamp pumping, in the side-pumped geometry radiation enters the gain medium perpendicular to the axis of the resonator mode. It offers almost unlimited power scaling and a simple coupling mechanism. Indeed, such systems have been demonstrated simply by placing the diode facet into close proximity to the gain medium in the absence of any focussing optics. Poor mode matching and unfavourable

thermal gradients are the penalty that is paid for this simple coupling scheme, however, resulting in poor efficiency and resonator mode quality. All of the systems described in this thesis are end pumped systems and so no further discussion of side-pumped geometry will be made here.

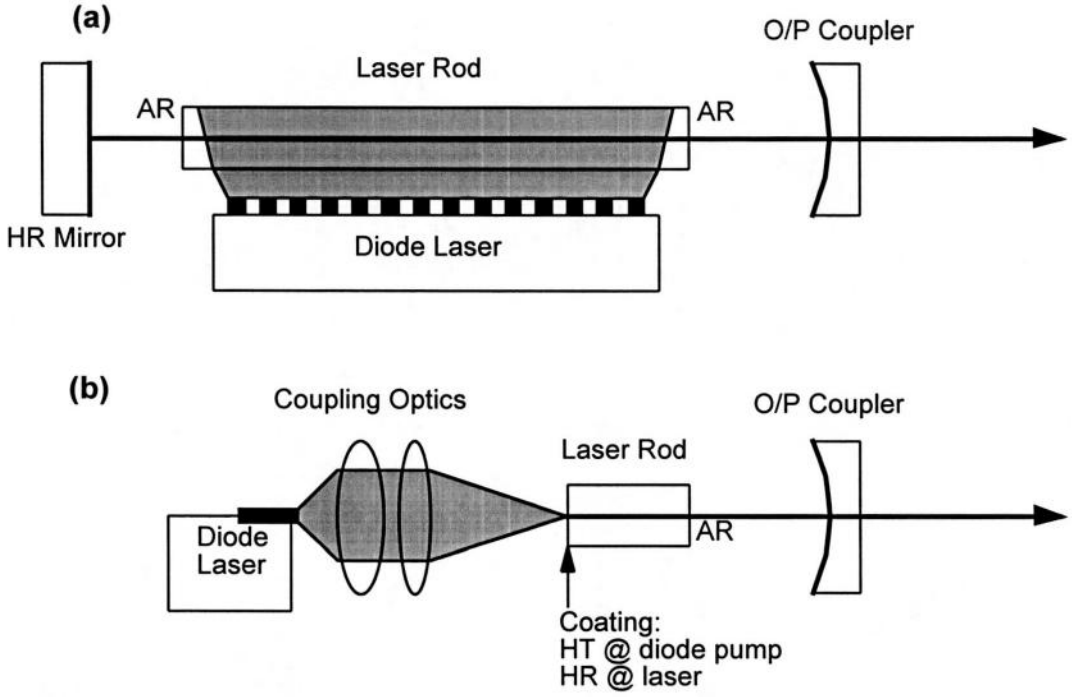

Figure 3.10: *The basic elements of a diode-pumped laser based on (a) side-pumping and (b) end-pumping. HR=highly reflective coating; AR=anti-reflecting coating.*

In the end-pumped technique, which is unique to diode pumping, the pump radiation is introduced longitudinally into the medium, co-axial with the resonator mode. Excellent mode matching between the pumped volume and a low-order resonator mode are therefore possible, leading to very good coupling efficiencies and diffraction limited output coupled beams. Matching the very high aspect ratio of the diode emission facet into the resonator mode is a challenging optical task and a number of design solutions are available to solve this problem.

In low power systems in which the diode facet dimensions are typically 1×100μm, light from the laser diode is coupled into the gain medium by means of one or more lenses, which can be simple singlets or a more complex compound lens (figure 3.11a). Such multi-element optics can give correction for spherical aberration, coma and astigmatism.

Due to the very high number of surfaces inherent to compound designs, anti-reflection coatings on such optics are essential to minimize pump power loss. It is common in such systems to use a short (~6mm) focal length lens to first collimate the diode output, then a slightly longer (~8mm) focal length lens to focus the mode down into the gain medium. For ultimate simplicity, a graded index (GRIN) rod can be used (figure 3.11b). These components combine refraction at the plane end surfaces with continuous refraction within the rod. Made from a radial graded index material, GRIN lenses are simple to use and are well suited to coupling the output of diode lasers into solid state gain media and optical fibers.

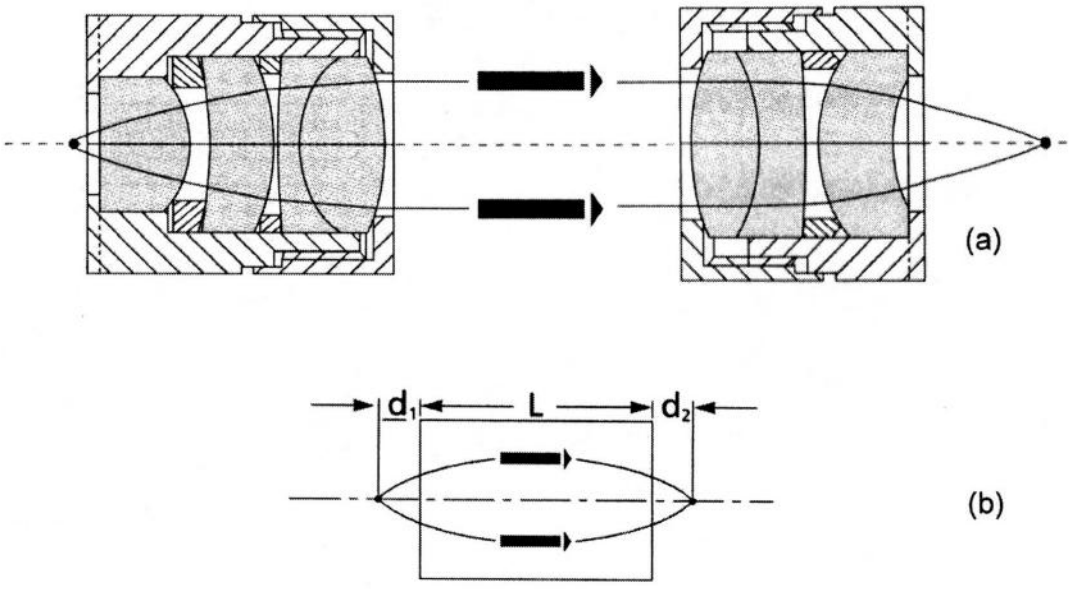

Figure 3.11: *Compound (a) and graded-index (b) coupling optics.*

The refractive index of the GRIN material varies parabolically as a function of radius. The index variation may be expressed as

$$n_f = n_0\left(1-\frac{A}{2}r^2\right) \tag{3-1}$$

where n_r is the refractive index of the material at a radius r from the center, and A is a positive constant. Incident light upon the rod which falls within its maximum acceptance angle, therefore, follows a sinusoidal path as it undergoes constant refraction. The cylindrical nature of the lens collimates and focuses the light from the laser diode into the

laser gain media without any curved surface, which makes manufacture of these components simple and cheap.

To compensate for the high aspect ratio of the emitted radiation from the diode facet, anamorphic prisms (figure 3.12) can be placed between the collimating and focusing lenses of the coupling system. As with compound lenses, there are many surfaces in this arrangement and so the prisms are AR coated for the diode pump wavelength, except for the first face as this is generally mounted at brewsters' angle. The prism pair refracts the beam in one plane, causing it to be expanded. Prism pairs such as this are available off the shelf, ready coated and are commonly supplied in two and four times magnification.

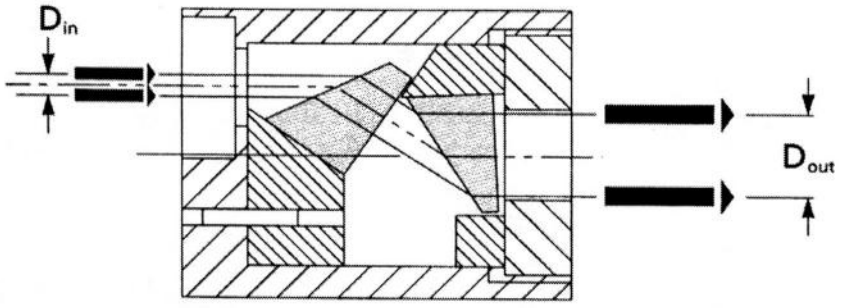

Figure 3.12: *Anamorphic prism pair.*

The very highly astigmatic output of high power, multi-stripe array diode lasers mandates the use of a more complex coupling geometry. Cylindrical lenses can be used to beam shape the diode output, but a more elegant method developed in the last decade or so is that of fibre-coupling. The poor quality mode from the multi-stripe array is beam shaped and coupled into a large-diameter (~500μm) fibre core. Although the light coming out of the other end of the fibre has become randomly polarised, such emission offers excellent circularity. Although one must tolerate the significant coupling loss at either end of the fibre, such losses are normally transparent to the end user as these devices are specified in terms of their actual useful output.

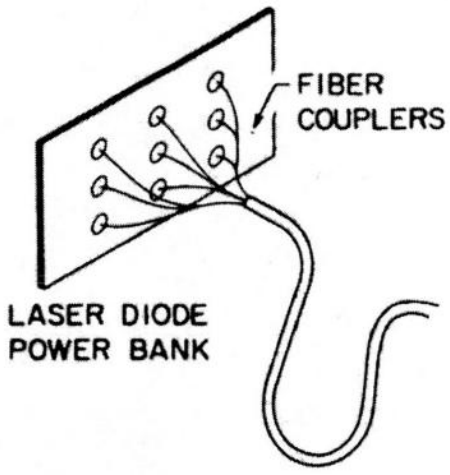

Figure 3.13: *Schematic of a fibre-coupled diode array.*

A pair of lenses can then be employed to collimate and then focus down the pump field into the gain medium. By choosing the correct ratio of lens focal lengths, the spot may be reduced in size from that of the fibre end when imaged into the laser crystal.

3.3.2.2. Mode optimisation

The choice of pump spot size in the laser gain medium is not an arbitrary one. Using a simplified rate equation approach [21], Clarkson [22] derived the following approximate expressions for threshold pump power P_{th} and slope efficiency η_S of a longitudinally pumped laser:

$$P_{th} = \frac{\pi h \nu_p (L+T)\cdot(\omega_p{}^2 + \omega_L{}^2)}{4\sigma\tau\eta_q\eta_{abs}} \tag{3-2}$$

and

$$\eta_s = \left(\frac{T}{T+L}\right)\cdot\left(\frac{\nu_L}{\nu_p}\right)\cdot\eta_{abs}\eta_q\eta_{PL} \tag{3-3}$$

where ν_P and ν_L are pump and lasing frequencies, h is Planck's constant, τ is the fluorescence lifetime, σ the stimulated laser cross section, η_q is the pumping quantum

efficiency (i.e. the fraction of absorbed pump photons that subsequently lead to excitation of the upper laser level) and η_{PL} is the effective overlap between the pumped volume and the resonated mode. T is the output coupler transmission, L is the residual round trip cavity loss, η_{abs} is the fraction of the incident pump radiation absorbed over the length of the gain medium ($\eta_{abs} \approx 1-\exp(-\alpha_p l)$, where α_p is the pump absorption coefficient and l is the gain medium length) and ω_L and ω_p are the effective TEM_{00} beam radii for the laser and pump, respectively, which are assumed to be constant over the length of the rod.

These expressions assume that both the pump and laser modes are gaussian in profile and that the total loss $(T+L) \ll 1$. The parameter η_{PL} takes into account the spatial mode matching between the pumped volume and the resonated mode. It is in this parameter that poor spatial mode quality of the pump volume, perhaps due to the high aspect ratio emission from a single stripe diode, and bad resonator design manifest themselves. For good coupling schemes and, most notably, for fibre-coupled systems where the emission is circular, η_{PL} can be assumed to be in the region 0.75 to 1 in the case $\omega_L = \omega_p$ [22]. We can see from these expressions that in order to achieve a high slope efficiency one must keep cavity losses to a minimum ($L \ll T$) and the laser gain medium should be long enough to ensure good pump absorption (typically the laser rod is ~twice that of the pump absorption length).

With fixed output coupling, we see that the threshold pump power is a function of only two system-design parameters: the pump and resonator mode size. Hence, for low pump power threshold, it is important to reduce intracavity loss to a minimum and also reduce the pump and laser mode radii. In an end pumped system, one usually chooses the pump and laser mode size to be approximately equal in order to obtain efficient, fundamental spatial mode operation [23], thus the limiting factor for low threshold operation is the ability to focus down the pump field to a small spot over the length of the laser gain medium.

It can be shown [23] that the optimum spot size, so as to minimise the pumped volume by a guassian beam with beam divergence M^2, for a given length of gain medium l with refractive index n is given by

$$\omega_{p\min} = \sqrt{\frac{\lambda l \mathrm{M}^2}{\pi n \sqrt{3}}} \tag{3-4}$$

We can see, then, that in order to reduce the pump spot radius $\omega_{p\min}$, and hence threshold, it is necessary to reduce the $l\mathrm{M}^2$ product; that is, use a pump source with good beam quality and/or a short gain medium crystal which implies a high coefficient of absorption at the pump wavelength.

3.3.2.3. Thermal loading of the laser gain medium

A major factor in the design and construction of any solid state laser, but particularly pertinent to that of diode-pumped systems, is that of thermal loading of the laser gain media by the pump source. Such loading is a problem as the extraction of heat requires a temperature gradient, which in turn leads to a non-uniform temperature distribution. This temperature distribution leads to the formation of a thermal lens in the laser gain medium and can cause stress-birefringence and, ultimately, mechanical fracture.

Thermal loading is present in any kind of laser system but particulalry manifests itself in solid-state systems due to the static nature of the gain medium. Heat is deposited into the medium due to the energy difference between the pump and laser photon, the 'quantum defect'. For example, in a Nd:YVO_4 laser system lasing at 1064nm and pumped by a laser diode operating at 808nm, the quantum defect implies that the minimum amount of heat produced is ~24% of the absorbed energy.

The passage of this heat through the laser gain media from the pumped volume to the crystal boundary (in contact with a heat sink) sets up a thermal gradient on the crystal. We can derive an expression for the resulting temperature distribution for an edge-cooled rod of length l and radius r_a mounted in a heat sink and pumped by a laser diode with power P_p. The heat flux flowing through the crystal must satisfy the heat equation

$$\nabla \cdot \mathbf{h}(r,z) = Q(r,z) \tag{3-5}$$

where **h** is the heat flux and $Q(r,z)=dP(r,z)/dV$ is the power per unit volume deposited as heat in the laser medium. The heat flux is related to the corresponding temperature distribution in the crystal by

$$\mathbf{h}(r,z) = -K_c \nabla T(r,z) \tag{3-6}$$

If we now assume that all of the heat flow is radial away from the pumped volume to the crystal boundary, and that the crystal boundary is at the temperature $T(r_a)$ of the heat sink with which it is in contact, eq. 3-5 can be integrated over a crystal volume bounded by a guassian surface of radius r and infintesimal thickness Δz, thus:

$$2\pi r \Delta z h(r,z) = \int_{z}^{z+\Delta z} \int_{0}^{r} Q(r',z') 2\pi r' dr' dz' \tag{3-7}$$

In his now classic paper, Innocenzi [24] solves this integral and relates the result to the corresponding refractive index dependence on temperature. From this the dioptric power and hence focal length of the medium is obtained. The result is simply quoted here:

$$f = \frac{\pi K_c \omega_p^{\,2}}{P_{ph}\left(dn/dt\right)} \left(\frac{1}{1-\exp(-\alpha l)} \right) \tag{3-8}$$

where ω_p is the gaussian pump spot radius, K_c the gain medium thermal conductivity, P_{ph} the amount of power contributing to the thermal lens and α the absorption coefficient of the gain medium at the pump wavelength. We can see that the magnitude of the focal length is dependent upon the square of the pump waist radius, but independent of the crystal radius or boundary temperature. Thus, in order to minimize the thermal focal length and maximise the performance of the laser at a given pump power, one should utilize the largest pump spot radius which still comfortably overlaps with the resonated mode and yet still yields practical pump threshold power.

3.3.3. $Nd:YVO_4$

Neodymium-doped yttrium orthovanadate ($Nd:YVO_4$) has several spectroscopic properties that are particularly relevant to diode pumping. The two outstanding features are a large stimulated emission cross section which is five times that of Nd:YAG, and an extremely strong absorption feature at 809nm [25].

The vanadate crystal is naturally birefringent and laser output is linearly polarised along the extraordinary π-direction. The polarised output has the advantage that it avoids undesirable thermally induced birefringence and obviates the need for an intracavity brewster plate.

The pump absorption in this uniaxial crystal is also polarisation dependant. The strongest absorption occurs for pump light polarised in the same direction as the laser radiation. The absorption coefficient is about four times higher compared to that in Nd:YAG in the π-direction [26]. The sublevels at the $4F_{5/2}$ pump band are more resolved in Nd:YAG, whereas in $Nd:YVO_4$ Stark splitting is smaller and the multiple transitions are more compacted. The result is a broader and less spiky absorption profile of $Nd:YVO_4$ when compared to Nd:YAG around the pump wavelength of 809nm.

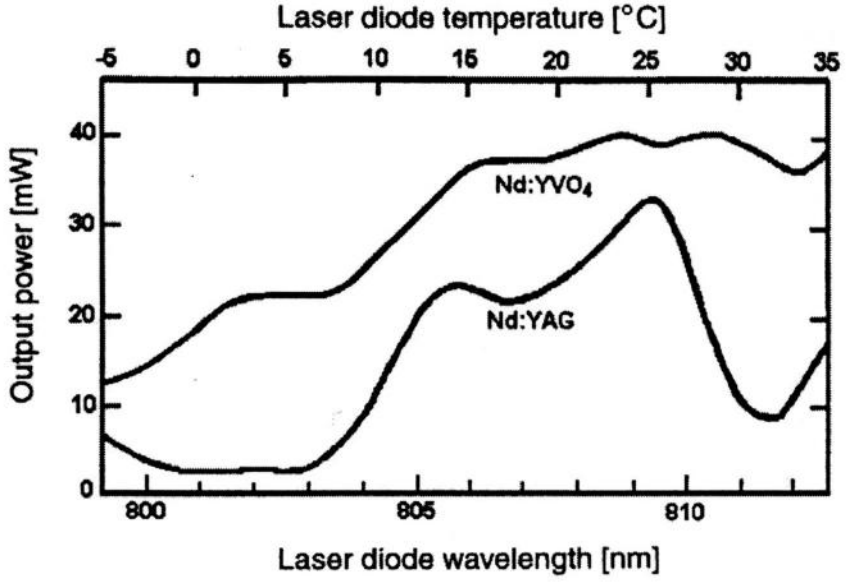

Figure 3.11: Output from a $Nd:YVO_4$ and Nd:YAG laser as a function of diode temperature and, hence, wavelength (after [27]).

Figure 3.11 above gives an indication of the broader and smoother absorption profile of this material compared to Nd:YAG. From this data it follows that a laser based upon Nd:YVO_4 is more tolerant to pump diode temperature variations and bandwidth than a similar system utilising Nd:YAG. If one defines the absorption bandwidth as the wavelength range of the pump source where at least 75% of the pump radiation is absorbed in a 5mm thick crystal, then one obtains a value of 15.7nm for Nd:YVO_4, 2.5nm for Nd:YAG [25].

Laser cross section	$15.6\times10^{-19}cm^2$
Laser wavelength	1064.3nm
Linewidth	0.8nm
Flourescence lifetime	100μs
Peak pump wavelength	808.5nm
Peak Absorption coefficient	37 (π-polarisation)
at 808nm (cm^{-1})	10 (σ-polarisation)
Nd doping	1% (atomic Nd)

Figure 3.12: Material properties of Nd:YVO_4 [25, 26].

The table above summarises the important material properties of Nd:YVO_4. The material does have some drawbacks, the principle one being the shorter excited state lifetime than Nd:YAG. As the pump input power required to reach threshold for cw operation depends upon the $\sigma\tau$ product, the large stimulated cross section σ of Nd:YVO_4 is somewhat offset by its shorter fluorescence life time τ. Fluorescence life time is also a measure of the energy storage capability in Q-switched operation, but as this technique falls beyond the scope of this thesis it shall not be considered here.

The properties of Nd:YVO_4 can best be exploited in an end pumped configuration and a number of commercial systems are based upon fibre- and lens- coupled diodes pumping a small vanadate crystal. In fact, Nd:YVO_4 has become the material of choice for cw end pumped lasers in the <5W output power region. In end pumped systems the pump beam is usually highly focussed and it is difficult to maintain a small beam waist over a distance of more than a few millimetres. In this case a material such as Nd:YVO_4 which exhibits high gain and extremely high absorption is very advantageous.

Impressive overall efficiencies have been achieved in Nd:YVO_4 as illustrated in figure 3.12. Considerably higher output is obtained from Nd:YVO_4 than from Nd:YAG. Indeed, the highest efficiency TEM_{00} performance has been demonstrated in this material [27].

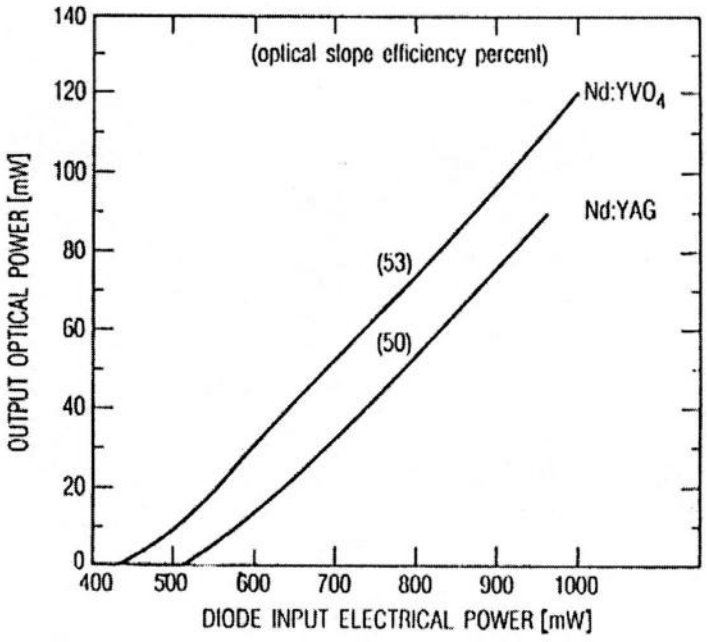

Figure 3.13: *Laser output power as a function of pump laser electrical input. Optical slope efficiencies are shown in parentheses (The cavities were output coupled at 3%). After [16].*

3.4. Conclusions

We conclude this revisionary chapter with a brief synopsis of the major beneficial attributes brought about by diode pumping solid-state gain media. It is clear that when viewed from almost any perspective, laser diodes are an excellent choice for the excitation mechanism in all but the most high power solid-state systems.

Perhaps the major impact of diode lasers in terms of performance is the overall system efficiency, which stems from the excellent spectral overlap between the diode emission and the Nd absorption bands at 809nm. In fact, flash tubes exhibit significantly higher electrical input to optical output conversion efficiencies (~70%) compared to laser diodes (25-50%). However, only a small fraction of the radiation is absorbed by the various Nd absorption bands. In contrast, the output wavelength of the laser diode can be chosen so that it falls completely within an absorption feature of the pumped crystal. A concomitant

advantage derived from the spectral match between the diode-laser emission and the long-wavelength Nd absorption band is a reduction in the amount of heat that is deposited in the laser material. This reduces thermo-optic effects and consequently better beam quality. In addition, the directionality of diode radiation allows designs with good spatial overlap between pump radiation and low-order modes in the resonator, which in turn leads to a high-brightness laser output.

System lifetime and reliability is higher in laser diode pumped solid-state lasers as compared to flashlamp based systems. Laser-diode arrays exhibit lifetimes on the order of 10^5 h in cw operation and 10^9 shots in the pulsed mode. Flashlamp life is on the order of 10^8 shots, and about 500h for cw operation.

The absence of high-voltage pulses, high temperatures and UV radiation encountered with arc lamps lead to more benign operating features of laser diode pumped systems. Furthermore, the high pump flux combined with a substantial UV content in lamp-pumped systems causes material degradation in the pump cavity and in the coolant, which lead to system degradation and contribute to maintenance requirements: such problems are virtually eliminated with diode laser pump sources.

The directionality of the diode output and the small emitting area, compared to lamp pump sources, made it possible to design whole new classes of solid-state lasers, such as end-pumped systems, microchip lasers and fibre lasers. The flexibility of shaping and transferring the output beam from the pump source to the laser medium provides a great opportunity for the invention of new pump configurations and design architectures. An almost endless variety of optical coupling schemes have been reported.

Many of the prominent laser materials that are pumped with diode pump sources can also be pumped with flashlamps. However, a number of very useful materials such as Nd:YVO_4, Yb:YAG and Tm:YAG have only reached prominence as a result of diode pumping.

References

1 Y. Watanabe and W. Nishizawa Japanese Patent "Semiconductor Maser", Patent no. 237217 (1957).

2 R. N. Hall, G. E. Fenner, J. O. Kingsley, T. J. Soltys and R. O. Carlson, "Coherent light emission from GaAs junctions," *Physical Review Letters* **9**, 366-368 (1962).

3 O. Svelto, *Principles of Lasers*. (3rd ed.) (Plenum Press, 1989).

4 H. Kroemer,," *Proceedings of the IEEE* **51**, 1782 (1963).

5 I. Hayashi and M. B. Panish, "GaAs-GaAlAs Heterostructure injection lasers which exhibit low thresholds at room temperature," *Journal of Applied Physics* **41**, 150-163 (1970).

6 I. Hayashi, M. B. Panish, P. W. Foy and S. Sumski, "Junction lasers which operate at room temperature," *Applied Physics Letteers* **17**, 109-111 (1970).

7 J. Wilson and J. F. B. Hawkes, *Lasers - Principles and Applications*. Prentice Hall International series in optoelectronics (Prentice Hall, 1987).

8 SDL Product Catalogue (1999).

9 K. A. Forrest and J. B. Abshire,"Time Evolution of Pulsed Far-Field Patterns of GaAlAs Phase-locked Laser Diode Arrays" *IEEE Journal of Quantum Electronics* **23**, 1287 (1987).

10 C. E. Wieman and L. Hollberg, "Using diode lasers for atomic physics," *Review of Scientific Instruments* **62**, 1-18 (1991).

11 A. M. S. Opto-electronics, *personal communication* (1998).

12 J. Chicken, *personal communication* (1998).

13 Coherent Product Catalogue (2000).

14 R. Newman, "Excitation of the Nd3+ fluorescence in CaWO4 by recombination radiation in GaAs," *Journal of Applied Physics* **34**, 437 (1963).

15 R. J. Keyes and T. M. Quist, "Injection luminescent pumping of CaF2:U3+ with GaAs diode lasers," *Applied Physics Letteers* **4**, 50-52 (1964).

16 W. Koechner, *Solid-State Laser Engineering*. A. L. Schawlow, Ed., (Fifth ed.) (Springer, 1999).

17 J. R. O'Connor, "Unusual crystal-field energy levels and efficient laser properties of YVO_4:Nd," *Applied Physics Letters* **9**, 407 (1966).

18 M. Ross, "Nd:YAG laser operation by semiconductor laser pumping," *Proceedings of the IEEE* **56**, 196-197 (1968).

19 D. A. Draegert, "Single-diode end-pumped Nd:YAG laser," *IEEE Journal of Quantum Electronics* **9**, 1146-1149 (1973).

20 L. J. Rosenkrantz, "GaAs diode-pumped Nd:YAG laser," *Journal of Applied Physics* **43**, 4603-4605 (1973).

21 K. Kubodera and K. Otsuka, "Single-transverse-mode LiNdP(4)O(12) slab waveguide laser," *Journal of Applied Physics* **50**, 653-659 (1979).

22 W. A. Clarkson and D. C. Hanna, "Effects of transverse mode-profile on slope efficiency and relaxation oscillations in a longitudinally-pumped laser," *Journal of Modern Optics* **36**, 483-498 (1989).

23 P. J. Hardman, *Power-scaling of diode-end-pumped solid-state lasers*, thesis, University of Southampton (1999).

24 M. E. Innocenzi, H. T. Yura, C. L. Fincher and R. A. Fields, "Thermal modeling of continuous-wave end-pumped solid-state lasers," *Applied Physics Letters* **56**, 831 (1990).

25 L. De Shazer Laser focus world, February 1994.

26 A. Brignon, G. Feugnet, J. P. Huingnard and J. P. Pocholle,"Compact Nd:YAG and Nd:YVO_4 amplifiers and end-pumped by a high-brightness stacked array," *IEEE Journal of Quantum Electronics* **34**, 577 (1998).

27 R. A. Fields, M. Birnbaum and C. L. Fincher, "Highly efficient Nd:YVO4 diode-laser end-pumped laser," *Applied Physics Letters* **51**, 1885 (1987).

4: Continuous-wave operation of a 1W diode pumped Nd:YVO_4 - PPLN ICSRO

4.1 Introduction

In the previous chapter we discussed the various merits associated with the diode pumping of solid-state gain media, and Nd:YVO_4 in particular. It was seen that such schemes can lead to extremely compact and efficient devices, due primarily to the spectral overlap between the diode emission and the absorption line in the Nd:YVO_4, the very high electrical to optical efficiency of the diode pump sources and the directional properties of their emission leading to very high intensities in the pumped volume. These advantageous characteristics obviate the need for forced cooling of the gain media, which has a tremendous impact on the simplicity of the device.

In this chapter we shall describe the exploitation of these characteristics in the design and realisation of an SRO based upon the nonlinear material periodically-poled $LiNbO_3$ (PPLN) pumped internal to a 1W diode-pumped Nd:YVO_4 mini-laser [1]. We start by describing the pump requirements of the laser gain medium and the concomitant coupling geometry, the characterisation of the simple laser cavity in the absence of down-conversion and finally the subsequent formation of an intra-cavity SRO. Through multi-parameter tuning of the poled nonlinear material we demonstrate broad tuning of the non-resonant idler over a spectrally important range. The power and spatial characteristics of the idler output are presented and discussed.

4.2 Pump Laser

We will start by describing the pump head, which includes the pump source, coupling system and laser gain media. The thermal lens induced into the gain medium by the absorption of the pump field will be measured and discussed in the context of a simple theoretical model and finally the power at optimum output coupling will be measured.

4.2.1 Pump Head

The pump head of this system comprised a 3×3×1mm 1% doped *c*-cut Nd:YVO_4 crystal [2] pumped by a 100x1μm facet area thermoelectrically stabilised 1W 810nm c-packaged diode laser [3] (figure 4.1). The pump light from the diode was coupled into the Nd:YVO_4 crystal by a graded-index rod [4], which was anti-reflection coated on both surfaces at 808nm. The temperature of the diode was stabilised by a servo-locked 9.2W peltier-effect heat pump. The diode was mounted via an indium washer on a copper block which was in turn adhered to the peltier device by means of thermal bonding compound. The copper allowed a thermal interface for the thermistor as near to the diode as possible, and aided the servo-locked temperature stabilisation by slightly increasing the thermal mass of the system. The emission of the diode was measured with a high-resolution grating spectrometer and seen to be ~3nm wide, centred on 808nm (figure 4.2); well matched to the wide absorption bandwidth of the peak line in Nd:YVO_4 [5].

The c-packed diode is manufactured with optical pumping / micro-machining applications in mind and as such is an extremely simple device, comprising a brass block upon which the diode semiconductor is mounted. The block serves both as a substrate for the diode semiconductor and as electrical anode. There is no integral photodiode within the device which mandates its use in 'constant current' mode. Electrical pumping requirements are also effected by the simplicity of the device; as the diode is not electrically isolated from the mechanical system in which it is situated, the entire mechanical assembly is at anode potential. This can complicate drive electronics as the current source must be floating with respect to the optical bench and other diagnostic instruments due to the risk of diode short-circuit. Any electrical fault on the mains to which the driver was connected could also result in the destruction of the diode due to the potential for large voltage spikes traceable to the finite resistance of the neutral line to earth. For this reason, a custom-built isolated low noise constant current source was designed and built to obviate these problems.

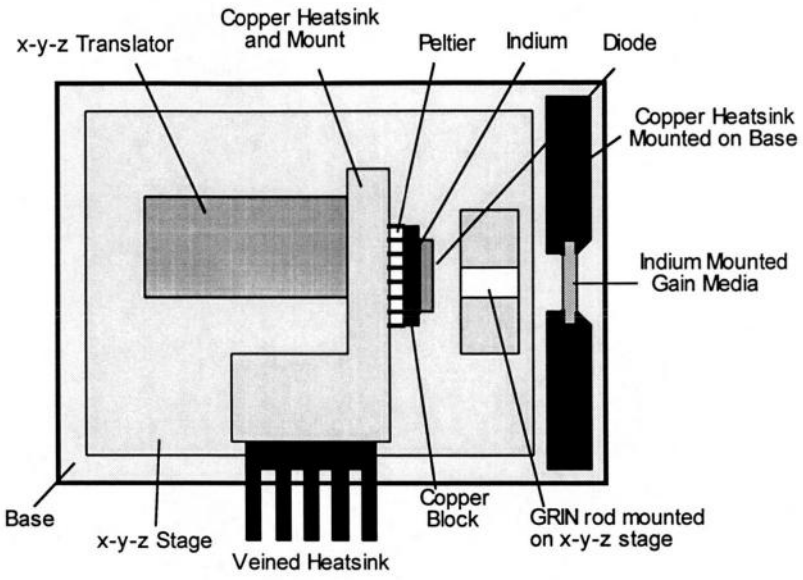

Figure 4.1: *Schematic diagram of the Laser pump head.*

The open nature of the c-package design meant that was important to ensure that the diode temperature was never allowed to fall significantly below room temperature and reach dew-point. Whilst running laser diodes at reduced temperatures has significant beneficial effects upon operational lifetime, the risk of catastrophic facet damage due to the build up of condensation at particularly low temperatures is considerable. This is not a problem faced by users of more sophisticated devices which are generally encased in a hermetically sealed container with an integral peltier device.

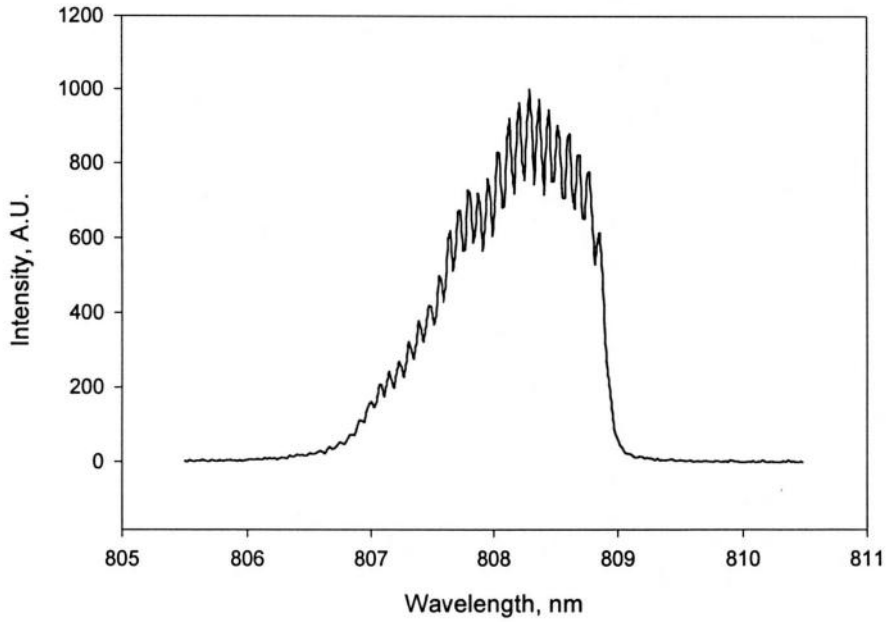

Figure 4.2: *Spectrum of diode laser [3] used to pump the Nd:YVO_4 crystal.*

The open facet design also made it important that no part of the mechanical system into which the diode was mounted could come into contact and damage the facet, leading to catastrophic diode failure. The operation temperature of the diode was not an arbitrary choice due to the importance of the spectral overlap between the diode emission and Nd:YVO_4 absorption. Figure 4.2 reveals the spectral characteristics of the diode. By comparing the line-width of the diode, measured at approximately 3nm, to the peak absorption line in the Nd:YVO_4 [5] we can see excellent spectral overlap. As the diode semiconductor band-gap is a function of temperature, the diode may be tuned to this peak absorption line empirically by scanning its temperature to minimise transmission through the Nd:YVO_4 chip. The diode wavelength was found to tune with temperature at a rate of approximately 0.3nm/°C, with peak absorption occurring in the Nd:YVO_4 at 40°C (figure 4.3) where only 3% of the incident pump light was transmitted, giving an absorption coefficient of 3.5cm^{-1}. This is in good agreement with the expected absorption coefficient of α=4cm^{-1} [5]. The small discrepancy may be due to uncertainty in the doping concentration of neodymium in the yttrium othovanadate host.

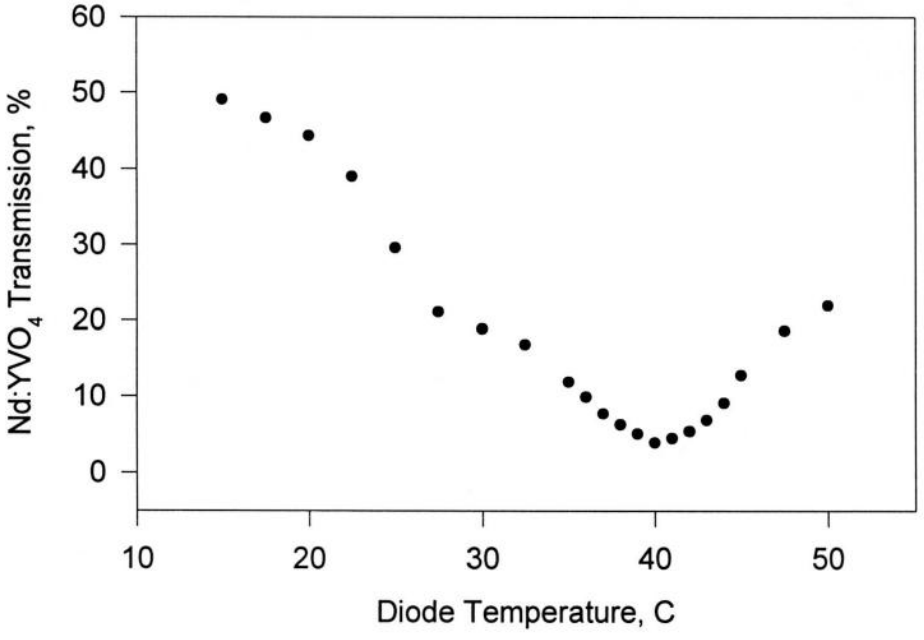

Figure 4.3: *Nd:YVO_4 transmission as a function of diode temperature.*

The current-power curve of the diode appears as figure 4.4. We can see that the device had a threshold of ~200mA and once above this point the power increased at a rate of ~1mW/mA. At the full drive current of 1.2A, a potential of 2.11V was developed across anode and cathode, leading to an electrical to optical efficiency of 40%

The disproportionate dimensions of the diode emission area led to highly divergent propagation in the plane perpendicular to the facet with respect to that in the parallel plane. To usefully exploit the diode laser emission for efficient pumping of the laser gain media, this light had to be caught and focused down to a tight spot [6]. Many systems employ separate lenses to firstly collimate and then focus down the diode emission. Although such schemes allow greater control over the pump spot size and position, a graded-index (GRIN) rod [4] was substituted for this purpose due to its simplicity. Such optics have the advantage of an extremely high numerical aperture and thus collect all the light in the highly divergent plane, are extremely compact & simple in design leading to very low optical loss, and are also inexpensive.

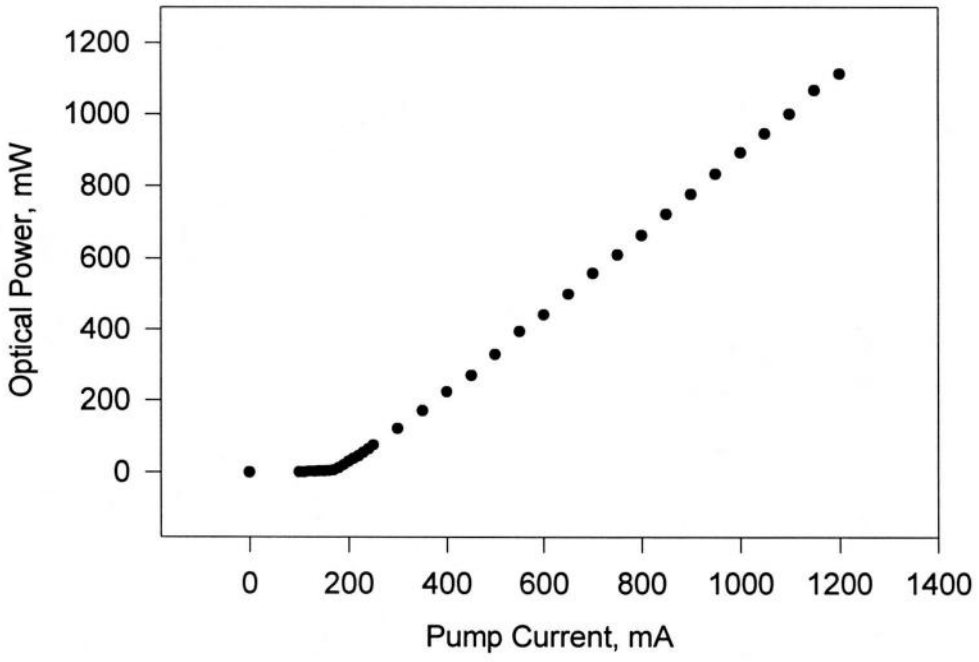

Figure 4.4: *Diode pump power vs. pump current.*

The optic employed in this system was anti-reflection coated for 808nm on both surfaces. The effective focal length of the GRIN rod was 7.6mm, was 4mm in length and 2mm in diameter. The profile of the diode pump field is shown in both planes in figure 4.5 (as measured with a moving blade profiler, outlined in figure 4.8), and the mode waist size is shown in figure 4.6. We can see both the highly astigmatic nature of the pump mode with ω_{0h} at 105μm and ω_{0v} at 40μm, and also that the beam waists in either plane are displaced by 3mm in the *z*-axis. Thus the principle disadvantage of such a simple coupling system is

revealed: in the absence of more complex beam shaping optics it is extremely difficult to obtain a circular pump mode in the Nd:YVO_4 crystal.

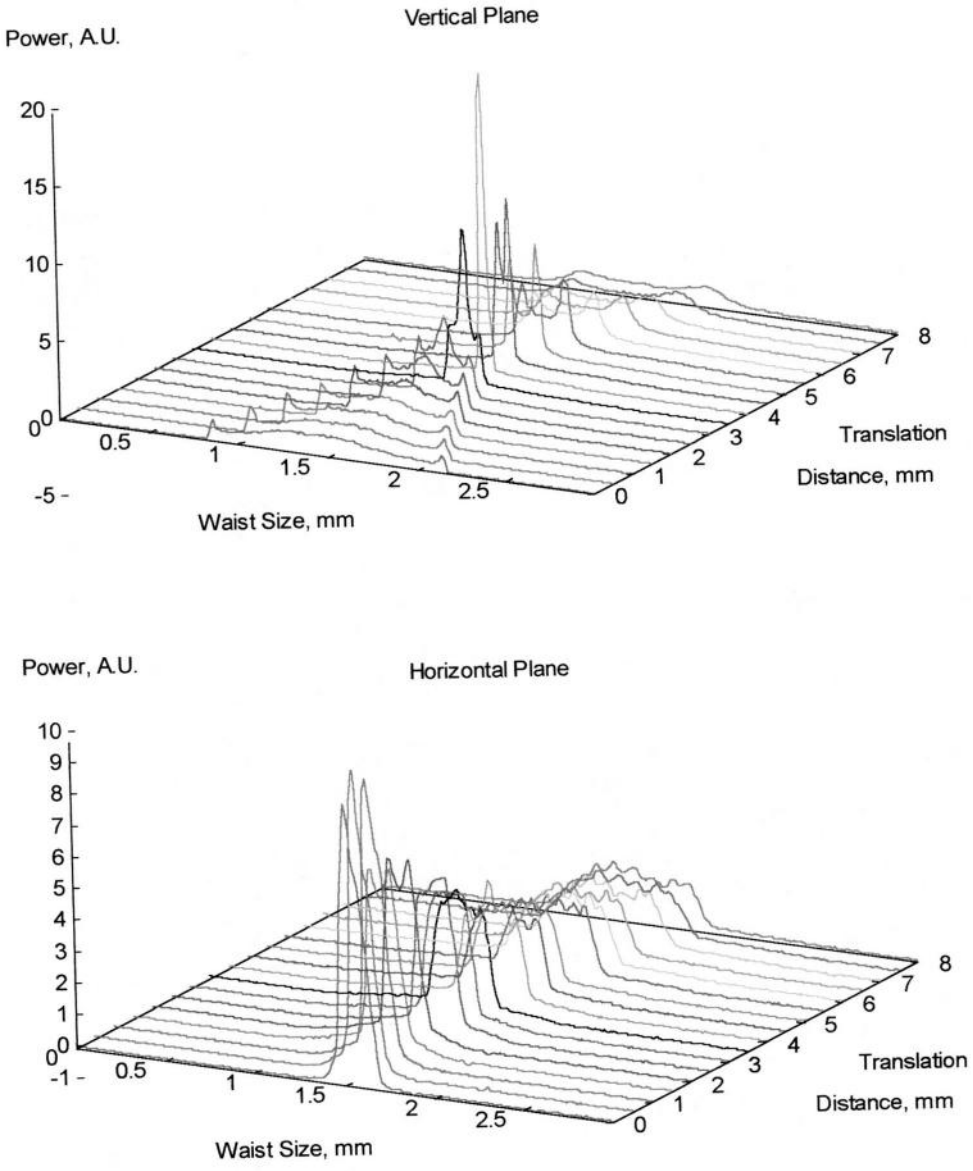

Figure 4.5: *Pump waist evolution in the z-axis after GRIN rod focusing.*
The zero position on the translation distance axis is at the face of the GRIN rod.

This leads to reduced spatial overlap between the excited volume of the gain media and the 1μm laser mode which both reduces the optical efficiency of the system and can lead to the formation of an astigmatic thermal lens in the vanadate with the associated problems that this will bring; i.e. poor mode quality. By placing the gain crystal at some point between the foci of the two pump waists, as shown in figure 4.6, it is possible to 'trade off' the inequality in the pump astigmatism against the size of the overall pumped volume. Figure 4.7 shows the resultant pump volume as measured by a calibrated CCD

camera. We can see that although the pump mode suffers from such astigmatism, the pump volume approaches rotational symmetry with ratio of 1:2 in the vertical:horizontal plane. We shall see that even with this disparity in the pump volume shape, excellent 1μm spatial mode quality is still demonstrable.

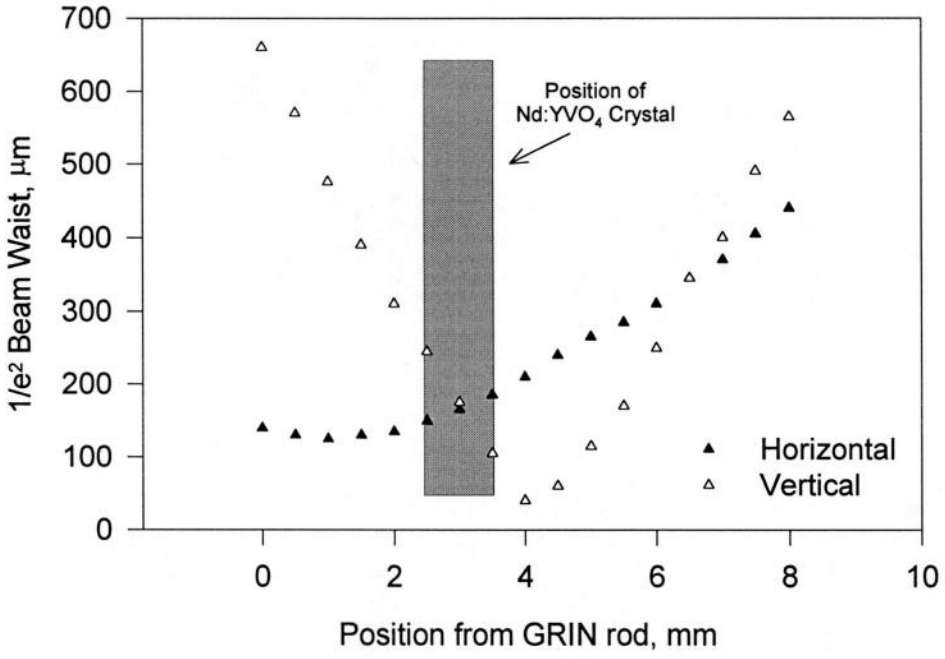

Figure 4.6: *Comparison of diode pump beam waist in each plane.*

4.2.2. 1μm laser cavity & Nd:YVO_4 thermal lens measurement

The Nd:YVO_4 was coated for AR/HR at 808nm and 1.064μm respectively on its pumped side, and AR for 1.064μm on the intra-cavity surface. The c-axis was aligned parallel to the polarisation of the pump diode to ensure full absorption of the incident pump light and to correctly polarise the intra-cavity field for the excitation of the nonlinear crystal. With the gain medium in place and the diode tuned for maximum absorption, the thermal lens induced into the crystal was measured.

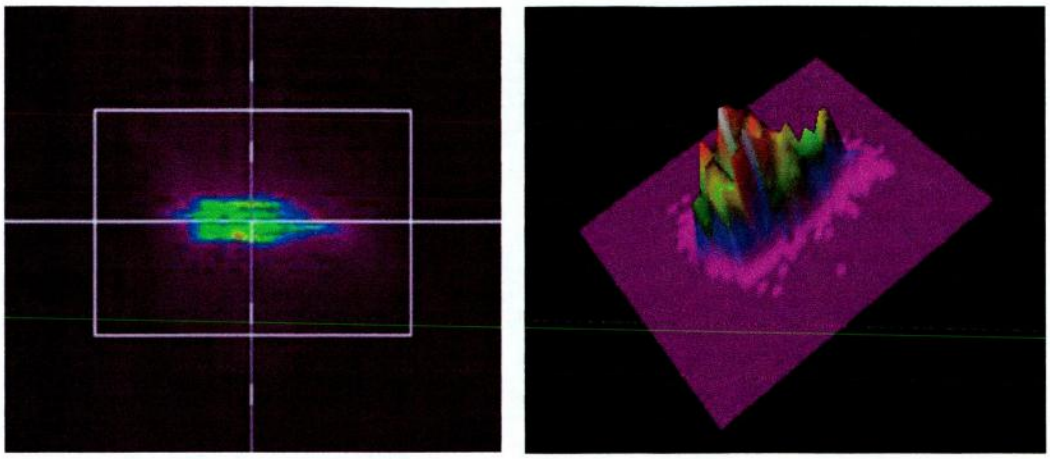

Figure 4.7: *Nd:YVO_4 pumped volume as imaged upon a CCD. The width of the box represents 400μm*

This was accomplished by configuring the 1μm laser cavity with a plano 2% transmissive output coupler. By using a plane output coupler, the stability of the cavity was rooted solely in the magnitude of the thermal lens induced in the Nd:YVO_4 crystal by the diode pump, placing the intra-cavity beam waist upon the surface of the output coupler. Thus, by measuring the spot size ω_z of the beam at a known distance z from the waist in the far field, the size of the waist ω_0 upon the output coupler can be calculated (eq. 4.1). The effective radius of curvature R in the vanadate can then be calculated by taking into account the cavity length L (eq. 4.2).

$$\omega_0 = \sqrt{\frac{\omega_z^{\,2} - 4 \cdot \sqrt{\left(\frac{\lambda \cdot z}{\pi}\right)^2}}{2}} \tag{4.1}$$

$$R = \frac{L}{1 - \frac{1}{\left[\left(\frac{L \cdot \lambda}{\pi}\right)^2 \cdot \frac{1}{\omega_0^{\,4}}\right] + 1}} \tag{4.2}$$

The beam radius was measured by a custom-built beam profiler, whose operation is outlined in figure 4.8. The profiler worked by mounting a razor edge on a computer controlled translation stage actuated by a four-phase, half step (96 position) stepper motor. By programming the computer with the pitch length of the lead screw used on the translation stage, the computer could move the razor edge to any position with a

repeatability of ~10μm. A lens was placed after the razor edge to focus the entire mode into a photodetector, which in turn was attached to a 12-bit A/D converter inside the computer. In this way, the computer could slowly reveal the beam to the photodetector and measure the amount of light upon it as a function of translation distance; the resulting curve represents an integral of the beam mode. Differentiating the data gives an accurate measurement of the beam mode profile in absolute units of distance.

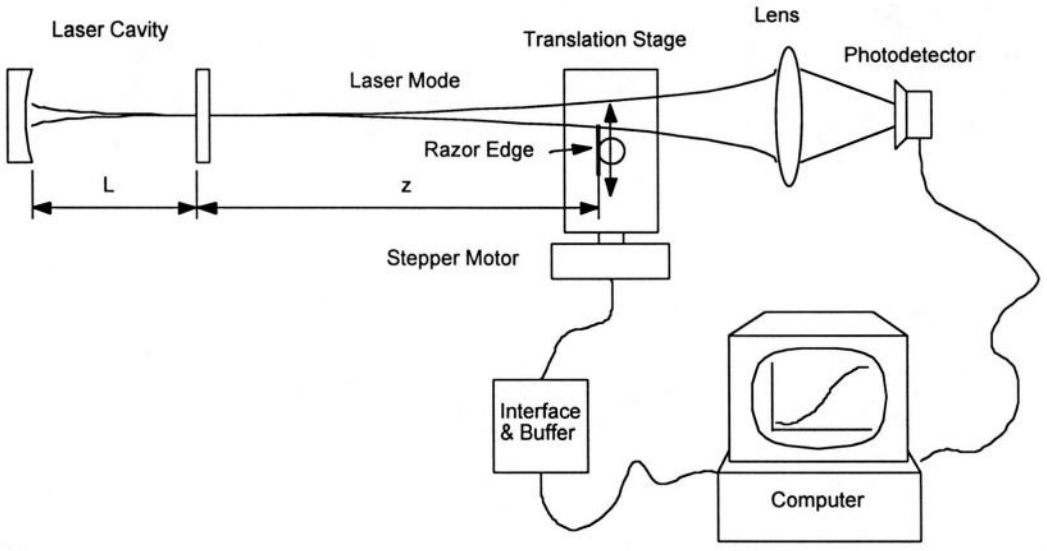

Figure 4.8: *Computerised beam profiler.*

The far-field beam radius was measured as a function of pump power, and the profiles are shown in figure 4.8. This is the raw data taken from the computerised beam profiler with no averaging or curve fitting shown. A gaussian curve was next fitted to each profile so that the $1/e^2$ width could be accurately obtained.

Using equations 4.1 and 4.2 above, the vanadate thermal lens could then be calculated. Figure 4.10 shows the effective equivalent radius of curvature ascribable to the Nd:YVO_4 crystal a function of pump power. It is interesting to note that the curvature rapidly increases with the initial growth of pump power and then remains far less dependant upon it. This is advantageous as small changes in the effective radius of curvature are required for cavity stability at both mid and high pump powers. We can see, then, that at full pump power the effective Nd:YVO_4 radius of curvature is approximately 1.5metres. This parameter was used to design the pump cavity for the intra-cavity OPO, which is the subject of the following section.

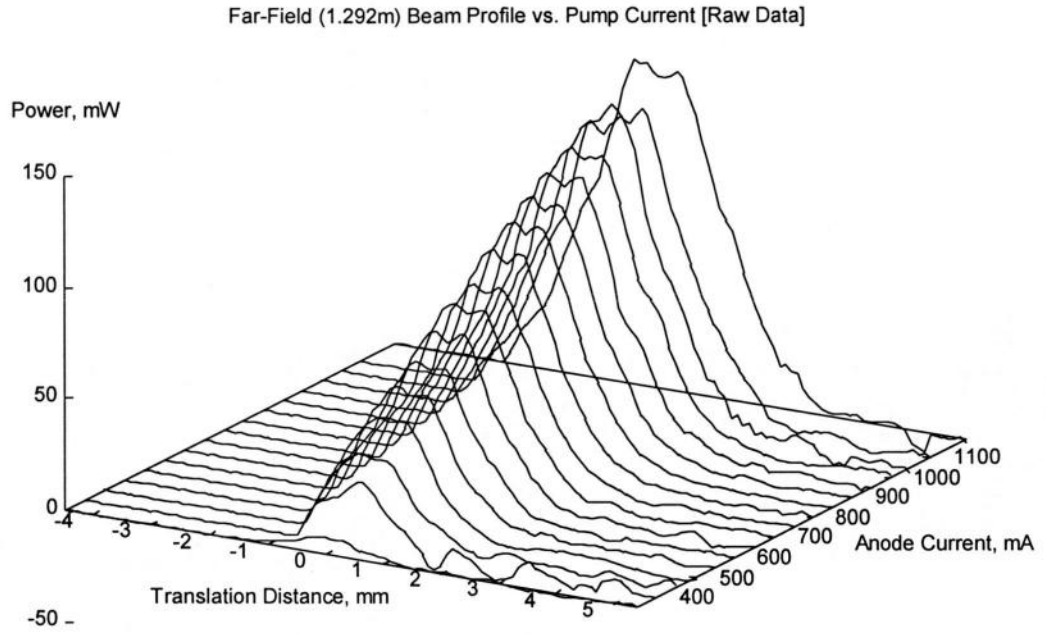

Figure 4.9: *1 μm mode profile in the far field as a function of pump current.*

One can now attempt to infer the pump mode waist size in the vanadate chip by placing the various physical properties of Nd:YVO_4 into equation 4.3 [7], where K and dn/dt are the thermal conductivity and refractive index dependence upon temperature respectively.

$$R = \frac{2\pi \cdot K \cdot \omega_p^{\,2}}{P_p \cdot \frac{dn}{dt}} \left(\frac{1}{1 - e^{(-\alpha \cdot L)}} \right) \tag{4.3}$$

This expression is plotted against the experimentally observed results is figure 4.10. We found that the best fit was obtained with a value of ω_{pump}=130μm, which is in fair agreement with that observed in figure 4.6. The poor agreement between the experimental result and the theoretical prediction shown in Figure 4.10 is attributed to the high astigmatism of the pumped volume and the concomitant poor spatial overlap between the pump volume and the circulating 1μm field.

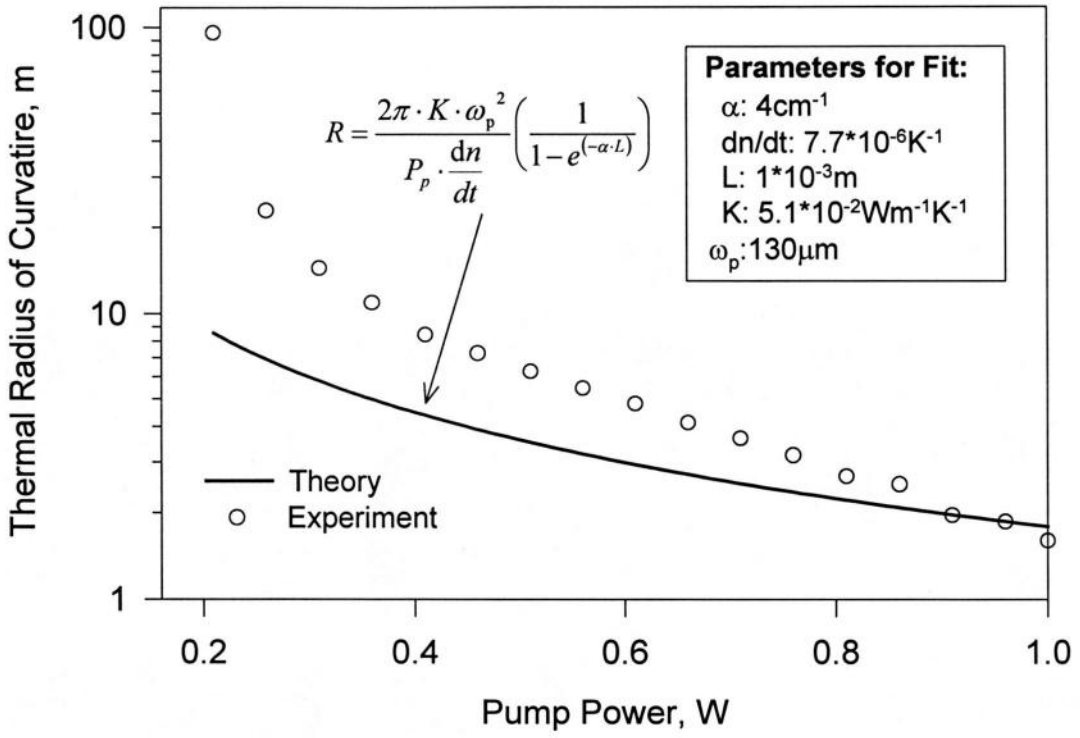

Figure 4.10: *Thermal radius of curvature shown as a function of diode pump power. The parameters for this fit, apart from ω_p, come from [5].*

A total of 430mW was extracted from this simple cavity with a 2% transmission plane output coupler (figure 4.10). Although a range of output couplers is required to find the optimum output coupled power, this value of 430mW is assumed to be optimum as no other output couplers were available at the time of this measurement. This value is used to calculate the down-conversion efficiency later in this report. It should be noted, however, that the calculated efficiency should be higher than the figure that will be stated as the optimum output efficiency does not take into account the extra loss of additional intra-cavity components such as lenses, beam-splitters and the nonlinear PPLN crystal.

4.3 Intracavity SRO

This system is based upon a design with two high finesse cavities for both the pump and signal with each sharing a common mirror and separated by a dichroic beam splitter. In this way it is simple to adjust each cavity mode independently. Such an approach also relaxes coating specifications on certain elements such as the laser gain media and intra-cavity focussing elements that only need to transmit the pump field. As the signal field is contained entirely in a separate cavity, anti-reflection coatings on optics that reside only

in the pump cavity can be much simplified to stock item 'vee' coating wavelength specification.

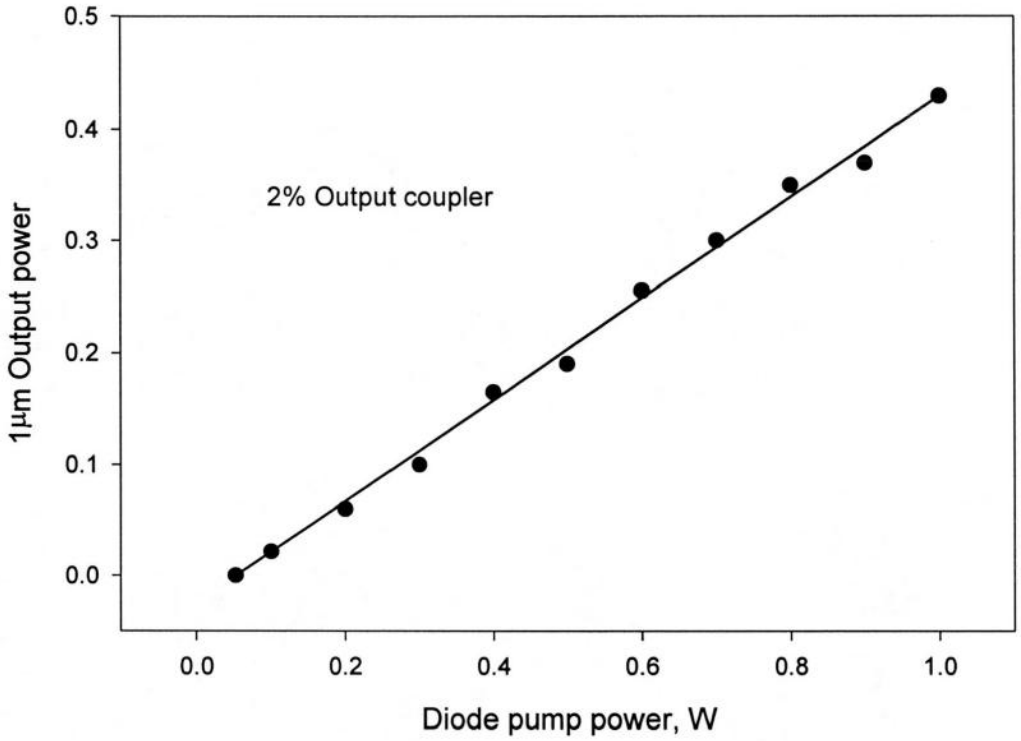

Figure 4.11: *Power in, power out for simple 1μm laser cavity with a 2% transmission plane output coupler (Cavity length=25mm).*

The experimental configuration of the device is shown in figure 4.12. The SRO cavity was defined by the common mirror M2 and a concave high reflector (M3 in figure 4.12). Mirror M2 was a concave high reflector with a radius of curvature of 100mm and was coated for high reflectivity (R>99.9%) for both the pump and resonant signal fields. M3 had a radius of curvature of 100mm and was specified to be highly reflecting (R>99.9%) at the signal wavelength only. The near concentric SRO cavity was discriminated from that of the pump by a dichroic beam-splitter that was AR coated for 1.064μm yet broad-band highly reflecting for the signal wavelengths centred at 1.5μm. The measured transmission of the beam-splitter was ~45% for the idler wavelengths. The common mirror M2 was specified to be highly transmissive (T>90%) at the idler wavelengths, and the residual reflectivity of M3 at the idler wavelengths was <5%, ensuring minimal idler feedback and therefore singly-resonant operation.

A mechanical chopper was placed in between the graded index coupling rod and the Nd:YVO_4 crystal in order to perturb the pump field and therefore induce relaxation oscillations. By measuring the frequency of these oscillations and taking into account the Nd:YVO_4 gain media upper-state lifetime and laser cavity length [8], a round-trip loss of 3.3% was inferred.

The PPLN crystal [9] was 50mm long with a 11×0.5mm aperture and had eight grating periods written upon it from Λ=28.5 to 29.9μm in 0.2μm steps. It was placed in a servo-controlled oven to facilitate signal and idler tuning by varying the crystal temperature. It was triple-band AR coated for the pump (T>99.8%), signal (T>99.8%) and idler waves (T>90%).

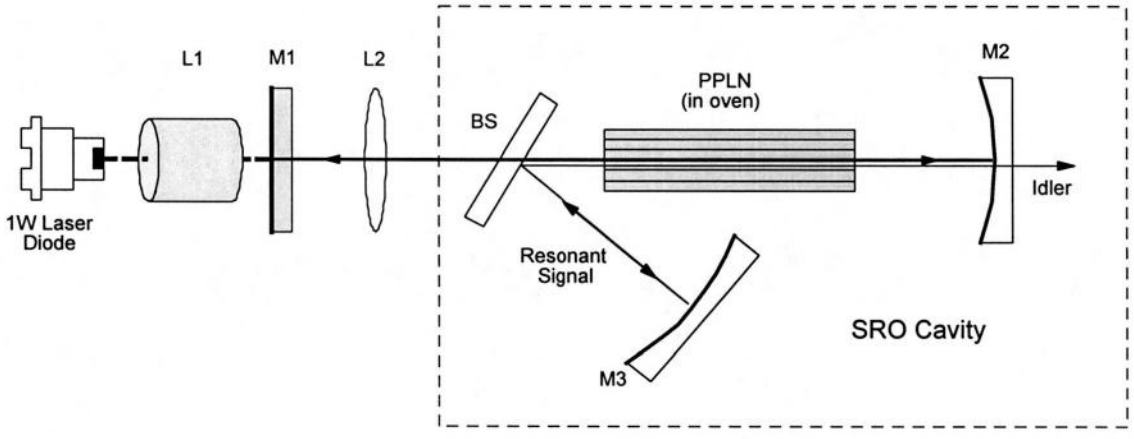

Figure 4.12: *Experimental configuration of the intracavity SRO.*

4.3.1 Design criterion and stability analysis

The design of the pump and signal cavity has to fulfil three parameters for the low threshold, efficient and stable operation if the ICSRO, which are as follows:

- That the cavities remain stable over the diode pump power range despite variations in the thermal lens induced in both the Nd:YVO_4 and PPLN crystals.

- Confocal focusing of both pump and signal fields that spatially overlap in the centre of the PPLN crystal.

- Reasonable mode matching between the 1μm fundamental resonator mode and pumped volume in the Nd:YVO_4 crystal.

As well as the traditional ABCD matrix methods of cavity stability modelling, use was made of tailored computer software developed at this university [10], which had the advantage of being able to model changes of cavity element positions/characteristics in 'real time'.

It is a well-documented problem [11] that PPLN is susceptible to the effects of thermal lensing when optically pumped, and the magnitude of this lens was a crucial parameter in the design of the laser cavity. The low power pump source of this system meant that it was important to generate a tight beam waist in both the pump and signal cavities inside the PPLN crystal, which is somewhat at odds with reducing the magnitude of the generated thermal lens. At the time of this experiment, crystal manufacturing technology had only reached the point of being able to pole through a PPLN crystal thickness of 0.5mm, making tight focussing in long crystals difficult due to mode aperturing at the crystal boundaries. It was therefore necessary to design a cavity that focussed down the 1.064μm pump to the point where OPO threshold became reasonable whilst, at the same time, keeping the thermal effects of the PPLN manageable. It was found that an intra-cavity lens could be used to fulfil these requirements.

To successfully model the cavity mode, it is necessary to simultaneously consider the waist at the centre of the PPLN crystal and the effect this has on both OPO threshold and the PPLN thermal lens. Mathematical programs were written to this effect based upon established models [7, 12]. It was found that a cavity whose stability was rooted solely in the thermal radius of curvature induced into the Nd:YVO_4 crystal and the radius of curvature of the common end mirror was incapable of producing a tight enough focus in the PPLN crystal, and even in the presence of this weak focussing was extremely sensitive to thermal lensing in the PPLN; see figure 4.13. In this figure the 1.064μm mode radius in both the Nd:YVO_4 and PPLN crystals are plotted as a function of intra-cavity field (which is proportional to the thermally induced refractive index component, n_2). To relate this thermal index of refraction to the circulating field one must first take into account the absorption of the PPLN crystal at the pump wavelength, then with a

knowledge of the thermal conductivity of the crystal obtain an expression for the temperature inside the crystal as a function of radial position from the laser axis. It is then a relatively simple task to calculate the thermal index of refraction by taking into account the refractive index dependence of the crystal upon temperature. It was to this end that a computer program was written in Mathsoft *Mathcad* to perform this calculation [13]. The results of this were compared to the analytical solution derived by Innocenzi *et al* [7] and found to be in good agreement. The model assumes that the heat source responsible for the formation of the thermal lens is gaussian and collimated throughout the extent of the PPLN crystal. Values of K_c=5.6$Wm^{-1}K^{-1}$ and α=0.15m^{-1} were used for the thermal conductivity and absorption coefficient of the PPLN crystal [14].

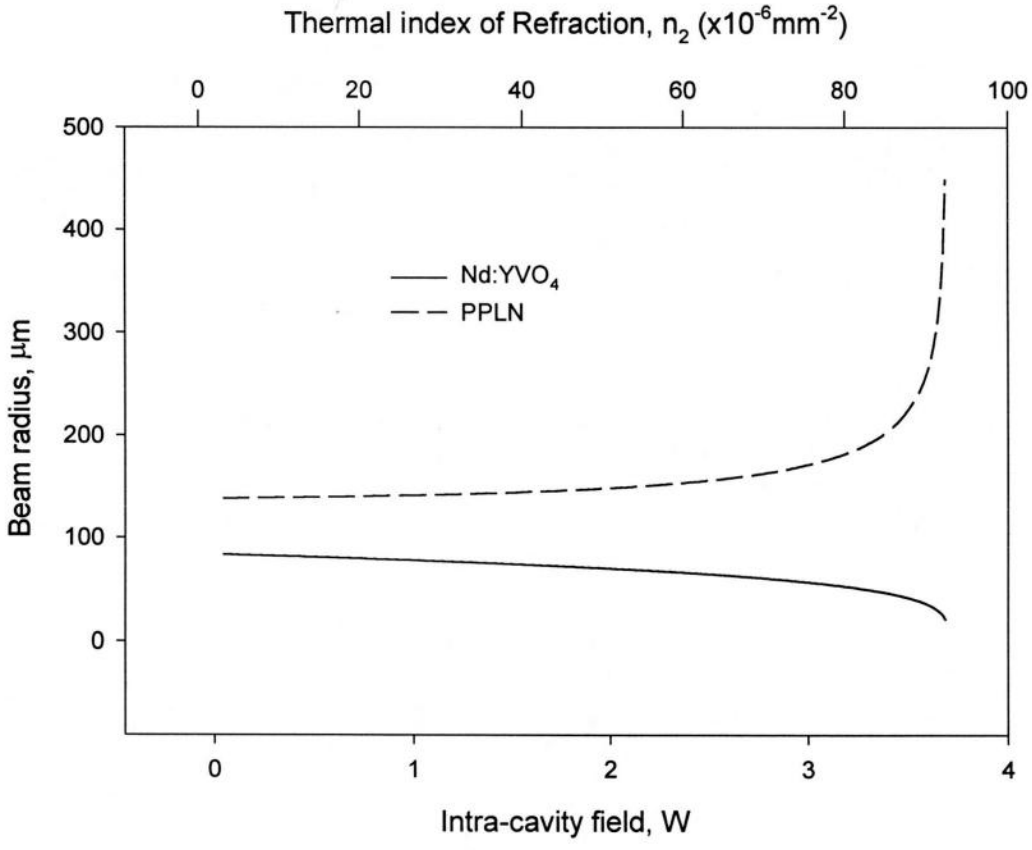

Figure 4.13: *Stability in the absence of an intra-cavity lens. The waist radii are shown at the plane HR surface of the Nd:YVO_4 and at the centre of the PPLN crystal*

The cavity mode became unstable at only moderate pump powers; well before the OPO had reached threshold due to the relatively large size of the mode in the PPLN crystal. The mode was also far from confocally focussed. By placing an anti-reflection coated short focal length lens into the cavity in the proximity of the PPLN crystal the mode was

focussed much more tightly to the extent that aperturing at the crystal surface was reduced and OPO thresholds became attainable. The cavity also remained stable over a much higher spread of incident pump power, up to five times expected OPO threshold for this waist size, as shown in figure 4.14.

We see that over the majority of the stability range the mode size changes very little, indicating the insensitivity of the intra-cavity mode as the induced PPLN thermal lens increases. Finally, however, as the g_1g_2 product tends to unity the beam waists rapidly expand, reaching instability as g_1g_2 becomes larger than one. It is also noticeable that the cavity can reasonably tolerate a circulating field of approximately 10W before mode miss-match between the Nd:YVO_4 pumped volume and circulating field becomes significant.

We have fulfilled three of the criterion for operation outlined above: Stable operation over the pump range, tight focussing and good spatial overlap between pump and signal modes in the PPLN crystal to enable attainable threshold, and good mode matching between diode pump and 1.064μm field. Mode aperturing at the PPLN crystal boundary has resulted in a somewhat under confocally-focussed waist in the nonlinear medium which manifests itself in a slightly higher OPO threshold.

It is worthy of note that the circulating pump field inside the cavity will be clamped (to a first approximation) at its threshold value as the OPO switches on, and will contribute no further to lensing in the PPLN crystal. Thermal problems will still augment in the crystal, however, as the circulating signal field starts to increase. This leads to nonlinear output coupling through the idler, however, and has less impact upon the cavity stability than the pump field.

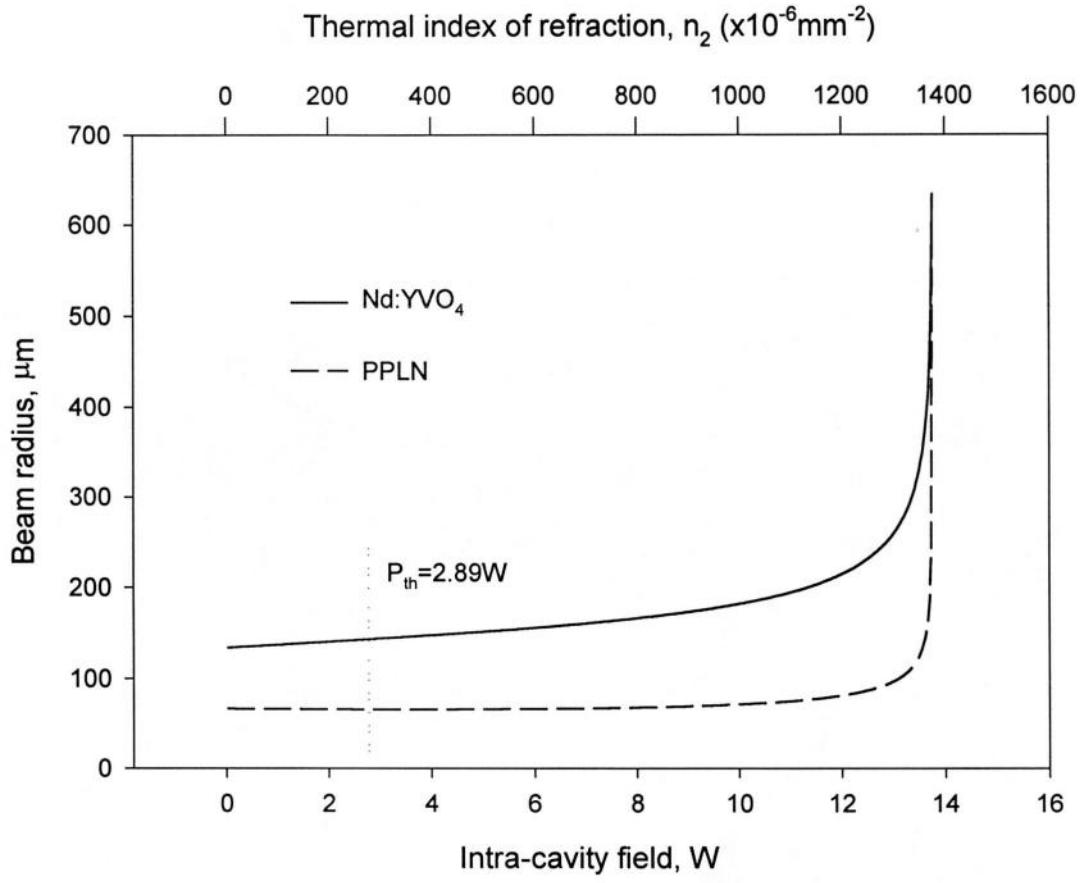

Figure 4.14: *Stability of pump mode in the presence of an intracavity lens. The waist radii are shown at the plane HR surface of the Nd:YVO_4 and at the centre of the PPLN crystal*

The signal mode experiences the thermal lens in the PPLN, just as the pump mode does. In figure 4.15, we see the effect that the pump-induced PPLN thermal lens has upon the signal mode. Once again, the figure shows the circulating field and the induced thermal index of refraction. The signal mode remains relatively unaffected by the thermal lens up to ~8W circulating field (~2.8 times expected OPO threshold). This analysis does not, however, take into account the clamping effect that the OPO process has upon the circulating field due to nonlinear output coupling through the idler field. Therefore, once the OPO field has reached threshold, increasing the diode pump power no longer leads to a linear increase in circulating pump field (figure 2.4). Although the signal field now resonates in the signal cavity, power is being extracted from the system in the form of the idler output. This means that the OPO can be pumped more than the ~2.8 times above OPO threshold without the significant modification to the signal cavity mode predicted by this simple analysis.

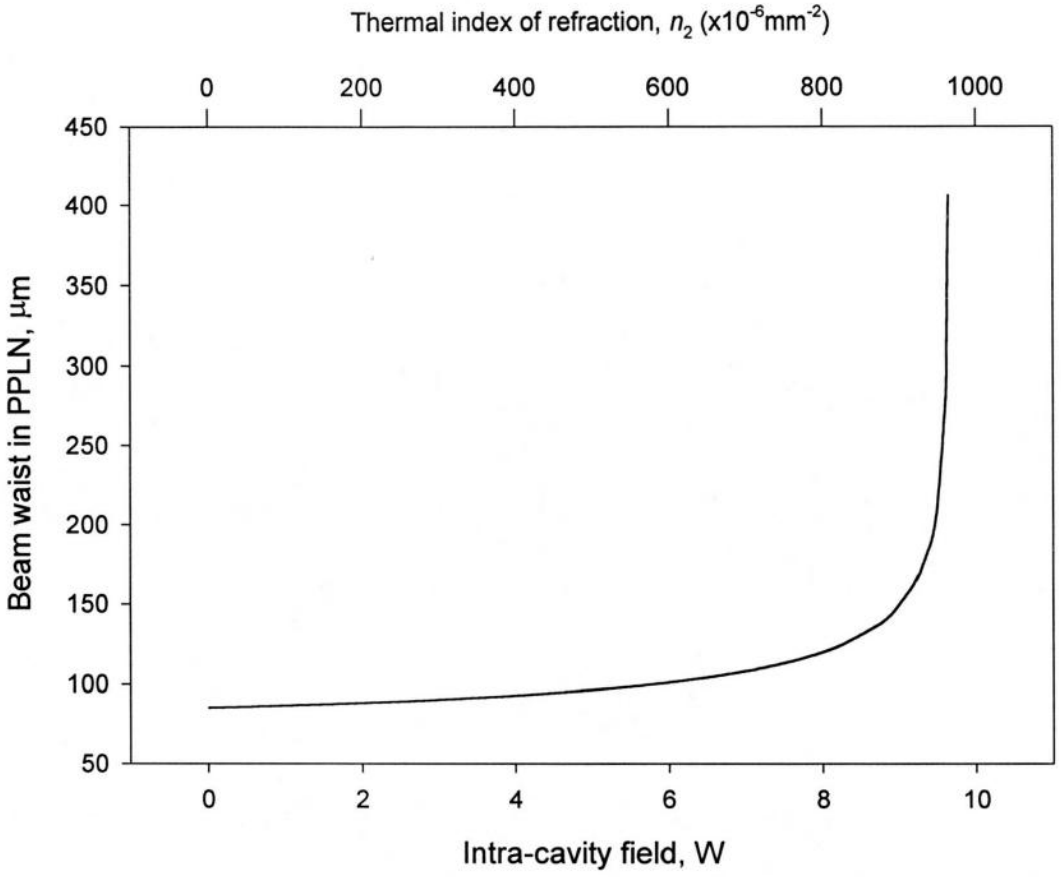

Figure 4.15: *PPLN thermal lens effect upon stability of the signal mode. The waist radius is shown at the centre of the PPLN crystal*

To summarise the cavity design, the diagram and table pairs outlined in figures 4.16 and 4.17 show the exact position, value and ray transfer matrix of each element.

4.2.2. Alignment Procedure

The principle difficulty in the alignment and operation of this system was rooted in the instability of the cavity in the absence of the PPLN crystal; it was therefore not possible to initially align the 1.064µm cavity defined by M1 and M2 before inserting the PPLN crystal in place. A retro-reflected HeNe laser was initially set up in the conventional way to reflect off of the Nd:YVO_4 crystal and hence M1. The intracavity lens was then placed at the appropriate distance from M1; its angular position optimised by looking at the reflected spot back on the HeNe laser, its *x-y* position optimised by looking at the transmitted beam and ensuring it was still incident upon the Nd:YVO_4 crystal. The beam

splitter was not put in place until the PPLN crystal and common mirror had been optimised and the 1.064μm cavity was operating.

Pump Cavity

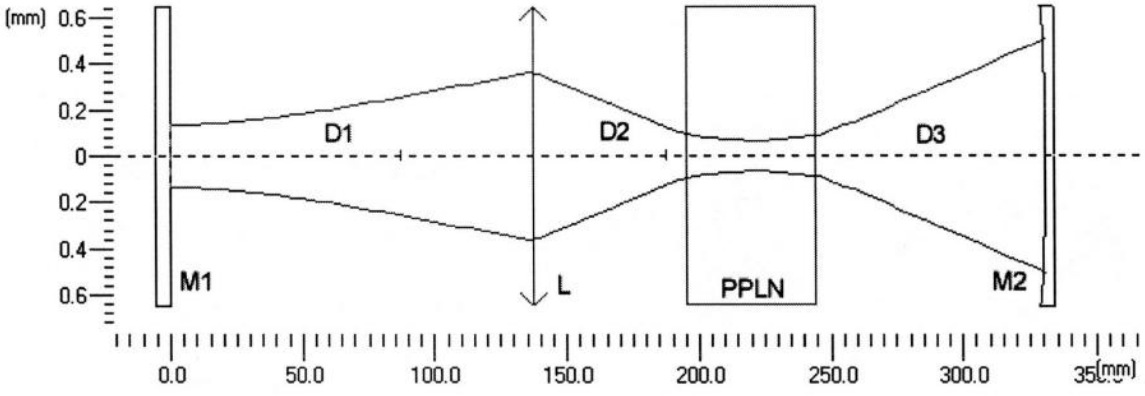

Element	Transfer Matrix	Properties
Nd:YVO4, M1	$\begin{pmatrix} 1 & 0 \\ -\frac{2}{r} & 1 \end{pmatrix}$	r=1.500m
Displacement D1	$\begin{pmatrix} 1 & d \\ 0 & 1 \end{pmatrix}$	d=138mm
Lens L1	$\begin{pmatrix} 1 & 0 \\ -\frac{1}{f} & 1 \end{pmatrix}$	f=50mm
Displacement D2	$\begin{pmatrix} 1 & d \\ 0 & 1 \end{pmatrix}$	d=58mm
PPLN	$\begin{pmatrix} \cos\left(\sqrt{\frac{n_2}{n_0}}\cdot d\right) & 2^{-1}\cdot\left(\sqrt{\frac{n_0}{n_2}}\cdot\sin\left(\sqrt{\frac{n_2}{n_0}}\cdot d\right)\right) \\ -2\cdot\sqrt{\frac{n_2}{n_0}}\cdot\sin\left(\sqrt{\frac{n_2}{n_0}}\cdot d\right) & \cos\left(\sqrt{\frac{n_2}{n_0}}\cdot d\right) \end{pmatrix}$	d=50mm n_0=2.16 n_2=0-1400 ($\times10^{-6}$mm^{-2})
Displacement D3	$\begin{pmatrix} 1 & d \\ 0 & 1 \end{pmatrix}$	d=86mm
Common Mirror M2	$\begin{pmatrix} 1 & 0 \\ -\frac{2}{r} & 1 \end{pmatrix}$	r=100mm

Figure 4.16: *Stability Analysis summary of Pump Cavity. Note that a dichroic beam splitter is present in the displacement D2 but is omitted from this analysis as it is optically inert.*

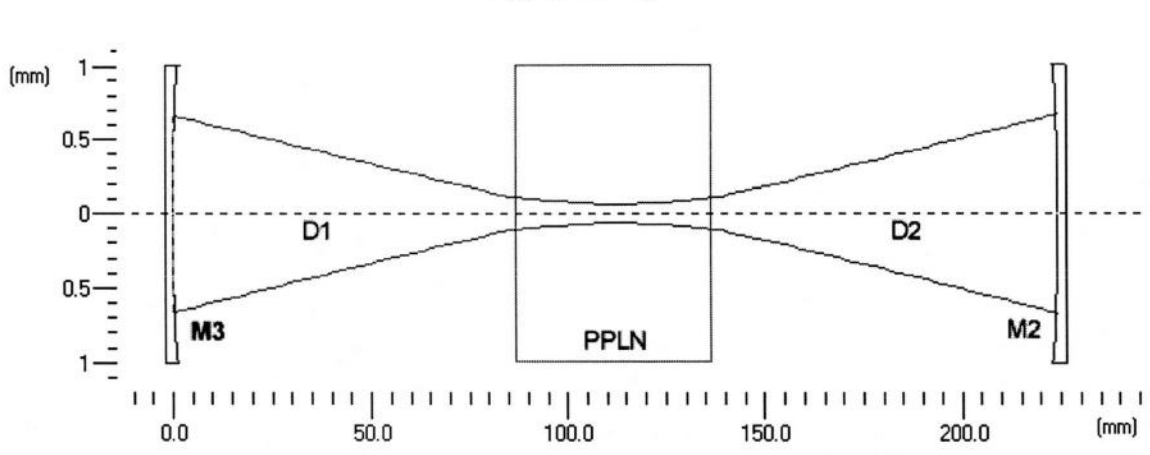

Element	Transfer Matrix	Properties
Mirror M3	$\begin{pmatrix} 1 & 0 \\ -\frac{2}{r} & 1 \end{pmatrix}$	r=100mm
Displacement D2	$\begin{pmatrix} 1 & d \\ 0 & 1 \end{pmatrix}$	d=86.5mm
PPLN	$\begin{pmatrix} \cos\left(\sqrt{\frac{n_2}{n_0}}\cdot d\right) & 2^{-1}\cdot\left(\sqrt{\frac{n_0}{n_2}}\cdot\sin\left(\sqrt{\frac{n_2}{n_0}}\cdot d\right)\right) \\ -2\cdot\sqrt{\frac{n_2}{n_0}}\cdot\sin\left(\sqrt{\frac{n_2}{n_0}}\cdot d\right) & \cos\left(\sqrt{\frac{n_2}{n_0}}\cdot d\right) \end{pmatrix}$	d=50mm n_0=2.17 n_2=0-1000 ($\times 10^{-6}$mm^{-2})
Displacement D3	$\begin{pmatrix} 1 & d \\ 0 & 1 \end{pmatrix}$	d=86.5mm
Common Mirror M2	$\begin{pmatrix} 1 & 0 \\ -\frac{2}{r} & 1 \end{pmatrix}$	r=100mm

Figure 4.17: *Stability analysis summary of the signal cavity.*

It was necessary to switch on the pump laser diode to obtain the initial position of the PPLN crystal. With the aid of an infra-red viewer, it was first necessary to ensure that the 1.064μm flourescence/808nm transmitted light was focussed down onto the PPLN surface. Then, by looking back at the pump head, the fluorescence could be seen in reflection from the PPLN surface. Due to the dimensions of the PPLN surface, a 'stripe' was imaged onto the Nd:YVO_4 mount by the intra-cavity lens. It was observed that error in the angular position of the PPLN manifested itself in curvature of this stripe which

disappeared when the crystal was correctly on axis. Any axial positional error was reflected in a spatial displacement away from the laser axis. The common mirror M3 was then put in place and, again using the viewer, adjusted so that the transmitted fluorescence through the PPLN was reflected back through its origin, essentially using the PPLN as an aperture. The pump cavity began to lase at this point.

The last component to be placed into the pump cavity was the beam splitter. With the pump cavity operating, it was initially placed into the cavity on axis and gradually tilted to the required angle. As this took place it was necessary to monitor the power transmitted through M2 with a sensitive semiconductor power meter and periodically adjust the axial position of the PPLN crystal and the angle of M2, as the finite thickness of the beam splitter displaced the optical axis of the laser (figure 4.19). Although the beam splitter represented an unwanted optical loss in the pump cavity, the 1.064μm field reflected off of the rear of this optic was useful as it gave another outlet for the monitoring of the pump field and the placement of various diagnostic instruments. The back reflected second harmonic green light from the beam splitter was also useful in the alignment of the OPO signal cavity.

With the pump cavity now constructed, the off-axis mirror M3 was put in place to complete the signal cavity. As this cavity was near concentric, the distance between the centre of the PPLN and M3 is the same as that with M2.

With the OPO cavity initially blocked by placing a beam stop in front of M3 (figure 4.11), the pump laser was optimised by monitoring the 1.064μm pump field leaking through the common mirror M2 with a sensitive semiconductor detector. It was found that crucial adjustments were the position and focussing of the diode pumped volume in the Nd:YVO_4 crystal which optimised the spatial overlap between the pump volume and 1.064μm field. Up to 3.2mW of 1.064μm power could be extracted through M2 with 1W diode pump power, corresponding to ~17W circulating field assuming a measured transmission of M2 at 0.019%. Weak generation of 532nm green was evident due to non-phase matched second harmonic generation in the PPLN crystal.

A measurement of circulating field in this way is unreliable due to the uncertainty of the high reflector M2 transmission. To overcome this, the circulating field rejected from the finite reflectivity of the anti-reflection coated beamsplitter was calibrated in terms of the circulating field by replacing M2 with an output coupler whose transmission was confidently known. Then, with the high reflector M2 back in place, a measurement of the circulating power was directly obtained by monitoring the power rejected from the beamsplitter and taking into account the previously obtained calibration factor. This result appears later in this chapter (figure 4.20).

To align the OPO cavity it was propitious to take advantage of the second harmonic light back-reflected off of the beam splitter. As the coating on the beam splitter was undefined at 532nm, a considerable amount of light at this wavelength was reflected off of it. If one considers light incident on the beam splitter from the left in figure 4.18 (i.e. approaching from the Nd:YVO_4 crystal) then it is clear that two spatially separated spots will be produced in reflection moving toward the top of this diagram, thus:

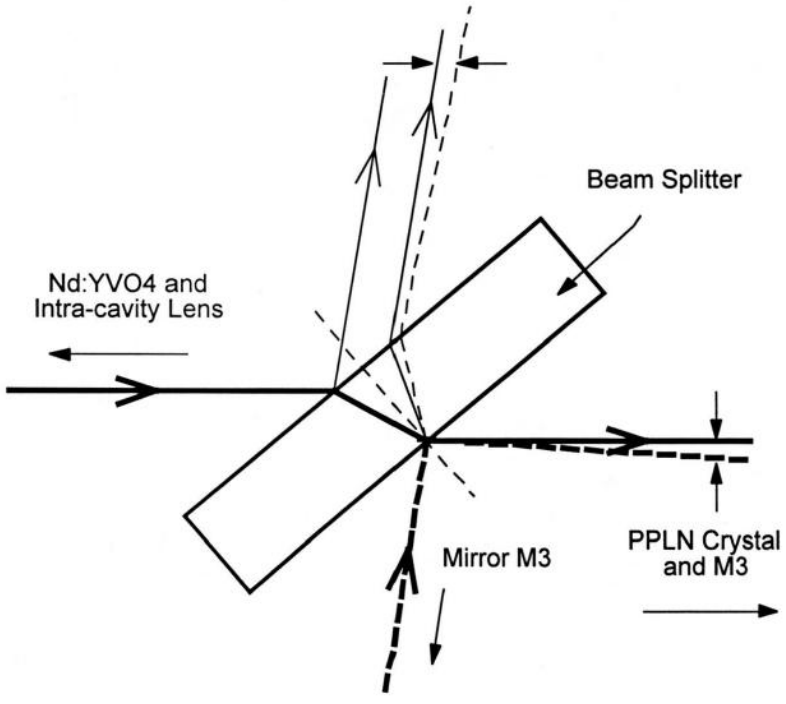

Figure 4.18: *Green modes coaxial with the pump mode (solid lines) and signal mode (broken lines) and their interaction with the beam-splitter. Note that here the signal cavity is shown slightly misaligned.*

We can see in this diagram that the impinging SHG light from the left and refracting at the surfaces of the beam splitter produces two parallel beams toward the top of the diagram. Also shown is the green light reflected off of M3 (thick broken line) coming up from the bottom of this figure. We can see here that M3 is slightly miss-aligned; it is clear that the SHG light reflected by M3 will become co-axial with the right hand reflected beam when M3, and hence the signal cavity, is aligned, indicated by the arrows. By placing a piece of white card on the bench in order to observe these spots more clearly, the alignment of this cavity becomes very straight forward. Indeed, as the spots are brought togther one can observe the SHG light reflected off of M3 as transmitted through the PPLN crystal and M2 becoming coaxial with the doubled pump light.

As both cavities become aligned and the OPO switches on, the pump field depleats and therefore the amount of SHG green light is significantly reduced. Non phase-matched sum-frequency mixed light between the pump and signal fields causes the production of red light at approximateley 632nm which is also clearly visible. It can be useful to place a red filter in front of M2 to block out the SHG green light and thus observe this red light even more clearly.

4.3.3. Operation

This section presents a characterisation of the OPO system in terms of threshold and ouput power properties, power and spatial mode stability characteristics and spectral coverage of the signal and idler as the PPLN temperature is varied and the spectral purity of the down converted fields.

4.3.3.1 Power

The operation thresholds for the pump laser and the SRO were achieved for input diode powers of 63 and 310mW into the Nd:YVO_4 crystal respectively. The SRO diode power threshold of 310mW is more than an order of magnitude lower than that achieved in an external SRO with similar design parameters [15], thus demonstrating the potential of the intra-cavity approach. The corresponding intra-cavity circulating pump power at 1.064 μm was inferred at 3.3 W (one way) at the SRO threshold, compared with a calculated

threshold of 2.6 W, assuming confocal focusing and an effective nonlinear coefficient of 14pm/V for PPLN [16]. This measurement was obtained by measuring the back reflected pump field incident upon the beamsplitter as described in the previous section. Figure 4.19 shows a typical plot of the extracted output power in the non-resonant idler and the total SRO down-converted power, deduced from this observed idler power, in the signal and the idler as a function of the diode pump power. The data was recorded at an idler wavelength of 3.66 μm and correspond to the two-way idler power extracted from the cavity in both directions. At the maximum diode power of 1W, the total idler power extracted from the SRO was 70mW. To measure the idler a germanium filter was placed in front of the power meter thermopile, thus blocking any leaking pump and signal field through M2.

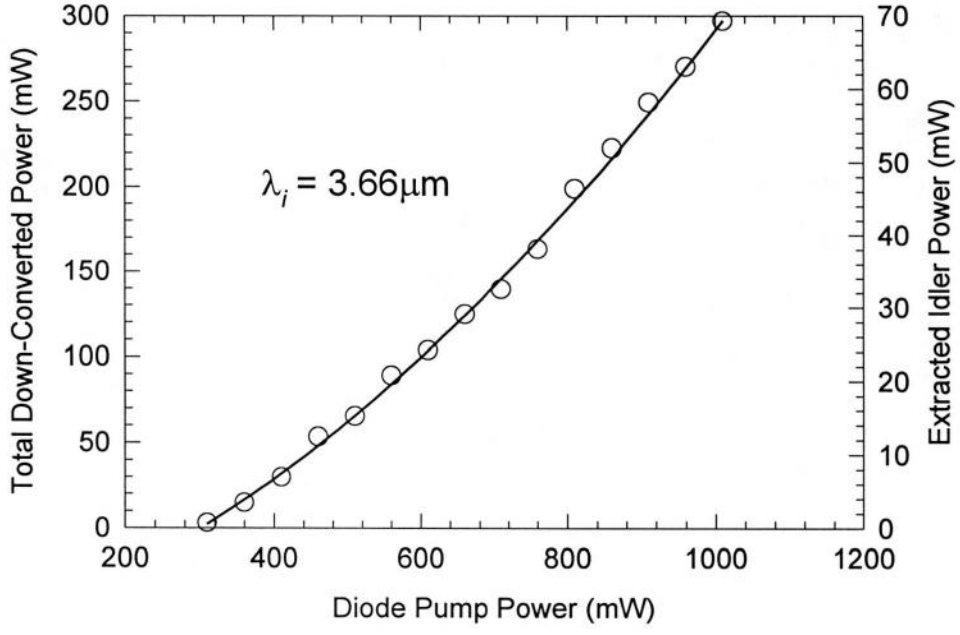

Figure 4.19: *Extracted idler power and the corresponding down converted power of the OPO as a function of input diode power. The solid curve is a best fit through the experimental data.*

We see from figure 4.19 that this device exhibited a steady increase in SRO output with diode input power, pointing to robust operation of the OPO at all available pump powers and indicating the insensitivity of the device to thermal lensing in the PPLN crystal. It is also clear that there is no evidence of power saturation, leading to the possibility of power scaling the pump source. The slightly super-linear nature of the power output is attributed to mode matching conditions changing slightly as the increasing circulating field inside the cavity leads to thermal lensing in the PPLN crystal.

In order to measure the down conversion efficiency it is necessary to know the pump power extractable from the laser at optimum 1.064μm output coupling. Ideally a range of output couplers should be inserted in place of M2 and, with the OPO cavity blocked, the optimum power extractable at full pumping power measured. At the time of this experiment, however, no reflectivity range of curved output couplers were available, and so the previously observed value of 430mW extracted from the simple 1.064μm cavity through a 1.6% plane output coupler was used. This value, of course, does not take into account the additional intra-cavity loss introduced into the system by the various intra-cavity components such as the lens, beam splitter and PPLN crystal. The value of the down-converted efficiency will therefore be somewhat higher in reality than that calculated here.

Using the value of 430mW and taking account of the quantum defect between the pump and the idler photons, we find that the 70-mW idler power represents an idler photon conversion efficiency of ~55% from the 1.064μm pump. These values did not account for the PPLN crystal coating loss (~3%) and the total transmission loss of mirror M_2 (~16%) at the idler wavelength. However, when these losses are accounted for we deduce that the total generated signal and idler power is ~295mW at 1W of diode pump power, corresponding to a down conversion efficiency of >68% from the maximum extractable 430mW. In chapter 2 we saw that for 100% down conversion efficiency,

$$P_{opo-th} = \sqrt{P_{laser-th} \cdot P_{pump}} \tag{4.4}$$

Therefore, 100% down conversion efficiency will occur when

$$P_{pump} = \frac{P_{opo-th}^{\ 2}}{P_{laser-th}} = \frac{310\text{mW}^2}{63\text{mW}} = 1525\text{mW} \tag{4.5}$$

By repeating this measurement with a spectrum of output couplers to obtain an accurate value of maximum extractable power, re-designing the cavity to allow better confocal focusing in the PPLN crystal and replacing the pump source with a more powerful laser diode to facilitate pumping up to ~2W, higher down-conversion efficiencies approaching 100% should be obtainable, as demonstrated in other intra-cavity systems [17], assuming

that thermal effects in the Nd:YVO_4 and PPLN crystals do not significantly manifest themselves at elevated pump powers.

Figure 4.20 shows the circulating pump field inside the laser cavity as a function of diode pump power both in the presence and absence of OPO operation. In order to disable OPO operation without perturbing the pump cavity, a beam block was placed between the beam splitter and the signal mirror, M3. We see the characteristic pump clamping effect in the presence of OPO operation.

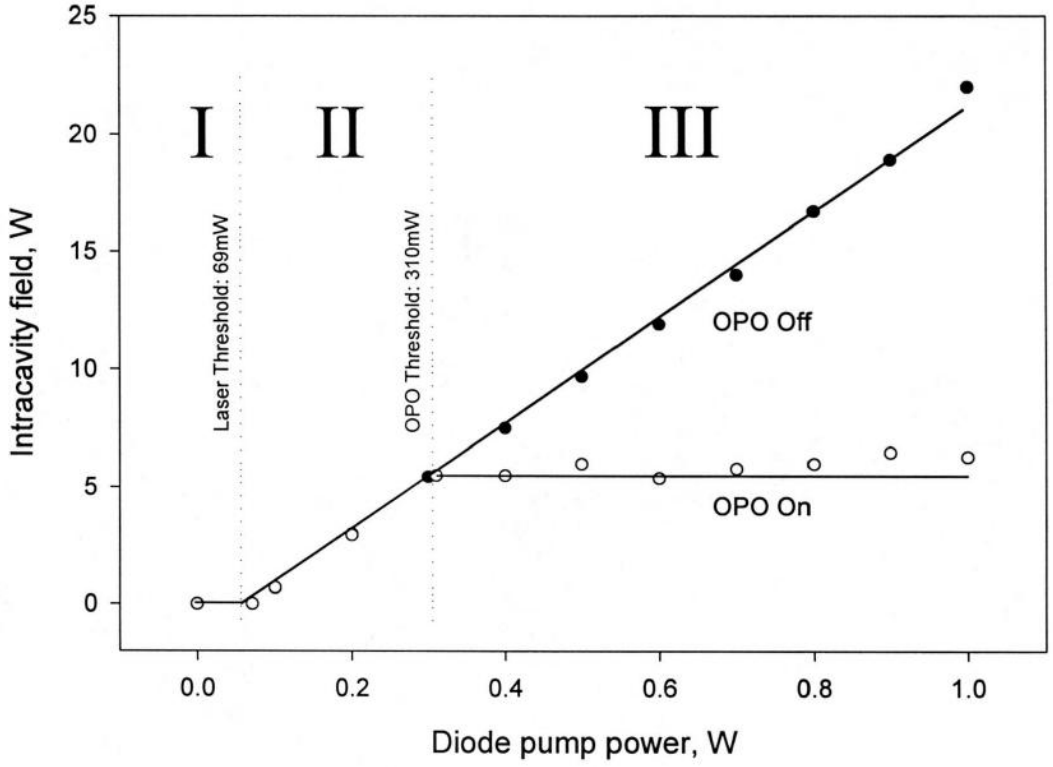

Figure 4.20: *Two-way circulating field within the pump cavity as a function of diode pump power in the presence and absence of OPO operation. The three regions correspond to those found in the discussion in chapter 2, section 2.6.4.*

Figure 4.21 shows the long-term stability of the idler produced by this system. This measurement was made by attaching the analogue output of a thermal power meter to an eight-bit digital storage adapter, taking a sample every few seconds over a long period. The peak-to-peak amplitude fluctuations in the idler output were no more than ±8% over the measurement period of three hours.

The inset of figure 4.21 shows the behavior of the idler after the interruption of SRO operation by the temporary removal of diode pump power. The self-recovering nature of the output is clear evidence of robust operation of the SRO and indicates that thermal lensing effects in PPLN do not destabilize either the pump or the signal cavities, demonstrating the turn-key performance of the device. The finite time interval between the interruption of SRO operation and its full recovery is attributable to the slow response of the thermal detector head used in the measurement.

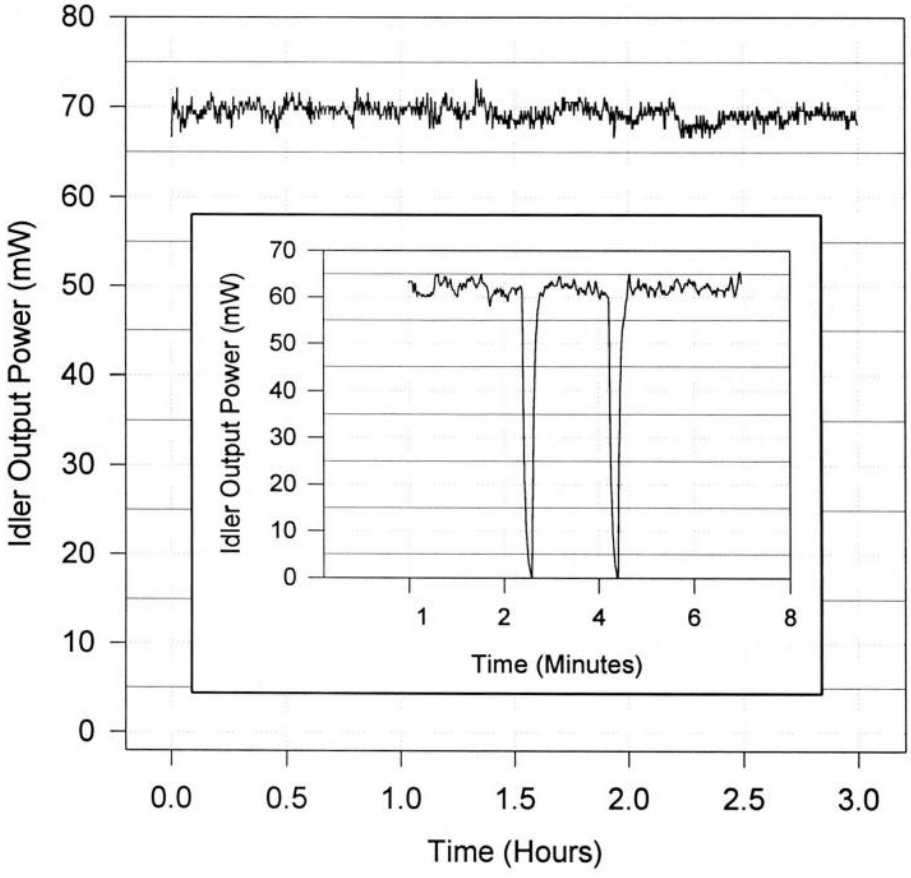

Figure 4.21: *Long term idler stability.*

The short term (~μS-mS) stability of the pump was observed by focussing the reflected pump field off of the beam splitter into a fast photo-detector. A typical measurement is shown in figure 4.22.

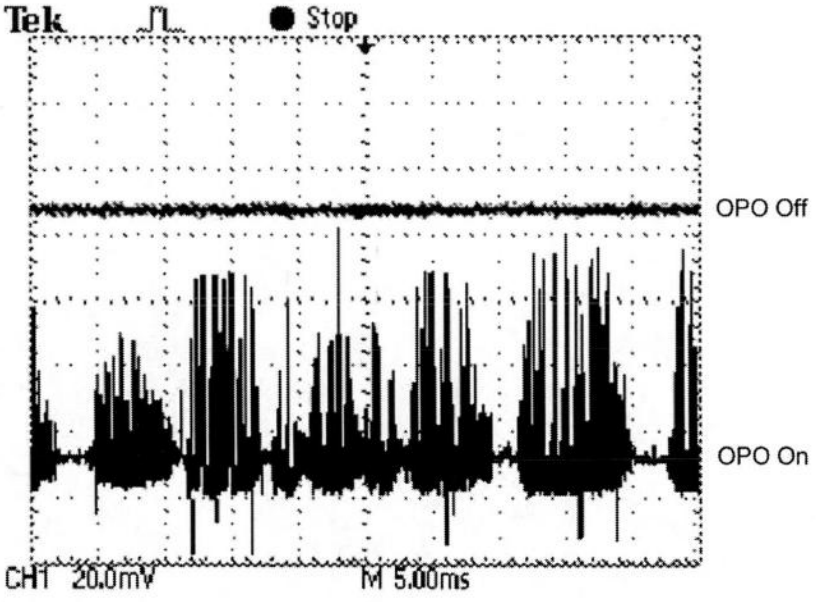

Figure 4.22: *Typical short term pump stability with and without OPO down conversion.*

We see that the pump field exhibits excellent stability in the absence of OPO down conversion (i.e. with the signal cavity blocked or mis-aligned), but severe amplitude modulation during OPO operation. Although the onset of these noise tone bursts was random in nature, their form resembled that of relaxation oscillations. The clamping effect of the ICSRO is also evident in this figure. In order to drive these perturbations in a repeatable fashion, a mechanical chopper was placed between the graded index coupling lens L1 and the Nd:YVO_4 crystal, causing 100% amplitude modulation of the diode pump light in a 50:50 duty cycle. The resultant repeatable oscillatory behaviour of the pump field is shown in figure 4.23.

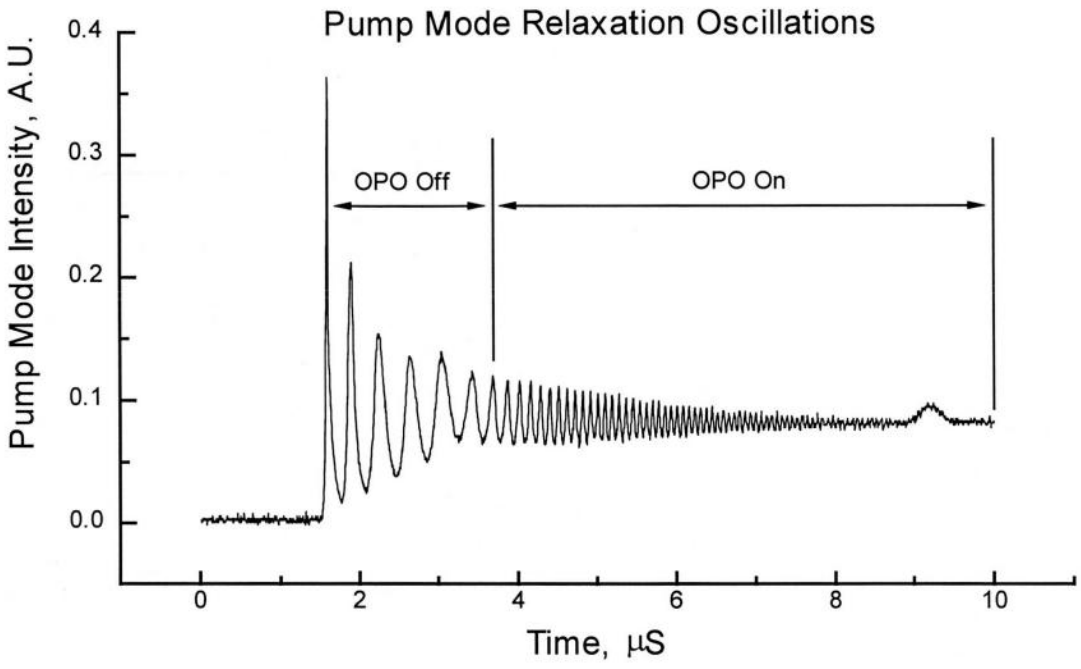

Figure 4.23: *Relaxation oscillations. Notice period change as OPO reaches threshold.*

As discussed in chapter 2, the inclusion of the SRO within the laser cavity significantly modifies the rate equations of the system and the relaxation oscillation behaviour. A full analysis of the ICSRO dynamics appears in chapter 6 and will not be discussed in detail here, except to state the most pertinent results that photon flow between the signal and pump cavities both dramatically increases the damping times of the system once perturbed, and reduces the perturbation needed to bring about the onset of oscillations. Although dynamics of this system do settle down into the steady state, the mean time between perturbations was shorter than the damping time of the relaxation oscillations resulting in a quasi-continuous train of oscillations. We theorise that air current fluctuations at the heated PPLN face or rapid thermal lensing effects within the PPLN crystal were significant enough to trigger relaxation oscillations in this system.

Weeks of operation saw the mean down-converted power fall off significantly to ~65% of initially recorded values. The PPLN crystal was extracted from its oven and it was noted that it had become slightly opaque with a pinkish tinge when observed in transmission. It is theorised that a chemical reaction took place between the PPLN crystal and the brass oven in which it was inserted which affected its optical properties. Subsequent studies were undertaken with a stainless-steel oven insert replacement. No further crystal degradation or reduction in power output was observed.

4.3.3.2. Spectral Characteristics

As the spectral output of a neodymium-based laser is incapable of being significantly tuned, the OPO was tuned by varying both the crystal temperature and grating period. Figure 4.24 shows the wavelength tuning range of the SRO. For each grating the crystal temperature was scanned from 35-180°C in a servo-controlled oven. In the figure, the symbols represent experimental data, and the solid curves show the predicted tuning range for each grating calculated from the Sellmeier data [12]. This data was obtained by observing the non phase matched pump and signal SFM light produced by the OPO on a wavemeter with suitable filters to block out other wavelengths that the internal CCD was sensitive to, such as the pump field or doubled signal. The resonant signal field tuned within the mirror bandwidth from 1.446 to 1.604μm and the non-resonant idler from 3.1-5.0μm by the appropriate choice of grating period and temperature. At lower temperatures (<100°C) it was noted that the idler power fell off after typically five minutes of operation, which was due to photo-refractive damage [16]. The small error between the predicted Sellmeier data and the experimentally recorded results is attributable to the finite bandwidth of the Nd:YVO_4 transition (and hence uncertainty in the exact pump wavelength) and some constant error in the temperature display of the servo-control oven.

The tuning bandwidth of the signal and idler is restricted solely by the grating period selection. With the optical coatings employed in this system, the idler tuning range could potentially extended from 3.1 to ~5.0μm by an appropriate grating period choice.

It is also worthy of note that there is significant spectral overlap between each grating, leading to possibility of greater difference in periods between adjacent gratings which would give far greater coverage from one crystal.

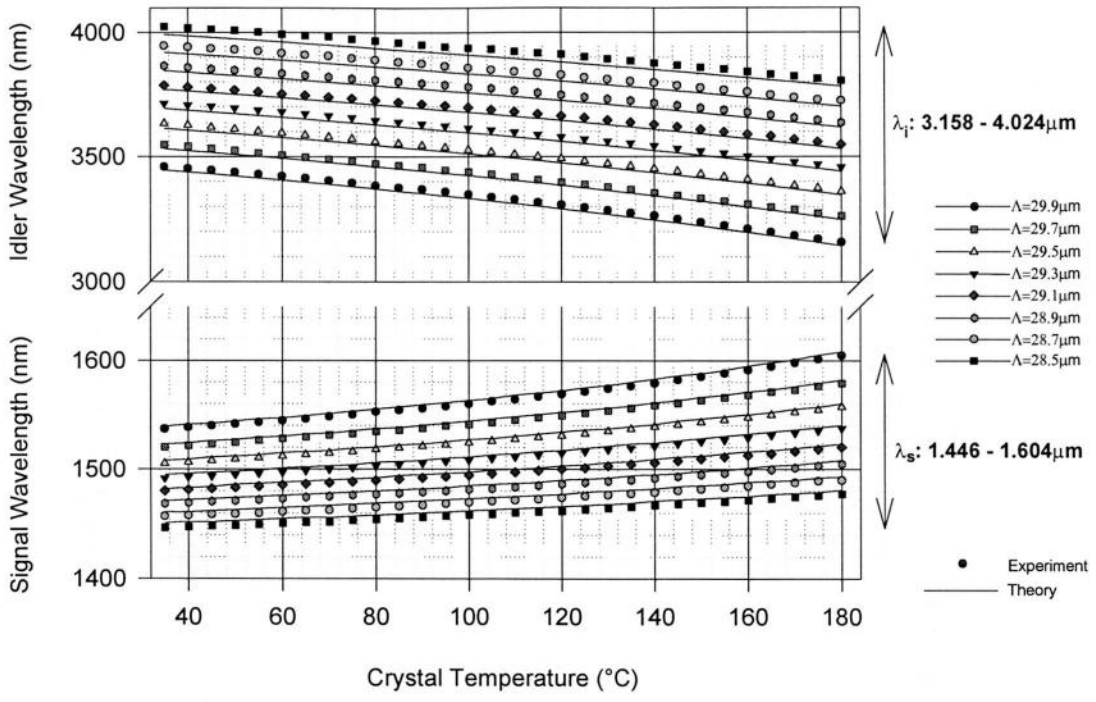

Figure 4.24: *Wavelength coverage of the signal and idler waves.*

As one of the principle applications for a system of this type is mid infrared spectroscopy, the linewidth of the non-resonant idler output is an extremely important parameter. Although a direct measurement of the idler linewidth with a high finesse confocal interferometer would be desirable, no such diagnostic was available and so the linewidth of the idler had to be inferred from that of the pump field.

The pump spectrum was measured by placing a confocal interferometer with a free spectral range of 2GHz located at the diagnostic position observing the rejected pump field from the beam splitter. A typical spectrum of the laser pump field appears as figure 4.25. The pump laser was found to operating on ~3-4 longitudinal modes with a frequency separation in integer multiples of ~300MHz, in line with the free spectral range of the pump cavity. Competition between the modes of the pump laser was evident on the ~10-100mS time scale. The total bandwidth of the 1.064μm pump laser was therefore not constant, and fluctuated between 900 and 1200MHz.

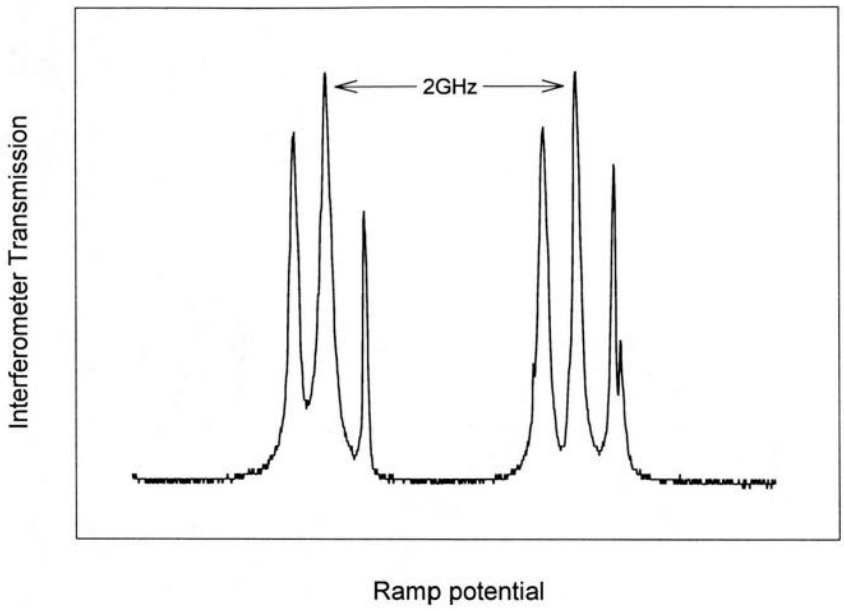

Figure 4.25: *Pump field spectrum.*

As there is no energy storage mechanism in the PPLN crystal, spatial hole burning does not occur in the OPO and therefore the signal field oscillates on a single longitudinal mode at the peak of the phase-matched bandwidth. Another interferometer with the same free spectral range as that used above but with suitable mirror coatings at the signal wavelength was used to measure the frequency spectrum of the leaking field from the signal cavity. The result of this measurement is shown in figure 4.26. We can see that the signal field does indeed oscillate on a single longitudinal mode.

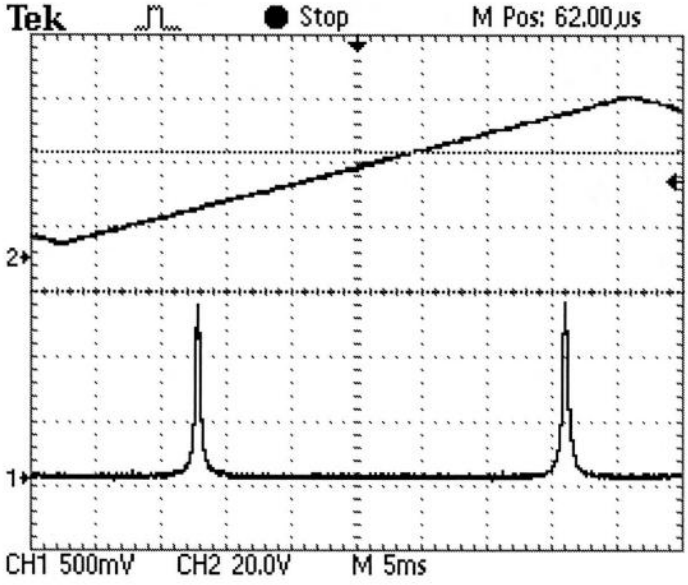

Figure 4.26: *Signal field spectrum (Interferometer FSR: 2GHz).*

As the frequency bandwidth of the pump is directly transferred to that of the idler in a SRO, the band-width of the idler is therefore ~1200MHz, which corresponds to approximately 0.5cm^{-1} at this wavelength.

4.3.3.3. Spatial Properties

As the idler wavelength was too long to be detected by conventional CCD profilers, the non phase-matched SFM red light was used. Although the 1.064μm leaking field through M2 could have been used, it is possible that whilst the pump cavity was operating on a fundamental mode the signal could have been resonating on a higher order mode. By detecting the SFM mode, which is produced by a mixture of the same two fields as the idler (albeit in a different mixing process), a confident conclusion of the idler spatial mode characteristics could be drawn. As the CCD profiler used to obtain this measurement was sensitive to the leaking 1.064μm pump field, filters were inserted into the path of the beam to block the pump and pass the SFM red light.

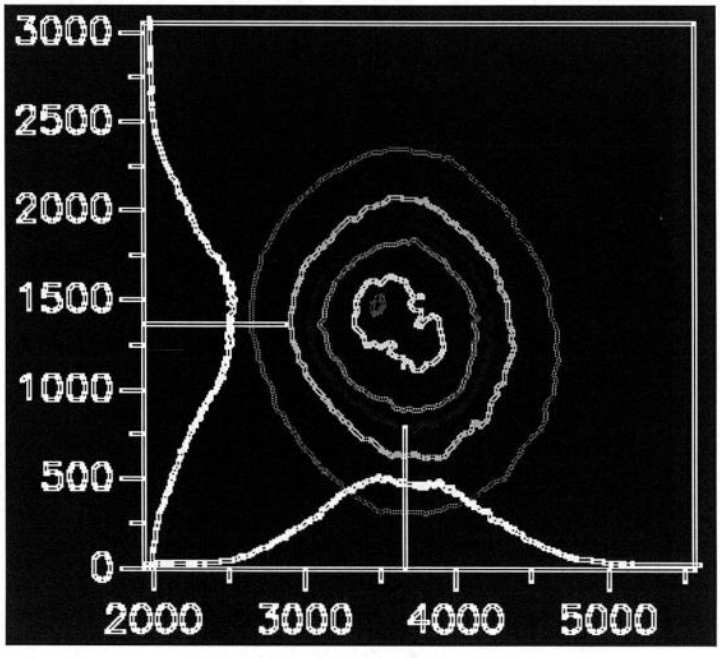

Figure 4.27: *SFM spatial mode.*

The spatial mode of the SFM red light is shown in figure 4.27. We can see that it is a fair quality TEM_{00} mode. Although the mode was seen to fluctuate when air currents were encouraged to flow in the vicinity of the PPLN crystal, the quality of the mode was

repeatable and, in general, stable. The stability of the mode was improved by inserting beam tubes around the PPLN oven to minimse the effects of thermal air currents.

4.4. Conclusions

We have successfully demonstrated a highly efficient and compact source of mid-infrared radiation based upon a synergie of intra-cavity optical parametric oscillator and diode-pumped solid state laser technoligies.

Laser and OPO threshold was achieved at a pump power of 63 and 310mW respectively. The system demonstrated down-conversion efficiencies in excess of 68%, corresponding to ~300mW of down-converted power into the signal and idler fields. Up to 70mW of idler could be extracted.

The extractable idler could be broadly tuned over the spectrally important range 3.16-4.02μm by the appropriate selection of the PPLN grating and temperature. The idler exhibited a spectral bandwidth of 1200MHz, and operated on a fundamental gaussian mode.

Configured in a simple cavity design, the SRO exhibits long-term amplitude stability and robust turn-key operation without the onset of thermal lensing effects. Less that 8% rms fluctuation in idler power was observed over three hours. However, serious noise was detected on the intra-cavity pump, and therefore the idler, on the ~μS timescale, brought about by the inclusion of the ICSRO resulting in the system being much more sensitive in the event of perturbation. Such oscillations cast a serious shadow over the further practical implementation of Nd-based ICSROs unless a successful strategy to damp them down can be found and implimented.

References

1 D. J. M. Stothard, M. Ebrahimzadeh and M. H. Dunn, "Low pump threshold, continuous-wave, singly resonant, optical parametric oscillator," *Optics Letters* **23**, 1895 (1998).

2 Casix part number DPO3102.

3 Casix part number CLD1000.

4 Casix part number PCH0022.

5 W. Koechner, *Solid-State Laser Engineering*. A. L. Schawlow, Ed., (Fifth ed.) (Springer, 1999).

6 W. A. Clarkson and D. C. Hanna, "Effects of transverse mode-profile on slope efficiency and relaxation oscillations in a longitudinally-pumped laser," *Journal of Modern Optics* **36**, 483-498 (1989).

7 M. E. Innocenzi, H. T. Yura, C. L. Fincher and R. A. Fields, "Thermal modeling of continuous-wave end-pumped solid-state lasers," *Applied Physics Letters* **56**, 831 (1990).

8 A. E. Siegman, *Lasers*. (University Science Books, Mill Valley, 1986).

9 Crystal Technology Inc. part no. 97-02384-07.

10 A. D. Gillies, M. H. Dunn and B. D. Sinclair Psst! Cavity Stability and Laser dynamics.

11 G. A. Turnbull, T. J. Edwards, M. H. Dunn and M. Ebrahimzadeh, "Continuous-wave singly-resonant intracavity optical parametric oscillator based on periodically-poled LiNbO3," *Electronics Letters* **33**, 1817-1818 (1997).

12 D. H. Jundt, "Temperature-dependent Sellmeier equation for the index of refraction n_e in congruent lithium niobate," *Optics Letters* **22**, 1553 (1997).

13 I extend my gratitude to Dr. I. D. Lindsay, whose help with this model was extensive

14 V. G. Dmitriev, G. G. Gurzadyan and D. N. Nikogosyan, *Handbook of nonlinear optical crystals*. (2nd ed.) (Springer-Verlag, Berlin, Heidelberg, New York, 1997).

15 W. R. Bosenberg, A. Drobshoff, J. I. Alexander, L. E. Myers and R. L. Byer, "Continuous-wave singly resonant optical parametric oscillator based on periodically poled LiNbO3," *Optics Letters* **21**, 713 (1996).

16 D. H. Jundt, G. A. Magel, M. M. Fejer and R. L. Byer, "Periodically Poled Linbo3 for High-Efficiency 2nd-Harmonic Generation," *Applied Physics Letters* **59**, 2657-2659 (1991).

17 T. J. Edwards, G. A. Turnbull, M. H. Dunn, M. Ebrahimzadeh and F. G. Colville, "High-power, continuous-wave, singly resonant, intracavity optical parametric oscillator," *Applied Physics Letters* **72**, 1527-1529 (1998).

5: High power operation of a Nd:YVO_4 ICSRO based upon PPLN and PPRTA

5.1. Introduction

In this chapter we shall capitalise on the low threshold system described in chapter four and outline a strategy for power scaling this device and demonstrate a device capable of delivering over 300mW of tunable idler power [1]. The high circulating field found in this device enables us to take advantage of a recent addition to the family of nonlinear poled crystals, namely periodically poled $RbTiOAsO_4$ (PPRTA) as well as PPLN. We shall see that PPRTA exhibits many favourable properties despite its reduced non-linear coefficient and interaction length in comparison to the PPLN crystal employed, attributed to its higher resistance to thermal lensing effects.

Substantial design work on the fibre-coupled diode pump cooling system and optical coupling telescope between the pump source and Nd:YVO_4 crystal employed in this system was undertaken by Pierre Yves-Fortain (University of Laval, Quebec, Canada), to whom I give due recognition and my gratitude. I also acknowledge Dr Cameron F. Rae of the Photonics Innovation Centre based in the department of physics and astronomy here in St. Andrews for providing the diode pump source, the cooling system and constant current power supply.

5.2. Diode characterisation and laser pump head

We begin by characterising the fibre coupled laser diode pump source used in this system, and describe the laser head containing the fibre alignment assembly, coupling optical design and the liquid cooled Nd:YVO_4 housing, shown in figure 5.1.

The pump source used in this experiment was a 15W, fibre coupled laser diode [2]. The cleaved fibre end had an emission diameter of 600μm and was terminated in a threaded (SMA) coupling. Due to the significant amount of heat produced by the laser diode

module, thermoelectric temperature control was deemed impractical and so a servo-controlled water chiller was employed to remove waste heat and stabilise the diode temperature, and therefore its emission wavelength.

The terminated fibre end was mounted in an *x-y-z* translation mount so that it could be accurately positioned in the optical axis of the laser and in the focal plane of the first collimating optic. The optical coupling design comprised two anti-reflection coated aspherical lenses configured as a 3:2 focal length telescope, forming a secondary focus diameter of 400μm incident upon the Nd:YVO_4 crystal boundary.

The 1.064μm plano high reflector, anti-reflection coated for the 808nm diode pump, defined one end of the laser cavity and was placed in a brass collar and bolted onto the Nd:YVO_4 housing over a compressed rubber 'O' ring, facilitating alignment of this optic perpendicular to the lasing axis. Embedded just beyond this in the water cooled mount was the 4x4x7mm, 0.5% doped Nd:YVO_4 crystal [3], both faces anti-reflection coated at 808nm and 1.064μm. Alignment of the rear mirror parallel to the facets of the Nd:YVO_4 crystal was facilitated by observing the back reflected spots from an on-axis helium-neon laser.

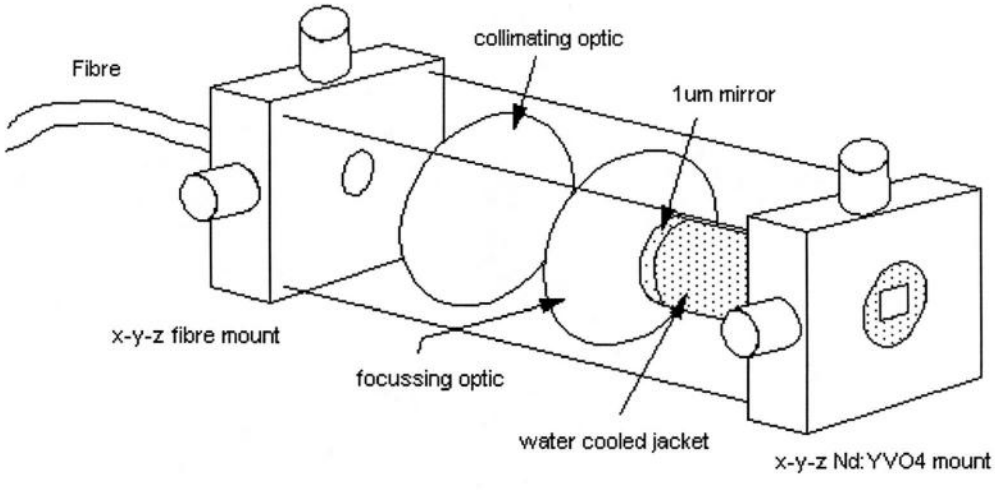

Figure 5.1: *Laser pump head design.*

The diode was forward biased by a high power constant current source; the output power from the fibre is shown as a function of pump current in figure 5.2. Also shown is the

power delivered to the Nd:YVO_4 crystal, taking into account the loss of the coupling optics and the cavity mirror. We can see that at 15W of optical power was incident upon the gain medium for 30A of pump current.

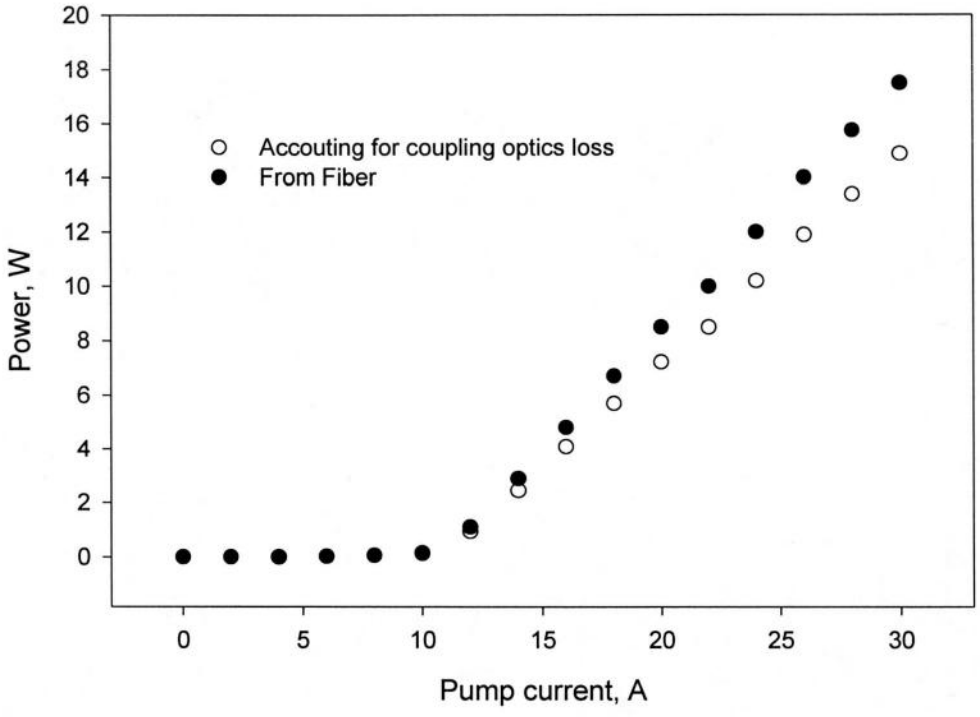

Figure 5.2: *Diode power shown as a function of pump current.*

Rather than the single diode junction employed in the system described in chapter 4, very high power diodes such as the one used in this device comprise a series of individual junctions bonded to a common substrate and coupled into the optical fibre via a micro lens array. Due to slight discrepancies in the growth manufacture of each individual junction and the lack of optical coupling between each cavity, the overall spectral emission from these multi-stripe diodes is significantly larger than each junction taken in isolation. Figure 5.3 shows the spectral emission from the fibre end; we can see that the bandwidth of the source was ~3.8nm. Although this is somewhat larger than the absorption feature we are trying to access in the Nd:YVO_4, the long (7mm) gain crystal used meant that ~97% of the diode pump power was absorbed. It was still important to temperature tune the mean diode wavelength to coincide with the peak absorption line in the Nd:YVO_4, however, to ensure that the majority of the pump power was absorbed in

the first couple of millimetres of the gain crystal where the mode matching between the 808nm pumped volume and the 1.064μm circulating mode were optimal.

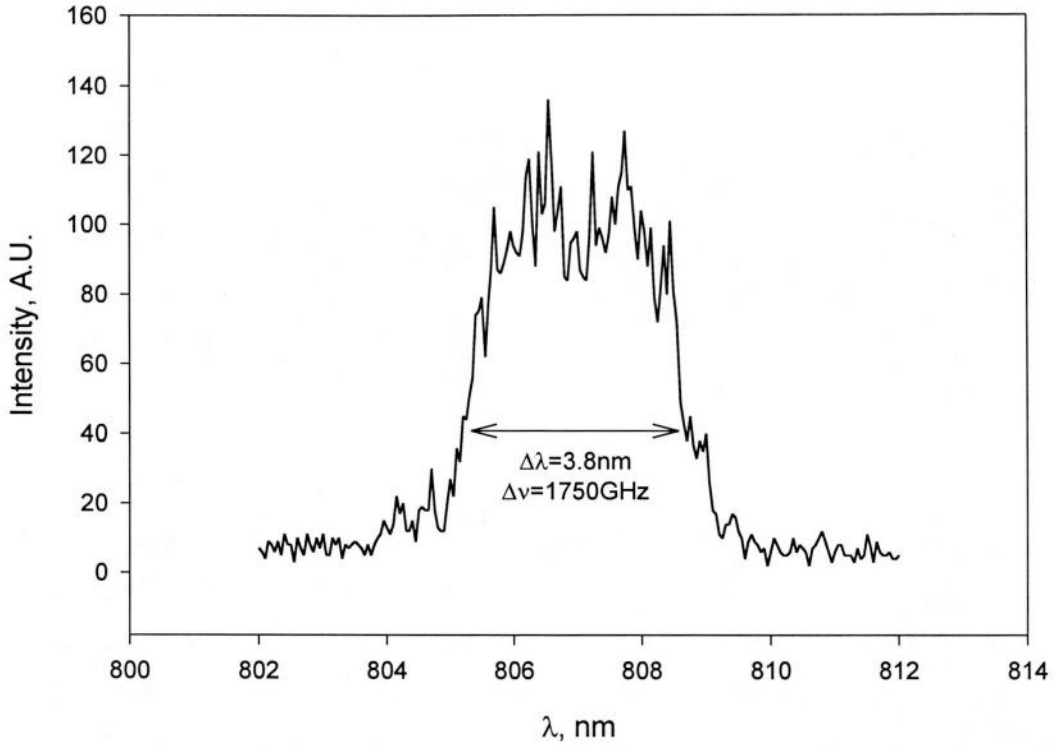

Figure 5.3: *Spectral emission from laser diode pump source.*

The evolution of the laser diode pump mode after the coupling lenses is shown in figure 5.4. The origin of the *z*-axis here is arbitrarily placed at the beam waist which is coincident with the entry facet of the Nd:YVO_4 crystal. We can see that the waist measurement of 215μm is in good agreement with the expected value of 200μm with the cleaved fibre end radius of 300μm focussed down with the 3:2 telescopic coupling optics. The three-dimensional plot of the pump mode profile as it evolves, shown in figure 5.5

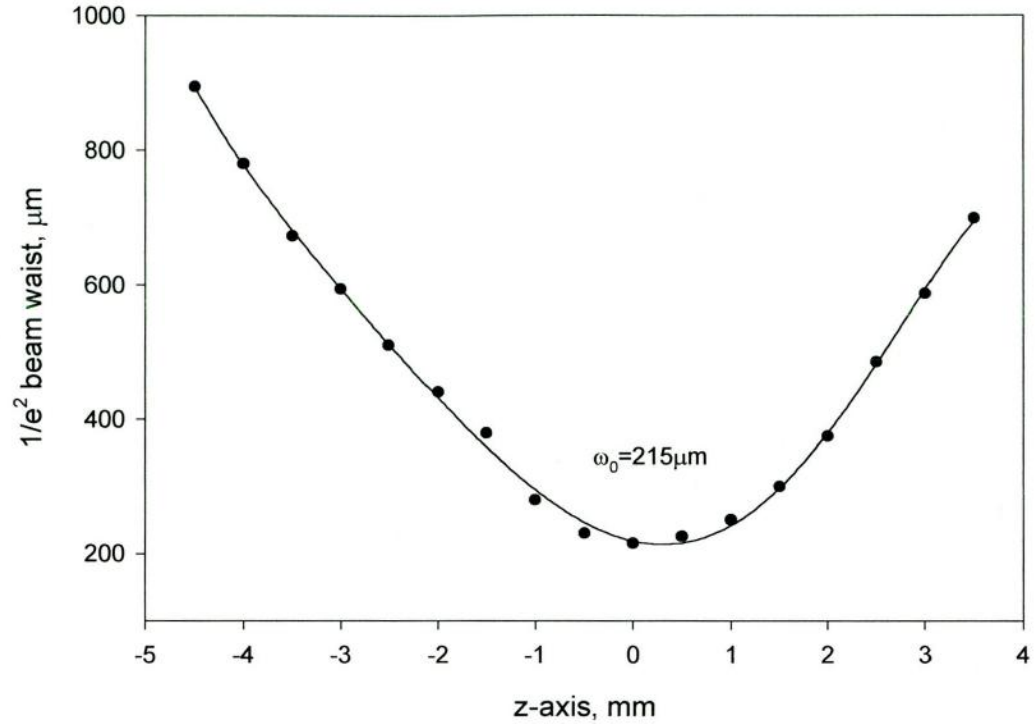

Figure 5.4: *Pump mode evolution after second coupling optic.*

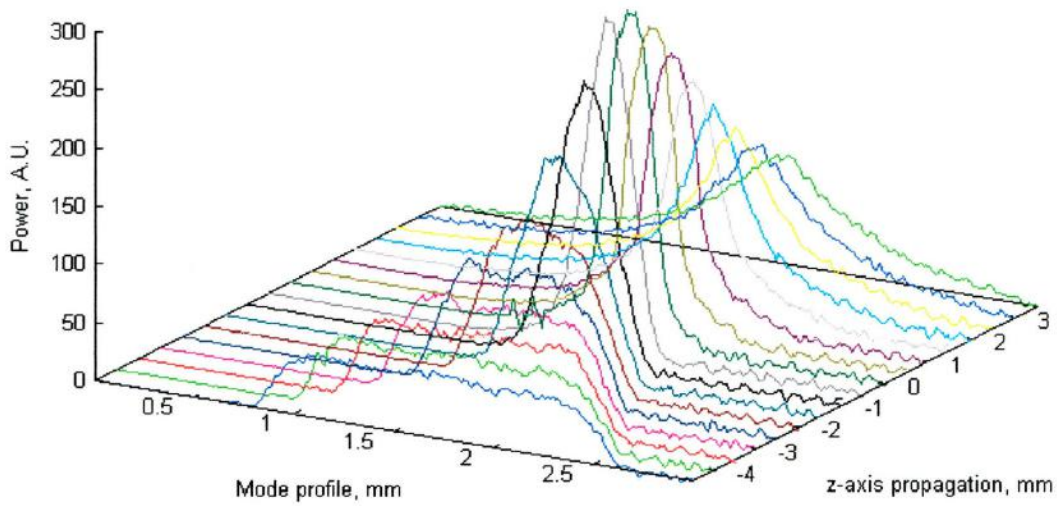

Figure 5.5: *Pump mode profile with evolution.*

To optimise the position of the fibre and the Nd:YVO_4 in the optical axis and the position of the coupling optics in order to minimise the pumped volume (and hence maximise the population inversion) in the gain crystal, the fluorescence from the pumped volume was 1:1 imaged into a calibrated CCD camera, the optical setup of which is shown in figure 5.6 and the resultant image is shown in figure 5.7. The focal length of the imaging lens was

was chosen to trade off the amount of captured light with the depth of focus, relaxing the placement tolerance upon the lens and the CCD camera. The RG1000 filter was placed in the beam path to block any transmitted 808nm pump light which would have saturated the CCD element or otherwise interfered with the measurement result.

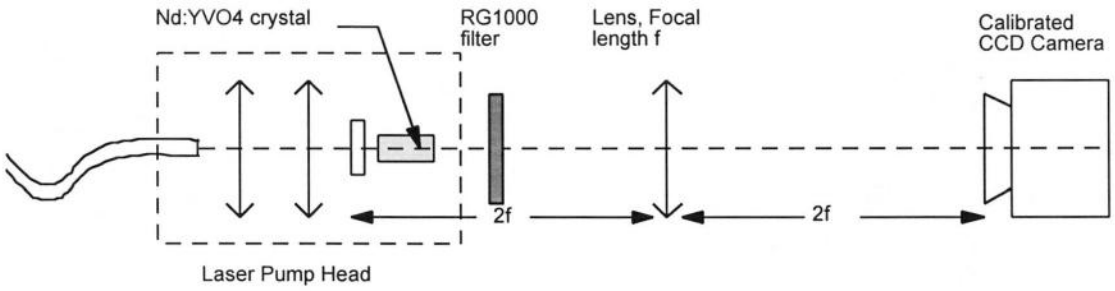

Figure 5.6: *Optical setup of pump volume measurement.*

The position of the fibre was adjusted so that the fluorescence was circularly symmetric about the optical axis. An imperfection in the Nd:YVO_4 is evident in this image and adjustment of the position the crystal allowed different areas of it to be pumped in order to avoid regions such as this (this crystal was eventually replaced and the pump mode re-optimised before the construction of the ICSRO).

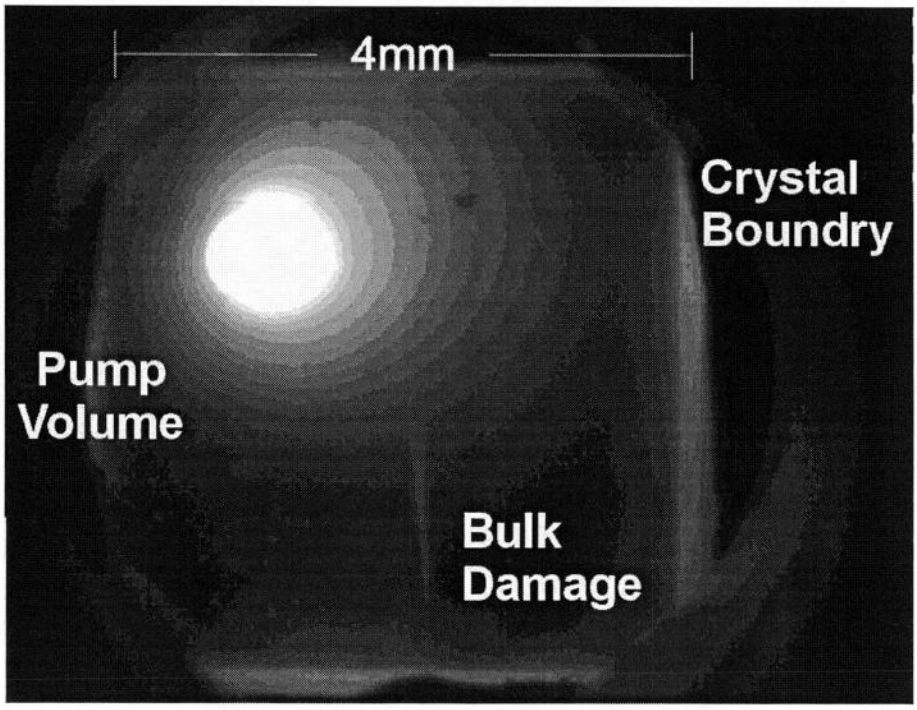

Figure 5.7: *Image of the Nd:YVO_4 pumped volume.*

Analysis of this image gave a more quantified measurement of the pumped volume. False colour images of the pumped region are shown in figure 5.8. We can see the excellent circularity of the pumped volume when compared to that of the same measurement in the case of the 1W diode pumped system, utilising a 100×1mm stripe c-packaged diode (figure 4.7). This, in addition to experimental convenience, is one of the very favourable characteristics of fibre-coupled diode pumping of solid state laser gain media as it leads to better mode matching between the pumped volume and the circulating mode leading to better efficiency and fewer deleterious thermal effects.

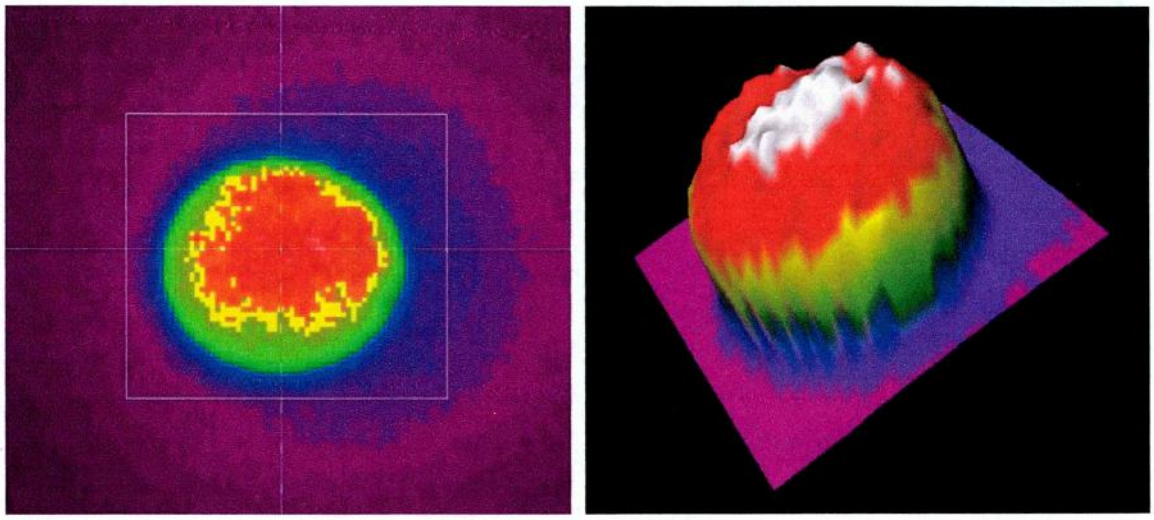

Figure 5.8: *Profile of the pumped volume.*

With the pump head characterised, a range of 1.064μm output couplers were used to form the laser cavity and facilitate a measurement of optimum output coupling and a means of optimising the adjustment on the pump head to maximise laser power output / spatial mode quality. A selection of 200mm radius of curvature output couplers were placed to form a cavity length of 160mm; the optical efficiency of the laser and the optimum output coupled power is shown in figures 5.10 and 5.11 respectively. We can see from both of these figures that output power was optimal at ≈10% output coupling, with little variation in output power as the output coupling was varied about this value. This indicates that the laser is relatively insensitive to intracavity loss and makes this system an ideal test bed for intracavity experiments of this nature as complex, multi-element configurations can be accommodated with little impact on power performance, as quality optical coatings applied to intracavity elements should yield round trip loss to typically ~2%

As an interesting aside, a 1.064μm high reflector was used to form the cavity in the place of an output coupler to investigate the upper limit of circulating field available inside the cavity. Even though this optic had extremely low transmission at 1.064μm, over 500mW of power was still extracted from the cavity, pointing to CW circulating fields of over 1.5kW. Indeed, the intracavity field was clearly visible in subdued lighting conditions as particles of dust were vaporised as they passed through the beam path.

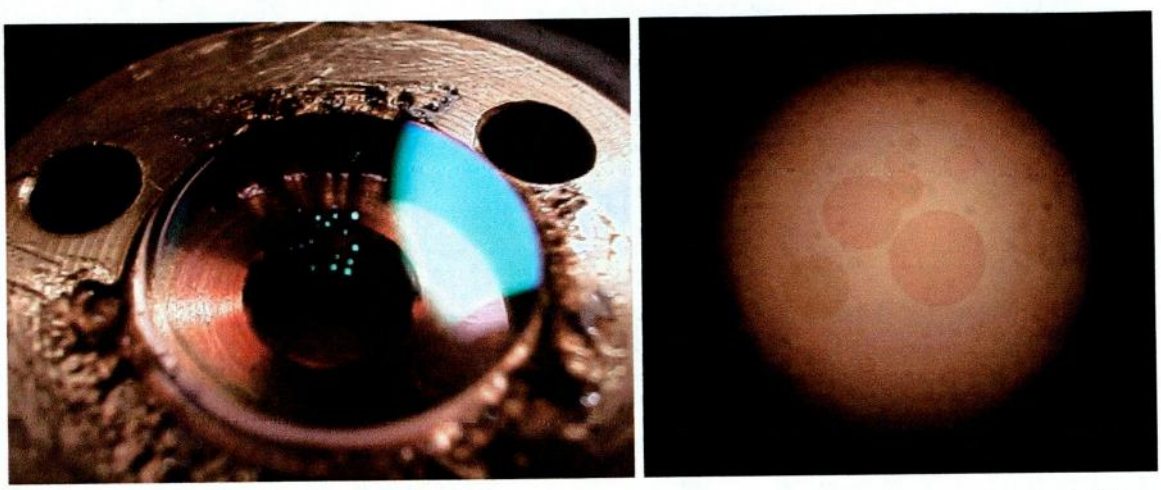

Figure 5.9: *Optical damage of rear 1.064μm high reflector due to the very high circulating field.*

This very high field had a regrettable effect upon the plane output coupler mounted behind the Nd:YVO_4 crystal, however, as is evident from figure 5.9. Here we see the dielectric coating ablated away from the glass substrate surface, and the coating damage shown in more detail under a microscope. Although poorly reproduced here, it is interesting to observe the rings produced where the multiple layers have been removed by the laser beam have near perfect gaussian contours.

The quality of the spatial mode was measured with a calibrated CCD camera coupled to a computer, and was found to be excellent for all pump powers. The long term temporal stability of the simple cavity was found to be <3% over many hours.

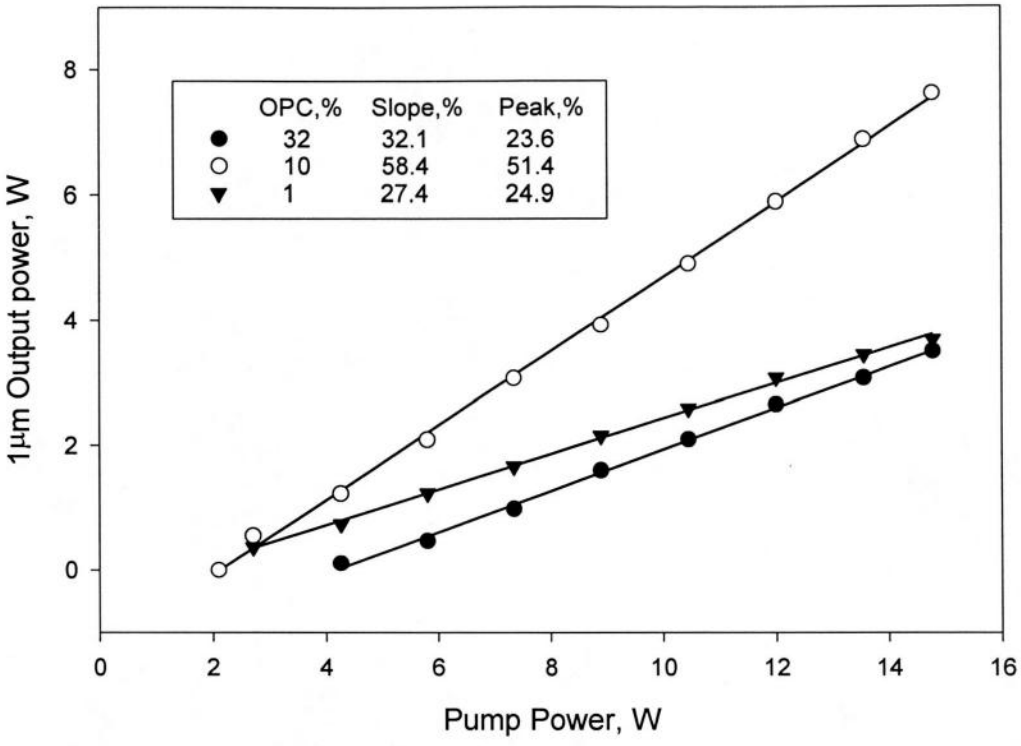

Figure 5.10: *Optical efficiency of the Nd:YVO_4 laser for three output couplers.*

5.3. Nd:YVO_4 Thermal lens

The behaviour of the thermal lens in this system was markedly different from that in the low power device outlined in chapter four, where only 1W of diode pump power was deployed. To measure the thermal radius of curvature induced in the gain crystal by the diode pump light, a similar method was employed as with the 1W pumped system. A 2% plane output coupler was used to form the laser cavity, so that the intracavity beam waist would be incident upon it for all thermally induced radii of curvature in the Nd:YVO_4 crystal.

A calibrated CCD camera was placed at a known distance z from the output coupler to measure its waist, ω_z. The waist upon the output coupler ω_0 could then be calculated and therefore the thermal radius of curvature in the Nd:YVO_4 present to cause a waist of this size. The beam waist in the far field, and therefore the thermal radius of curvature, was measured in both planes to identify any aberration that may be caused by an-isotropic thermal paths in the gain crystal. These results are shown in figure 5.12.

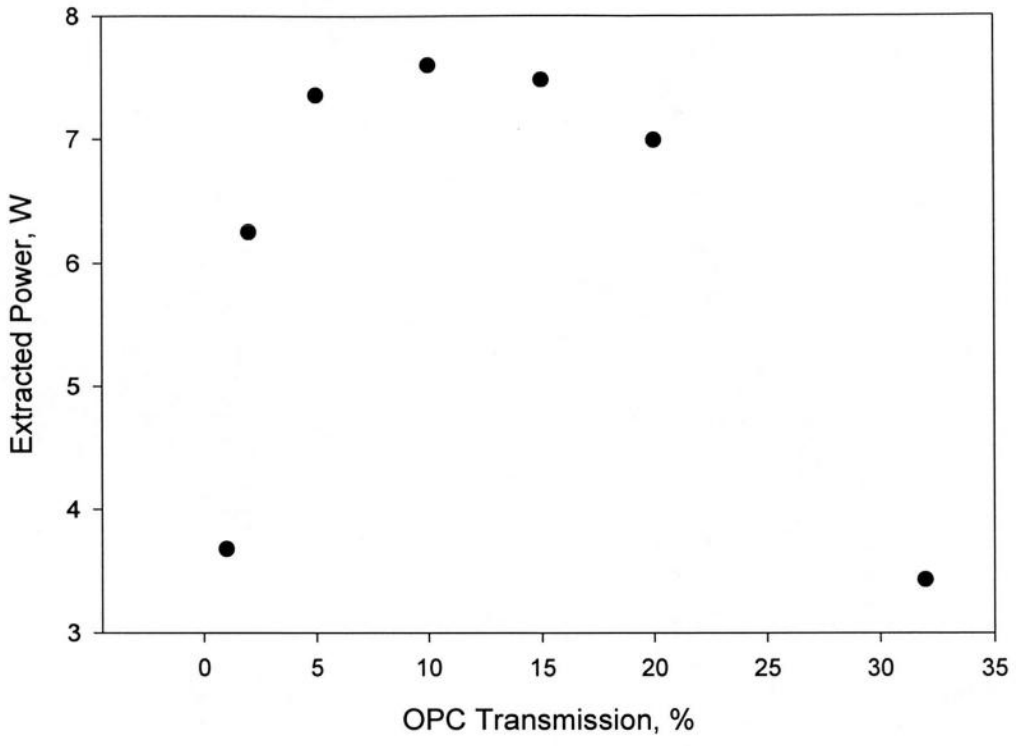

Figure 5.11: *Optimum output coupling. Here the laser was pumped with 15W of diode power.*

The plane output coupler was placed to form an optical cavity of 20cm. Lasing on a fundamental spatial mode occurred up to an incident pump power of ≈10.5W. We can see from the graph that this corresponds to an effective radius of curvature in the region of ~25cm, which is in fair agreement with the thermal radius of curvature at which one would expect the cavity to lose stability, taking into account the cavity length. As the laser began to resonate on a higher spatial mode, the theory used in this analysis breaks down and so no further meaningful measurements could be made beyond this point. A projection is made of the thermal effect for continued increase and this is indicated by the broken line in the figure. From this extrapolation we would expect a thermal radius of curvature of approximately 16cm at 15W of diode pump power.

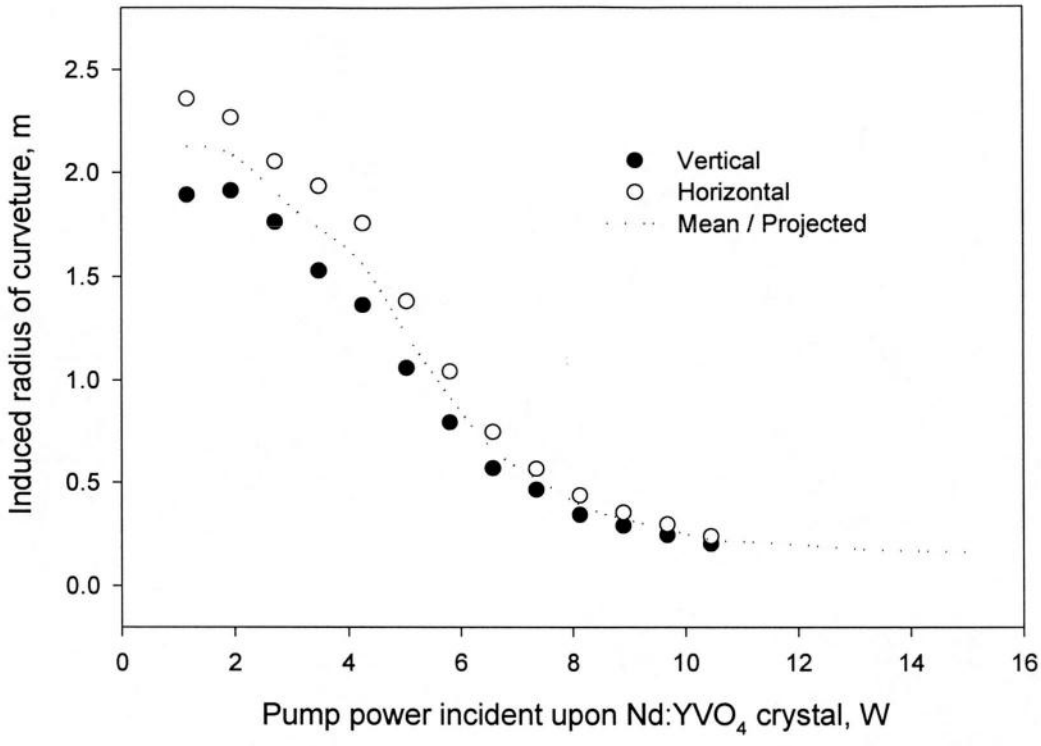

Figure 5.12: *Measured thermal lens in the Nd:YVO4 crystal.*

A simple model derived by Innocenzi *et al* [4] was employed to give confidence to the measured value of the thermal lens induced in the Nd:YVO_4 by the diode pump. The expression

$$f = \frac{\pi K \omega^2}{P_{th} \cdot \frac{dn}{dt}} \cdot \left(\frac{1}{1 - \exp(-\alpha L)} \right) \tag{5.1}$$

was used where f is the value of the induced lens, K the thermal conductivity of the material, ω the pump spot size in the lensing medium, P_{th} the thermal power deposited in the crystal, dn/dt the dispersion of refractive index with temperature, α the absorption of the pump field in the lensed medium and L the medium length. Figure 5.13 below shows the theoretical focal length of the induced thermal lens as a function of diode pump power, taking into account of the quantum defect between the diode pump and 1μm circulating field.

We can see that the focal length of the lens induced in the Nd:YVO_4 crystal is predicted at 16.4cm, giving an effective radius of curvature of 33cm. The beam passes twice through the crystal on its round trip through the cavity, however, and so the apparent radius of curvature of the plane high reflector mounted behind the crystal is predicted to be 16.4cm. This is in excellent agreement with the extrapolated observed value of ~16cm at 15W of diode pump power.

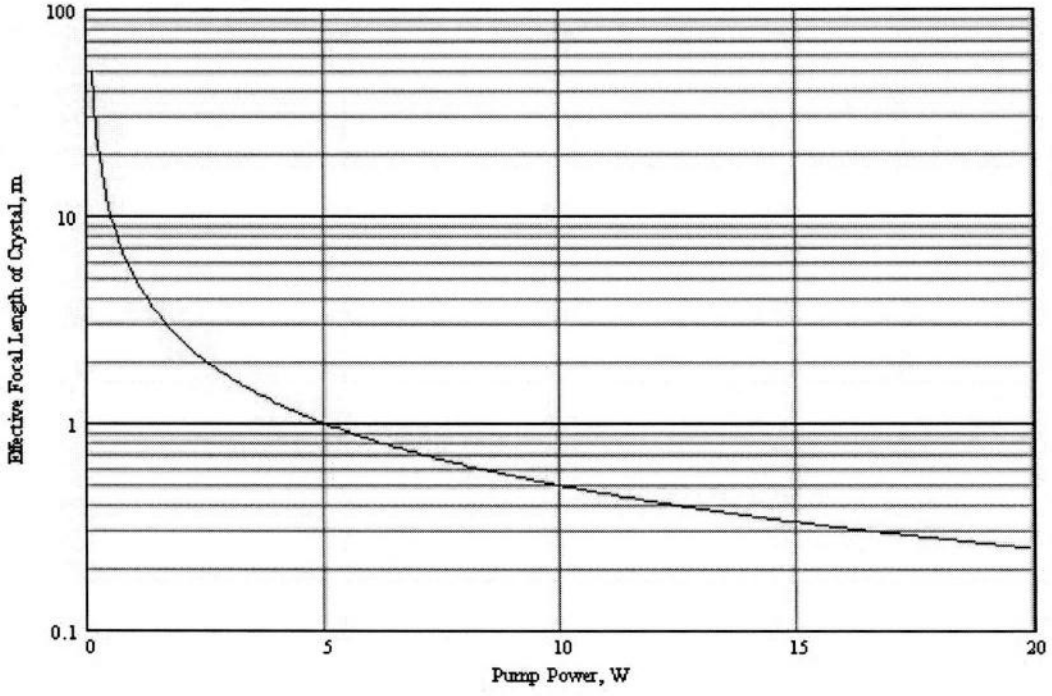

Figure 5.13: *Thermal lens in Nd:YVO_4 as a function of diode pump power, after [4].*

We have assumed thus far that the magnitude of the thermal lens within the Nd:YVO_4 crystal is solely dependant upon the absorption of the diode pump power. When there is no optical feedback within the laser cavity, this is indeed the case. However, when feedback is present and stimulated emission occurs (i.e. the laser is operating) then power is extracted and the thermal lens is reduced. This mechanism has more impact upon the thermal lens than re-absorption of the resonated field contributing to the thermal lens. Hence the thermal lens within the laser gain medium is inversely proportional to the circulating field within the laser cavity.

To quantify this effect the magnitude of the thermal lens in the Nd:YVO_4 crystal was inferred using a similar technique as outlined above, but with a range of 200mm R.O.C. output couplers with different reflectivities. In this way the thermal lens present in the gain medium could be obtained as a function of both pump power and circulating field.

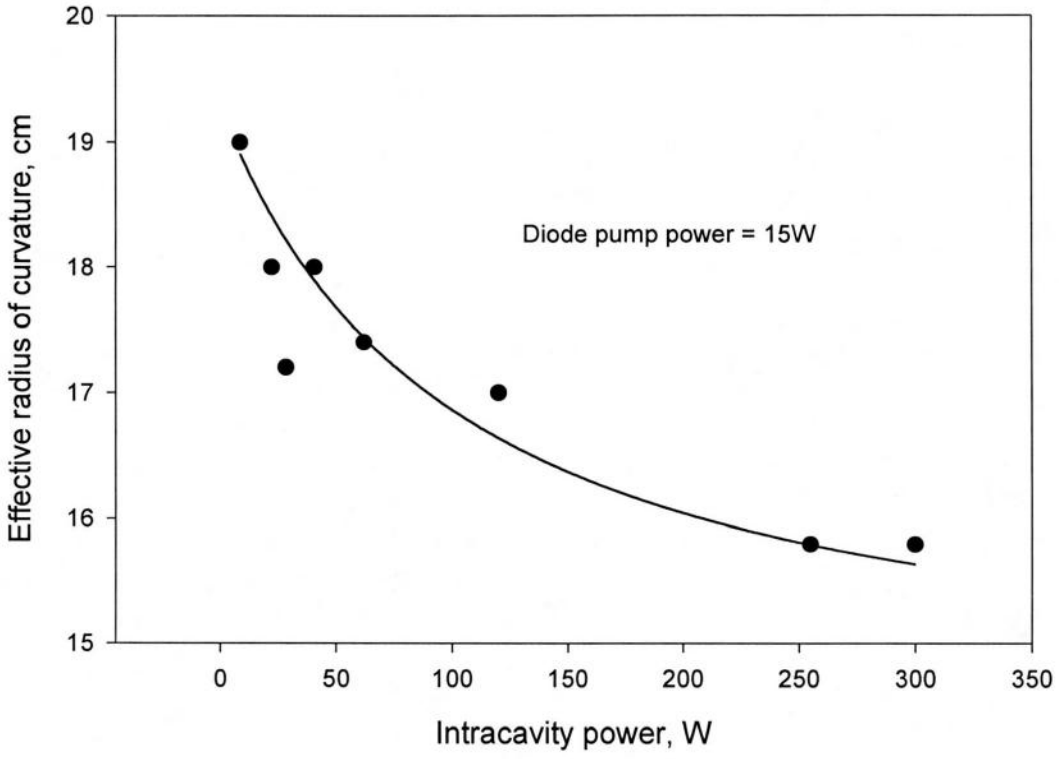

Figure 5.14: *The impact of intracavity power on Nd:YVO_4 thermal lens. The solid line represents a best fit to the experimental data*

We see from figure 5.14 that the circulating power inside the cavity of the laser does indeed have a significant impact upon the magnitude of the thermally induced radius of curvature in the Nd:YVO_4 crystal. As the resonating field varies over the range 8 - 300W, the thermally induced radius of curvature decreases ~15% from 19 to 16cm. We conclude, then, that although the thermally induced radius of curvature exhibited by the Nd:YVO_4 crystal is rooted principally in the absorption of the diode laser pump power, the circulating field resident within the laser cavity has a lesser yet significant effect on this important cavity design parameter. As the thermally induced radius of curvature in the Nd:YVO_4 is dynamic as the circulating field is varied, the ICSRO cavity design will have to be stable over the region of which this curvature varies.

5.4. ICSRO based upon PPLN and PPRTA

With the pump head, and particularly the thermal behaviour of the Nd:YVO_4 characterised and the size of the pumped volume, the design and construction of the ICSRO was realised. A similar approach was adopted as with the lower power, 1W diode pumped system; namely to use an intracavity lens to form a pump waist in the non-linear crystal and stabilise the cavity in the presence of a thermal lens in this component.

5.4.1 Comparison of PPLN and PPRTA

In this section we shall present a comparison of two non-linear crystals, the well-established material PPLN and the more recently developed PPRTA. A summary of the characteristics exhibited by these two materials is summarised in figure 5.15 below.

Property	*PPLN*	*PPRTA*	*Comments*
Non-linearity	17pm/V	8pm/V	
Interaction Length	<50mm	<20mm	
Grating Availability	Multiple/Fanned	Single	PPRTA restricted to temperature tuning
Transparency	Beyond 5μm	Beyond 5μm	
Establishment	Well established	New material	Few suppliers of PPRTA
Thermal Behaviour	Susceptible	Relatively immune	PPLN detrimental to intracavity operation
Photo-refractive behaviour	Susceptible	Immune	PPLN must be heated
Poling Depth	Up to 1mm	Up to 3mm	PPRTA easy to accommodate
Conclusions	Ideal for use in low power, low threshold systems	Ideal for use in high power systems	

Figure 5.15: *Properties of PPLN and PPRTA.*

We can see that although PPLN is superior to PPRTA in terms of non-linearity and interaction length availability (and will therefore exhibit a lower OPO threshold), it also has a few crucial unfavourable characteristics which adversely impact its use in a high power, intracavity system of this kind. The susceptibility of PPLN to photo-refractive

damage immediately mandates the location of a high temperature oven inside the laser cavity which, as well as complicating the mechanical design of the experimental setup, also introduces instability as air current perturbations to the intracavity field are promoted. We have seen that the long upper-state lifetime of Nd:YVO_4 and the addition of a third rate equation into the system describing the energy interchange between the pump and signal cavities makes the system acutely sensitive to the onset of relaxation oscillations if any of the photon parameters (i.e. upper-state population, pump and signal photon numbers) are perturbed, and the presence of a hot oven inside the cavity causes modulation in amplitude space that could trigger such oscillations. PPRTA is immune from the effects of photo-refractive damage and may therefore be utilised at room temperature without any kind of thermal stabilisation, although in practice it would be prudent to stabilise it with a servo-controlled peltier so as to control its temperature tuning characteristics.

The other significant problem associated with PPLN in higher power systems is its large dependence of refractive index upon temperature. Although this gives broad temperature tuning characteristics, this property also makes PPLN much more vulnerable to thermal lensing than PPRTA. In an extra cavity system, where the thermal lens formed in a crystal is somewhat decoupled from the pump laser, such thermal behaviour is more easily compensated. However such a large dynamic lens inside a laser cavity which is so susceptible to the onset of relaxation oscillations causes serious problems as the situation arises where there is positive 'feedback' between the magnitude of the thermal lens destabilising the laser cavity to the point where the circulating field collapses, which in turn reduces the thermal lens allowing the field to recover and the cycle is made. Although this problem is also present in a system based upon PPRTA, its relatively robust performance in the presence of a high circulating field significantly reduces the issue.

Although PPRTA is presently available in lengths of only up to 20mm, compared to 50mm for PPLN, and has less than half the non-linearity of PPLN (8pm/V compared to 17pm/V), PPRTA is still particularly suitable for intracavity devices because of its strengths outlined above, and in a high power system such as this a higher threshold is easily accommodated due to the very high circulating fields available.

5.4.2 Cavity design

The design criterion laid down for this system was identical to that for the system outlined in the previous chapter, namely a sufficiently small beam radii of the pump and signal fields mode matched at the centre of the non-linear crystal, stability of the two fields in the presence of thermal effects which manifest themselves as power applied to the system is increased, and good mode matching between the circulating pump field and the diode pumped volume in the laser gain media. Figure 5.16 gives details of the mode radii in the Nd:YVO_4, PPRTA and PPLN crystals as the thermal lens in the Nd:YVO_4 in increased. The separation of the optical components that comprise these two systems, as shown in figure 5.18, are given in figure 5.17.

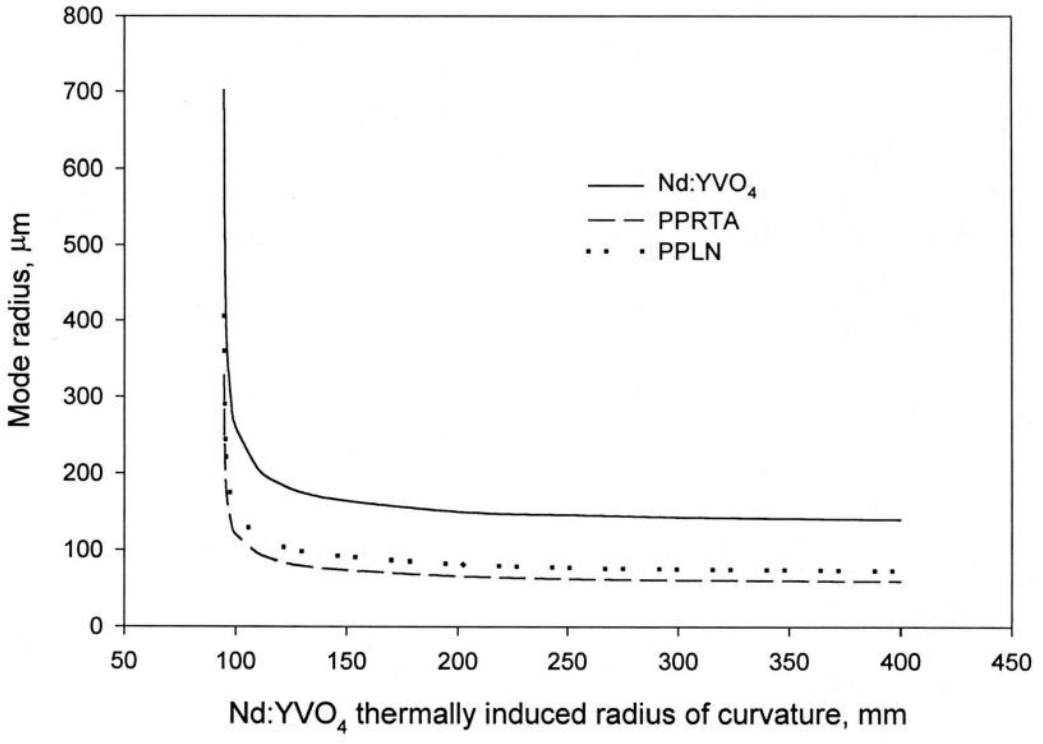

Figure 5.16: *Stability of the mode as a function of Nd:YVO_4 thermally induced radius of curvature.*

The mode size in the non-linear crystal in each case was selected to take into account of the non-linearity in each case and the susceptibility of each crystal to thermal lens. In the case of PPLN, the mode waist was relaxed to reduce the effects of thermal lensing without too much penalty in terms of OPO threshold as the non-linearity of this crystal was large. As the dispersion of refractive index with temperature in PPRTA is ~one third

that of PPLN [5] the focussing was tighter in the case of PPRTA to reduce OPO threshold without serious manifestation of thermal lensing.

Optical Element	PPRTA ICSRO	PPLN ICSRO
Mirror M1	∞	∞
Nd:YVO_4	4×4×7mm, 0.5% doped	4×4×7mm, 0.5% doped
Displacement	175mm	175mm
Lens	63mm f.l.	63mm f.l.
Displacement	88mm	97mm
Non-linear crystal	20mm	25mm
Displacement	194mm	178mm
Mirror M2	200mm R.O.C.	200mm R.O.C

Figure 5.17: *Design parameters of the two ICSRO devices.*

The optical layout of the system is shown in figure 5.18 below. The focussed diode pump enters the Nd:YVO_4 crystal via the 1μm high reflector from the left. As stated above, the thermal lens induced in the gain crystal by the diode pump light gives the plane 1μm high reflector an effective radius of curvature of ~150-200mm.

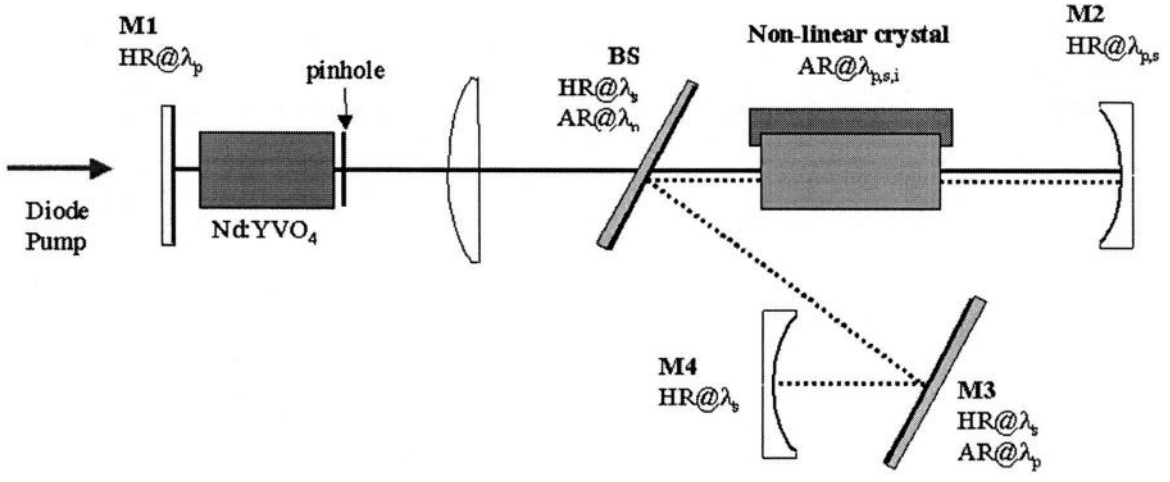

Figure 5.18: *Intracavity SRO design.*

The aperture was included for aid alignment and was useful under certain circumstances in order to suppress higher order laser mode oscillation. The AR/AR lens served to form a 1μm pump waist with M2 (200mm R.O.C.) in the non-linear crystal, and also stabilised the cavity as the thermal lens was formed in the non-linear crystal as the pump field was increased. The triple-band ($\lambda_{p,s,i}$) AR/AR coated non-linear crystal was placed in an oven in the case of the PPLN and upon a thermo-electrically stabilised copper plate in the case of PPRTA. The double high reflector (HR@ $\lambda_{p,s}$, AR@ λ_i) mirror completes the pump cavity. The signal cavity is defined by M2, the dichroic beamsplitter BS and mirrors M4 (200mm R.O.C.) and the plane mirror M3. Although the signal cavity could be configured with the curved M4 on axis with the signal field reflected from the beam splitter, M3 was included to eliminate any interferometric feedback of the 1.064μm pump in the signal cavity back into the pump cavity. We found that such feedback effects induced large intensity fluctuations in the circulating pump field, exacerbating the onset of relaxation oscillations. The curvature and separation of mirrors M2 and M4 was chosen to form a concentric cavity for the signal in order to produce the appropriate signal waist at the centre of the crystal.

The distance between the laser pump head and the intracavity lens was chosen such that the cavity remained stable over a large range of effective radii of curvature of the mirror M1 in order to accommodate the thermal lens in the Nd:YVO_4 crystal, and to mode match the 1μm circulating field efficiently into the pumped volume.

The PPLN crystal was 0.5×11×25mm in size and had eight gratings written upon it over the range 28.5-29.9μm in 0.2μm steps. The pump field was focussed down to form a waist of ~50μm but varied between this and ~80μm due to thermal lensing effects. The PPRTA crystal dimensions were 3×11×20mm with only one grating at a period of 39.6μm to phase match the signal and idler at 1.525 and 3.525μm, respectively, at 20°C. The pump field was focussed down to form a waist of 50-60μm. The PPLN was operated at a temperature of 150°C in order to match the signal and idler wavelengths to that of the PPRTA operated at room temperature. The PPRTA was adhered to a thermoelectrically stabilised copper block which allowed the crystal temperature to varied over the range 0-

100°C to facilitate temperature tuning, although the temperature was not reduced below 10°C in order to avoid condensation build up on the crystal facets.

With confocal focussing to these values, and using the expressions for SRO threshold derived in chapter two, namely

$$P_{th} = \frac{(n_p \cdot n_s \cdot n_i \cdot \varepsilon_0 \cdot c^3) \cdot \pi \cdot [\omega_p{}^2 + \omega_s{}^2]}{4 \cdot \Psi_s \cdot \Psi_i \cdot d^2 \cdot l^2 \cdot h_m} \cdot a_s \tag{5.1}$$

where n_p, n_S and n_i are the refractive indices of the crystal at the pump, signal and idler, ω_p and ω_S are the pump and signal waist sizes, Ψ_S and Ψ_i the angular frequency of the signal and idler waves, d is the non-linear coefficient, l the crystal length, h_m the confocal parameter and finally a_S the signal cavity round trip loss, we can calculate the expected intracavity circulating field at threshold for the two devices.

Assuming a ~4% signal cavity round trip loss, we expect to see OPO threshold occur at 10.3W in the case of PPLN, and ~24W for the PPRTA system. These figures are significantly larger than that which was expected/observed in the 1W ICSRO described in the previous chapter. This is due to a shorter nonlinear medium and weaker focussing of the pump and signal in order to minimise thermal effects within the nonlinear medium.

The figure for PPLN threshold were significantly higher in this system than that predicted in the 1W diode pumped system outlined in the previous chapter due to the increased loss experienced by the signal field brought about by the inclusion of the second plane mirror in the signal cavity, and the shorter PPLN crystal.

The alignment procedure of this system closely resembled that of the low power ICSRO outlined in chapter 4. Adjustment of both the pump and signal cavities was particularly easy in the case of the PPRTA due to its very large aperture, 3mm compared to 0.5mm for the PPLN. For the benefit of the reader attempting to repeat this experiment, it was found that aligning the system at reduced diode pump powers (~10W) brought about operation

of the OPO with more certainty than at full power due to thermal issues in both the non-linear material and the Nd:YVO_4 crystal which shall be discussed shortly.

5.4.3 Operation

With the pump and signal cavities aligned and optimised, the OPO was operated and characterised. We present the power characteristics of the two devices in terms of extractable idler and threshold power, the temporal stability and transient dynamic behaviour of each system and finally the tuning behaviour of the idler extracted from the PPRTA ICSRO.

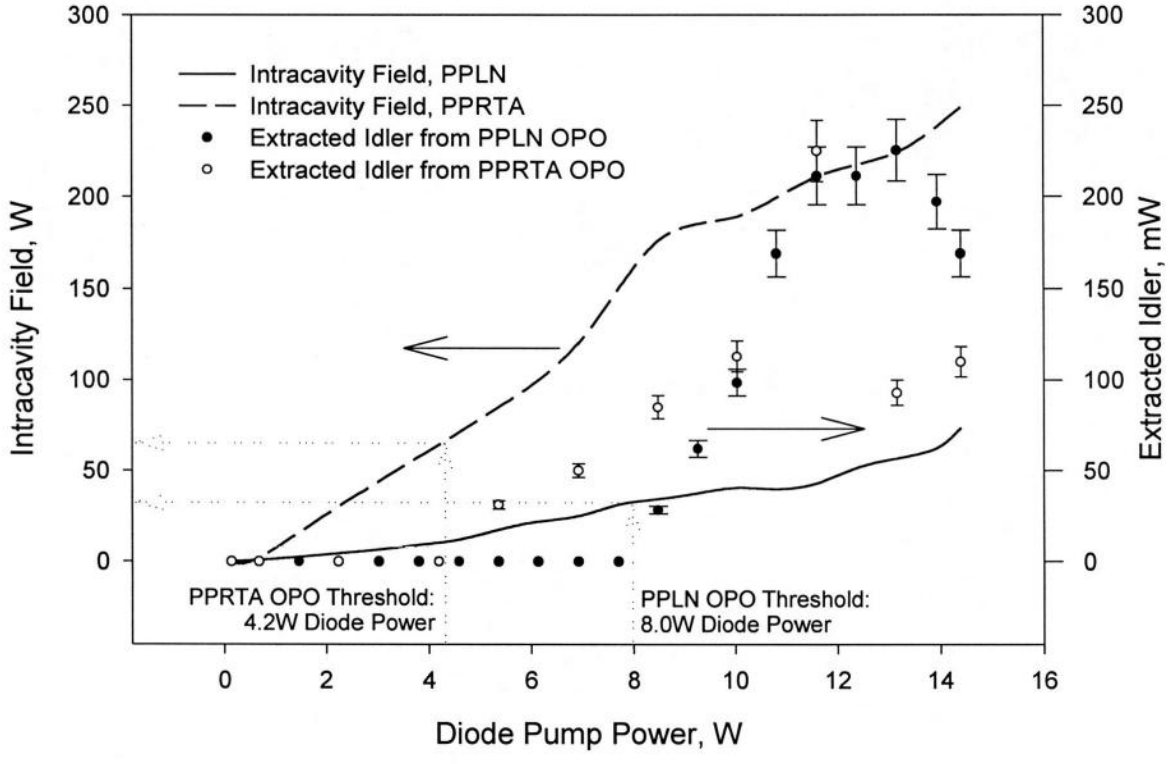

Figure 5.19: *Extracted one way idler output power and the one way circulating intracavity pump power at 1.064μm as a function of the external pump power from the diode laser for the case of PPLN and PPRTA.*

Figure 5.19 summarises the power characteristics of the two devices. In it are shown the one way extracted idler power (through M2) and the intracavity circulating field, both as a function of diode pump power for the two devices. It presents us with some unexpected results. In terms of the circulating 1μm field, the threshold in the case of PPLN was lower than that of the PPRTA (30W compared to 65W), in line with its higher non-linear

coefficient and longer interaction length. When one looks at SRO threshold in terms of external diode pumping power, however, it is the PPRTA that has the lower threshold as a result of a higher slope efficiency shown by the intracavity field; 4.2W compared to 8.0W in the case of the PPLN. The higher slope efficiency of the circulating field in the case of the PPRTA is ascribed to the higher resistance of this material to the formation of thermal lens effects, and far reduced aperturing of the laser cavity mode in comparison with PPLN. As the circulating field in the PPLN was increased, a significant thermal lens was formed and this effect caused the circulating mode to expand, being apertured by the thickness of the crystal. The changing thermal properties of the Nd:YVO_4 crystal were also significant as the (~3 times) higher than expected SRO threshold powers for both devices show. Indeed, threshold powers on the order of those observed in the low power, 1W diode pumped ICSRO were never observed in this system. It is theorised that the beam waist formed at the centre of the nonlinear crystal was constantly expanding, and therefore threshold power increased, as the thermal lens formed in the Nd:YVO_4 crystal became more significant. Further refinement to this cavity design in order to obviate the effects of thermal lensing in the vanadate crystal would be advantageous.

The figure shows that both devices produced ~220mW of idler for 12W of diode pump power. This was the power extracted through mirror M2; taking into account the signal and idler wavelengths, and the idler loss of the coating this optic and that on the non-linear crystal, and also that the idler was produced in both directions, we obtain a total down converted power of 1.61W, assuming 5% loss at each coating. This compared with 5.5W of 1μm power extractable through M2 when it was replaced by an optimal output coupler of 90% transmission.

There was almost no discernable evidence of the OPO clamping the intracavity field, as is evident from the figure. This is attributed to the changing mode sizes of both the pump and signal waists in the non-linear crystal as the thermal lens in this and the laser gain crystal are constantly evolving as the diode pump power is increased. In effect, the cavity geometry is dynamic as pump power and circulating field are varied, and so the OPO has a different effective threshold as these parameters change. This makes an estimate of the down conversion efficiency extremely difficult as this parameter depends upon the

threshold of the laser and the OPO as well as the down-converted power produced for a given operating pump power. The laser and OPO thresholds are easily measured as a function of pump power, but as the cavity geometry has significantly changed due to thermal lensing at higher pump powers, a comparison between measured thresholds and down-converted power at these enhanced pump powers becomes meaningless.

It is interesting to note that the idler power extracted from the two devices falters beyond diode pump powers of ~12W, and yet the circulating field continues to increase. This is due to the thermal lens formed in the respective non-linear media destabilising the signal cavity, which has no lens within it to act as an optical ballast as the pump cavity has. It was unfortunate that no suitably coated optic was available to redesign this cavity and better stabilise it in the presence of the crystal thermal lens.

A rather striking comparison between the thermal lensing behaviour of the two crystals was evident by observing the quality of the spatial mode in each system. Figure 5.20 shows the spatial mode of the non phase-matched sum-frequency mixed light emitted by the PPLN and PPRTA devices, as measured on a calibrated CCD camera. The two crystals exhibited very different behaviour in this respect. Soon above OPO threshold a very poor mode was observed in the case of PPLN, which was constantly 'breathing' (i.e. changing spatial profile on the ~1s timescale) and very difficult to collapse down to a fundamental gaussian mode. The trace shown here is typical as the observed mode was so dynamic. The PPRTA, in contrast, exhibited an excellent mode which remained stable up to pump powers of ~13.5W.

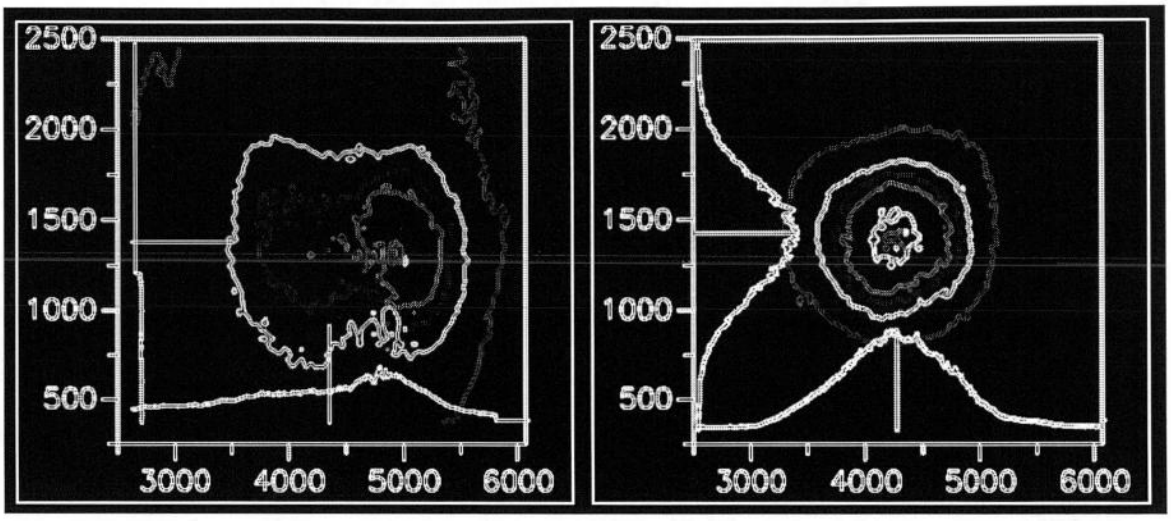

Figure 5.20: *Sum frequency mixed spatial mode quality for the PPLN and PPRTA SRO's pumped at 12W. Left trace: PPLN, Right trace: PPRTA.*

The instability of the thermal lens in the PPLN crystal is evident from the behaviour of the extracted idler power as measured over an extended time period. Figure 5.21 shows such a measurement over a period of three hours. These traces were measured with a thermal power meter attached to an 8-bit digital storage adapter sampling every 10 seconds, and so any transients are lost due to the time response of the power meter thermopile and the relatively wide sample spacing. It is evident from the figure that the power stability of the PPRTA system was roughly twice that of the PPLN SRO. The poor performance of the PPLN system is caused by the unstable thermal lens in the PPLN crystal and also thermal currents caused at the facets of the crystal as air was heated by the oven and rapidly accelerated over its surface. This problem is not present in the case of PPRTA as it was operated at room temperature. The temperature of the PPLN oven was reduced from 150°C to 100°C and this caused the RMS noise to fall from ~20% to ~17%. Clearly, the thermal lens formed in the PPLN is the most significant factor in the output stability of the device.

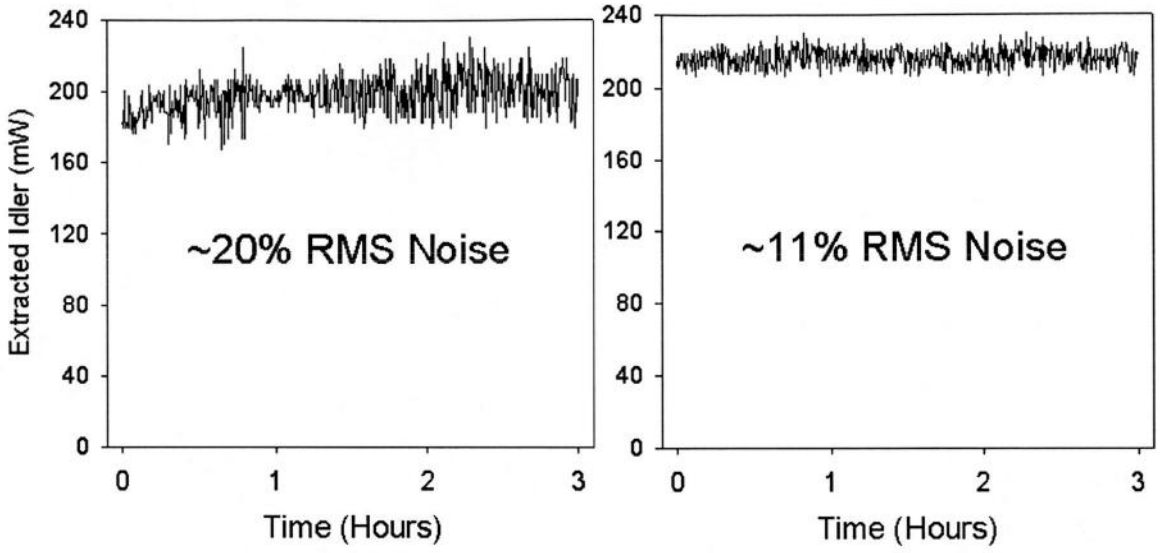

Figure 5.21: *Long term idler stability of the two devices pumped at 12W. Left trace: PPLN, Right trace: PPRTA.*

The pump field rejected from the left face of the beam splitter (figure 5.18) was focussed into a fast photodiode to observe the transient dynamic behaviour of the two devices, and this result appears as figure 5.22. The Nd laser in the case of PPLN exhibited a continuous train of pseudo-random relaxation oscillation pulses, whereas the circulating field in the PPRTA system was true cw. We recall that whilst intracavity systems of this type, which employ laser gain media with a long upper state life time, are inherently stable, they are extremely sensitive to the onset of relaxation oscillations if the cavity is perturbed. One initial source of this perturbation was interferometric feedback of the pump field off of the beam splitter and M4 and under whose effects the PPRTA system was also observed to suffer from relaxation oscillations. However, with this feedback eliminated by the inclusion of the AR @ 1064nm mirror M3 the OPO exhibited excellent transient stability.

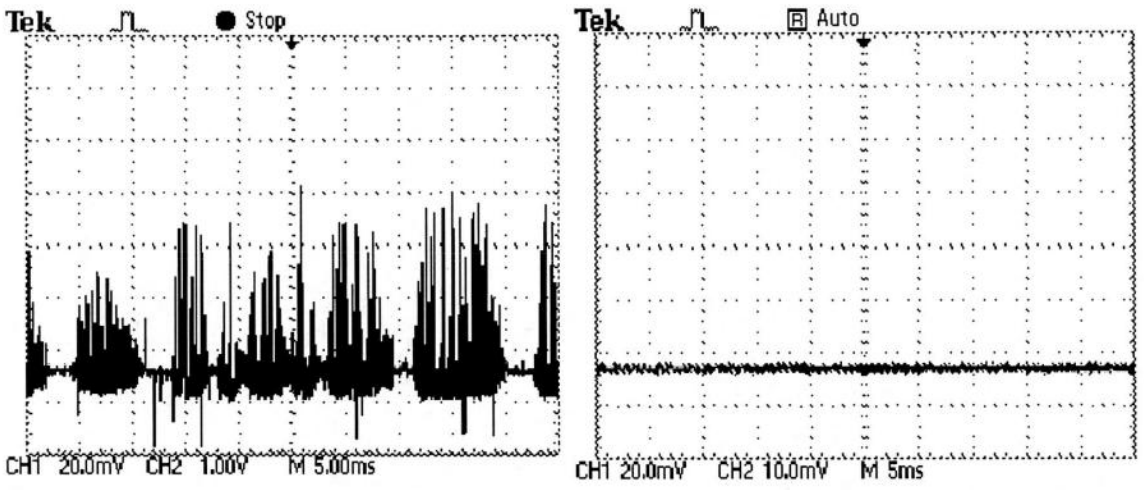

Figure 5.22: *Transient dynamics of the intracavity pump field for the PPLN and PPRTA ICSRO's pumped at 12W. Left trace: PPLN, Right trace: PPRTA. Both traces have a time base of 5mS/div and are zero'ed at –4 divisions.*

The PPLN system still suffered from relaxation oscillations even with the inclusion of M3 and we theorise that the 'breathing' of the pump and signal mode through the erratic thermal lens formed in the PPLN crystal and the thermal air currents discussed above had sufficient effect to trigger the onset of these pulse trains.

We now turn our attention to the tuning characteristics of the PPRTA ICSRO. As the grating periods written upon the PPLN crystal were identical to that used in the system described in chapter 4, the temperature tuning behaviour of the PPLN system is not replicated here (see figure 4.24) As the PPRTA had only a single grating written upon it, tuning of the signal and idler was restricted to varying the temperature of the crystal. As stated above, the PPRTA crystal was mounted upon a thermo-electrically stabilised copper block whose temperature could be varied over the range 10-100°C. As the diagnostics available in the laboratory were insensitive to the mid-infrared idler, and only partially reliable at the near infrared signal, the red sum-frequency mixed light produced by non-phase matched mixing of the pump and signal was measured in order to obtain the signal and idler wavelengths. The results are shown below.

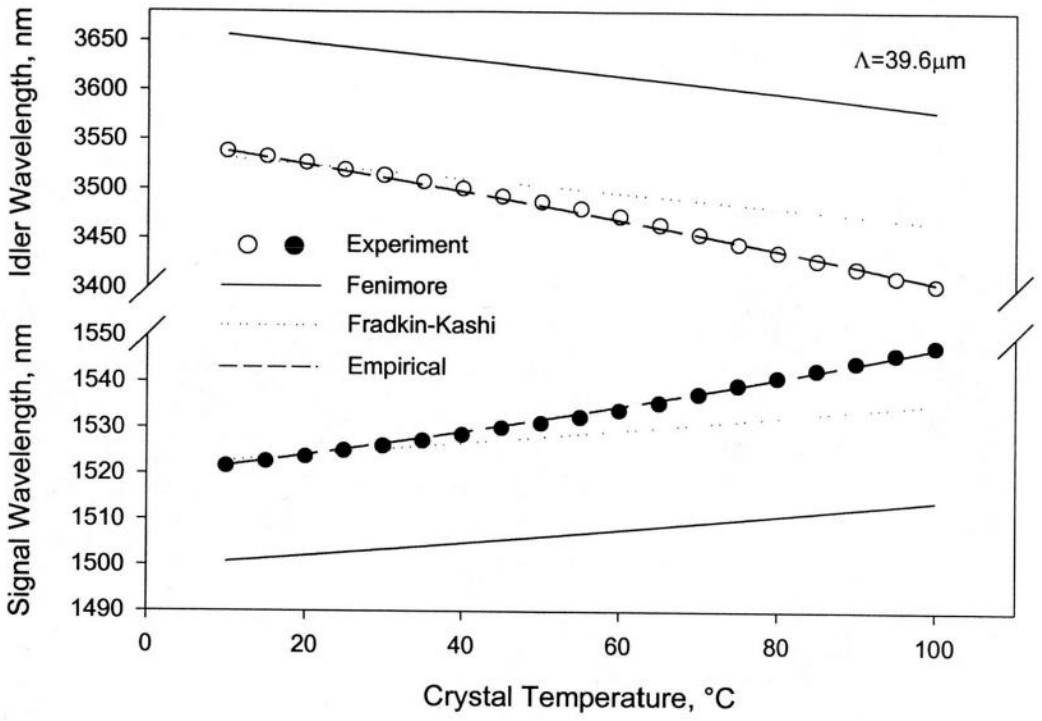

Figure 5.23: *Temperature tuning characteristics of the PPRTA ICSRO.*

We can see that over the range 10-100°C, the idler tuned over the range 3538-3404nm (133nm) and the signal 1522-1548nm (26nm). The PPRTA idler tuning rate with temperature of ~1.5nm/°C compares with ~2.1nm/°C in the case of PPLN.

Overlayed on the graph are three sets of theoretical temperature tuning curves. The solid line uses the sellmeier equation of Fennimore and the dn/dt expression of Karlsson [6]. The dotted line uses the sellmeier equation of Fradkin-Kashi [7] and again the dn/dt expression of Karlsson. The signal and idler wavelength pair predicted by the sellmeier equation of Fradkin-Kashi at room temperature was in excellent agreement with experimentally observed results. To yield better agreement between theory and results, the dn/dt coefficients were modified for best fit (1.9 × the dn/dt coefficients of [6]). The full expression for refractive index as a function of temperature and wavelength is given below, along with its coefficients.

$$n_x = \sqrt{A + \frac{B}{1-\left(\frac{C}{\lambda_x}\right)^2} + \frac{D}{1-\left(\frac{E}{\lambda_x}\right)^2} - F\cdot\lambda_x^{\,2} + (T-rt)\cdot\left[\left(G\cdot\lambda_x^{\,-3} + H\cdot\lambda_x^{\,-2} + I\cdot\lambda_x^{\,-1} + J\right)\cdot 10^{-4}\right]} \tag{5.2}$$

where

A = 2.182064	F = 0.008921 (μm^{-2})
B = 1.307519	G = -1.45046 (μm^3)
C = 0.228244 (μm)	H = 4.88661 (μm^2)
D = 0.354743	I = -4.52143 (μm)
E = 9.0190959 (μm)	J = 0

And rt is room temperature, T is crystal temperature and n_X the refractive index at λ_X. These parameters come from [6, 7]. The units, where present, are shown in parenthesis.

To conclude this chapter, we briefly discuss an alternative cavity design which was developed with the reduction of the thermal lens effects in the Nd:YVO_4 crystal as well as the non-linear crystal in mind. This work was carried out in collaboration with Philip Schlup (University of Otago, New Zealand), to whom I extend my gratitude.

The cavity was re-configured as shown in figure 5.24. We see that focussing of the pump through the non-linear crystal is formed by the off axis mirror R_F and R_2, both highly reflecting at the pump and signal wavelengths. The signal cavity of defined by R_2, R_F, BS and R_{S1}. Here the signal cavity is closer to confocally focussed than in the previous design, where the signal cavity was near concentric about the non-linear crystal. The AR@1.064μm lens is now placed near the laser gain medium to desensitise the cavity from the effects of thermal lensing in this component. This intracavity lens was placed at its focal length away from the beam waist formed upon the plane mirror R_1 in order to form an optical ballast in this arm of the cavity.

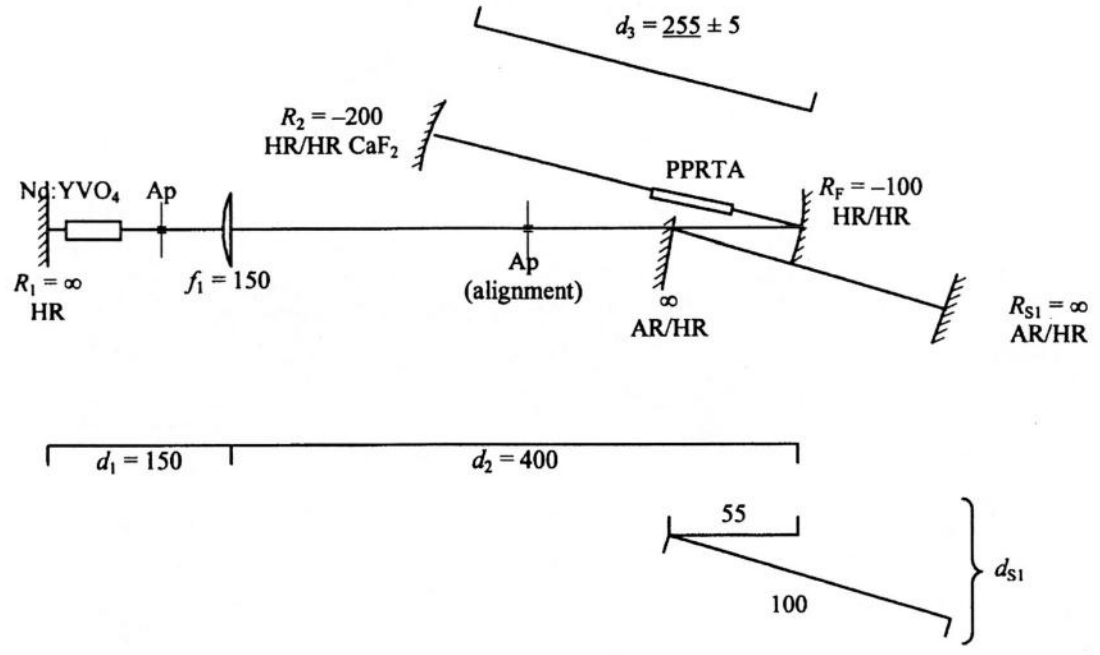

Figure 5.24: *Experimental setup of the modified cavity design.*

Figure 5.25 demonstrates the fine attributes of this cavity design in terms of the circulating pump mode stability as the thermal lens in the Nd:YVO_4 is increased. In it are shown the beam radii incident upon the plane mirror M1 and at the centre of the PPRTA crystal as a function of M1 effective thermal radius of curvature. We can see that the cavity is stable with M1 assuming an effective radius of curvature down to 21mm, compared to ~100mm as demonstrated by the previous system.

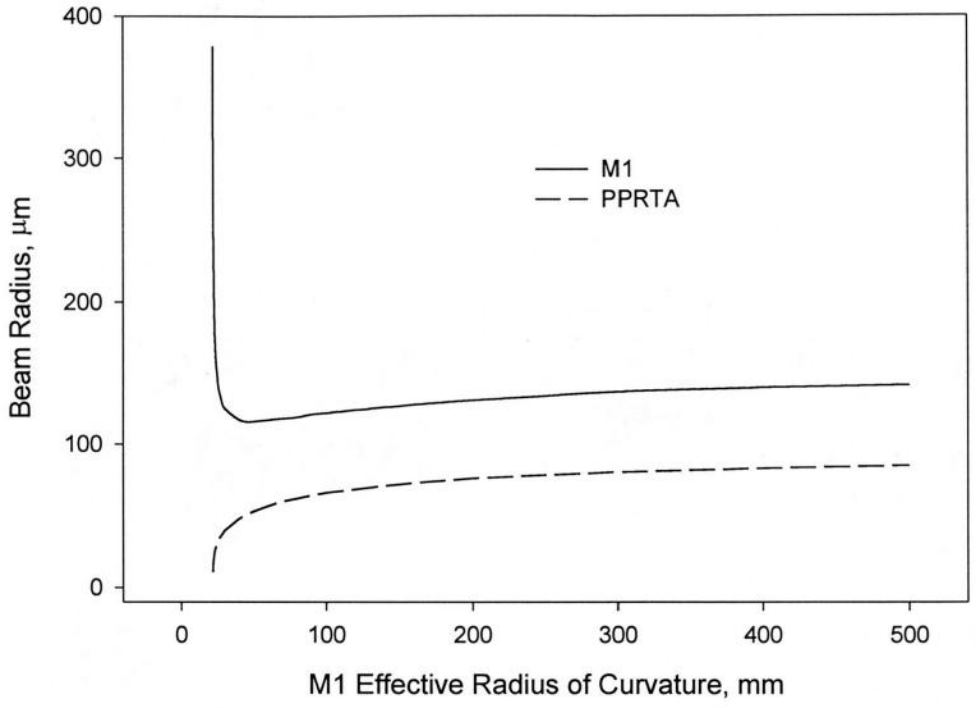

Figure 5.25: *Cavity stability as a function of Nd:YVO_4 thermal lens.*

The robust performance of this cavity in the face of thermal lens effects is demonstrated by plotting the extracted idler as a function of diode pump power (figure 5.26). We can see that there is a reasonable linear relationship between the two parameters, with no evidence of power saturation in the extracted idler pointing to the possibility of the operation of this device at elevated pump powers. Laser and OPO threshold occurred at 0.38W and 5.84W respectively. At a pump power of 15W, ~180mW of idler was extracted in one direction. Whilst represented less power than demonstrated by the previous system, the stability of the idler in terms of power and spatial characteristics were superior. The linear nature of the power output with respect to the diode pump power points to the possibility of power scaling the pump source to compensate for this discrepancy. Further optimisation of the mode matching between the astigmatic pump and signal fields in the PPRTA crystal may also increase the extracted idler from this system. The presence of relaxation oscillations in the circulating pump field was not detected.

The spatial mode of the SFM mode was of excellent quality and very stable at all pump powers.

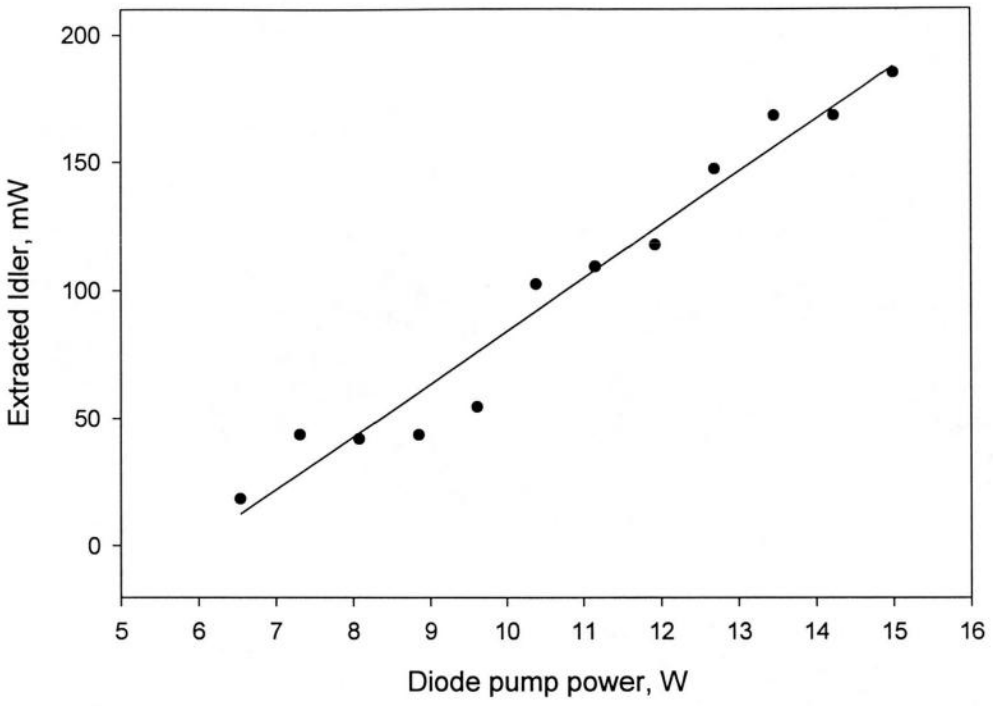

Figure 5.26: *Extracted idler as a function of diode pump power. The solid line is a regression fit to the data.*

Unfortunately, this research was conducted towards the end of this Ph.D programme and as such time did not permit a thorough characterisation of this device. However, the results obtained in the brief time available to us pointed to a cavity design which was robust in the face of thermal lensing effects in both the laser gain and non-linear crystals. The use of a curved mirror to focus the signal field near to the non-linear crystal desensitises this cavity to the effects of thermal lensing. The use of off-axis concave mirrors introduces astigmatism into the mode, however, and so further research would profit from a design employing suitably anti-reflection coated lenses.

5.5. Conclusions

We have demonstrated two ICSRO's based upon PPLN and PPRTA and pumped internal to a high power diode pumped Nd:YVO_4 laser. Although the PPRTA had a lower non-linear coefficient and was shorter in length in comparison to the PPLN, it exhibited comparable power performance in terms of extracted idler and superior and temporal performance.

Thermal lensing effects in the PPLN crystal resulted in poor spatial stability of the sum-frequency mixed light and the circulating pump field, and also caused sufficient perturbation to the pump and signal cavities to result in driving the pump laser into a continuous stream of relaxation oscillations. A fundamental spatial mode observed in the PPRTA ICSRO and monitoring of the circulating pump field showed that the system was operating in the absence of relaxation oscillations once the effects of interferometric feedback had been eliminated by the inclusion of M3: a crucial advantage as the true potential of this device will be realised in the CW regime.

Although the temperature tuning of the PPRTA ICSRO yielded less tuning in the idler than with the PPLN system, a PPRTA grating period choice for application specific wavelengths should make this a relatively minor problem. Indeed, a reduced rate of change of idler with crystal temperature would relax tolerance on the crystal temperature servo-loop in applications requiring stable idler wavelengths. Further development by crystal manufacturers will bring about the availability of multiple / fanned gratings upon a single chip enabling very broad tunability in the idler, comparable with that demonstrated by similar PPLN systems.

In a system such as this, careful cavity design and robust performance in the face of thermal lensing in intracavity elements is crucial. The poor thermal performance of PPLN in comparison to PPRTA was largely attributed to its propensity to thermal lens due to its higher absorption coefficient at 1.064μm and larger refractive index dispersion with temperature.

Estimation of the thermal lens induced in the Nd:YVO_4 crystal proved to be non-trivial due to its dependence upon both diode pump power and circulating field. As this parameter is dynamic as the cavity is pumped harder, and more circulating field is output coupled through non-linear down conversion, optimisation of the cavity at a single pump power is much preferable to an attempt to gain a meaningful measurement of extracted idler as a function of diode pump power.

An estimation of the down-conversion efficiency of this system was not possible due to the dynamic nature of the pump cavity as the diode pump power was increased. Although this system with its present cavity design failed to give comparable down conversion powers as that extractable at the pump wavelength with an appropriate choice of output coupling, the >250mW of useful idler output power demonstrated by the PPRTA system hold the promise of finding new and interesting applications.

A new cavity design realised a more robust performance in the face of thermal lensing in the Nd:YVO_4 crystal. Whilst this system did not exhibit as much power output in the idler when compared to the design discussed throughout the majority of this chapter. It did, however, point to a strategy to overcome thermal issues in the laser gain medium and further optimisation of this design may yield enhanced extractable idler powers.

References

1 D. J. M. Stothard, P.-Y. Fortin, M. Ebrahimzadeh and M. H. Dunn, CLEO (The Optical society of America, Baltimore, USA, (2001),

2 SDL part number SDL-3460.

3 Casix part number DPO4204.

4 M. E. Innocenzi, H. T. Yura, C. L. Fincher and R. A. Fields, "Thermal modeling of continuous-wave end-pumped solid-state lasers," *Applied Physics Letters* **56**, 831 (1990).

5 D. L. Fenimore, K. L. Schepler, D. Zelmon, S. Kuck, U. B. Ramabadran, P. Von Richter and D. Small, "Rubidium titanyl arsenate difference-frequency generation and validation of new Sellmeier coefficients," *Journal of the Optical Society of America B-Optical Physics* **13**, 1935 (1996).

6 H. Karlsson, F. Laurell, P. Henriksson and G. Arvidsson, "Frequency-doubling in periodically poled RbTiOAsO4," *Electronics Letters* **32**, 556 (1996).

7 K. Fradkin-Kashi, A. Arie, P. Urenski and G. Rosenman, "Characterization of optical and nonlinear properties of periodically-poled $RbTiOAsO_4$ in the mid-infrared range via difference-frequency generation," *Applied Physics B-Lasers and Optics* **71**, 251-255 (2000).

6: A numerical analysis of relaxation oscillations

6.1 Introduction

We have seen that the ICSRO systems outlined in chapters four and five were seriously affected by relaxation oscillations. It seems that the inclusion of the SRO within the cavity of the pump laser significantly modifies the transient dynamics of these systems [1,2]. In figure 6.1 we can see the dynamic behaviour of the system described in chapter four both in the absence and presence of parametric down-conversion. We can see that in the case of the simple laser in the absence of down-conversion, the oscillations of the intracavity field dies down in ~30μS and have a frequency of ~300kHz, but once the OPO cavity was unblocked and down-conversion allowed to occur, the oscillations take ~230μS to damp down and have a frequency of ~1.5MHz. The cavity dynamics were perturbed in both cases by inserting a mechanical chopper in between the diode pump source and the laser gain medium.

In this chapter, we shall derive the coupled rate equations which describe the parameters governing the dynamics of the ICSRO, namely the population in the laser gain medium upper state and the power in the pump and signal fields. These equations will then be normalised in terms of simple experimentally observable parameters. Finally, these three coupled rate equations will be numerically solved, with different feedback options included to point towards a strategy for damping down the relaxation oscillations to the point that they no longer pose a serious restriction on the practical application of neodymium based ICSRO systems.

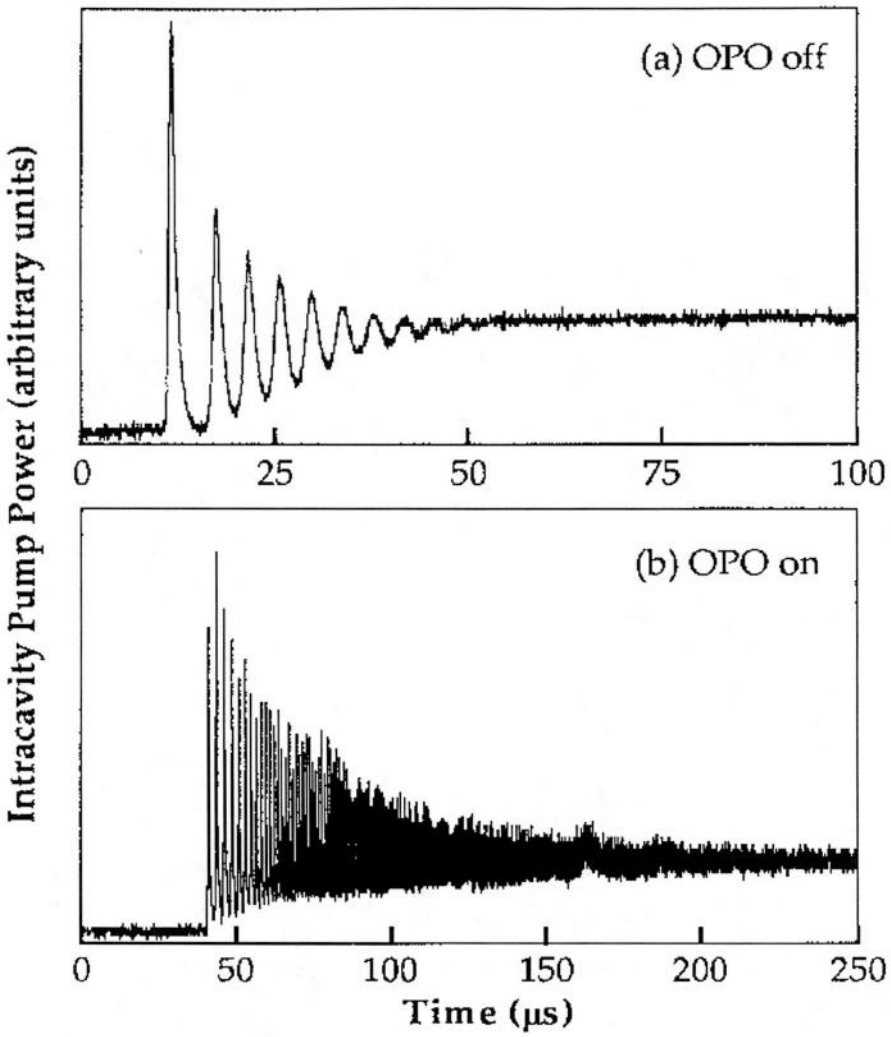

Figure 6.1: *Transient dynamics of 1.064mm pump field (a) in the absence of, and (b) in the presence of, parametric down conversion at a pump rate of 2× OPO threshold [2].*

6.2 Coupled rate equations

Consider the schematic ICSRO system depicted in figure 6.2. We can see that the population of the upper lasing level is brought about by the external pumping rate, σ. It is depopulated by stimulated emission, proportional to the power in the circulating field, and spontaneous emission which is proportional to the population of the upper state. The rate equation of this population is therefore [3]

$$\tau_u \cdot \dot{N}_j = s_j - N_j \cdot \left(1 + x \cdot P_p\right) \tag{6.1}$$

Where τ_u is the upper state lifetime. The power in the pump field is increased by the gain (i.e. population in the upper state, N_j) in the laser gain crystal but is reduced by the linear loss of the cavity caused by imperfect mirror/crystal coatings, and is also transferred to the signal power by coupling through the non-linear crystal. The parameter x is defined in chapter 2, section 2.6.1.

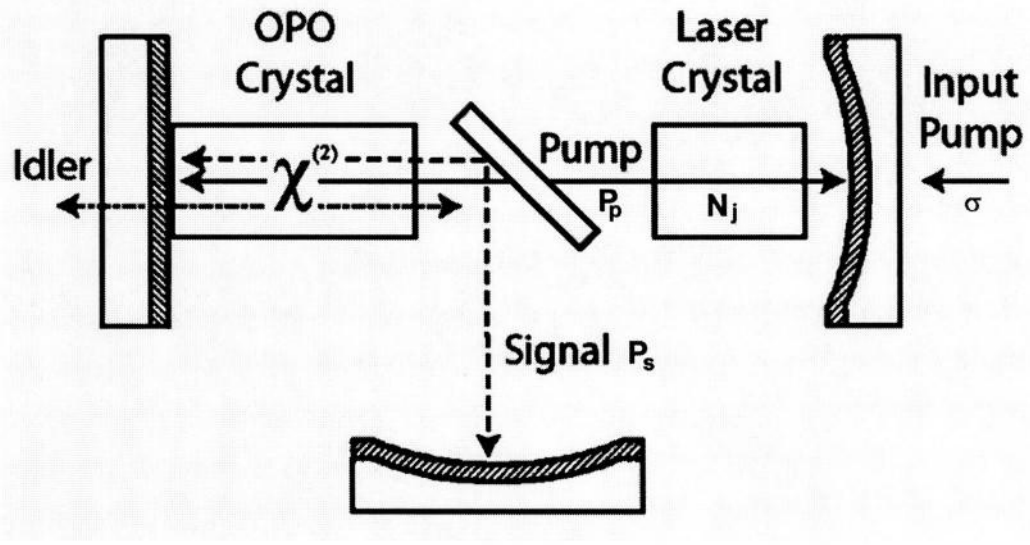

Figure 6.2: *Schematic of an ICSRO [4].*

The rate of change of power circulating in the pump cavity is therefore given by

$$\tau_p \cdot \dot{P}_p = P_p \cdot \left(N_j - 1 - F \cdot P_s\right) \tag{6.2}$$

where f is some is the ratio of the pump and signal cavity finesse which takes into account the coupling of the pump power through the non-linear medium into the signal power [5]. τ_p represents the lifetime of the photons in the pump cavity.

The last dynamic parameter which needs to be taken into account is the power in the signal field. As we have just stated, power is coupled through the non-linear medium from the pump field into the signal field. Power is reduced due to the linear loss of the signal cavity. The rate equation governing this parameter is therefore

$$\tau_s \cdot \dot{P}_s = P_s\left(P_p - 1\right) \tag{6.3}$$

Where τ_s is the lifetime of the photons in the signal cavity. We now need to normalize these three equations in order to make them meaningful in terms of experimentally observable parameters, such as laser threshold, pump power at its clamped value, etc.

Setting the time derivatives to zero, [2-3,5] yield the steady state solution for operation above OPO threshold, $\sigma \geq \sigma_{th\text{-}OPO} = 1+x$, as

$$P_p^0 = 1 \tag{6.4a}$$

$$N_j^0 = \frac{\sigma}{(1+x)} \tag{6.4b}$$

$$P_s^0 = \frac{(N_j^0 - 1)}{F} \tag{6.4c}$$

This is shown graphically in region III of figure 2.5. Above OPO threshold, the pump field is clamped at its threshold value, independent of the level of external pumping. Power is down converted into the signal and idler fields which increase linearly with external pumping.

By making the appropriate substitutions, and following the treatment of [3, 5, 6] the three rate equations for the pump power, signal power and upper state population become

$$\dot{P}_p = \frac{P_p}{\tau_p}\left[\frac{\sigma \cdot N_j}{1+x} - 1 - \frac{(\sigma - 1 - x)\cdot P_s}{1+x}\right] \tag{6.5}$$

$$\dot{P}_s = \frac{P_s}{\tau_s}(P_p - 1) \tag{6.6}$$

$$\dot{N}_j = \frac{1+\kappa - N_j - (N_j \cdot P_p \cdot \kappa)}{\tau_u} \tag{6.7}$$

The equations are normalised such that the upper state population N_j, pump power P_p and signal power P_s are equal to unity in the steady state. The numerical values of x and σ are described in appendix A.

6.3 Numerical model

Having now established a set of coupled rate equations which are normalised in terms of meaningful experimental parameters, a computer model was written to solve the equations numerically. Although such models are traditionally written in high level compiled computer languages, such as Fortran or Pascal, we chose to use a modern real time platform in which to solve these equations. The equations were transferred into Mathsoft *MathCAD* 2000, which employed the *runge-kutta* algorithm to find a solution to the equation set for a given set of input values. The worksheet of each model used to in this analysis appears in the appendix of this thesis.

We explored several feedback options to investigate which, if any, would suppress the relaxation oscillations once triggered. In this model, we assume that any feedback mechanism employed was instantaneous. Six feedback options were considered:

Option A: **Pump power feedback onto signal cavity.** The loss experienced by the signal field is proportional to the instantaneous power of the pump field

Option B: **Signal power feedback onto pump cavity.** The loss experienced by the pump field is proportional to the instantaneous power of the signal field

Option C: **Pump power feedback onto pump cavity.** The loss experienced by the pump field is proportional to the instantaneous power of the pump field

Option D: **Signal power feedback onto signal cavity.** The loss experienced by the signal field is proportional to the instantaneous power of the signal field

Option E: **External pump power dependant upon pump field.** The external (diode) pump power is inversely proportional to the instantaneous power of the pump field

Option F: **Non-linear loss of the pump field.** The additional loss experienced by the pump field is proportional to the square of the instantaneous power of the pump field

We shall consider each option in turn. Figure 6.3 shows the results of the model when no feedback mechanism is employed and so once perturbed, the pump and signal fields are allowed to settle down to their steady state as they would in the system outlined in chapter four. In this case the system is described by the previously stated rate equations (6.5 - 6.7). The system is perturbed in the model by setting the signal field to a value 10% above its steady state value at time t=0.

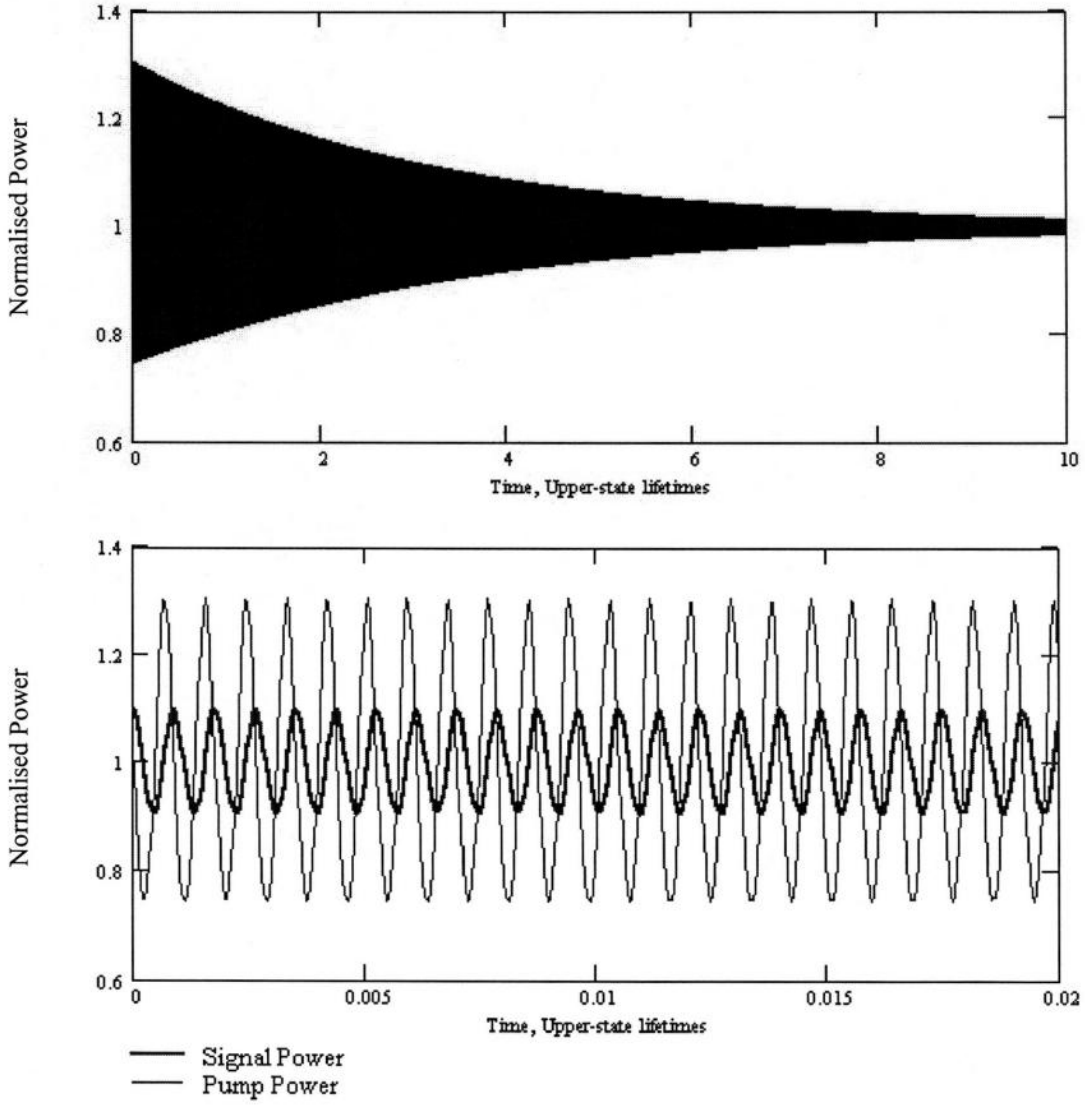

Figure 6.3: *Relaxation oscillations of pump and signal fields due to perturbation of signal field. (The signal is not visible in upper trace due to graphical aliasing).*

We can see that in the advent of a perturbation from the steady state, the system takes >10 upper state lifetimes (>2mS) to resettle to its steady state values. The lower trace shows the oscillations of the pump and signal fields on a much smaller time scale. We can see

that the damping time predicted by the model is nearly an order of magnitude longer than what was experimentally observed in figure 6.1. This is accounted for both by the experimental parameters chosen when this measurement was made (the OPO was only two times above threshold; this model was calculated at three times above OPO threshold) and also that the model does not take into account the thermal effects so abundant in the laser and, in particular, the nonlinear crystals present in the system. The model expects the power characteristics to behave in accordance with the expressions derived in section 2.6.2 (see figure 2.5). As thermal effects augment in the optical components, the cavity geometry is altered and this effectively alters the effective OPO threshold, resulting in the power characteristics somewhat deviating from theory. As the aim of this chapter is to point towards a strategy for the reduction of the relaxation oscillations exhibited by the ICSRO's outlined in this thesis, this deviation from theoretical behaviour is not important as the results presented here are meant to be qualitative, not quantitative, in nature.

6.3.1 Option A: Pump power feedback onto signal cavity loss

Consider figure 6.4. Here we see the familiar layout of the ICSRO, but with the inclusion of some extra components. The instantaneous power of the pump field is obtained by monitoring a small part of it which is rejected from the beam splitter. This signal, once amplified, is then fed into a lossy medium located in the signal cavity, whose loss is dependent upon the potential across it. In a practical realisation of this setup one might employ a Q-switching crystal, such as bulk $LiNbO_3$, operated well below its Q-switching potential with insufficient voltage to spoil the Q of the cavity, but just enough to introduce a little loss into the cavity in which it is situated. Another option could be the implementation of an electro-optic polarisation rotator in tandem with an intracavity polarisor.

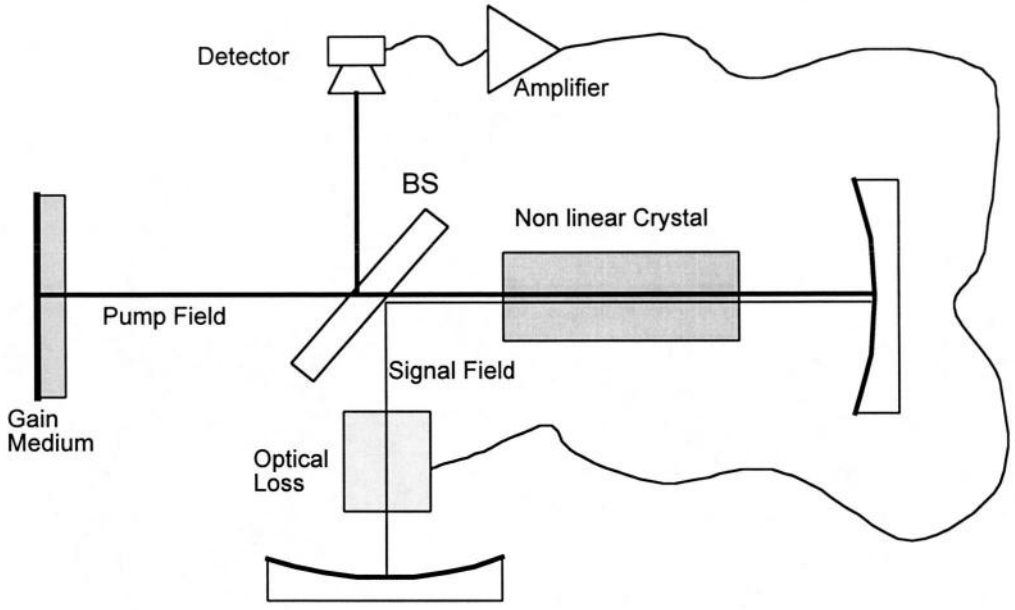

Figure 6.4: *Schematic to show how one might induce loss into the signal cavity as a function of the instantaneous pump field power.*

As the voltage across the loss inducing medium is increased, and hence the round trip loss in the signal cavity, the photon lifetime in this cavity will be reduced. The photon lifetime within a Fabry-Perot optical cavity may be expressed as

$$\tau = \frac{2 \cdot l}{c \cdot \beta} \tag{6.8}$$

And so

$$\frac{1}{\tau} = \frac{c \cdot \beta}{2 \cdot l} \tag{6.9}$$

where β is the fractional round trip loss of the cavity, l the cavity length and c the speed of light. Modulating the loss of the signal cavity therefore corresponds to a modulation of its photon lifetime. Separating the inherent optical loss present within the cavity with that introduced by the loss-modulating mechanism, we have

$$\frac{1}{\tau} = \frac{c}{2 \cdot l} \beta \left[1 + \delta S (P_p - 1) \right] \tag{6.10}$$

Where P_p is the instantaneous pump field power and δS represents the amount of feedback present in the system, analogous to the gain of the amplifier shown in figure 6.3. The factor (P_p-1) represents the fractional change in loss per unit change in normalised pump mean power. It is worthy of note that when the pump power P_p falls to a value less than one, the loss term $\delta S(P_p\text{-}1)$ becomes positive, i.e. has *negative* loss, or gain. This would of course not happen in the laboratory, but is still physically valid as the loss inducing mechanism could be biased for P_p=1, about which the loss could vary.

The rate equation governing the signal field, with the inclusion of this modification, becomes

$$\dot{P}_s = \frac{P_s}{\tau_s}\left(P_p - 1 - \delta S(P_p - 1)\right) \tag{6.11}$$

We now run the numerical model to obtain a solution for different values of δS, the results of which are discussed below.

We find that this feedback mechanism has a large impact upon the damping time of the system; unfortunately not the effect desired. The top trace of figure 6.5 shows that for a value of δS=0.8, the oscillations have shown very little evidence of damping even after 10 upper state lifetimes have passed. The lower trace reveals that the frequency of the oscillations is decreased by this feedback mechanism (c.f. the lower trace of figure 6.3)

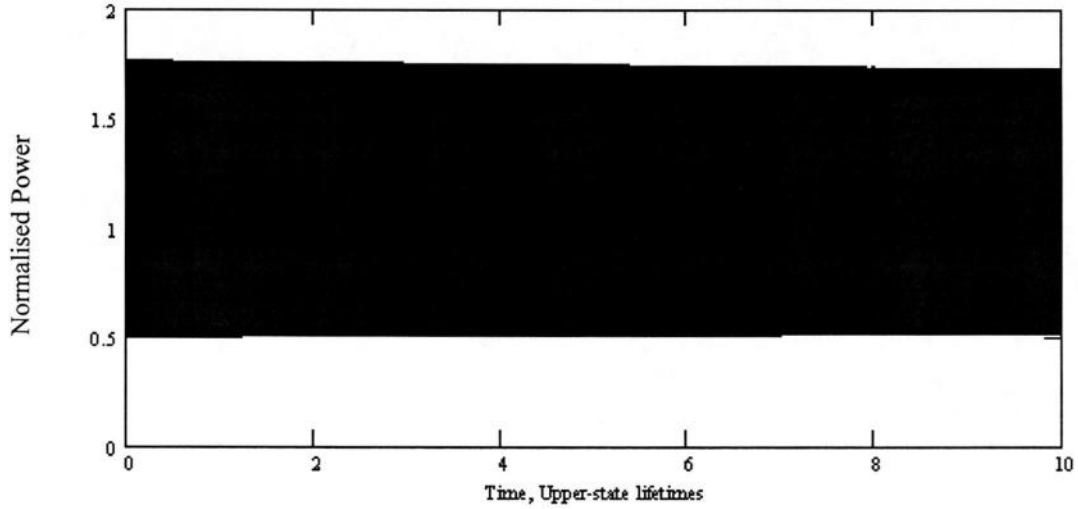

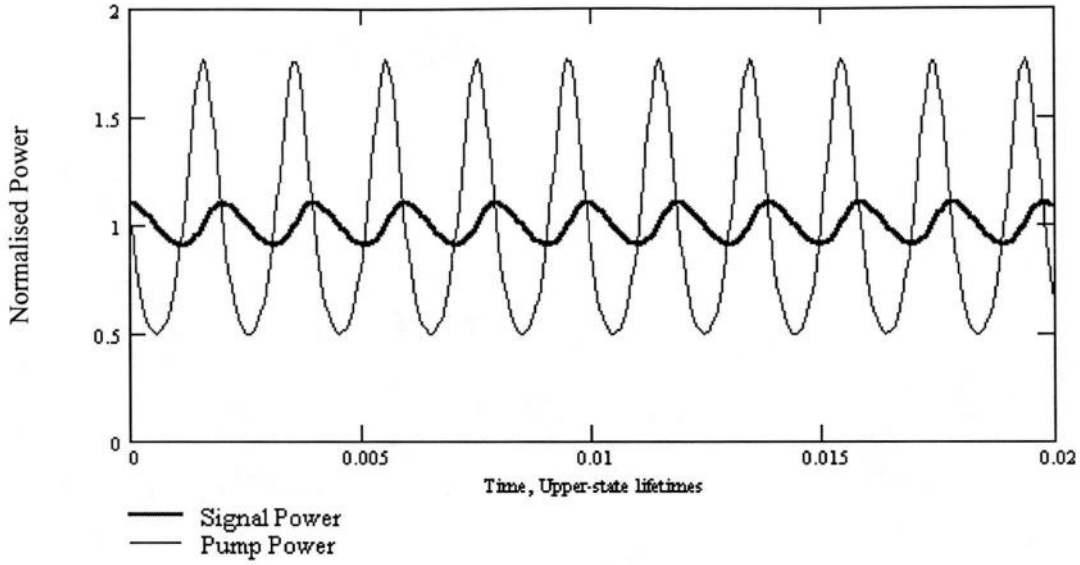

Figure 6.5: *The effect of pump feedback on signal cavity loss. Here, δS=0.8.*

We conclude that this feedback mechanism as it stands is unsuitable for the active suppression of relaxation oscillations. We note from the lower part of figure 6.5 that the pump field lags behind the signal field by $\pi/2$ radians, and therefore the gradient of the signal field is negative as the pump field power is positive. The rate equation governing the signal field power was modified to simulate an inverting buffer placed in between the amplifier and loss-inducing mechanism as shown in figure 6.4. This was simply accomplished by changing the sign of the additional term in the initial modification to the expression, which now becomes

$$\dot{P}_s = \frac{P_s}{\tau_s}\left(P_p - 1 + \delta S(P_p - 1)\right) \tag{6.12}$$

This modification indicates that this feedback mechanism would perform better than it did before the polarity of the loss mechanism with respect to pump power was changed, and we can see by comparing figure 6.6 with figure 6.3 that the damping time has been reduced by a factor of ~3

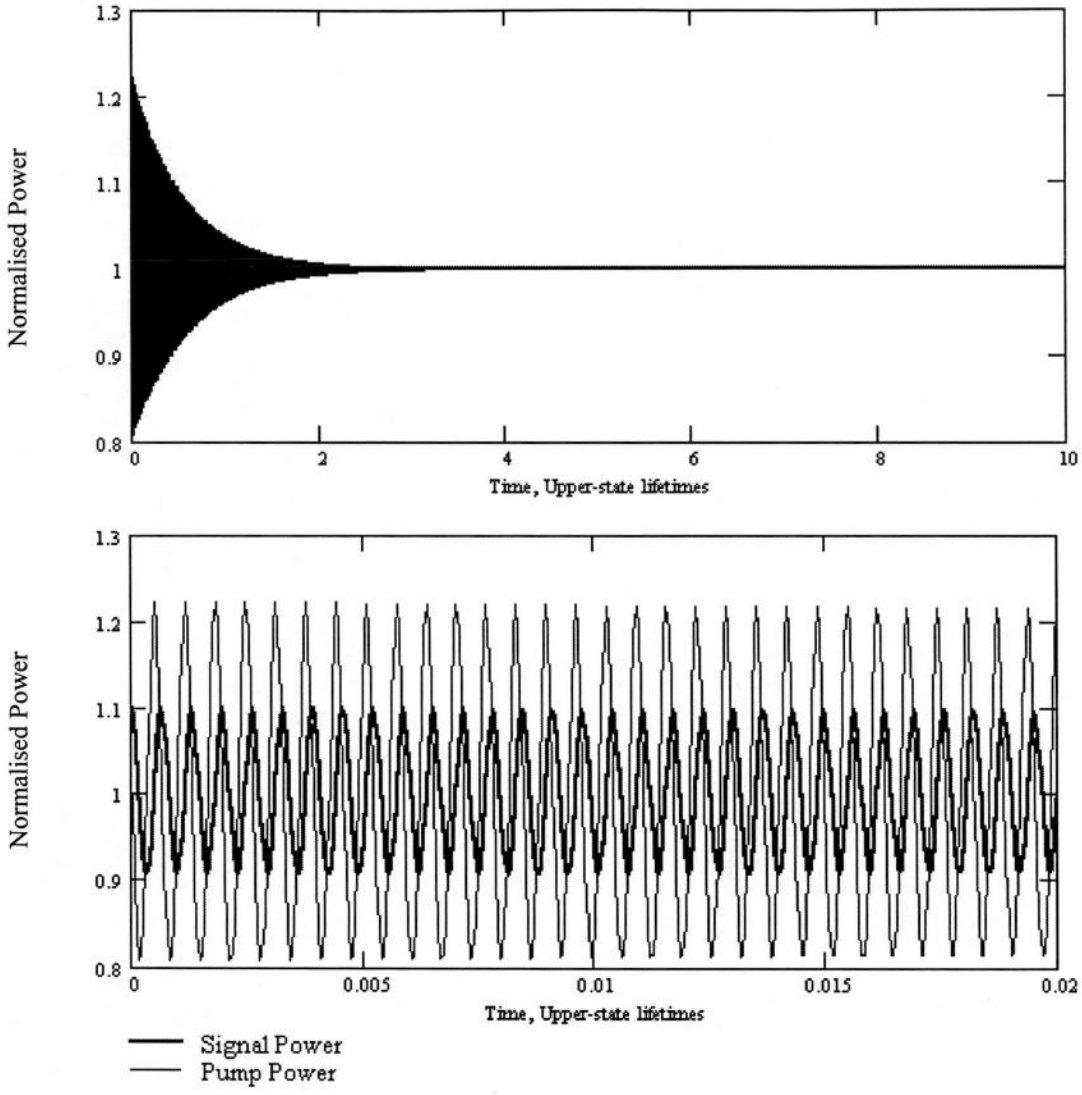

Figure 6.6: *The effects of Option A upon damping time with the loss dependence on pump power inverted, with the feedback parameter δS=0.8.*

This still represents an overall damping time on the order of ~0.5mS, and if interferometric effects or air currents are the cause of perturbation in the cavity then these could easily occur on this time scale. We conclude that although this feedback option, with the appropriate sign, does reduce the damping time of the system it is insufficient to avoid a continual stream of oscillations occurring as the mean time between triggering the oscillations may well still be less than their damping time. Other manipulations of the feedback signal also exist which may improve the performance of this feedback mechanism, such as the addition of some phase inducing mechanism between the amplifier shown in figure 6.4 and the loss inducing mechanism or differentiating the signal so that the loss term becomes $\delta S \cdot dP_p / dt$.

6.3.2. Option B: Signal power feedback onto pump cavity loss

This feedback mechanism is similar to that outlined in the previous section, except now it is the power resident within the signal cavity which is monitored and fed back to the loss inducing mechanism present in the pump cavity. The rate equation governing the pump field if therefore modified to include a loss term which is proportional to the instantaneous power resident in the signal cavity, which becomes

$$\dot{P}_p = \frac{P_p}{\tau_p}\left[\frac{\sigma \cdot N_j}{1+x} - 1 - \frac{(\sigma - 1 - x)\cdot P_s}{1+x} - \delta P(P_s - 1)\right] \tag{6.13}$$

Where δP is analogous to the gain of the amplifier governing the amount of feedback prevalent in the system. Figure 6.7 shows the results of the numerical analysis for a value of δP=0.8.

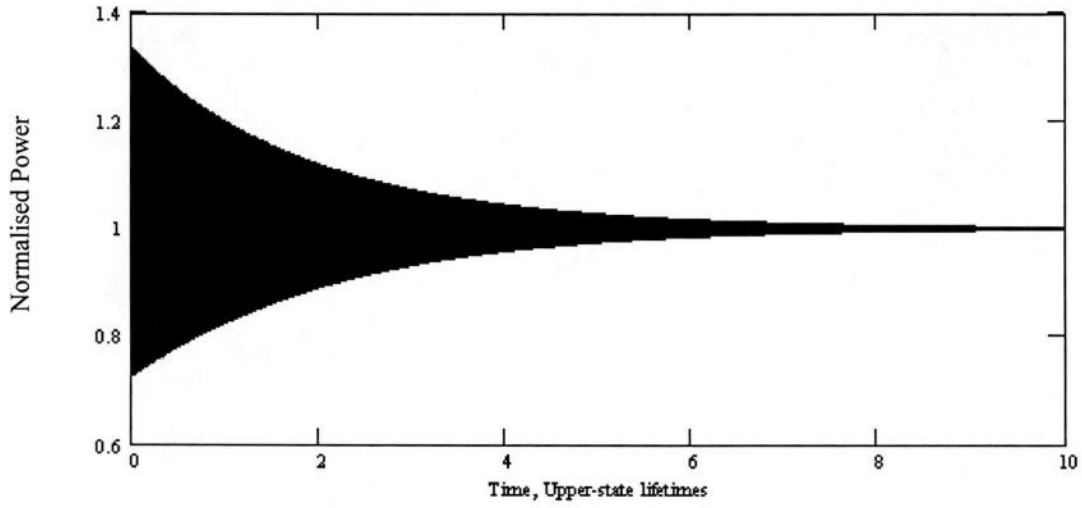

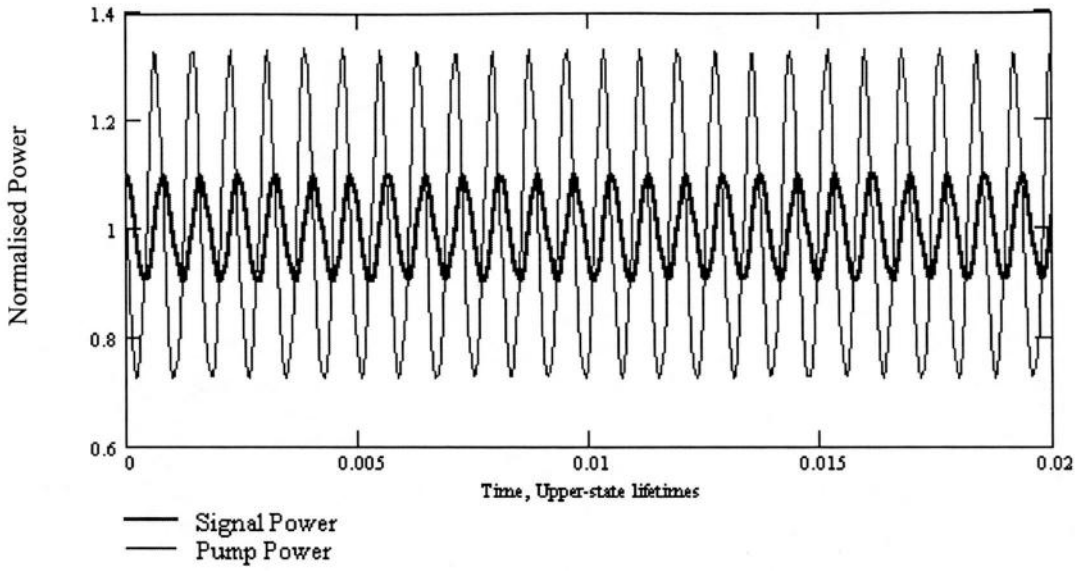

Figure 6.6: *Pump cavity loss dependant upon instantaneous power in signal cavity. Here the value of* $\delta P = 0.8$.

We see that this feedback mechanism has little impact upon the damping time of the relaxation oscillations (c.f. figure 6.3).

6.3.3. Option C: Pump power feedback onto pump cavity loss

We now modify the schematic shown in figure 6.4 so that the loss inducing mechanism resides inside the cavity whose power is being monitored to drive it; in this feedback option we choose to place it in the pump cavity as shown in figure 6.7.

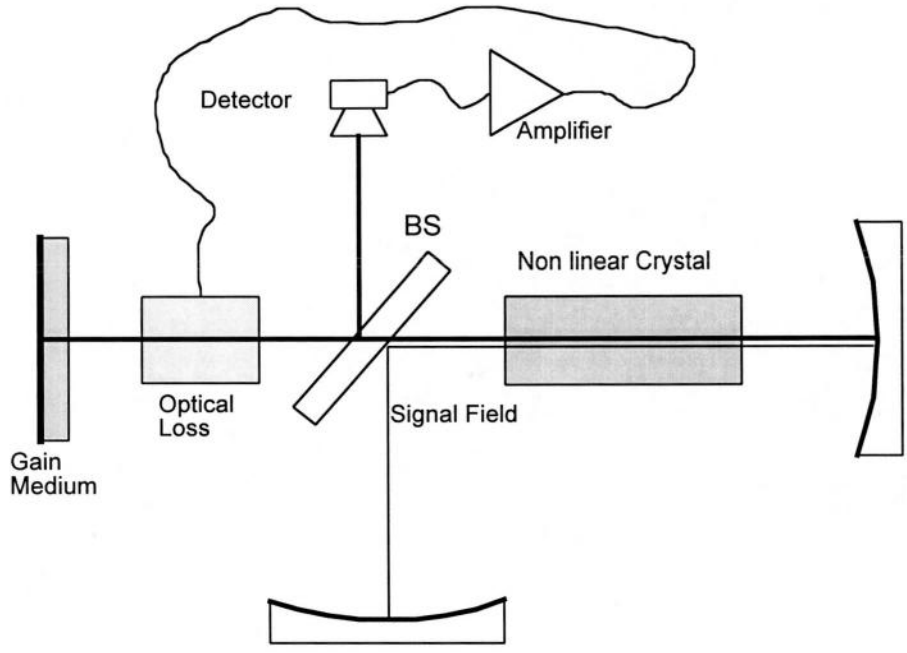

Figure 6.7: *Schematic of Feedback option C; pump cavity loss dependent upon instantaneous pump field power.*

The rate equation is modified to include a loss term that is proportional to the instantaneous power circulating within the pump cavity.

$$\dot{P}_p = \frac{P_p}{\tau_p}\left[\frac{\sigma \cdot N_j}{1+x} - 1 - \frac{(\sigma - 1 - x)\cdot P_s}{1+x} - \delta P\left(P_p - 1\right)\right] \tag{6.14}$$

Once again, the unity term in the term (P_p-1) appears to normalise both the pump and signal field in the steady state. We note that the rate equations are normalised such that the pump and signal fields settle to unity once the system has reached the steady state. By removing this unity term, we can model the impact that the additional loss that resides within the pump cavity on the performance of the system. We will therefore model the rate equation set both in the presence and absence of this term to investigate this effect.

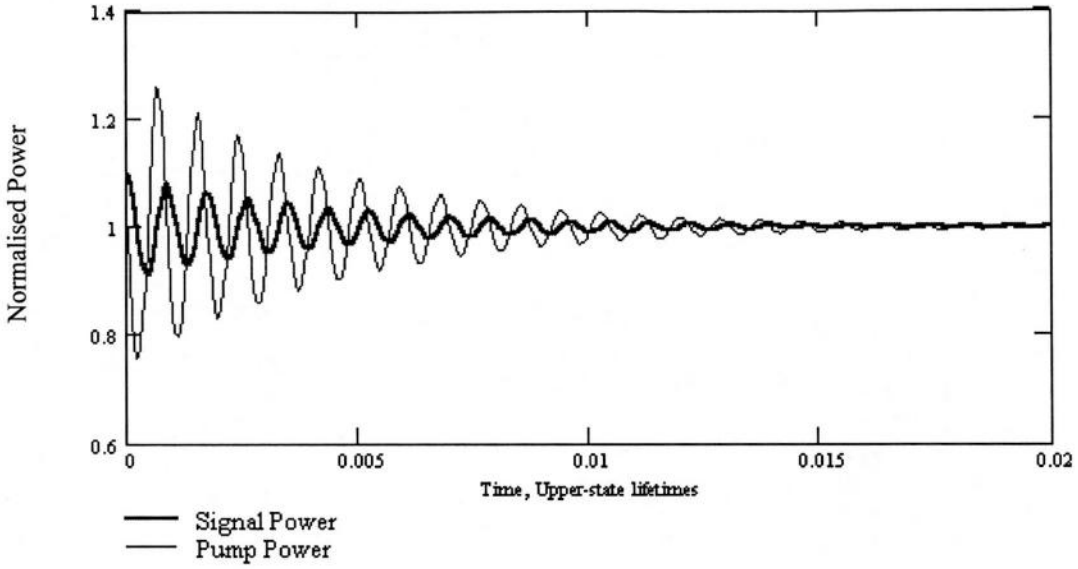

Figure 6.7: *Pump cavity loss dependant upon pump field power. Here, $\delta P=0.1$.*

We can see that this feedback mechanism has an enormous impact upon the transient dynamics of the ICSRO. If we compare this figure 6.7 to the dynamic modelling of the system in the absence of any feedback mechanism (figure 6.3), we see that the inclusion of this feedback technique reduces the damping time by almost three orders of magnitude, from ~12 to ~0.02 upper state lifetimes. Further increases in the feedback parameter δP damp the oscillations even further: figure 6.8 shows the oscillations for δP having the value 0.6.

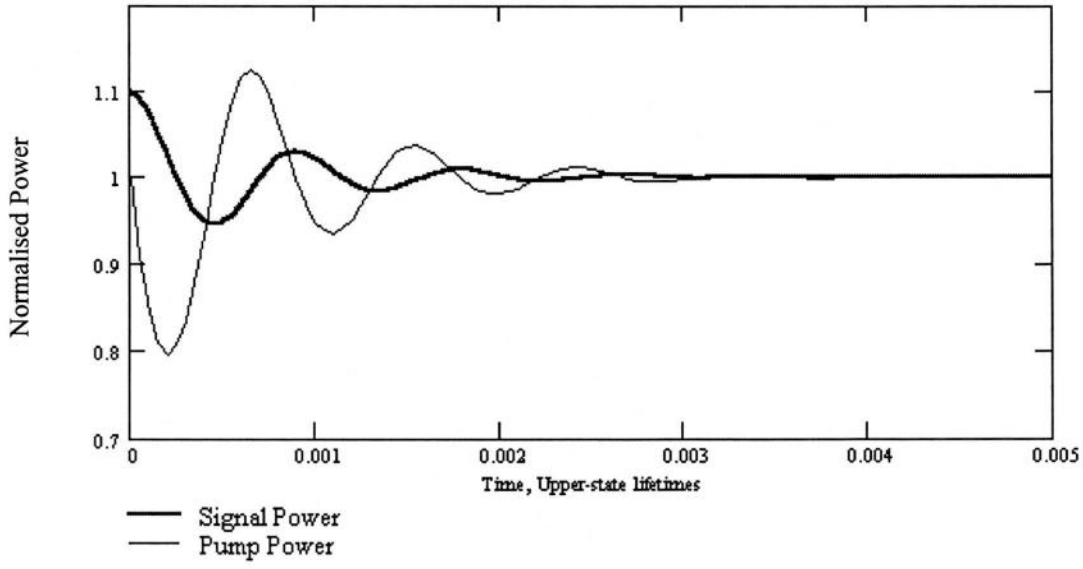

Figure 6.8: *Severely damped oscillations for $\delta P=0.6$.*

The oscillations are now damped in little more than seven cycles. Although further increases in δP lead to critical damping of the oscillations, we cannot go on increasing this parameter indefinitely as it will result in excessive loss within the pump cavity in the steady state. To show this effect, we will remove the nomalising factor in equation (6.14), resulting in the pump power rate equation taking on the following form:

$$\dot{P}_p = \frac{P_p}{\tau_p}\left[\frac{\sigma \cdot N_j}{1+\kappa} - 1 - \frac{(\sigma - 1 - \kappa)\cdot P_s}{1+\kappa} - \delta P \cdot P_p\right] \tag{6.15}$$

Figure 6.9 repeats the results shown in figures 6.7 and 6.8 with this factor removed. We see that as the parameter δP is increased and the damping time is decreased, the steady state power of the signal settles on a value less than unity.

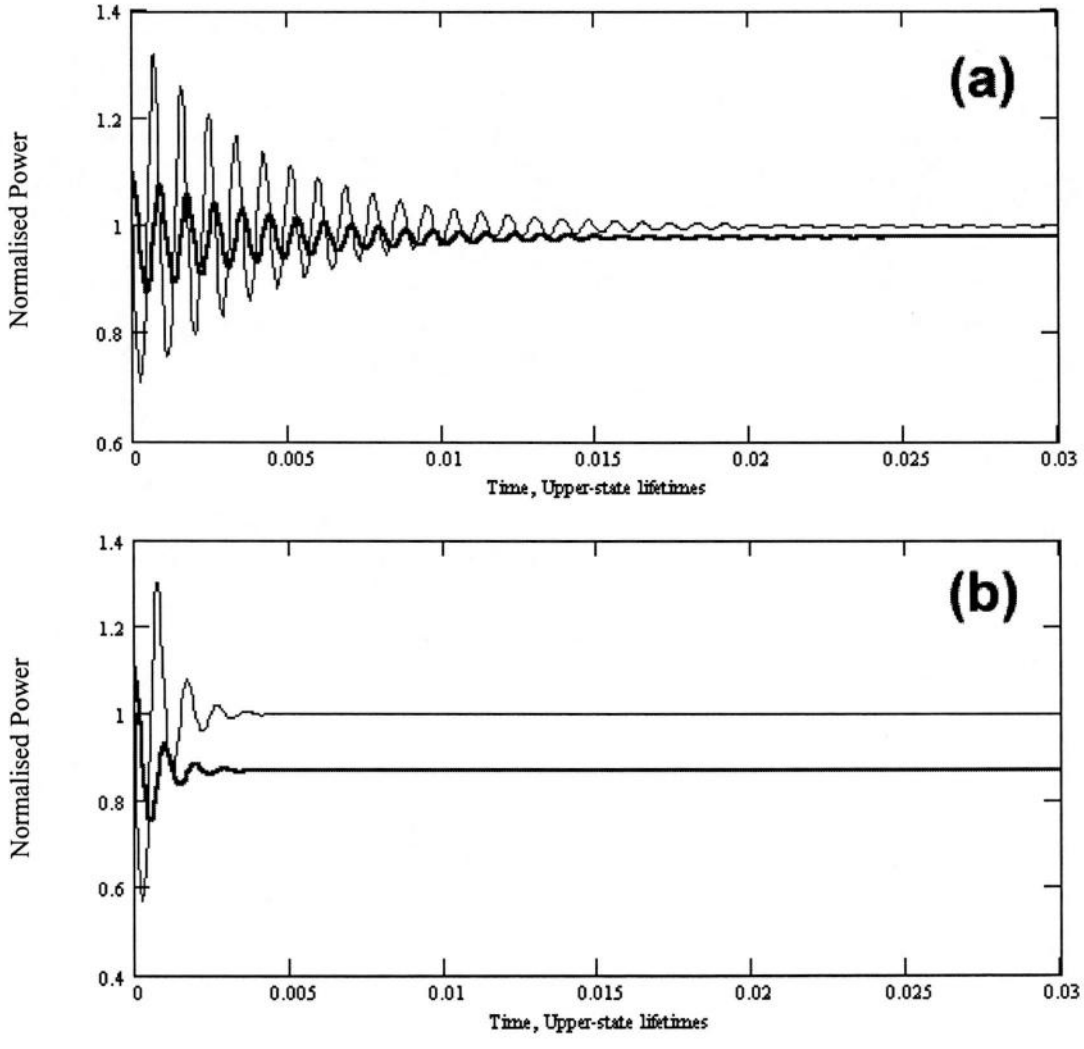

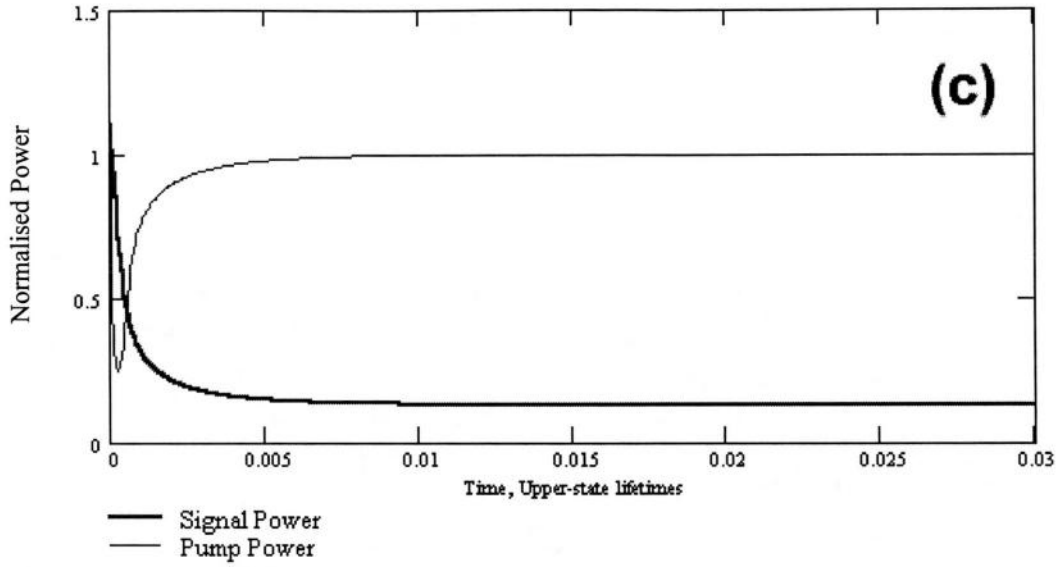

Figure 6.9: *The effect of the feedback parameter δP on signal power. (a) δP=0.1, (b) δP=0.6, (c) δP=4.0.*

We see that for δP=0.1, the impact upon the signal field power is small, reducing it by only ~3% when compared to the system in the absence of feedback techniques and yet has reduced the damping time from ~12 upper state lifetimes (figure 6.3) to ~0.02 upper state lifetimes. As the parameter dP is increased, the damping time (and steady state signal power) are reduced until the point at which the system becomes critically damped when the time for the steady state to occur increases as the system falls back to the steady state without undulation (figure 6.9(c)). It is useful to plot the signal power in the steady state and the damping time if the system as a function of the feedback parameter δP, shown in figure 6.10.

We see that the time taken for the system to return to the steady state reaches a minimum when $\delta P \approx 2$, but at this point the signal power has been reduced by ~40%. This numerical analysis points to a suitable value of dP at ~0.3, at which point the damping time has been reduced by a factor of ~1200 from ~12 to ~0.01 upper state lifetimes with only a 10% drop in signal power.

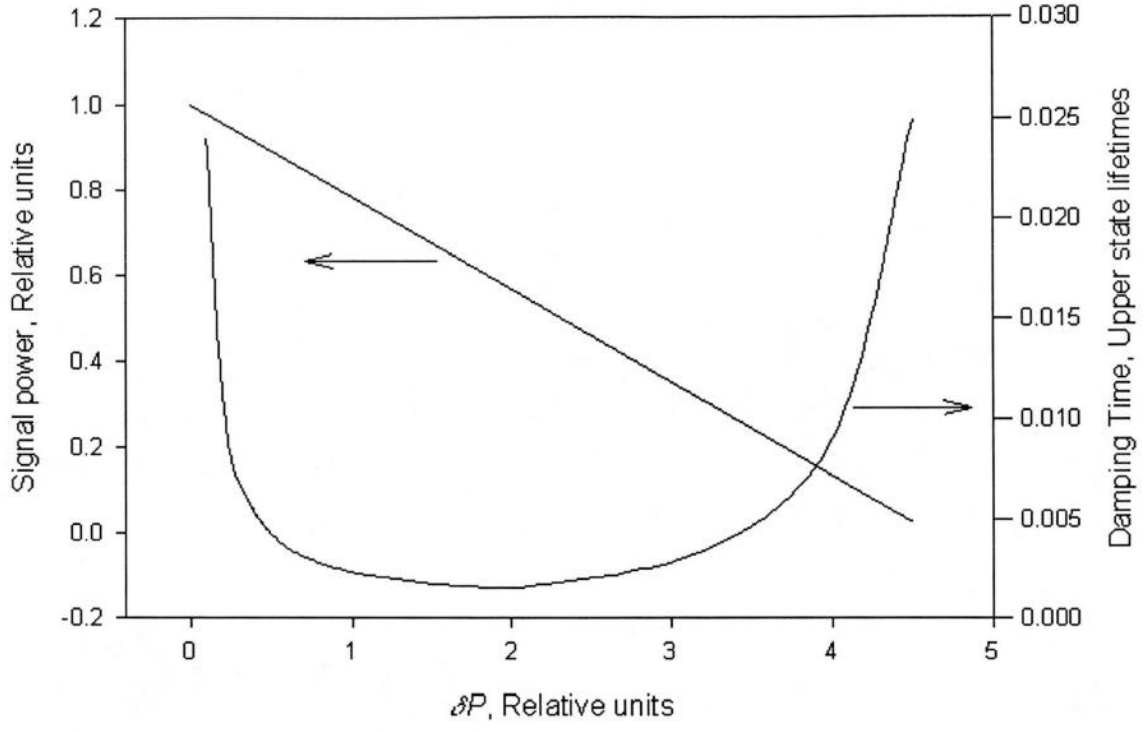

Figure 6.10: *Impact of feedback parameter δP upon damping time and steady state signal power.*

We conclude that this feedback option represents an excellent method for the suppression of relaxations oscillations present in this system. Option F, which shall be considered shortly, offers a feedback mechanism which is equivalent to that described here with the exception that it is completely passive.

6.3.4 Option D: Signal power feedback onto signal cavity loss

This feedback mechanism is very similar to that outlined in the previous section, except now it is the loss of the signal cavity which is modulated as a function of the power which resides within that cavity. As before, the rate equation governing the signal cavity is modified to model the additional loss term. We omit the normalising unity factor to gauge the impact upon the steady state power

$$\dot{P}_s = \frac{P_s}{\tau_s}\left(P_p - 1 - \delta S \cdot P_s\right) \tag{6.16}$$

By running the model, we see that this feedback scheme also dampens down the relaxation oscillations extremely quickly when compared to the undamped case (figure 6.11).

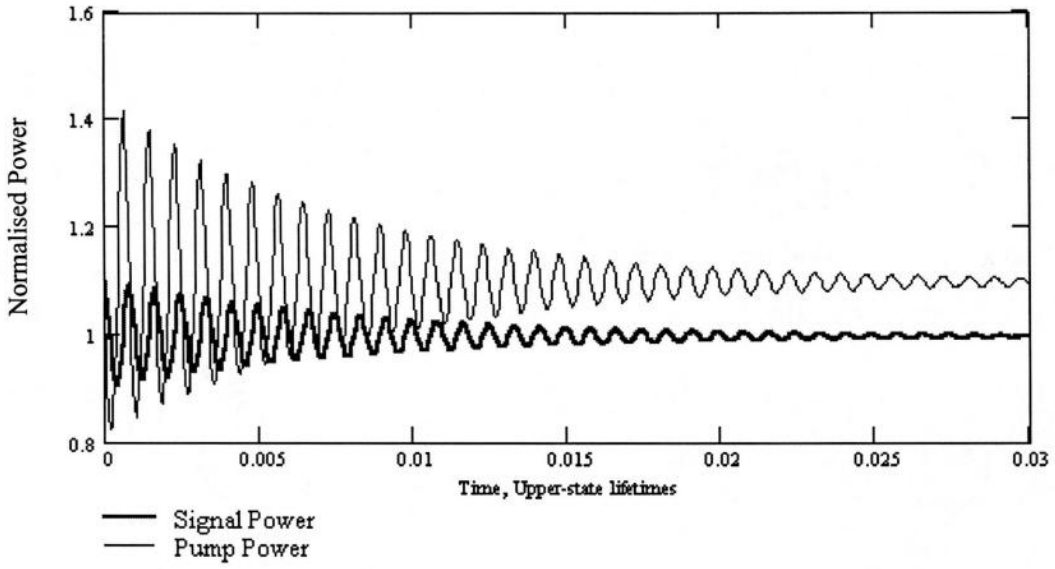

Figure 6.11: *Relaxation oscillation damping with signal cavity loss as a function of signal power. Here, δS=0.1.*

Note that the normalisation treatment makes the signal power tend to unity in the steady state, so that as loss is introduced into the signal cavity then the steady state power in the pump cavity must settle upon a value greater than one in order to compensate for the signal cavity loss and produce the same signal power.

Although the oscillations damp down very quickly, the system does in fact take many upper state lifetimes to settle upon its steady state, as shown in figure 6.12. We see that for δS=0.1, the signal and pump fields do not settle until ~2 upper state lifetimes have passed. This is due to the slow return of the upper state population to the steady state.

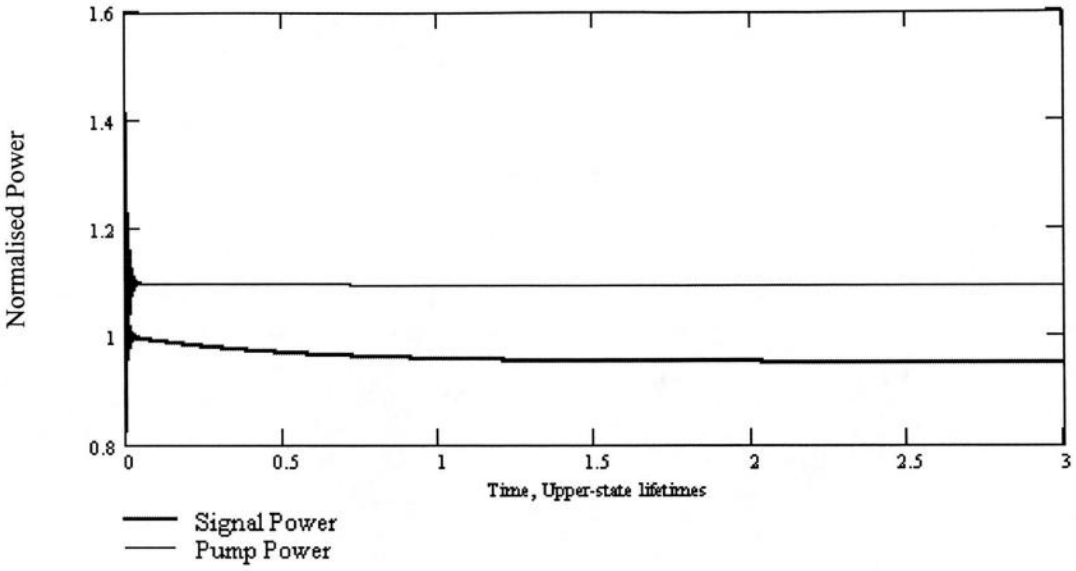

Figure 6.12: *Long term dynamics for option D feedback scheme. δS=0.1.*

For larger values of δS, this effect is more pronounced (figure 6.13). Although this feedback mechanism is successful in damping down the transient dynamics of the ICSRO, it does not return the system back to the steady state as quickly as feedback option C, and also loss within the signal cavity must be kept to a minimum in order to keep OPO threshold to an acceptable level.

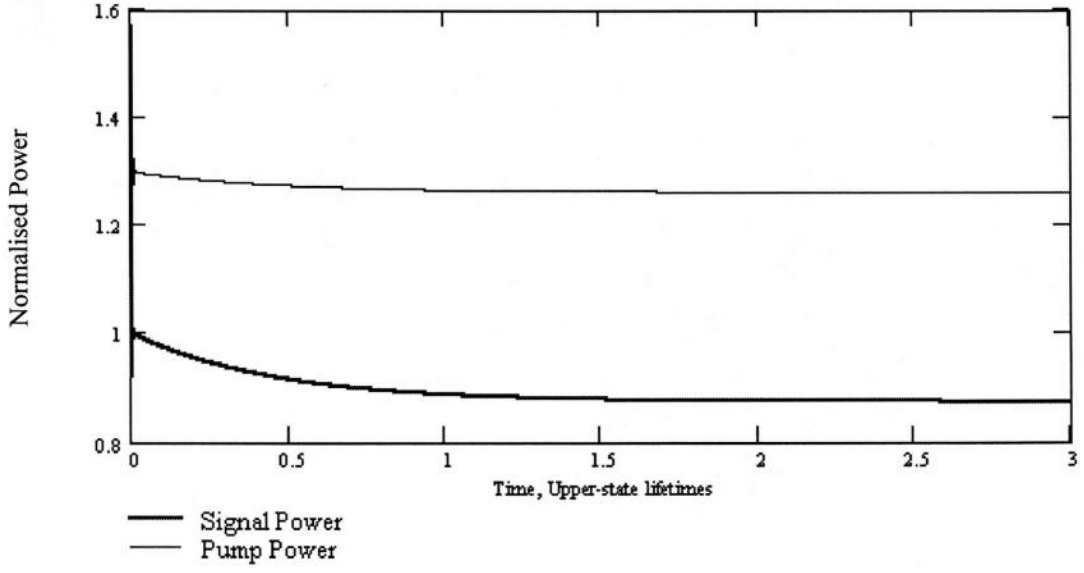

Figure 6.13: *Increased impact of δS on time taken to settle on steady state. Here, δS=0.3.*

In the case of option C, where the extra loss resides in the pump cavity, it is a simple matter of increasing the external (diode) pump power to the system in order to

compensate and achieve comparable output powers to that of the undamped system. This would also compensate for the increase in OPO threshold caused by the insertion of additional loss within the signal cavity, of course, but one must then take into account the increased thermal lensing effects within the nonlinear medium. We conclude, then, that although this damping mechanism does have a significant impact upon the transient dynamics of the system, option C would be a preferable choice in the laboratory as it is of the same complexity yet has fewer side effects on the performance of the system.

6.3.5 Option E: Pump power feedback onto External pump power

We now turn our attention to a significantly different mechanism for the damping of the ICSRO transient dynamics. Instead of modulating the loss of either the signal or pump cavities, the external diode pump power incident upon the laser gain media will be modulated as a function of the power circulating within the pump cavity (figure 6.14).

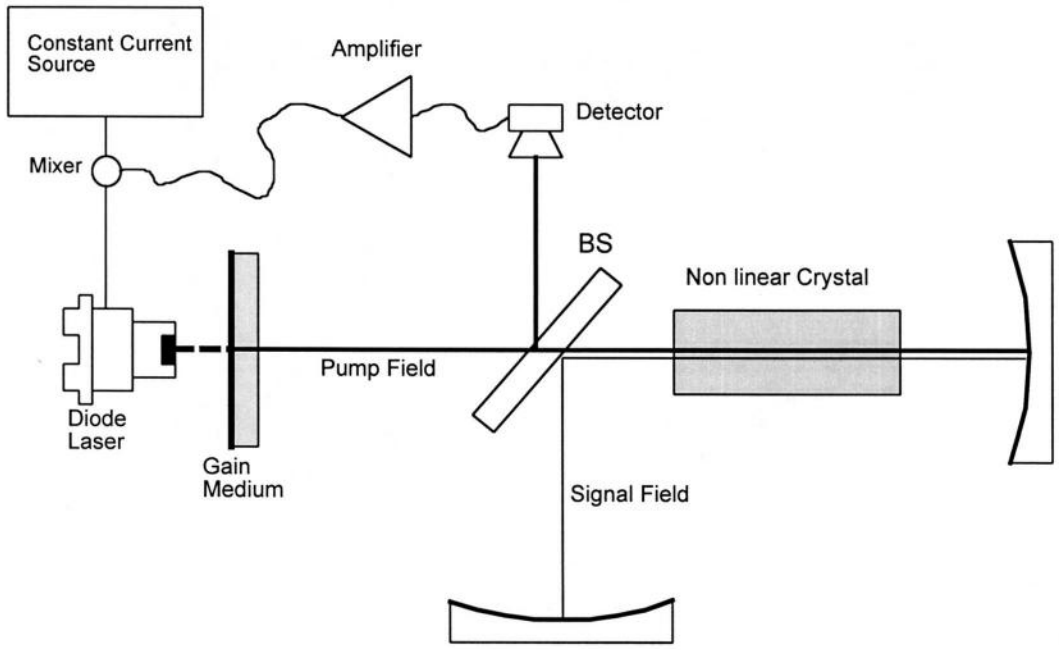

Figure 6.15: *Schematic setup of external diode pump power modulated by circulating field in pump cavity.*

The laser diode is forward biased in the conventional way by the constant current source, but some amplitude modulation is added to this dc bias by the mixer in order facilitate modulation of the diode laser pump power.

The advantages of this feedback scheme are two fold: as the feedback mechanism is essentially electronic (drive current onto the anode of the laser diode), we need put no loss inducing mechanism into either the pump or signal cavities. This makes such a feedback option far simpler to implement than those discussed so far, and will also mean that power performance in the steady state will not be adversely affected by the increased loss within an optical cavity [7,8].

The rate equation for the upper-state population under this feedback mechanism becomes

$$\dot{N}_j = \frac{1+\kappa - N_j - \left(N_j \cdot P_p \cdot x\right) - \delta P \cdot \left(P_p - 1\right)}{\tau_u} \tag{6.17}$$

Where δP is analogous to the gain of the amplifier feeding the electronic mixer. The parameters κ and x are derived in appendix A of this thesis. The factor (P_p-1) is constructed such that the loss term vanishes in the steady state and so the feedback mechanism has no impact upon the system.

We model the relaxation oscillations in the presence of this effect, but find that it has little impact upon the damping time (Figure 6.16). Here, δP=1 and the figure is plotted over 10 upper state lifetimes.

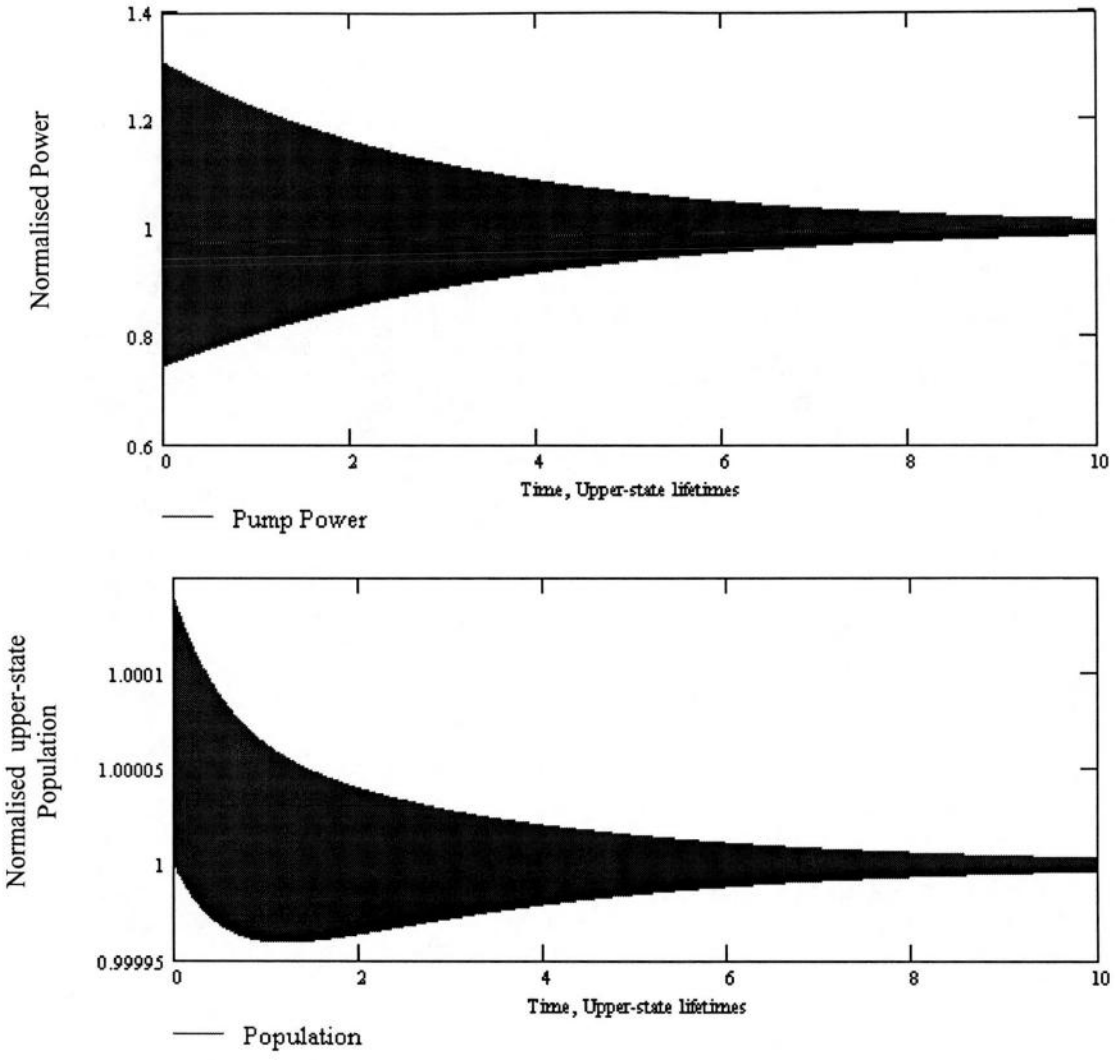

Figure 6.16: *Circulating pump power and upper state population in the presence of feedback option E. $\delta P = 1$.*

We see that oscillations within the pump cavity have very little impact upon the upper state population N_j. This is due to the very long upper state lifetime (~200μS) with respect to the photon lifetime of the pump cavity (~45nS). One can see that even if the external pump power were completely removed, the circulating pump field would be relatively unaffected on the time scale of this photon lifetime. In effect, the gain medium is analogous to an optical capacitor, which 'smooths out' the photons incident upon it on the time scale of the photon lifetime in the pump cavity. To illustrate this, we will look again at the analysis used to generate figure 6.7, which employed circulating pump power feedback onto pump cavity loss. We replicate the figure here with the upper state population behaviour.

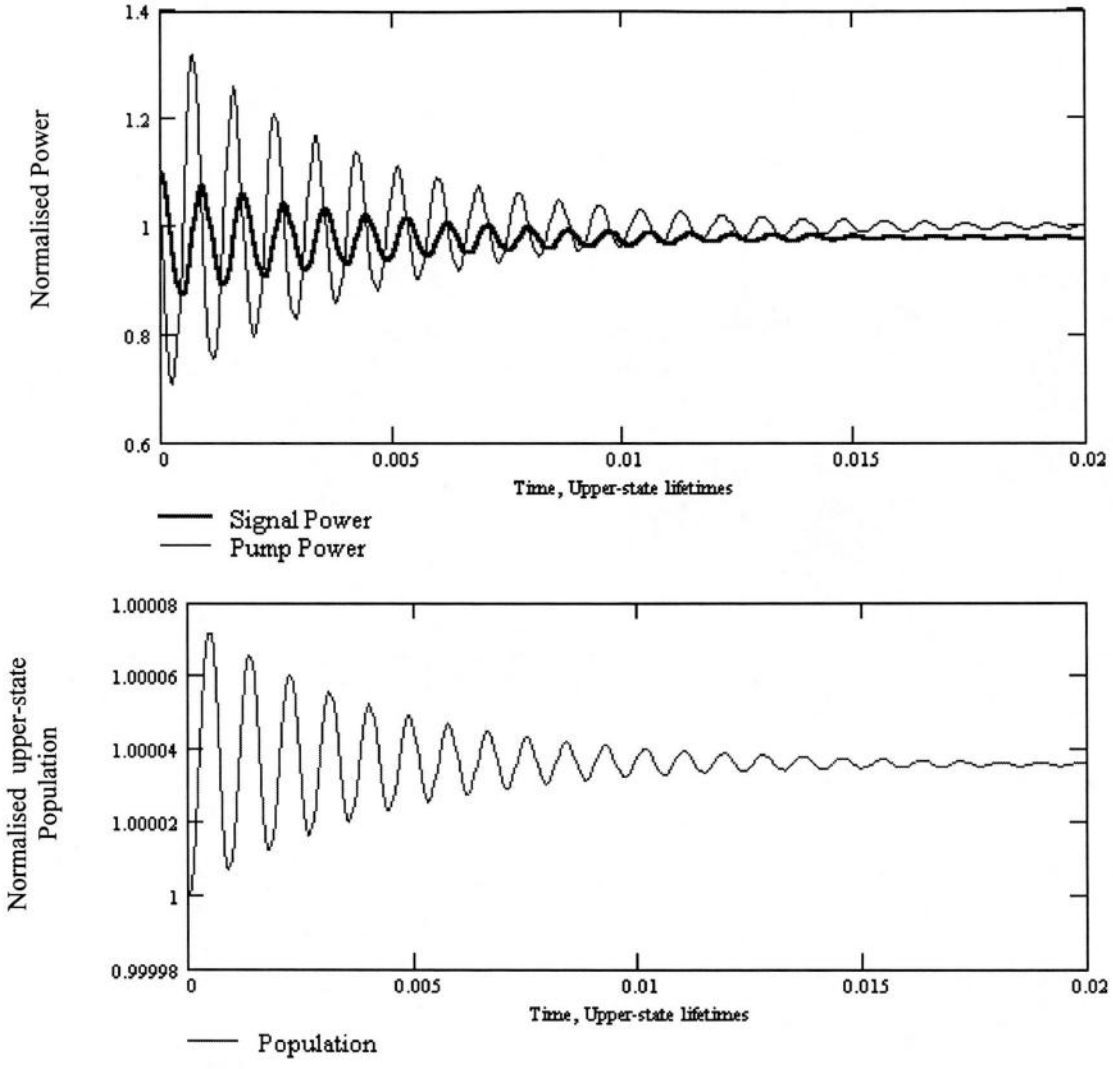

Figure 6.17: *Upper state population behaviour in the presence of feedback option C.*

We see that the upper state population is only perturbed on the order of one part in 10^5. Indeed, by modifying the rate equation governing the upper population to be $\dot{N}j = 0$ and setting N_j=1 for all t, the numerical analysis shown almost no impact upon the short term dynamics of the ICSRO. In the absence of any feedback mechanism, the upper state population is the damping mechanism of the ICSRO. If we set N_j to unity and run the model in the absence of any feedback mechanism, we find that the system remains unstable with energy constantly oscillating between the two optical cavities. Although negative feedback of the circulating pump field power noise onto the diode pump power has been seen to significantly reduce intensity noise and even dampen relaxation oscillations in simple diode-pumped solid state lasers [7,8], this scheme has little impact

on the ICSRO because of the optical capacitor effect of the long upper state lifetime in conjunction with power flow between the pump and signal cavities.

In conclusion, although this feedback mechanism would be simple to implement and would have no impact upon the steady state power performance of the ICSRO, the very long upper state lifetime of the gain medium with respect to the pump cavity photon lifetime prohibits the effectiveness of this feedback mechanism in the suppression of relaxation oscillations.

6.3.6 Option F: Nonlinear loss within the pump cavity

We conclude this analysis with considering the effect of a nonlinear loss placed within the pump cavity, as shown in figure 6.18. The loss inducing mechanism takes the form of a second harmonic crystal placed within the pump cavity.

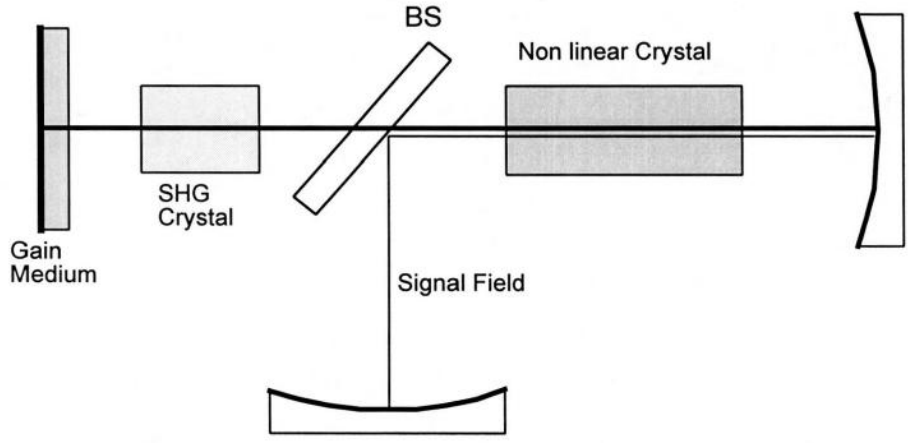

Figure 6.18: *Suppression of relaxation oscillations by the inclusion of an SHG crystal in the pump cavity.*

The up conversion of the second harmonic crystal is proportional to the square of the fundamental power impinging upon it. By placing an SHG crystal in the pump cavity in this way, we therefore introduce a loss mechanism which scales with the square of the pump field. This is similar to feedback option C, except this system has the extremely favourable characteristic of being completely passive – there is no need to monitor the power in the pump cavity, implement any electronics or concern oneself with the response time of such electronic systems. The up conversion process in the SHG crystal is essentially instantaneous.

The pump field rate equation is modified to accommodate this nonlinear loss

$$\dot{P}_p = \frac{P_p}{\tau_p}\left[\frac{\sigma \cdot N_j}{1+x} - 1 - \frac{(\sigma - 1 - x)\cdot P_s}{1+x} - \delta P_p \cdot P_p\right] \tag{6.18}$$

We see that the loss term becomes a quadratic function of P_p once the multiplying factor P_p/τ_p which resides outside the square brackets has been taken into account.

The δP term corresponds to the magnitude of the up conversion effect. Being a passive system, the magnitude of the loss inducing mechanism can no longer be controlled by adjusting the gain of any electronic feedback amplifier. This parameter can still be adjusted by controlling the conversion efficiency in the SHG crystal. If a birefringent crystal were implemented, δP could be varied by altering the focussing in the crystal. With a QPM crystal, the temperature could be varied to move the phase matching point and therefore adjust the conversion efficiency and hence δP. It may be preferable to implement a type I or QPM phase matching scheme rather than using a type II phase matched SHG crystal as the latter may interfere with the polarisation of the circulating field.

We run the model with encouraging results, as shown in figure 6.19. We see for δP=0.1, the oscillations are damped to the steady state in only ~0.01 upper state lifetimes.

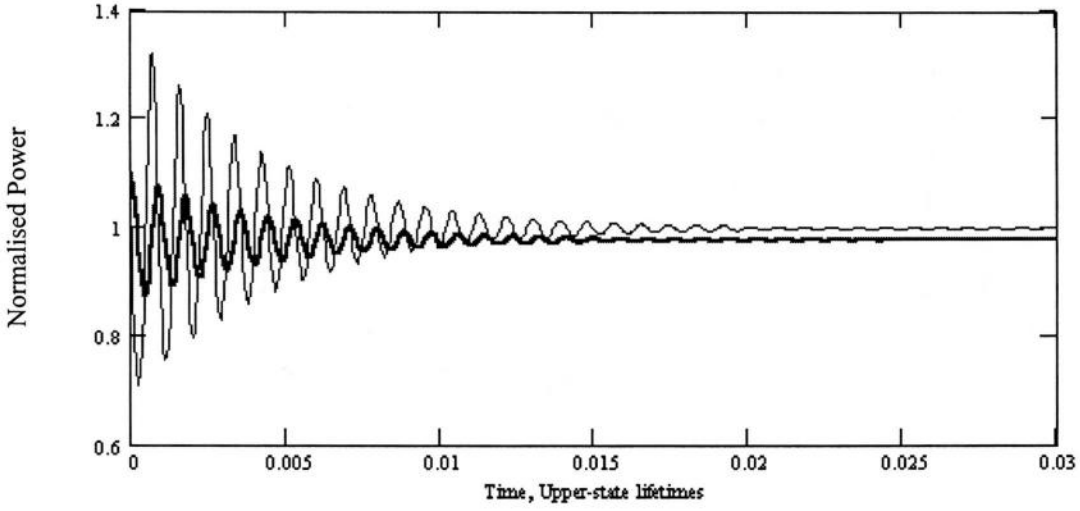

Figure 6.19: *Damped oscillations in the presence of feedback option E. δP=0.1.*

We see that the damping time of the oscillations is identical to that of feedback option C (figure 6.9(a)) .It is clear that there is very little drop (~4%) in the circulating signal field power, making this feedback option extremely attractive, in terms of damping time, tolerable loss in signal circulating field and the simplicity of implementing this scheme experimentally.

6.4 Conclusions

We conclude this chapter by reviewing the results obtained by this analysis. Six feedback options were considered as a mechanism for dampening the relaxation oscillations prevalent in ICSRO systems which utilise laser gain media with a long upper state lifetime.

We found that options A and B, where the loss of one optical cavity was modulated as a function of the power circulating in the other, were ineffective in suppressing oscillations due to the phase difference between the amplitude oscillations in these cavities.

Option C, where the loss of the pump cavity was modulated as a function of the power circulating within that cavity, proved to be extremely successful in suppressing the oscillations with very little penalty in reduced signal power. By introducing a steady state loss which would cause a ~10% drop in the circulating signal field power, the damping time of the oscillations were reduced from ~12 to ~0.01 upper state lifetimes. This scheme would not be difficult to implement in practice; adjusting the magnitude of the feedback effect would simply be a case of changing the electronic gain of the photodiode/high voltage amplifier driving the intracavity loss inducing mechanism. Increasing the external diode pump power to the laser gain medium would compensate for the extra loss included within the pump cavity.

We found that although option D, in which the signal cavity loss was modulated as a function of the power circulating within it, was also effective in suppressing the oscillations, the system took many upper state lifetimes to completely settle back to the steady state, and the extra loss located within the signal cavity may cause intolerable OPO thresholds. Compensating for this extra loss is more complicated than that for option C.

Although option E, where the external diode pump power incident upon the laser gain medium is modulated as a function of circulating pump field power, would be very simple to implement, the very long upper state lifetime of the gain medium acts as an 'optical capacitor' and therefore makes this mechanism ineffective.

Placing a SHG crystal into the pump cavity and thereby modulating the loss of this cavity completely passively damped the relaxation oscillations of the ICSRO extremely quickly. The model predicts that introducing enough up conversion loss into the pump cavity to reduce the signal power by only 4% in the steady state causes the relaxation oscillations to be damped in only ~0.02 upper state lifetimes. Being the simplest mechanism to implement experimentally due to the passive nature of this scheme, this feedback option offers the best performance in terms of experimental simplicity and damping time reduction and impact on power reduction due to enhanced intracavity loss. This again could be compensated for by increasing the external diode pump power. Adjusting the magnitude of the feedback effect is a simple matter of controlling the up conversion efficiency by moving the SHG crystal through a pump field waist or changing the phase matching by temperature tuning in the case of QPM materials.

We conclude that this latter feedback mechanism offers the best solution to the problem of the relaxation oscillations which are characteristic in the ICSRO systems outlined in this thesis.

References

1 G. A. Turnbull, D. J. M. Stothard, M. Ebrahimzadeh and M. H. Dunn, "Transient Dynamics of CW Intracavity Singly Resonant Optical Parametric Oscillators," *IEEE Journal of Quantum Electronics* **35**, 1666-1672 (1999).

2 G. A. Turnbull, *Continuous-wave intracavity optical parametric oscillators*, PhD thesis, St Andrews University (1999).

3 G. A. Turnbull, M. H. Dunn and M. Ebrahimzadeh, "Continuous-wave, intracavity optical parametric oscillators: an analysis of power characteristics," *Applied Physics B-Lasers and Optics* **66**, 701 (1998).

4 T. J. Edwards, *Continuous wave, singly-resonant optical parametric oscillation internal to the Ti: sapphire laser*, thesis, St. Andrews University (2000).

5 T. Debuisschert, J. Raffy, J. P. Pocholle and M. Papuchon, "Intracavity optical parametric oscillator: Study of the dynamics in pulsed regime," *Journal of the Optical Society of America B-Optical Physics* **13**, 1569-1587 (1996).

6 T. Baer, "Large amplitude fluctuations due to longitudinal mode-coupling in diode-pumped intracavity doubled Nd:YAG lasers.," *Journal of the Optical Society of America B-Optical Physics* **3**, 1175 (1986).

7 J. Zhang, Y. Cheng, T. Zhang, K. Zhang, C. Xie, and K. Peng, "Investigation of the characteristics of the intensity noise of singly resonant active second-harmonic generation," *Journal of the Optical Society of America B* **17**, 1695 (2000)

8 S. Rowann, A. M. Campbell, K. Skeldon and J. Hough, "Broadband intensity stabilisation of a diode-pumped monolithic miniature Nd:YAG ring laser," *Journal of Modern Optics* **41**, 1263 (1994).

7: Conclusions

7.1 Introduction

We now draw this thesis to a close by reviewing the results obtained and conclusions drawn over the course of this research program, and the implications these may have upon possible future avenues of investigation.

7.2 Summary of experimental results and conclusions

In the introductory chapter we classified two separate operational configurations for the OPO, namely the singly- and doubly-resonant OPO. We stated that whilst the DRO had a very low threshold, it was generally over constrained in terms of cavity length and pump frequency stability to be a practical mid infrared source of tunable radiation [1, 2]. The SRO, on the other hand, had no such constraint on cavity length and pump laser frequency but had a prohibitively high operational threshold [3]. We therefore concluded that one possible mechanism to implement the SRO in order to take advantage of its robust operating characteristics, whilst overcoming its high threshold requirements, was to make use of the very high circulating field available inside the cavity of the pump laser, thereby allowing OPO threshold to be reached for only modest external pump powers [4]. We also discussed the concept of quasi phase matching [5] as a means of arbitrarily choosing the phase matching condition of the OPO whilst still taking advantage of the highest nonlinearity in the material. This theme was expanded in the theoretical analysis which was undertaken in the chapter 2, which showed that whilst the tolerance of the error in the poling parameters was small, this did not present any difficulty in implementing such a QPM material given current poling technology [5, 6]. We also saw that the phase matching conditions of the QPM material could be varied with the pump frequency, the grating period or the crystal temperature, these latter two characteristics pointing to a mechanism by which the OPO output could be tuned even if a fixed frequency laser were employed. An analysis of the power characteristics of the ICSRO showed that, unlike the ICDRO, once above threshold the device was stable for all pump powers [7, 8].

In chapter 3, we went on to discuss the many favourable characteristics exhibited by diode pumped solid state lasers, and the diode pumping of the Nd^{3+} species in particular. We saw how the continual development of laser diodes had led from the early simple p-n junction devices, which exhibited extremely high current density thresholds and could only be operated in the pulsed regime due to ohmic heating, to modern-day complex heterostructure devices capable of delivering many watts of cw power from a single stripe, with electrical to optical efficiencies approaching ~40%. Multi-stripe devices are capable of delivering >10's of watts of power and, if fibre coupled, can do so in a circularly symmetric beam, ideal for pumping solid state laser gain media. The discussion then focussed on neodymium-doped yttrium orthovanadate (Nd:YVO_4) as a laser gain medium particularly suitable for diode pumped applications. Neglected as a laser gain medium for many years due to its inability to be grown in large bulk crystals without defects, Nd:YVO_4 has come to the forefront of solid state laser technology due to being particularly well suited to diode pumping. The characteristics it exhibits that make it such are a wide and very strong absorption feature at 808.5nm leading to very short absorption depths (depending upon doping concentration), a very large stimulated emission cross section and a naturally polarised output due to the birefringent nature of the crystal, obviating the need for intracavity brewster plates. These properties have been capitalised upon only in the context of diode pumped schemes, and have led to devices exhibiting >50% electrical-to-optical slope efficiencies [9].

Chapter 4 described the design and characterisation of an ICSRO based upon a 50mm PPLN crystal with grating periods Λ=28.5 - 29.9μm, operating internal to an all solid state, 1W diode pumped Nd:YVO_4 laser [4]. The use of a graded index lens to couple the output of the laser diode into the Nd:YVO_4 crystal enabled an extremely simple and inexpensive pump head design. The inclusion of an AR-coated lens situated in the pump cavity formed an appropriate beam waist in the PPLN crystal which both reduced the OPO threshold to an appropriate level, and crucially desensitised the pump cavity from thermal lensing effects which occurred in the PPLN crystal as the power in the circulating pump field was increased. At 1W of pump power, the thermal lens in the Nd:YVO_4 crystal was negligible. The operation thresholds for the laser and OPO were only 63 and 310mW, respectively, more than an order of magnitude lower than that achieved in an externally pumped SRO with similar design parameters [10]. The one way intracavity

power at which the SRO reached threshold was 3.3W, compared to the calculated value of 2.6W. Up to 70mW of two-way idler was extracted from the device at 1W of diode pump power. This corresponds to ~295mW of total down converted power and therefore >68% down conversion efficiency. 100% down conversion efficiency should occur at a diode pump power of ~1.5W assuming this enhanced pump power did not introduce thermal lensing effects into the Nd:YVO_4 crystal or exacerbate those already present in the PPLN crystal. The circulating field exhibited clamping behaviour once the OPO was above threshold. The long term stability of the idler output was ±8% peak-to-peak over a measurement period of 3 hours, and no evidence of thermal latching was experienced in the event of interruption to the diode pump source. Serious modulation to the pump field, and therefore the signal and idler, was evident on the microsecond time scale due to both the susceptibility of the ICSRO to the onset of relaxation oscillations and the longevity of the oscillations once triggered. Weeks of operation saw the performance of the system deteriorate due to the degradation of the PPLN crystal. We attributed this to a chemical reaction between the crystal and the brass oven in which it was housed; no further deterioration was observed once a stainless steel replacement had been implemented.

The wavelength of the signal and idler pair was tuned by varying the PPLN crystal temperature and grating period. We obtained a total tuning range of 3.1 - 4.0μm (900nm) in the idler and 1.4 – 1.7μm (160nm) in the resonant signal. An idler tuning range of ~300nm was obtained on each grating period by varying the crystal temperature over the range 35-180°C. The bandwidth of the pump field, and therefore the idler output, was ~1GHz. The signal field resonated on a single longitudinal mode.

The intracavity lens served to compensate for the effects of PPLN thermal lensing, as evident from the power performance after diode pump power interruption and the stable fundamental spatial profile of the SFM output, resultant from non phase matched mixing of the pump and signal fields.

The system described in chapter 4 demonstrates the merits of the intracavity approach, married with broad tunability of the OPO brought about by employing a QPM nonlinear crystal even when the pump laser is incapable of significant tuning, and the compact, efficient and simple pump laser design facilitated by the diode pumping of a solid state

laser. The only significant problem associated with this device was its susceptibility to the onset of relaxation oscillations. The application of this system to the fields of spectroscopy or interferometry will be severely hampered unless this issue can be addressed.

The success of the system outlined in chapter 4 was capitalised upon in the work described in chapter 5. The diode pump laser was power scaled to a 15W, fibre coupled device. To reduce the thermal stresses in the Nd:YVO_4 crystal due to the enhanced pump power, the doping was reduced from 1 to 0.5%, which increased the absorption depth and hence a longer crystal was employed to maximise diode pump absorption. Two SRO's were realised with this pump system, one based on a 25mm PPLN crystal identical to that used in chapter 4, apart from interaction length, the other utilising the new nonlinear QPM material PPRTA which was 20mm long with a single 39.6μm grating. As well as the thermal issues associated with the nonlinear crystal due to the very high field circulating within the laser cavity, the thermal lens formed in the Nd:YVO_4 crystal was also a major parameter in the design of the cavity. Although this thermal lens was rooted principally in the absorption of the diode pump power, the circulating field was also found to have a significant impact upon it.

The two SRO's were characterised and contrasted. Although the nonlinearity and interaction length of the PPRTA was less than that of the PPLN, the performance of the SRO based on this crystal was comparable or superior to that of the system based on the PPLN crystal, attributed to its robust thermal performance. The observed SRO threshold in both systems was significantly higher than theoretical prediction due to increased mode size in the nonlinear crystal as the thermal lens in the Nd:YVO_4 / nonlinear crystal augmented. Significant lensing in the case of PPLN reduced the slope efficiency of the circulating field as the external diode pump power was increased. This meant that PPRTA OPO threshold was obtained for a lower diode pump power, albeit higher circulating field (4.2W diode pump power, 65W circulating field) than in the case of PPLN (8.0W diode pump power, 30W circulating field). Almost no clamping of the intracavity field was evident in either system, again attributed to the onset of thermal lensing within the laser cavity. Both devices produced ~440mW of extractable two-way idler for a diode pump power of 12W; beyond this the idler power declined as thermal effects impacted upon the

laser cavity. This corresponds to 1.61W of total down converted power. Obtaining a value of the down conversion efficiency was made difficult by the modification of the laser cavity due to thermal lensing as the circulating field was increased.

Relaxation oscillations were initially present in both systems. The inclusion of an extra mirror in the signal cavity which was highly reflecting at the signal wavelength, highly transmitting at the pump wavelength, served to reduce interferometric feedback of the pump from the signal mirror. This eliminated relaxation oscillations in the case of the PPRTA ICSRO but made little difference to the PPLN system due to the dominance of the thermal air current triggering mechanism.

The spatial mode and long term idler power stability exhibited by the ICSRO based on PPRTA was superior to that of PPLN. The RMS amplitude noise was ~11% in the case of PPRTA and ~20% in the case of PPLN.

The temperature of the PPRTA crystal was varied over the range 10-100°C in order to tune the signal and idler wavelengths. We obtained a tuning range of 1.522 - 1.546μm (26nm) in the signal, 3.538 – 3.404μm (133nm) in the idler. The Sellmeier equations of Fradkin-Kashi [11] were found to be in excellent agreement with the signal and idler wavelengths at room temperature. An empirical modification to the dn/dt expression of Karlsson [12] gave very good agreement between observed and predicted tuning behaviour.

A separate cavity geometry was designed and implemented which showed more robust performance in the face of thermal lensing in the laser gain and nonlinear materials. A lens was used to desensitise the cavity to the Nd:YVO_4 thermal lens, an off axis curved mirror performed this function for the PPRTA. Although the total extracted idler power from this system was less than previously observed, the linear nature of the idler output with increasing diode pump power and excellent spatial quality of the SFM mode indicated that this cavity was much more impervious to thermal issues than the previous cavity geometry, and also pointed towards the possibility of power scaling the diode pump source.

We see, then, that in a high power system such as this, it is the thermal issues which dominate the cavity design and operational performance. Although the PPLN crystal has a higher nonlinearity and is available in longer interaction lengths in comparison to PPRTA, it was the system based on PPRTA which exhibited superior performance. The higher circulating field resident within the pump field meant that the ICSRO could tolerate more loss in the signal cavity introduced by the extra high transmission pump mirror. Crucially, this reduced interferometric feedback of the pump to the point at which the relaxation oscillations in this system were eliminated. We believe that a similar effect was not evident in the case of the PPLN ICSRO due to the thermal 'shimmering' effects of the oven dominating the relaxation oscillation triggering process.

In chapter 6, we derived a set of rate equations which govern the dynamics of the ICSRO system in an attempt to model the relaxation oscillations and obtain a strategy to eliminate them from the system. Six feedback 'options' were considered to this end and simulated in a numerical model.

Introducing optical loss into the pump cavity and modulating it as a function of the instantaneous power resonating in the signal cavity, or vice versa, was found to have little impact on the damping time of the system due to the phase difference between the oscillations in each cavity. Introducing loss into the signal cavity and modulating as a function of the instantaneous signal field did have a very significant impact on the damping time of the oscillations, but the system took many upper state lifetimes to completely return to the steady state condition. We found that the very high upper state lifetime of the laser gain medium in comparison to the oscillation period of the relaxation oscillations made it act as an 'optical capacitor', making external diode pump power modulated by the instantaneous power circulating in the field in the pump cavity ineffectual. Indeed, negligible difference in the model was noticed when the upper state population was made independent from the power in the circulating field by setting this parameter to unity for all t.

Modelling an introduction of loss into the pump cavity and varying it as a function of pump power led to excellent suppression of the relaxation oscillations once triggered. We saw that increasing the magnitude of the feedback to the point at which a ~10% drop in signal power was experienced led to the oscillation damping time reduced from ~12 to

0.005 upper state lifetimes. At higher feedback effects, the oscillations became critically damped, the time taken to return to the steady state then limited by the photon lifetime of the respective cavities. The model of nonlinear loss in the pump cavity which scaled with the square of the pump power gave even more encouraging results and pointed to a feedback scheme which was totally passive. We noted that the magnitude of the feedback effect could be varied by varying the focussing of the pump field in the nonlinear SHG crystal or changing the temperature, and hence the phase matching condition, in the case of a QPM crystal.

7.3 Future work

To decide on a strategy to carry this research forward, it is necessary to identify eventual applications or desired attributes of any device that may be developed, and relate that to the present state of the art in the context of this thesis.

The most obvious application for a system such as this is mid infrared spectroscopy, environmental monitoring of pollutants or interferometric surface inspection. Applications such as this of course imply the use of single frequency idler to produce reasonable resolution. This implies that the pump field resonating within the ICSRO must oscillate on a single longitudinal mode (as we have seen, the signal mode naturally oscillates in this manner), resulting in a single frequency idler. Throughout the course of this research, almost no effort was expended in controlling the longitudinal mode structure of the pump laser, which was allowed to oscillate on as many modes as it would support. There are four strategies which one can readily implement in order to achieve single frequency oscillation of the pump field:

- Reduce the length of the pump laser cavity to the point at which its free spectral range becomes comparable or larger than the gain bandwidth of the laser gain medium.

- Include intracavity étalons to introduce loss to all but one of the longitudinal modes.

- Seed the pump laser with an external low power single frequency laser

- Redesign the pump cavity in order to abandon the standing wave geometry in favour of a ring cavity with an intracavity unidirectional device.

With the accommodation of the additional intracavity components necessary to make the ICSRO operational within the cavity of the pump laser, it is difficult to envisage how the length of the laser cavity could be reduced to the point where the free spectral range would exceed the laser gain bandwidth. For Nd:YVO_4, with a gain bandwidth of ~200GHz, the laser cavity length would have to be on the order of 1mm long. However, a combination of cavity length reduction and the inclusion of a suitable intracavty étalon to suppress longitudinal modes oscillating away from line centre would be straight forward to implement experimentally. Significant reductions in cavity length and complexity could be achieved by the use of a semi-monolithic nonlinear crystal, that is, a nonlinear crystal with a high reflection dielectric coating applied directly to one of its surfaces. Such a scheme would eliminate the need for the common end mirror (M2 in figures 4.12 and 5.18) and the space between this and the nonlinear crystal. This would, of course, lead to non-confocal focussing in the nonlinear crystal as the beam waist would now be placed on the high reflector face of the crystal which would in turn lead to an increase in threshold, a drop in conversion efficiency, and hence idler output power; this would be somewhat offset by the drop in inctracavity loss which this cavity design would facilitate.

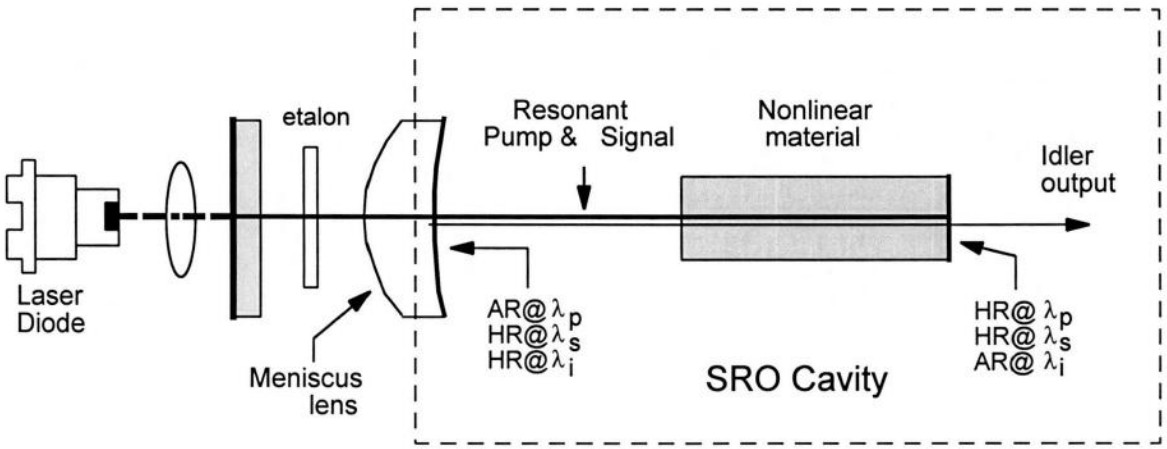

Figure 7.1: *Possible cavity configuration of a single frequency, in line semi-monolithic ICSRO.*

Further significant reductions in the signal cavity loss and overall system complexity could be brought about by the use of a meniscus lens in place of the convex lens used in the present cavity designs. Both sides of this optic would be antireflection coated for the pump, with the concave surface highly reflective at the signal wavelength. This 'in line' beam splitter configuration would eliminate the need for the outboard signal mirror in the cavity designs outlined in this thesis, reducing signal loss and making the entire system 'uniaxial', a significant step forward in the process of producing an inexpensive, robust and, from an engineering perspective, volume production suitable device. Intracavity étalons could be placed between the meniscus lens and the laser gain medium where only the resonating pump field is present. A schematic of such a device appears in figure 7.1.

We can see here that the dielectric coating on the concave surface of the meniscus lens is specified to be highly reflecting at the idler, double passing the idler so that all of this field exits the system in one coaxial beam, doubling the output power and leading to a reduction in OPO threshold. We have seen that interferometric feedback from antireflection coated components can trigger relaxation oscillations and so the antireflection coating on the meniscus lens at the pump wavelength would have to extremely well specified.

All of the PPLN ICSRO systems outlined in this thesis suffered from chronic relaxation oscillation problems, whilst the PPRTA system described in chapter 5 did not after the interferometric triggering mechanism had been removed. We believe that the necessity to enclose the PPLN crystal within a high temperature oven introduces air currents to the cavity which dominate the triggering process. We have seen that the PPRTA system outperformed its PPLN based counterpart in every respect, except for the tunability of its output, due to its reduced dispersion of refractive index with temperature and single crystal grating availability. By implementing the system outlined in figure 7.1 with a PPRTA crystal and ensuring that all coatings are specified such that interferometric feedback issues are obviated, it should be possible to construct a device which will operate in the absence of relaxation oscillations without the need for any of the feedback schemes discussed in chapter 6. The ability to realise such a device without the need for an intracavity oven would also reduce cost, complexity and power requirements. Since commencing this research, diode laser technology has progressed to the point where 3W,

200×1μm stripe *c*-packaged diodes are readily available. Such a pump source could be implemented to offset the reduced nonlinearity of the PPRTA in comparison to PPLN and the non-confocal focussing of this cavity geometry. Further developments will no doubt lead to the availability of PPRTA crystals with longer interaction lengths and multiple / fanned grating periods. To obtain a stable idler output in frequency space, the PPRTA crystal would still need to be temperature stabilised via a servo-locked thermoelectric device, but this would introduce almost none of the thermal 'shimmering' which was so prevalent in the presence of the PPLN oven. If broad tunability is not a requirement from the system, the reduced d*n*/d*t* coefficient of the PPRTA would be advantageous as this would relax the temperature stability requirements of the servo loop whilst still obtaining frequency stable idler output.

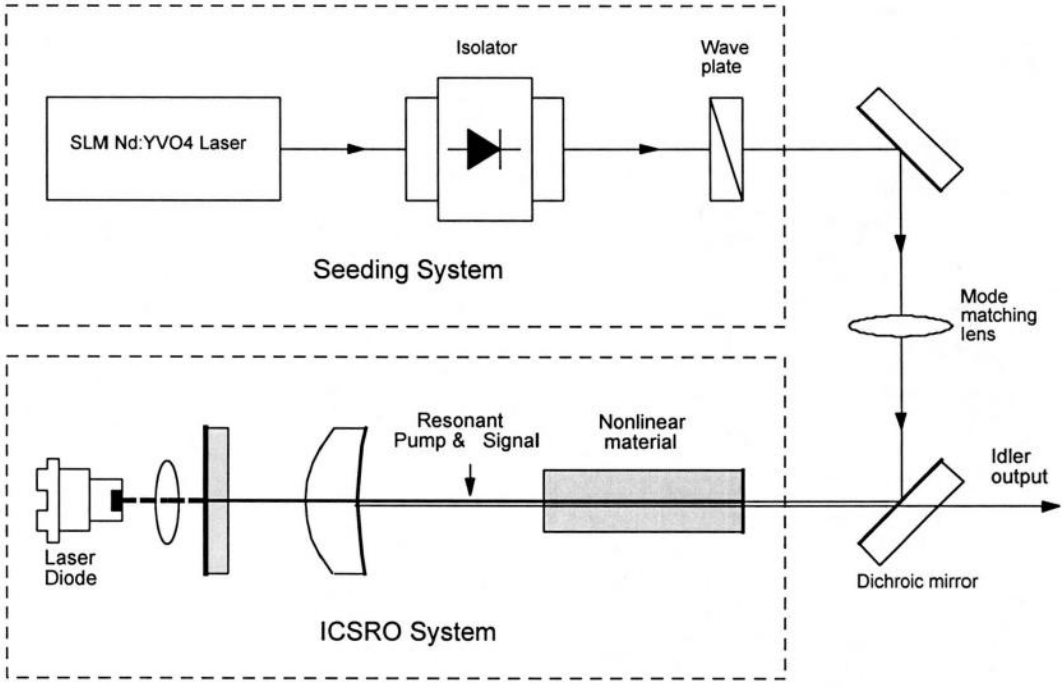

Figure 7.2: *Injection seeded ICSRO system.*

Such a system would be easy to implement both experimentally and commercially in a compact package, would be a broadly tuneable source of single longitudinal mode mid infrared light at the >10's mW power level, could be fine tuned by tilting the intracavity etalon and importantly would not be an expensive system to produce.

The system outlined above would be compatible with the injection seeding mechanism previously mentioned in order to induce single frequency operation of the 1.064μm pump field. Such a scheme would take the form of the system outlined in figure 7.2.

Not shown in this diagram is the locking mechanism that would have to be in place in order to keep the ICSRO pump cavity on resonance with the single frequency seed laser, or vice versa. Such a locking mechanism would almost certainly be based upon the Pound-Drever r.f. locking scheme [13]. The isolator is included to prevent leaking pump or reflected seeding field disrupting the single frequency operation of the seed laser. The half-wave wave plate serves to compensate for the polarisation rotation introduced by the optical isolator. This system would produce a single frequency pump field resonant within the ICSRO, and therefore a single frequency idler. Although the addition of the seed laser significantly adds to the complexity of the system, the frequency of the idler could be scanned extremely precisely by locking the ICSRO pump cavity to the seed laser, then scanning the seed frequency over the gain bandwidth of its laser gain medium in order to obtain >10's GHz tuning in the idler. Such a system would be ideal for high resolution spectroscopic applications: the idler could be tuned to the wavelength range of interest by temperature tuning of the nonlinear material, then scanning over perhaps an absorption feature with the seeding laser. Seeding the ICSRO may also reduce the susceptibility of the ICSRO to the effects of relaxation oscillations [14].

A system such as this would present more problems in terms of practical applicability and commercialisation. The addition of the seed laser and associated locking electronics would significantly increase the component cost of the system, due to expensive items such as the SLM seed laser, the optical isolator and the r.f. phase modulator used by the Pound-Drever locking mechanism.

We finally consider the possibility of placing the SRO within the cavity of a ring laser. With the effects of spatial hole burning within the laser gain medium removed by the travelling wave nature of the circulating field, the laser naturally oscillates on a single longitudinal mode at gain centre. ICSRO systems pumped internal to ring lasers have been implemented using argon ion pumped titanium sapphire lasers [15]. Such systems mandate the use of intracavity unidirectional devices in order to force the resonating field

to circulate in the desired direction by introducing a fraction of a percent of loss in the undesired direction. The principal difficulty in the implementation of SRO's operating internal to a ring laser is that the parametric process represents a loss of several percent in the direction the laser is oscillating. This loss dominates over the unidirectional device loss within the cavity and induces the laser to oscillate in the wrong direction. Intracavity unidirectional devices will have to be improved to offer significant discrimination in order for ring based ICSRO to offer robust performance. Again, injection seeding may obviate this problem, but the complexity and expense of implementing an SRO pumped internal to a seeded ring oscillator would limit such a device to the research laboratory in the short to medium term. Power scaling of the diode pump would be necessary as the circulating field experiences gain only once on its round trip, rather than twice in the case of the standing wave cavity.

7.4 Summary

In this thesis we have presented various all solid state laser devices capable of providing >10's to >100's mW of cw tuneable coherent laser light in compact geometries which, due to the elegance of the intracavity technique, require only modest external pump powers. We have seen how a synergy of diode pumped solid state laser technology, novel quasi phase matching schemes and the intracavity process have enabled the implementation of these systems to be simple and straight forward in cost effective designs. Further research will enable the potential of these devices to be realised both in the laboratory and commercial sectors, opening up a rich new field of applications for mid infrared coherent sources at these power levels.

References

1 R. C. Eckardt, C. D. Nabors, W. J. Kozlovsky and R. L. Byer, "Optical Parametric Oscillator Frequency Tuning and Control," *Journal of the Optical Society of America B-Optical Physics* **8**, 647-667 (1991).

2 A. J. Henderson, M. J. Padgett, F. G. Colville, J. Zhang and M. H. Dunn, "Doubly-resonant optical parametric oscillators: Tuning behaviour and stability requirements," *Optics Communications* **119**, 256 (1995).

3 W. R. Bosenberg, A. Drobshoff, J. I. Alexander, L. E. Myers and R. L. Byer, "93% pump depletion, 3.5-W continuous-wave, singly resonant optical parametric oscillator," *Optics Letters* **21**, 1336 (1996).

4 D. J. M. Stothard, M. Ebrahimzadeh and M. H. Dunn, "Low pump threshold, continuous-wave, singly resonant, optical parametric oscillator," *Optics Letters* **23**, 1895 (1998).

5 L. E. Myers, *Periodically poled materials for nonlinear optics*. in *Advances in lasers and applications,* D. M. Finlayson, B. D. Sinclair, Eds. (Scottish Universities Summer School in Physics, Edinburgh, 1998).

6 M. M. Fejer, G. A. Magel, D. H. Jundt and R. L. Byer, "Quasi-Phase-Matched Second Harmonic Generation: Tuning and Tolerances," *IEEE Journal of Quantum Electronics* **QE-28**, 2631 (1992).

7 M. K. Oshman and S. E. Harris, "Theory of Optical Parametric Oscillation Internal to the Laser Cavity," *IEEE Journal of Quantum Electronics* **QE-4**, 491-502 (1968).

8 G. A. Turnbull, M. H. Dunn and M. Ebrahimzadeh, "Continuous-wave, intracavity optical parametric oscillators: an analysis of power characteristics," *Applied Physics B-Lasers and Optics* **66**, 701 (1998).

9 W. Koechner, *Solid-State Laser Engineering*. A. L. Schawlow, Ed., (Fifth ed.) (Springer, 1999).

10 W. R. Bosenberg, A. Drobshoff, J. I. Alexander, L. E. Myers and R. L. Byer, "Continuous-wave singly resonant optical parametric oscillator based on periodically poled LiNbO3," *Optics Letters* **21**, 713 (1996).

11 K. Fradkin-Kashi, A. Arie, P. Urenski and G. Rosenman, "Characterization of optical and nonlinear properties of periodically-poled RbTiOAsO4 in the mid-infrared range via difference-frequency generation," *Applied Physics B-Lasers and Optics* **71**, 251-255 (2000).

12 H. Karlsson, F. Laurell, P. Henriksson and G. Arvidsson, "Frequency doubling in periodically poled RbTiOAsO4," *Electronics Letters* **32**, 556-557 (1996).

13 R. W. P. Drever, J. L. Hall, F. V. Kowalski, J. Hough, G. M. Ford, A. J. Munley and H. Ward, "Laser Phase and Frequency Stabilisation Using an Optical Resonator," *Applied Physics B-Lasers and Optics* **31**, 97-105 (1983).

14 G. A. Turnbull, *personal communication* (1999).

15 T. J. Edwards, *Continuous-wave, singly-resonant optical parametric oscillation internal to the Ti: sapphire laser*, thesis, St. Andrews University (2000).

Appendix A: Numerical model of relaxation oscillations – MathCAD worksheets

We present the numerical model solved using mathematical routines written in MathCAD. These programs operate by defining a three element vector array D(t,x), where t simulates the passing if time and x is another three element array in which the coupled rate equations reside. The runge-kutta operator *rkfixed* is then implemented to obtain a numerical solution for the system. In the worksheet, $x_0 \equiv P_s$, $x_1 \equiv P_p$ and $x_2 \equiv N_j$. Obtaining suitable values of x, σ, τ_u, τ_p and τ_s are discussed below

From the discussion in chapters 2 and 6, and references [2,3,5] found in this latter chapter, we obtain

$$\mathfrak{P}_{operate} = (1+x) \tag{A-1}$$

$$\mathfrak{P}_{laser\_threshold} = \frac{(1+x)}{\sigma} \tag{A-2}$$

$$\mathfrak{P}_{opo\_threshold} = 1 \tag{A-3}$$

Where the $\mathfrak{P}$ parameters represent the diode pump power, in absolute units, at the conditions indicated by the subscripts. We see, then, that

$$\sigma = \frac{\mathfrak{P}_{operate}}{\mathfrak{P}_{laser\_threshold}} \tag{A-4}$$

$$x = \left(\frac{\mathfrak{P}_{operate}}{\mathfrak{P}_{laser\_threshold}} \right) - 1 \tag{A-5}$$

This, then enables us to obtain values for σ and x, derived from experimentally observed values. From chapter 4, we saw that laser and OPO threshold occurred at 63 and 330mW, respectively. We also mentioned, however, that the performance of the system

deteriorated due to detrimental change in the nonlinear crystal. As this analysis was derived, it was hoped to implement some of the feedback options outlined in chapter 6, and so it was the laser and OPO thresholds under the reduced performance characteristics which were used. It this case, the laser and OPO threshold were 100 and 560mW, respectively. We therefore obtain values of σ and x of 10 and 0.79, respectively, for an operational pump power of 1W.

Note that the parameter x is denoted k in the worksheet.

τ_u, τ_p and τ_s represent the upper state lifetime and the photon lifetimes in the pump and signal cavities, respectively. These values are normalised to the upper state lifetime. With a round trip cavity loss of ~3% in each cavity, and using the expression

$$\tau = \frac{2 \cdot l}{c \cdot \beta} \tag{A-6}$$

where l is the length of the pump or signal cavity, and β the round trip loss, we obtain values of τ_p=80nS and τ_s=44ns. Normalised to the upper state lifetime of 200μS, we obtain values of τ_u=1, τ_p=0.0004 and τ_s=0.00022.

Nd:YVO_4 ICOPO Coupled Rate Equations

Option "A" : OPO Cavity loss dependant upon Pump field

$\tau_s := .0004$ Signal Cavity Lifetime

$\tau_p := .00022$ Pump Cavity Lifetime

$\tau_u := 1$ Upper-State Lifetime

$\sigma_j := 10$ Pumping rate

$k := .79$ Clamping constant

$P_p := 1.0$

$P_s := 1.1$

$n_j := 1.0$

Starting Conditions for Pump, Signal and Population Inversion

$$x := \begin{pmatrix} P_s \\ P_p \\ n_j \end{pmatrix}$$

$$D(t,x) := \begin{bmatrix} \frac{x_0}{\tau_s}\cdot\left[x_1 - 1 - \delta s\cdot(x_1 - 1)\right] \\ \frac{x_1}{\tau_p}\cdot\left[\frac{x_2\cdot\sigma_j}{1+k} - 1 - \frac{(\sigma_j - 1 - k)\cdot x_0}{1+k}\right] \\ \frac{1 + k - x_2 - (k\cdot x_1\cdot x_2)}{\tau_u} \end{bmatrix}$$

$a := 0.02$ Calculate to this number of upper-state lifetimes

$Z := \text{rkfixed}(x, 0, a, 20000\cdot a, D)$ Calculate equations

$r := 50$ x-range of graph below $r := \text{if}(r > a, a, r)$

$n := 0 .. (r\cdot 20000)$ $\delta s \equiv 0.8$

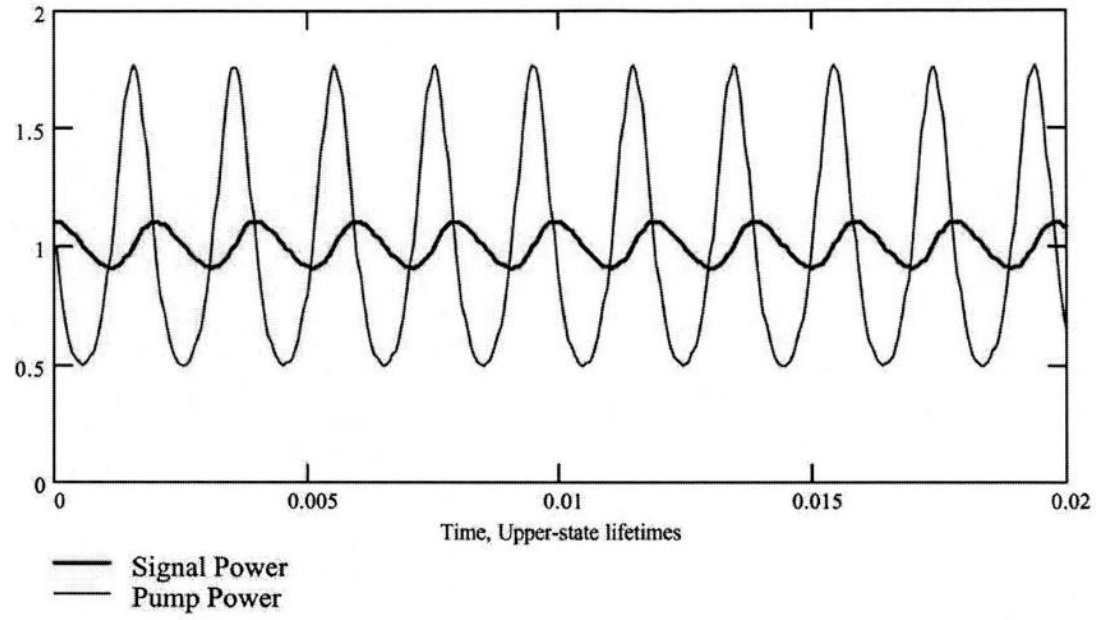
2
1.5
1
0.5
0
0
0.005
0.01
0.015
0.02
Time, Upper-state lifetimes
Signal Power
Pump Power

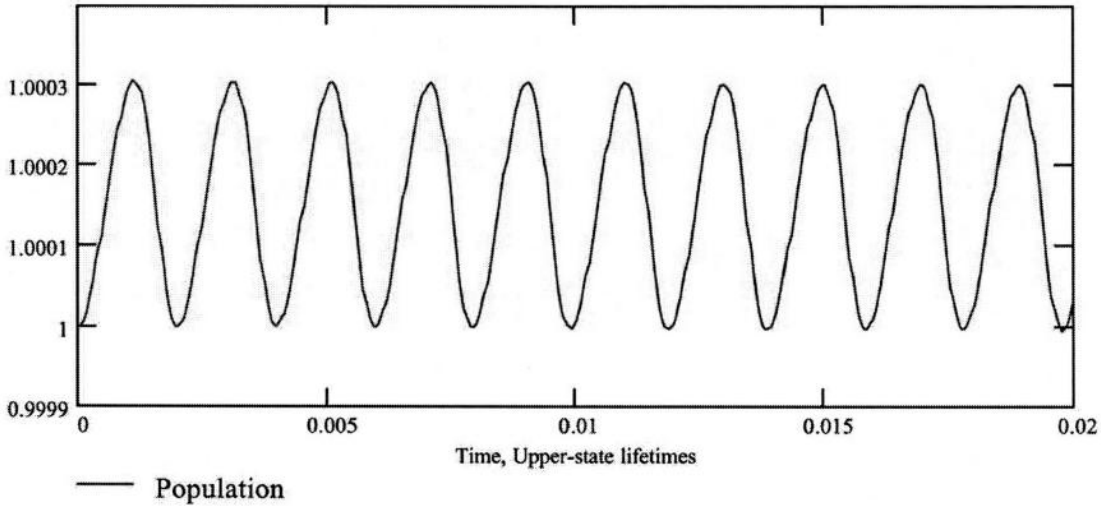
1.0003
1.0002
1.0001
1
0.9999
0
0.005
0.01
0.015
0.02
Time, Upper-state lifetimes
Population

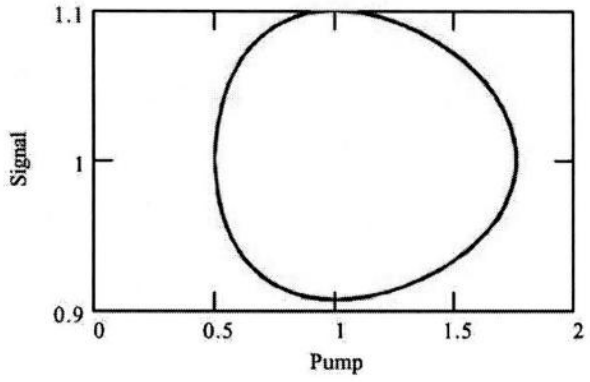
1.1
1
0.9
Signal
0
0.5
1
1.5
2
Pump

Nd:YVO_4 ICOPO Coupled Rate Equations

Option "B" : Pump Cavity loss dependant upon Signal field

$\tau_s := .0004$ Signal Cavity Lifetime

$\tau_p := .00022$ Pump Cavity Lifetime

$\tau_u := 1$ Upper-State Lifetime

$\sigma_j := 10$ Cross Section

$k := .79$ Constant

$P_p := 1.0$

$P_s := 1.1$

$n_j := 1.0$

Starting Conditions for Pump, Signal and Population Inversion

$$x := \begin{pmatrix} P_s \\ P_p \\ n_j \end{pmatrix}$$

$$D(t,x) := \begin{bmatrix} \frac{x_0}{\tau_s}\cdot(x_1 - 1) \\ \frac{x_1}{\tau_p}\cdot\left[\frac{x_2\cdot\sigma_j}{1+k} - 1 - \frac{(\sigma_j - 1 - k)\cdot x_0}{1+k} - \delta p\cdot(x_0 - 1)\right] \\ \frac{1 + k - x_2 - (k\cdot x_1\cdot x_2)}{\tau_u} \end{bmatrix}$$

$a := .02$ Calculate to this number of upper-state lifetimes

$Z := \text{rkfixed}(x, 0, a, 20000\cdot a, D)$ Calculate equations

$r := 10$ x-range of graph below $r := \text{if}(r > a, a, r)$

$n := 0 .. (r\cdot 20000)$ $\delta p \equiv 0.8$

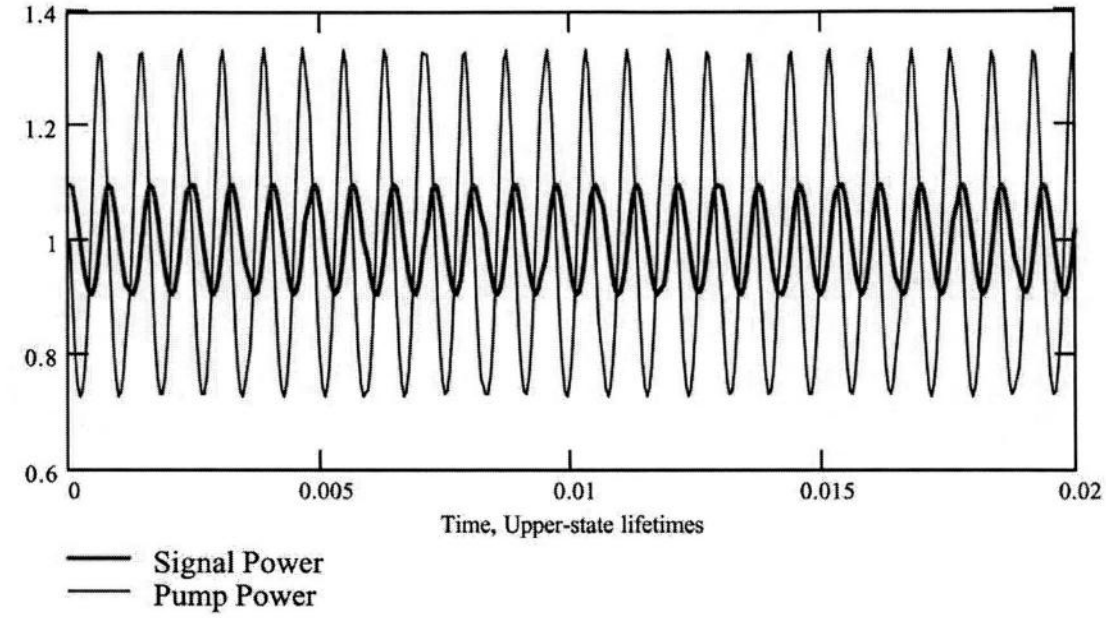
1.4
1.2
1
0.8
0.6
0
0.005
0.01
0.015
0.02
Time, Upper-state lifetimes
Signal Power
Pump Power

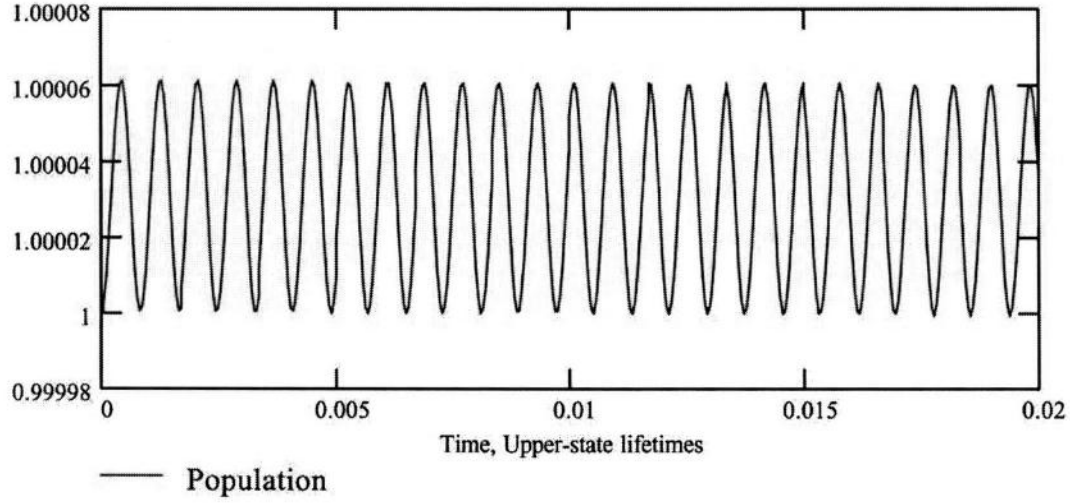
1.00008
1.00006
1.00004
1.00002
1
0.99998
0
0.005
0.01
0.015
0.02
Time, Upper-state lifetimes
Population

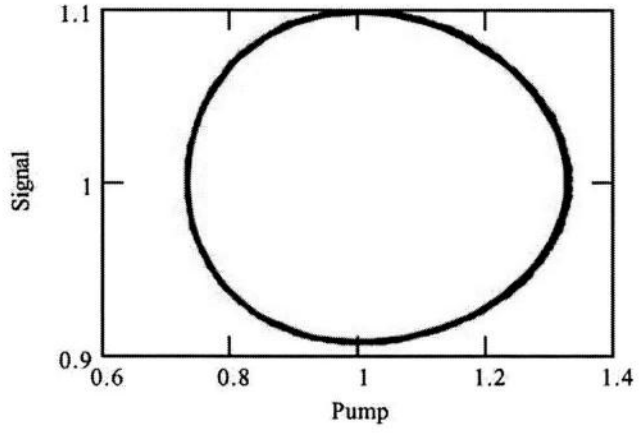
1.1
1
0.9
Signal
0.6
0.8
1
1.2
1.4
Pump

Nd:YVO_4 ICOPO Coupled Rate Equations

Option "C" : Pump Cavity loss dependant upon Pump field

$\tau_s := .0004$ Signal Cavity Lifetime

$\tau_p := .00022$ Pump Cavity Lifetime

$\tau_u := 1$ Upper-State Lifetime

$\sigma_j := 10$ Cross Section

$k := .79$ Constant

$P_p := 1.0$

$P_s := 1.1$

$n_j := 1.0$

Starting Conditions for Pump, Signal and Population Inversion

$$x := \begin{pmatrix} P_s \\ P_p \\ n_j \end{pmatrix} \qquad D(t,x) := \begin{bmatrix} \frac{x_0}{\tau_s}\cdot(x_1 - 1) \\ \frac{x_1}{\tau_p}\cdot\left[\frac{x_2\cdot\sigma_j}{1+k} - 1 - \frac{(\sigma_j - 1 - k)\cdot x_0}{1+k} - \delta p\cdot(x_1 - 0)\right] \\ \frac{1 + k - x_2 - (k\cdot x_1\cdot x_2)}{\tau_u} \end{bmatrix}$$

$a := 0.03$ Calculate to this number of upper-state lifetimes

$Z := \text{rkfixed}(x, 0, a, 20000\cdot a, D)$ Calculate equations

$r := 1$ x-range of graph below $r := \text{if}(r > a, a, r)$

$n := 0 .. (r\cdot 20000)$ $\delta p \equiv .1$

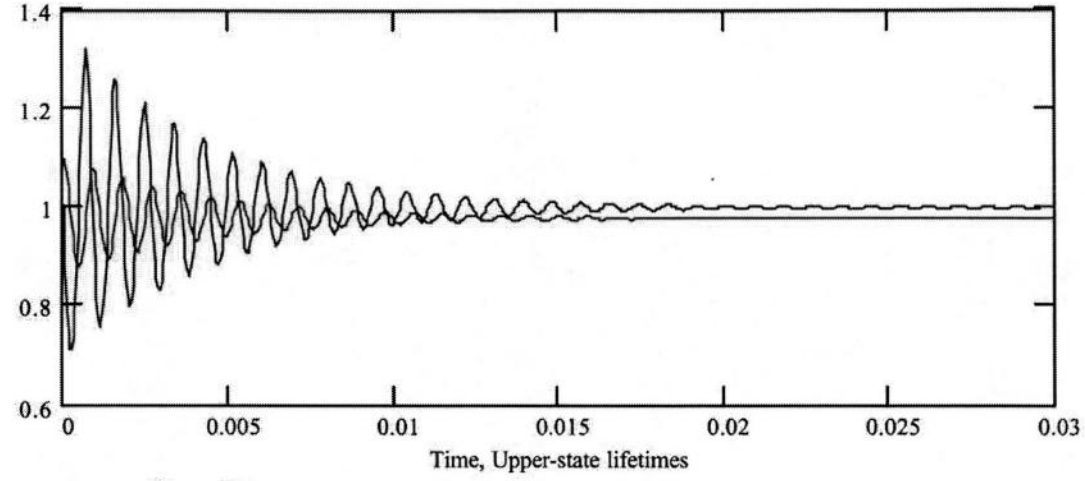
1.4
1.2
1
0.8
0.6
0
0.005
0.01
0.015
0.02
0.025
0.03
Time, Upper-state lifetimes
Signal Power
Pump Power

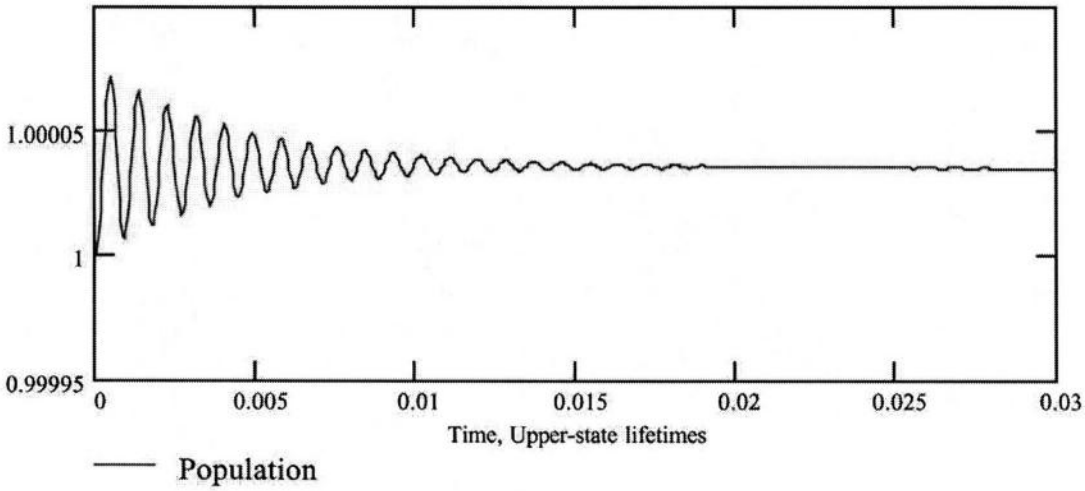
1.00005
1
0.99995
0
0.005
0.01
0.015
0.02
0.025
0.03
Time, Upper-state lifetimes
Population

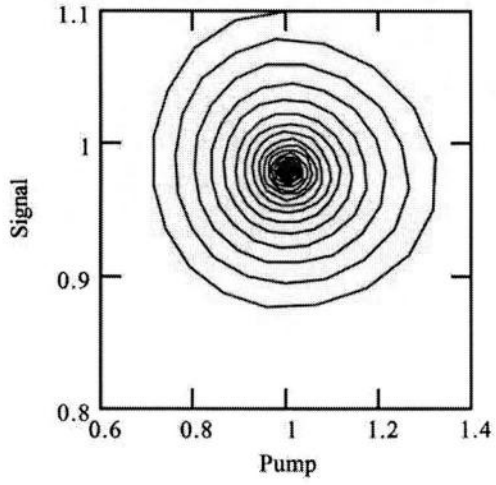
1.1
1
0.9
0.8
Signal
0.6
0.8
1
1.2
1.4
Pump

$Z_{500,1} = 0.978$

Nd:YVO_4 ICOPO Coupled Rate Equations

Option "D" : Signal Cavity loss dependant upon Signal field

$\tau_s := .0004$ Signal Cavity Lifetime

$\tau_p := .00022$ Pump Cavity Lifetime

$\tau_u := 1$ Upper-State Lifetime

$\sigma_j := 10$ Cross Section

$k := .79$ Constant

$P_p := 1.0$

$P_s := 1.1$ Starting Conditions for Pump, Signal and Population Inversion

$n_j := 1.0$

$$x := \begin{pmatrix} P_s \\ P_p \\ n_j \end{pmatrix}$$

$$D(t,x) := \begin{bmatrix} \frac{x_0}{\tau_s}\cdot\left[x_1 - 1 - \delta s\cdot\left(x_0 - 0\right)\right] \\ \frac{x_1}{\tau_p}\cdot\left[\frac{x_2\cdot\sigma_j}{1+k} - 1 - \frac{\left(\sigma_j - 1 - k\right)\cdot x_0}{1+k}\right] \\ \frac{1 + k - x_2 - \left(k\cdot x_1\cdot x_2\right)}{\tau_u} \end{bmatrix}$$

$a := .03$ Calculate to this number of upper-state lifetimes

$Z := \text{rkfixed}(x, 0, a, 20000\cdot a, D)$ Calculate equations

$r := 3$ x-range of graph below $r := \text{if}(r > a, a, r)$

$n := 0 .. (r\cdot 20000)$ $\delta s \equiv .1$

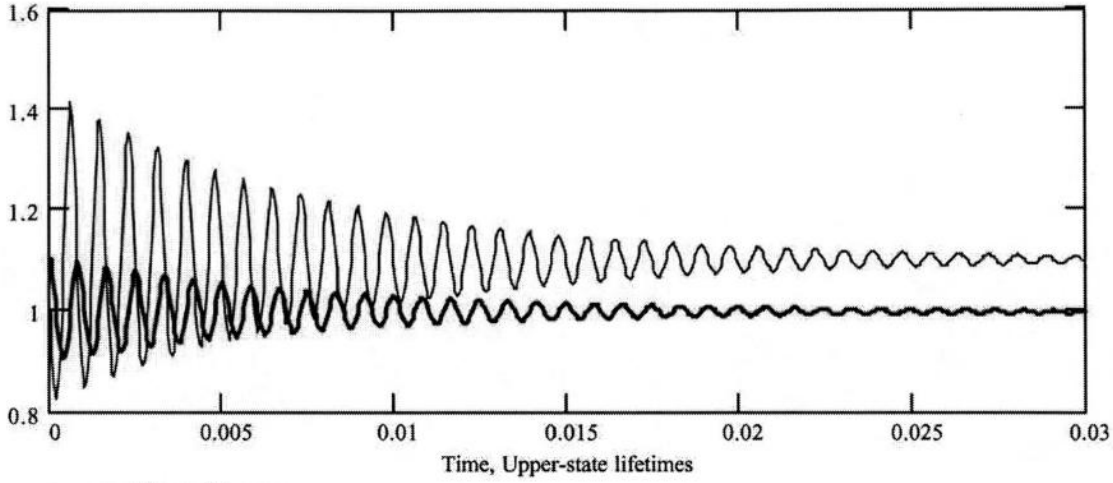
1.6
1.4
1.2
1
0.8
0
0.005
0.01
0.015
0.02
0.025
0.03
Time, Upper-state lifetimes
Signal Power
Pump Power

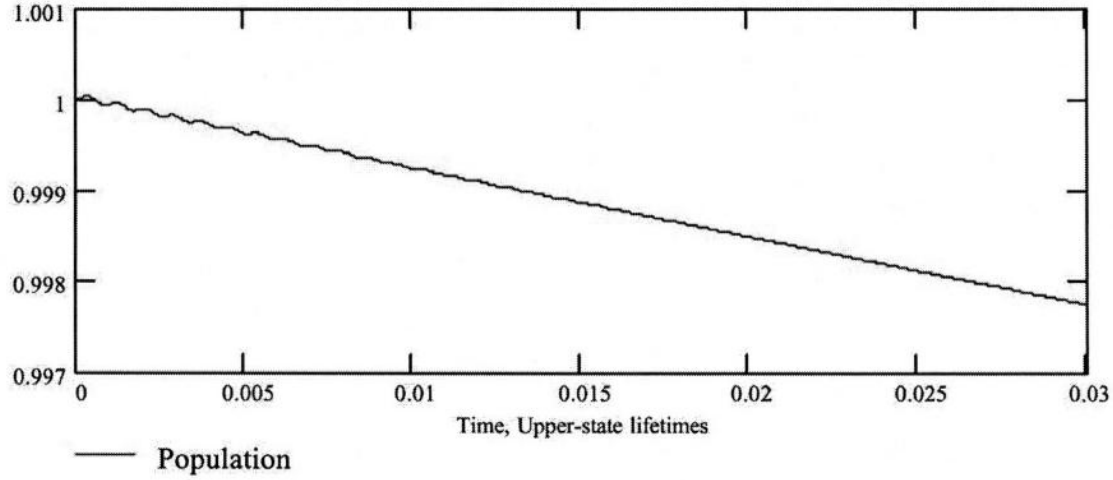
1.001
1
0.999
0.998
0.997
0
0.005
0.01
0.015
0.02
0.025
0.03
Time, Upper-state lifetimes
Population

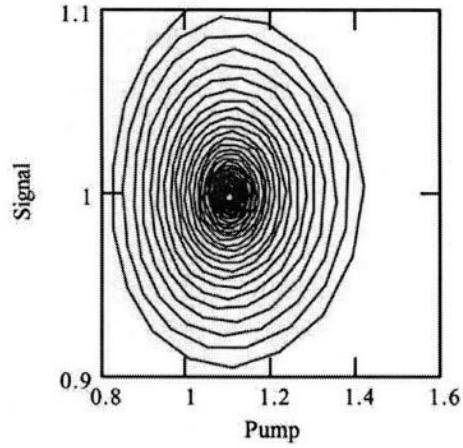
1.1
1
0.9
Signal
0.8
1
1.2
1.4
1.6
Pump

Nd:YVO_4 ICOPO Coupled Rate Equations

Option "E" : External pump power as a function of pump field

$\tau_s := .0004$ Signal Cavity Lifetime

$\tau_p := .00022$ Pump Cavity Lifetime

$\tau_u := 1$ Upper-State Lifetime

$\sigma_j := 10$ Cross Section

$k := .79$ Constant

$P_p := 1.0$

$P_s := 1.1$ Starting Conditions for Pump, Signal and Population Inversion

$n_j := 1.0$

$$x := \begin{pmatrix} P_s \\ P_p \\ n_j \end{pmatrix} \qquad D(t,x) := \begin{bmatrix} \frac{x_0}{\tau_s}\cdot(x_1 - 1) \\ \frac{x_1}{\tau_p}\cdot\left[\frac{x_2\cdot\sigma_j}{1+k} - 1 - \frac{(\sigma_j - 1 - k)\cdot x_0}{1+k}\right] \\ \frac{1 + k - x_2 - (k\cdot x_1\cdot x_2) - \delta P\cdot(x_1 - 1)}{\tau_u} \end{bmatrix}$$

$a := .03$ Calculate to this number of upper-state lifetimes

$Z := \text{rkfixed}(x, 0, a, 20000\cdot a, D)$ Calculate equations

$r := 3$ x-range of graph below $r := \text{if}(r > a, a, r)$

$n := 0 .. (r\cdot 20000)$ $\delta P \equiv 1$

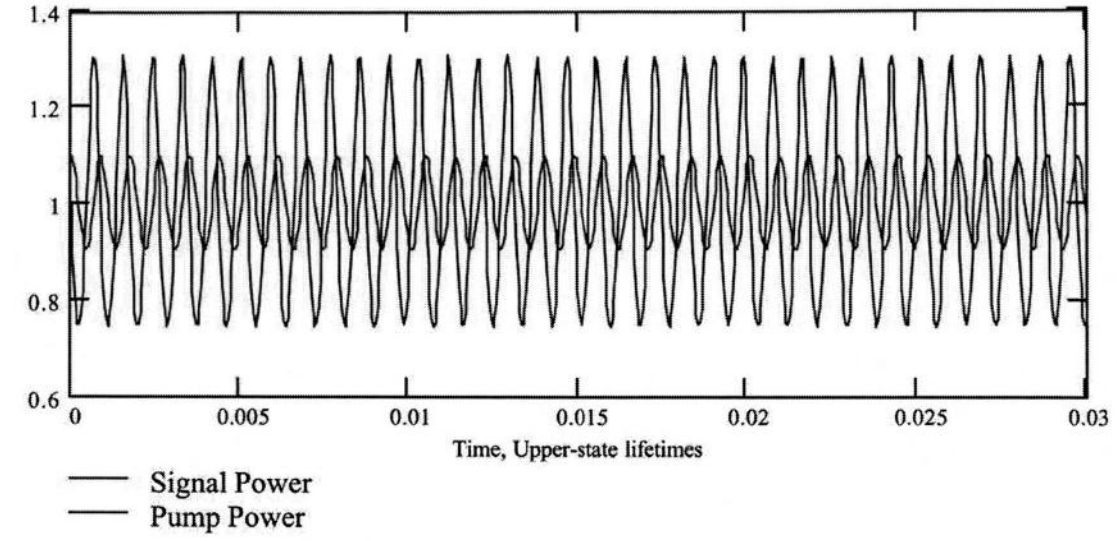
1.4
1.2
1
0.8
0.6
0
0.005
0.01
0.015
0.02
0.025
0.03
Time, Upper-state lifetimes
Signal Power
Pump Power

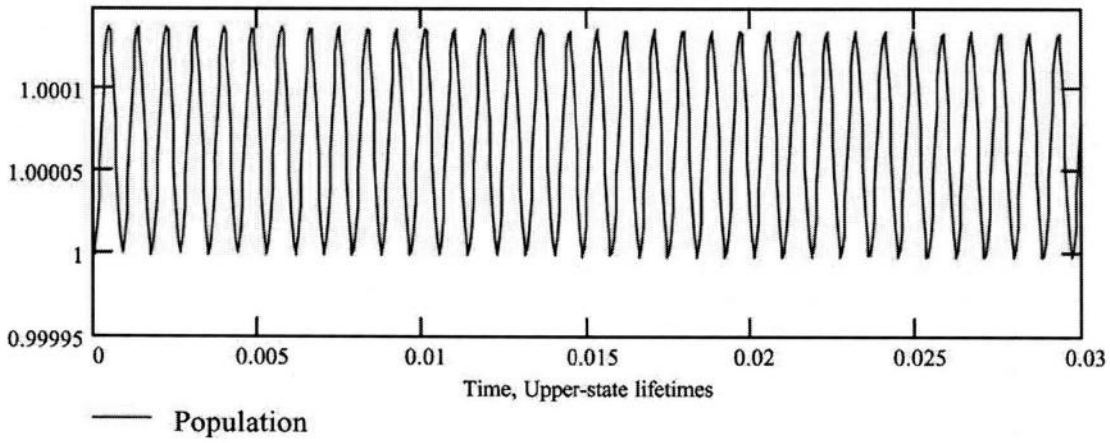
1.0001
1.00005
1
0.99995
0
0.005
0.01
0.015
0.02
0.025
0.03
Time, Upper-state lifetimes
Population

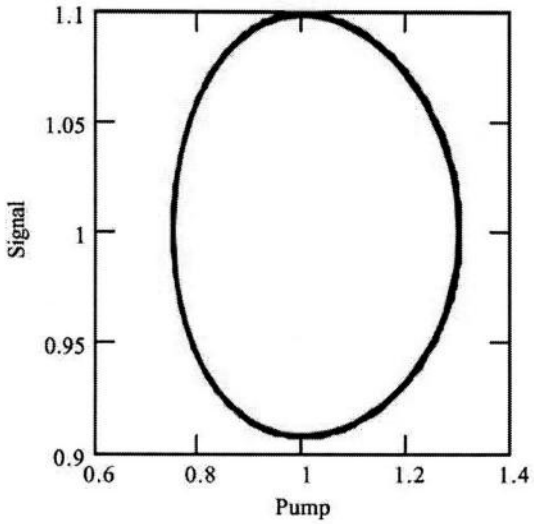
1.1
1.05
1
0.95
0.9
Signal
0.6
0.8
1
1.2
1.4
Pump

Nd:YVO_4 ICOPO Coupled Rate Equations

Option "F" : Non-Linear SHG Intracavity Loss

$\tau_s := .0004$ Signal Cavity Lifetime

$\tau_p := .00022$ Pump Cavity Lifetime

$\tau_u := 1$ Upper-State Lifetime

$\sigma_j := 10$ Cross Section

$k := 0.79$ Constant

$P_p := 1.0$

$P_s := 1.1$

$n_j := 1.0$

Starting Conditions for Pump, Signal and Population Inversion

$$x := \begin{pmatrix} P_s \\ P_p \\ n_j \end{pmatrix}$$

$$D(t,x) := \begin{bmatrix} \frac{x_0}{\tau_s}\cdot(x_1 - 1) \\ \frac{x_1}{\tau_p}\cdot\left[\frac{x_2\cdot\sigma_j}{1+k} - 1 - \frac{(\sigma_j - 1 - k)\cdot x_0}{1+k} - \delta p\cdot(x_1)^1\right] \\ \frac{1 + k - x_2 - (k\cdot x_1\cdot x_2)}{\tau_u} \end{bmatrix}$$

$a := 0.03$ Calculate to this number of upper-state lifetimes

$Z := \text{rkfixed}(x, 0, a, 20000\cdot a, D)$ Calculate equations

$r := 1$ x-range of graph below $r := \text{if}(r > a, a, r)$

$n := 0 .. (r\cdot 20000)$ $\delta p \equiv 0.01$

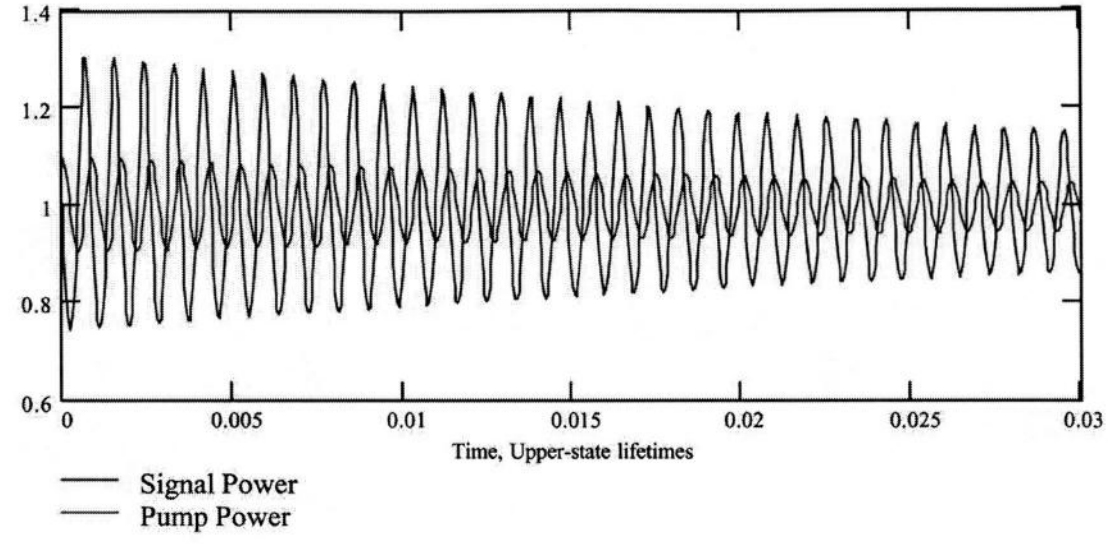
1.4
1.2
1
0.8
0.6
0
0.005
0.01
0.015
0.02
0.025
0.03
Time, Upper-state lifetimes
Signal Power
Pump Power

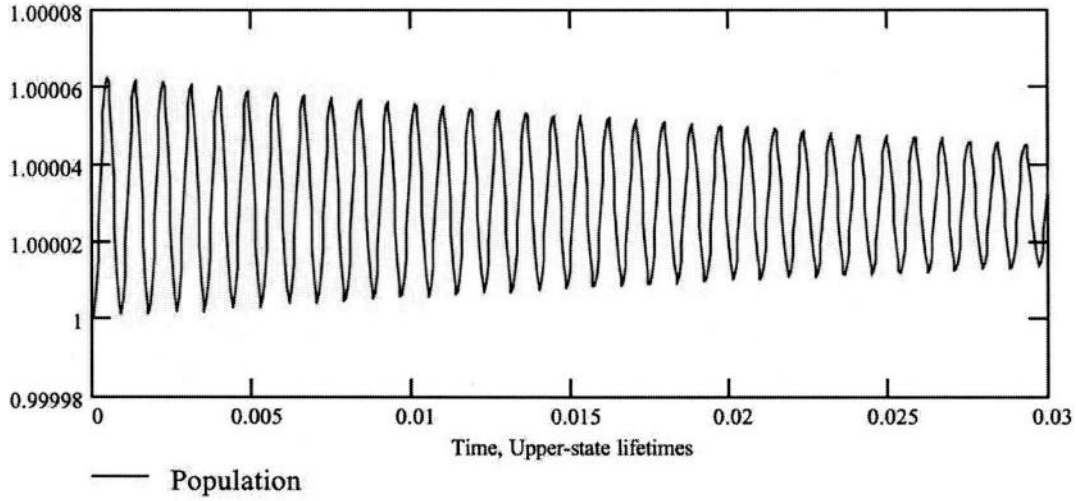
1.00008
1.00006
1.00004
1.00002
1
0.99998
0
0.005
0.01
0.015
0.02
0.025
0.03
Time, Upper-state lifetimes
Population

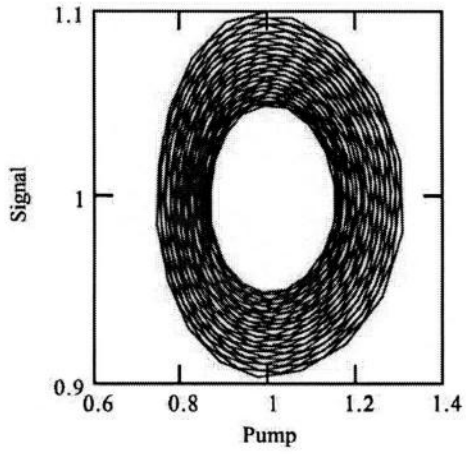
1.1
1
0.9
Signal
0.6
0.8
1
1.2
1.4
Pump

Appendix B: Journal publications and conference proceedings

B-1 Journal Publications

1 D. J. M. Stothard, M. Ebrahimzadeh and M. H. Dunn, "Low pump threshold, continuous-wave, singly resonant, optical parametric oscillator," *Optics Letters* **23**, 1895 (1998).

2 M. Ebrahimzadeh, G. A. Turnbull, T. J. Edwards, D. J. M. Stothard, I. D. Lindsay and M. H. Dunn, "Intracavity continuous-wave singly resonant optical parametric oscillators," *Journal of the Optical Society of America B - Optical Physics* **16**, 1499-1511 (1999).

3 G. A. Turnbull, D. J. M. Stothard, M. Ebrahimzadeh and M. H. Dunn, "Transient Dynamics of CW Intracavity Singly Resonant Optical Parametric Oscillators," *IEEE Journal of Quantum Electronics* **35**, 1666-1672 (1999).

4 C. Petridis, I. D. Lindsay, D. J. M. Stothard and M. Ebrahimzadeh, "Mode-hop-free tuning over 80GHz of an extended cavity diode laser without antireflection coating," *Review of Scientific Instruments* **72**, (2001).

5 D. J. M. Stothard, M. Ebrahimzadeh and M. H. Dunn, "A comparison of continuous-wave, singly-resonant intracavity optical parametric oscillators based upon periodically-poled $LiNbO_3$ and $RbTiOAaO_4$ pumped internal to a high power Nd:YVO_4 laser," *Submitted to Applied Physics Letters.*

B-2 Conference Proceedings

1 G. A. Turnbull, D. J. M. Stothard, M. Ebrahimzadeh and M. H. Dunn, "Transient dynamics of intracavity singly-resonant, continuous-wave optical parametric oscillators". *Conference on lasers and electro-optics 1999*, Baltimore, USA (May 1998).

2 T. J. Edwards, G. A. Turnbull, D. J. M. Stothard, M. H. Dunn and M. Ebrahimzadeh, "Laser sources for the near-to-mid infrared". *Physics research for Britain*, Oxford, UK (November 1998).

3 D. J. M. Stothard, P-Y Fortin, M. Ebrahimzadeh and M. H. Dunn, "Comparison of periodically-poled $LiNbO_3$ and $RbTiOAsO_4$ as nonlinear media in continuous-wave optical parametric oscillators pumped internal to an all-solid-state Nd:vanadate laser". *Conference on lasers and electro-optics 2001*, Baltimore, USA (May 2001).

4 C. Petridis, I. D. Lindsay, D. J. M. Stothard, M. H. Dunn and M. Ebrahimzadeh, "80 GHz mode hop free tuning of an extended cavity diode laser without antireflection coating". *Quantum electronics and photonics 15*, Glasgow, UK (September 2001).

5 A. Carleton, D. J. M. Stothard, M. Ebrahimzadeh and M. H. Dunn, "Continuous-wave singly resonant optical parametric oscillator based on periodically-poled $RbTiOAsO_4$". *Conference on lasers and electro-optics 2002*, Long Beach, USA (May 2002).